# The effects of cobalt and chromium ions and nanoparticles on macrophage and fibroblast behaviour

Jing Xu

Submitted in accordance with the requirements for the degree
of Doctor of Philosophy

School of Engineering and Materials Sciences
Queen Mary, University of London
March 2018

Supervisor: Professor Julia Shelton

## Statement of originality

I, Jing Xu, confirm that the research included within this thesis is my own work or that where it has been carried out in collaboration with, or supported by others, that this is duly acknowledged below and my contribution indicated.

I attest that I have exercised reasonable care to ensure that the work is original, and does not to the best of my knowledge break any UK law, infringe any third party's copyright or other Intellectual Property Right, or contain any confidential material.

I accept that the College has the right to use plagiarism detection software to check the electronic version of the thesis.

I confirm that this thesis has not been previously submit ted for the award of a degree by this or any other university.

The copyright of this thesis rests with the author and no quotation from it or information derived from it may be published without the prior written consent of the author.

Signature: Jing Xu

Date: 27/03/2018

## Acknowledgements

In the first instance, I would like to thank my supervisors Prof Julia Shelton for providing me with the opportunity to do the PhD and allowing me to develop as a researcher. Thank you, Prof Martin Knight and Dr Agata Nyga for the constant guidance and advice and for encouraging me through the various problems. I am also very grateful to Prof Wen Wang for encouraging me to apply for this PhD and the finance support of Chinese Scholarship Council.

I would like to acknowledge Junyao, Danielle, Xiaoli, Weiqi, Sufu, Shafir, Dongsheng, Steve for their help around the lab and passing on thier knowledge on a lot of techniques.

I would like to extend my gratitude to Dr Lingfang Zeng, Mazdak and Ana at King's College London for their support of the *in vivo* study.

I would like to thank Prof Alister Hart at Royal National Orthopaedic Hospital for his help in obtaining clinical samples and the patients that involved in this study.

Finally, I would like to express my gratitude to my friends and family for their support and understanding during the PhD.

## Abstract

Adverse tissue reactions to hip prostheses containing CoCr alloys have been widely reported, particularly for implants utilising a metal-on-metal bearing surface or, more recently, a modular taper junction and have been termed Adverse Response to Metal Debris (ARMD). Histological assessments of synovial tissues from patients at revision operation often demonstrate an extensive accumulation of macrophages and abundant tissue necrosis or fibrosis. The inflammatory response starts with the recruitment of immune cells and requires the egress of macrophages from the inflamed site for resolution of the reaction. Metal particles have previously been shown to affect cell migration but the effects of cobalt and chromium on macrophages' motility remain largely unknown.

*In vitro* and *in vivo* macrophage migration during exposure to cobalt and chromium ions and nanoparticles were examined in this thesis. Cobalt, but not chromium, was found to significantly reduced macrophage motility (>50%). This was found to involve an increase in both cell spreading and the formation of intracellular podosome-type adhesion structures, as well as enhanced cell adhesion to the extracellular matrix (ECM). The formation of podosomes was also associated with the production and activation of matrix metalloproteinase-9 (MMP9) and enhanced ECM degradation. These effects were driven by the down-regulation of RhoA signalling through the generation of reactive oxygen species (ROS).

The effect of the $Co^{2+}$ and $Cr^{3+}$ metal ions on tissue remodelling and pseudotumour formation which can lead to pain, swelling, limited range of joint movement and extensive tissue lesions, was explored using a multiscale approach. Both 2D and 3D *in* vitro culture systems were deplored to examine the effects of these ions on human fibroblast activation and mechanobiology. It was observed that $Co^{2+}$ induced a fibrotic response characterised by cytoskeletal remodelling and enhanced collagen matrix contraction. This was associated with an increase in cell stiffness (~45%) and contractile forces (~80%) measured by atomic force microscopy and traction force microscopy, respectively. These effects were also triggered by the generation of ROS. Moreover, this fibrotic response was enhanced in the presence of macrophages, which increased the prevalence of α-SMA positive fibroblasts and collagen synthesis. These events were verified *in vivo* by examining the synovial fibroblasts and tissues from hips of patients with metal-on-metal hip implants and patients undergoing primary hip replacement. The findings revealed that fibroblasts isolated from patients undergoing MoM revision THA were more biomechanically active than the control group. Moreover, synovial tissues from patients undergoing MoM revision THA displayed evidence of extensive tissue remodelling and fibrosis.

These findings revealed that cobalt leads to adverse tissue reactions via inducing macrophage retention, fibroblast-mediated matrix remodelling and modulating the interplay between macrophage and fibroblast. These distinctive effects can help us understand the pathogenesis of ARMD and the cellular response to cobalt-based alloys, which will inform biocompatibility test protocols and future implant designs.

# Table of content

## List of figures

## List of tables

## List of abbreviations

| | |
|---|---|
| Ac-tubulin | Acetylated-α-tubulin |
| α-SMA | α -smooth muscle actin |
| APS | Ammonium persulfate (10% |
| AFM | Atomic force measurements |
| ALVAL | Aseptic lymphocytic vasculitis-associated lesion |
| ANOVA | Analysis of variance |
| ARMD | Adverse reaction to metal debris |
| BSA | Bovine serum albumin |
| BMDMs | Bone marrow-derived macrophages |
| Cdc42 | Cell division control protein 42 homolog |
| CM-H2DCFDA | 5-(and 6-)-chloromethyl-2’7’-dichlorodihydrofluorescein diacetate |
| $Co^{2+}$/Co (II) | Cobalt ions |
| $CoCl_2$ | Cobalt chloride |
| CoC | ceramic-on -ceramic |
| CoP | ceramic-on-polyethylene |
| GM-CSF | colony-stimulating factor |
| CoCr | Cobalt chromium alloy |
| CoNPs | Cobalt nanoparticles |
| $Cr^{3+}$/Cr (III) | Chromium ions |
| CrNPs | Chromium nanoparticles |
| DMSO | Dimethyl sulfoxide |
| DMEM | Dulbecco’s Modified Eagle’s Medium |
| ECM | Extra cellular matrix |
| EDTA | Ethylenediaminetetraacetic acid |
| EGF | Epidermal growth factor |
| FACS | Fluorescence-activated cell sorting |
| FBS | Foetal bovine serum |
| GAPDH | Glyceraldehyde 3-phosphate dehydrogenase |
| $H_2O_2$ | Hydrogen peroxide |
| HO• | Reactive hydroxyl radicals |
| HBSS | Hanks’ balanced salt solution |
| HDAC6 | Histone deacetylase 6 |
| HIF | Hypoxia-inducible factor |
| HRP | Horseradish peroxidase |
| HMDS | Hexamethyldisilazane |
| IFN | Interferon |
| IL | Interleukin |
| LPS | Lipopolysaccharide |
| LDH-THA | large-diameter head THAs |
| MMPs | Matrix metalloproteinases |
| MACC | Mechanically assisted crevice corrosion |
| M-CSF | Macrophage colony stimulating factor |
| MEM | Minimum Essential Media |
| MLCK | Myosin Light Chain Kinase |
| MoM | Metal-on-metal |
| MoP | Metal-on-Polyethylene |
| MT | Microtubule |

| | |
|---|---|
| MFs | Myofibroblasts (), |
| NAC | N-acetyl-L-cysteine |
| NADPH | Nicotinamide adenine dinucleotide phosphate |
| NFκB | Nuclear factor kappa-B |
| PBS | Phosphate buffer solution |
| pMLC | Phospho-myosin Light Chain |
| pMYPT | Phospho-myosin-binding subunit of myosin phosphatase). |
| PDGF | Platelet-derived growth factor |
| PKC | Protein kinase C |
| PMA | Phorbol 12-myristate 13-acetate |
| Rac1 | Ras-related C3 botulinum toxin substrate 1 |
| RhoA | Ras homolog gene family, member A |
| ROCK | Rho-associated coiled-coil–forming kinase |
| ROS | Reactive oxygen species |
| RPMI | Roswell Park Memorial Institute media |
| RT | Room temperature |
| SDS | Sodium dodecyl sulphate |
| SEM[1] | Standard error of the mean |
| SEM[2] | Scanning electron microscope |
| TEMED | 1, 2-Bis (dimethylamino) ethane |
| TFM | Traction force measurements |
| THA | Total hip arthroplasty |
| TBS | Tris-buffered saline |
| TBST | Tris-buffered saline plus Tween 20 |
| TGF | Transforming growth factor |
| TGF-α | Transforming growth factor α |
| TEM | Transmission electron microscopy |
| TNF-α | Tumour necrosis factor alpha |
| VEGF | Vascular endothelial growth factor |

# Chapter 1. Introduction

Millions of people worldwide suffer from end-stage hip joint diseases that require treatment to restore their function and eliminate pain to provide an improved life of quality. One of the widely applied procedures is a total hip arthroplasty (THA). In 2016, 87,733 primary hip replacements were conducted in the UK alone with nearly 8,000 hip revision procedures performed largely due to the aseptic loosening, pain and adverse reaction to metal debris (ARMD) from CoCr alloys. These numbers are increasing every year according to the National Joint Registry (National Joint Registry for England, 2017). Although the use of metal-on-metal hip replacements has virtually ceased, implants containing CoCr alloys are still being widely utilised, including in dental and spinal prostheses and modular heads in metal-on-polyethylene couplings.

There have been numerous studies to investigate the causes of ARMD (Matharu et al., 2016). A wide range of *in vivo* and *in vitro* studies have been conducted to elucidate the contributing factors and mechanisms underline the pathogenesis of ARMD. However, the factors involved in its progression have not been completely understood. In an attempt to link the cellular response to the deleterious effects related to CoCr products *in vivo*, the health endpoint of most *in vitro* studies are cytotoxicity and cell death. Although the metal content detected *in vivo* can vary greatly among different patients (Davda et al., 2011), it seems unlikely that investigations focused on acute toxicity will provide a solution to fully understanding CoCr debris related ARMD. It is reasonable to assume that cells *in vivo* will be exposed to highly varying levels of $Co^{2+}$ and $Cr^{3+}$ ions and particles, which in most cases, rather than directly inducing cell death or triggering acute inflammatory responses, have effects on the cellular behaviour or functionality that disrupt tissue homeostasis. Understanding the cell-type specific reactions will provide a better understanding of the pathogenesis of the ARMD and the cellular response to

cobalt and chromium based alloys, and provide useful information for future implant design and biocompatibility testing.

# Chapter 2. Literature review

## 2.1 The hip joint

The hip approximates to a ball and socket joint and is connected between the longest bone in the body, the femur, and the pelvis at the distal to the trunk (Dowson and Wright, 1981). It is one of the largest and heavily loaded joint in the human body the conditions which both a natural and prosthetic hip operates in are complex and challenging.

2.1.1 Anatomy

The hip joint is a well-structured mechanism that transfers the upper body weight to the lower limb and enables motion. The hip joint can be divided into three main components, namely the femur, acetabulum and acetabular capsule that is formed by surrounding soft tissues.

2.1.1.1 Femur

The femur consists of a long cylindrical shaft (diaphysis), which joins the metaphyses. The proximal region of femur consists of the femoral neck, the greater and lesser trochanters and the femoral head. The approximately spherical femoral head is covered with articular cartilage to articulate with the pelvis at the acetabulum; the structure allows the accommodation of a wide range of motion, suitable for locomotion and other activities. In addition, an uncovered cartilage area occurs on the central area of the femoral head – the fovea capitis, where a small depression region allows the capsule ligament to be attached. The femoral neck connects the femoral shaft to the head as a superomedial projection, which extends inferolaterally from the head at an angle of approximately$125^{o}$ to the femoral long axis. The head is located anterior to the midline of the shaft of the femur thereby creating an approximately 5-$15^{o}$ neck-shaft angle. The femoral neck and its orientation allows space between the head and shaft, which results in facilitating a wide range of movement of the hip joint. Importantly, the muscles and ligaments around the hip attach to the greater and lesser trochanters to allow joint mobility. The diaphysis

is formed by cortical bone with the epiphysis and metaphysis consisting of primarily cancellous bone that covered with a thin layer of cortical bone.

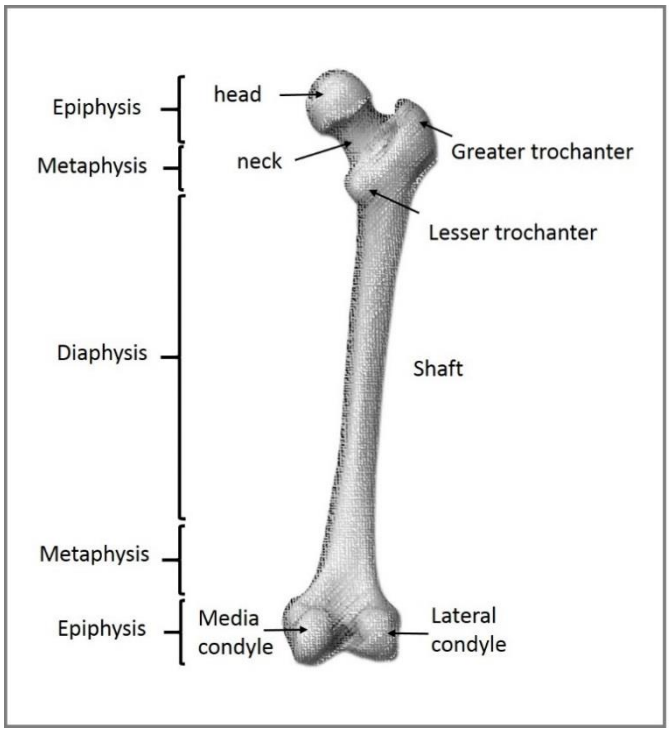


Figure 2.1 Illustration showing the basic anatomy of the femur.

2.1.1.2 Acetabulum

There are three components forming the acetabulum namely the pubis, the ilium and the ischium; these are fused to create the acetabulum within the pelvis that thereby creates an articulation surface for the femoral head. The stability of the hip joint is provided by the acetabulum accommodating the surface of the femoral head, with soft tissues providing restraints. The surface of the acetabulum includes the articulating lunate surface as well as the non-articular part, the acetabular fossa. The acetabulum is broadest in the superior region of the cup where most of the body weight is transmitted from the bony pelvis to the femur.

2.1.1.3 Synovial membrane and the joint capsule

The synovial membrane is a layer of connective tissue that lines the joint capsule. The Synovial membrane of the hip joint originates from the margins of the articulation region and attaches to the femur neck. It also extends and covers the non-articular area of the acetabulum thus providing a tubular covering for the ligament of the femoral head. In addition, a thick fibrous membrane, external to the synovial membrane, encloses the joint and seals the joint capsule from its surrounding. The joint is further stabilised by three ligaments - the ilio-femoral, ischo-femoral and pubo-femoral ligaments. These ligaments retain the femur lightly in the capsule, preventing extension beyond the straight position, limiting abduction and movements of rotational movements whilst permitting flexion up to approximately 130$^{o}$. The synovial fluid is generated by the synovial membrane; this fluid provides both lubrication and nutrition to the bearing surface. The iliopectineal bursa acts as a fluid reservoir to contain synovial fluid that egresses from the joint space when the pressure within the joint capsule is excessive. The flow is reversed when the pressure of the joint capsule decreases below that of the bursa. The pressure in normal and healthy joints is maintained approximately constant utilising this mechanism during physical activity. In some problematic joints, it is known that the pressure can rise up to 69 kPa in some cases while it is only just above the atmospheric pressure in normal and healthy joints (Wingstrand et al., 1990, Hendrix et al., 1983).

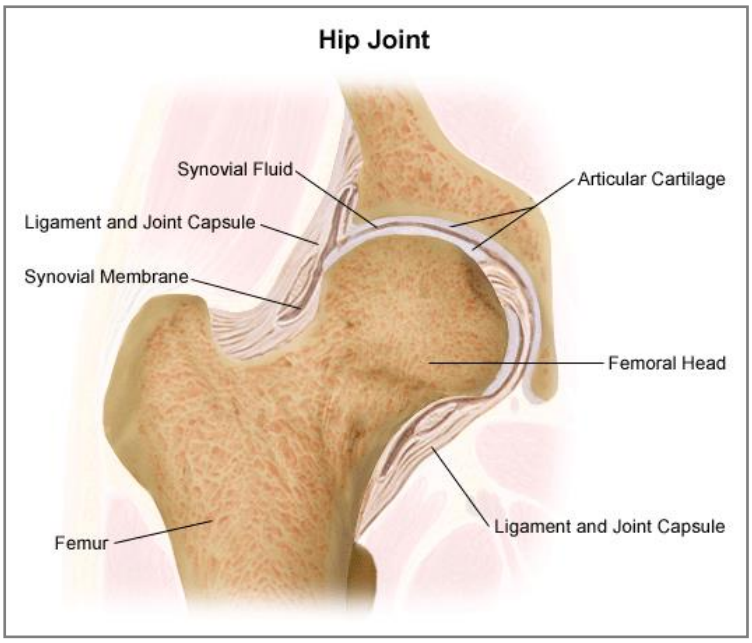


Figure 2.2 Image showing the cross-section view of the hip joint capsule. (Source: www.stanfordhealth.org)

2.1.2 Kinematics and biomechanics of the hip

The morphology of the hip joint and the organisation of ligaments around the capsule provides a structure that make the best use of muscle force for standing and joint movement. Motion of the hip joint may be described as extension, abduction, flexion, adduction, internal and external rotations with circumduction described as a combination of all the other motions. Walking transmits forces which are multiples of body weight through the hip joint, while jogging, running and activities in many sports generating forces which are significantly greater. Many *in vivo* measurements have been carried out using prostheses and endoprostheses instrumented with transducers (strain-gauges). Rydell (1966) was the first to attempt measuring direct hip joint forces using an instrumented hip prosthesis, which yielded force magnitudes of 2.3 to 2.9 times body weight for single leg stance and 1.6 to 3.3 times body weight for level walking (Cowin, 2001). More extensive studies have been carried out, summarised in Table 2.1, which have shown that although patients in the early postoperative period can execute planned activities of daily living with relatively low joint contact forces, unexpected events such as

stumbling or periods of instability during single leg stance can generate resultant forces in excess of eight times of body weight.

Table 2.1. Hip contact forces measured *in vivo* in patients with instrumented implants (Callaghan et al., 2007).

| Activity | Typical Peak Force (BW) | Total Number of Patients | Time Since Surgery (Months) |
|---|---|---|---|
| Walking, slow | 1.6-4.1 | 9 | 1-30 |
| Walking, normal | 2.1-3.3 | 6 | 1-31 |
| Walking, fast | 1.8-4.3 | 7 | 2-30 |
| Jogging, running | 4.3-5.0 | 2 | 6-30 |
| Ascending stairs | 1.5-5.5 | 8 | 6-33 |
| Descending stairs | 1.6-5.1 | 7 | 6-30 |
| Standing up | 1.8-2.2 | 4 | 11-31 |
| Sitting down | 1.5-2.0 | 4 | 11-31 |
| Knee bend | 1.2-1.8 | 3 | 11-14 |
| Stumbling | 7.2-8.7 | 2 | 4-18 |

## 2.2 Total hip arthroplasty

Total hip arthroplasty (THA) is a highly successful and widespread surgical treatment in restoring function to the synovial joints of the body. There are nearly 895,292 primary total joint replacements performed in United Kingdom according to the National Joint Registry 14th Annual Report (2017). From the perspective of healthcare cost savings associated with implants with extended service life, there is a great interest in better understanding the factors that contribute to the success and longevity of total joint replacements.

### 2.2.1 A brief history of total hip arthroplasty

THA has completely revolutionised the way that a diseased hip is treated, and is considered to be one of the most successful surgical treatments of its generation. Surgeons had employed a variety of biocompatible materials ranging from muscles, chromatised pig bladder to glasses, ivory, magnesium and zinc to restore mechanical functionality of the joint. Glück made the first attempt in hip replacement by using ivory to replace femoral heads of patients whose hip joints had been severely damaged by tuberculosis in 1891. Smith-Petersen in 1925 designed a

surface for motion utilising a glass hollow hemisphere fitting over the femoral head. However, it failed to withstand the forces transmitted through the hip joint and shattered. Later, stainless steel was applied to create the first total hip replacement that was fitted to bone with bolts and screws. The orthopaedic surgeon Sir John Charnley is considered the father of the modern THA, who designed the low friction arthroplasty in the early 1960's, which is consider as the forerunner to the modern prostheses in use today. This implant can be considered in three parts: a polyethylene acetabular cup, a metal femoral stem and acrylic bone cement (Charnley, 1961). It was called the low friction arthroplasty as he advocated the application of small femoral heads which could decrease wear due to a small articulating surface area. Despite its great success, not all THA provide the patient with satisfactory long-term results due to associated complications, with, in some cases, means a revision surgery is required to replace the problematic implant, which is typically a more demanding procedure with inferior results compared to the primary procedure.

### 2.2.2 Conditions leading to total hip arthroplasty

The need for a total hip replacement results from damage to the articular cartilage associated with disease, trauma, or normal "wear and tear". Cartilage is not innervated and hence the lubrication mechanisms operating in healthy tissue can withstand repetitive loading of the joint without causing any pain. However, if the cartilage is damaged by disease, extended use or trauma, intense pain may occur as the innervated bones of the synovial joint come into direct contact. Osteoarthritis, Rheumatoid arthritis, and trauma are the three primary sources of damage in articular cartilage (AAOS, 2010). The primary disease of the hip is degenerative arthritis (osteoarthritis), and is usually described as the degeneration and progressive loss of normal structure and function of articular cartilage (Buckwalter and Mankin, 1998), which ultimately results in painful bone contact. Rheumatoid arthritis is a systemic disease in which the synovial capsules become inflamed, produce too much synovial fluid, and damages a large

number of synovial joints in the body. In addition, trauma is the result of physical injury that damages the cartilage or fractures the hip joint.

2.2.3 Components of a total hip replacement

The components of a modern total hip replacement include the femoral elements comprising the head, neck, and stem that fixate into the femur as well as the acetabular components encompassing the acetabular shell and liner, which are positioned in the acetabula region of the pelvis. Each of these components contributes to the functional requirements of the total hip replacement, including articulation and wear resistance of the acetabular liner and femoral head and fatigue resistance of the stem. Table 2.2 summarises the functional properties of components in THAs.

Table 2.2 Functional properties of the components in THAs

| Component | Functional requirement | Materials | Modern THA |
|---|---|---|---|
| Acetabular shell | Compressive strength<br>Integration with bone | Titanium alloy<br>CoCr alloys | 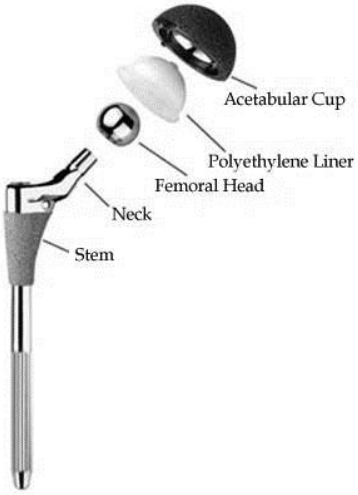 |
| Acetabular shell (Liner) | Wear resistance | UHMWPE<br>CoCr alloys<br>Zirconia | |
| Femoral head | Hardness<br>Wear resistance<br>Corrosion resistance | CoCr alloys<br>Stainless steel<br>Zirconia<br>or alumina | |
| Neck | Flexural strength<br>Corrosion resistance<br>Fatigue resistance | CoCr alloys<br>Titanium alloy<br>Stainless steel | |
| Femoral stem | Fatigue resistance<br>Corrosion resistance<br>Compliance match to the bone | Titanium alloy<br>CoCr alloys<br>Stainless steel | |

2.2.4 Metal bearing surfaces

2.2.4.1 Bearing surface combinations and the phasing out of MoM bearing

Over the past decades, diverse bearing combinations have been introduced, abandoned and reintroduced, reflecting the constant studies, improved understanding and improved material options since THA was first introduced. The bearing articulation has included the development of several combinations including metal-on-polyethylene (MOP), ceramic-on-polyethylene (COP), metal-on-metal (MOM) and ceramic-on-ceramic (COC). A comparison of different bearing surface combinations is illustrated in Table 2.3.

Table 2.3 Comparison of different bearing surface combinations (Barsoum, 2010).

| Bearing surfaces combinations | Advantages/Indications | Disadvantages |
|---|---|---|
| Metal-on-polyethylene | • Most forgiving combination in terms of component placement<br>• Least expensive<br>• Used for elderly patients with low functional demands | • Highest wear of all three combinations<br>• Smaller femoral heads with relative decrease in stability and range of motion compared to metal-on-metal<br>• Boundary lubrication mechanism which increases wear with bigger femoral head<br>• Backside wear |
| Ceramic-on-polyethylene | • Increased hardness, scratch resistance and burst strength<br>• Increased wettability for improved lubrication<br>• Lower wear rates compared with metal-on-polyethylene<br>• Excellent clinical results | • Risk of fracture of the ceramic<br>• Higher wear rates than ceramic-on-ceramic |
| Metal-on-metal | • Larger femoral heads available with increased stability, jump distance and range of motion<br>• Mixed fluid film lubrication mechanism which decreases wear with bigger femoral heads<br>• Self polishing capacity<br>• Better wear resistance than metal-on-polyethylene (low volumetric wear)<br>• Used in young patients with high functional demands | • Highest biological reactivity and cytotoxicity with highest number of wear particles<br>• High levels of metal ions in blood, urine and remote organs<br>• Not used in females in their reproductive years or patients with renal failure<br>• Metal sensitivity (Delayed type hypersensitivity)<br>• Possible carcinogenesis and genetic damage<br>• Perfect component positioning is essential to prevent failure |
| Ceramic-on-ceramic | • Lowest biologic reactivity<br>• Low friction and wettability<br>• Low surface roughness<br>• Highest wear resistance<br>• Reserved for young, high functional demand patients with metal sensitivity | • Brittleness and possible component fractures<br>• Small femoral heads with decreased range of motion<br>• Stripe wear with possible squeaking<br>• Less forgiving combination<br>• Most expensive |

Metal bearings were introduced in the early stages in the development of THAs. An advantage of utilising MOM bearing surfaces is that it could drastically reduce the risk of postoperative instability and demonstrated favourable wear rates as a result of the possibility to use of larger femoral heads compared with traditional MOP bearing surfaces. In addition, MOM bearings were shown to present extremely low volumetric wear compared with metal or ceramic on

polyethylene. However, the particles generated by the MOM bearings could be 13–500 times smaller than that of MOP bearings (Doorn et al., 1998). These particles were found to lead to both a local soft tissue reactions and a systemic increase in serum $Co^{2+}$ and $Cr^{3+}$ levels (Davda et al., 2011). In 2010, Depuy issued a recall of its articular surface replacement (ASR) MOM arthroplasty system based on the devices' high failure rate. The recall was based on data from the National Joint Registry of England and Wales that showed the five-year revision rate for arthroplasties involving the ASR XL Acetabular System and the ASR Hip Resurfacing System was 13% and 12% respectively (National Joint Registry for England, 2010). This was regarded as unacceptably high level as artificial hips are widely expected to function properly *in situ* for at least 10 to 15 years. The loosening, osteolysis and metal sensitivity that resulted from the generation of metal particle were thought to be the main reasons of the recall (de Steiger et al., 2011). It was also revealed that large diameter metal-on-metal implants from other manufacturers showed high failure rates, especially in women (Cohen, 2012). In 2011, a two year follow-up study of 144 patients reported an incremental increase in metal levels with large head MOM hip prostheses from manufactures which included Zimmer, DePuy, and Smith and Nephew (Lavigne et al., 2011). Since the recall, the application of large-head MOM THA has sharply decreased from 20 % in 2005 to less than 1 % in 2012. Currently, there exists no role for large-head MOM THA in current clinical practice, although there are still many factors unknown about the MOM bearing.

2.2.4.2 Characterisation of the wear particles generated from THA implants

Electron microscopy and energy dispersive X-ray spectroscopy (EDS) have been applied to study the physicochemical characteristics of the wear particles in tissues, retrieved prostheses, or the isolated wear particles derived from MOM implants (Goode et al., 2012, Doorn et al., 1998, Xia et al., 2011). Doorn et al. investigated the particles from revision MOM hip arthroplasties, and found that the CoCr wear particles have a round to oval morphology with

irregular boundaries and some of them displayed a spike-like shape. In addition, they were in general smaller than 50 nm (range 6-834 nm) (Madl et al., 2015a, Doorn et al., 1998). Campbell et al. isolated particles from the periprosthetic tissues of a patient with well-functioning MOM total hip prosthesis and showed wear particles to be of a comparable size range (18-472 nm). Similarly, the majority of them were oval-shaped (around 40%) or needle-shaped (around 40%) with the rest spherical (Campbell et al., 2003). Although the metal particulates from the tissue samples and retrieved implants were largely within the nanometer size range, it has also been shown that these particles may agglomerate and form larger or micron sized particles (Buscher et al., 2005, Morlock et al., 2008). Wear particles from periprosthetic tissues of patients with failed MOM prostheses are significantly smaller than those generated in MOP prostheses, when the CoCr wear particles, which were found to be spherical and elongated shaped particles, ranged from 0.07 to 6.3 μm in diameter (0.38 μm mean) compared to 0.57 to 12.2 μm in length (2.19 μm mean). Chemical analysis was also performed to investigate the chemical elements of wear debris of the periprosthetic tissue samples from MOM hip implant patients. Campbell et al. reported that nearly 50% of the particles in the tissues were CoCr alloy particles with the rest comprising a chromium oxide compound (Campbell et al., 2003). While Topolovec et al. only detected CoCr alloy particles and Ti particles from their analysis of the retrieved tissues of patients with MoM hip prostheses (Topolovec and Milosev, 2014). Although chromium has been found to be the main constituent, interestingly, some authors indicated that there were no particles which are solely comprised of purely Co (without Cr and Mo).

Only a relatively small number of studies have characterised metal particles from synovial fluids. De Pasquale et al. analysed metal wear particulates from synovial fluid following the revision of MOM hips and reported that there were mostly micron-sized CoCr wear particles with only few particles with little or no cobalt content (De Pasquale et al., 2014). However it is suggested that this study may not accurately reflect the actual chemical characteristics of *in*

*vivo* wear particles due to the use of sodium hypochlorite, an alkaline solution for particles extraction that could significantly enhance the Cr dissolution from the particles and affect their physicochemical characteristics. Davda et al. used an acid oxidative digestion approache to isolate metal nanoparticles from 5 patients and found that the nanoparticles in the hip joint fluid contained primarily Cr (Davda et al., 2011). A study that included a much wider record of cases (32 unilateral MOM and 22 controls) reported that in the synovial fluid, the range of Co concentration was 11.50–64,550 mg/l (average 7,963.15 mg/l) for patients with MOM hip prostheses and 0.12–3.24 mg/l (average 0.93 mg/l) for the ‘‘healthy patients’’ undergoing primary hip surgery (Beraudi et al., 2013). Moreover, a retrospective study by Davda et al., 2011 analysed chromium and cobalt concentrations in synovial fluid from a group of 92 patients with failed MOM hip replacements using an acid oxidative digestion method. It was found that there was no significant difference for either Cr or Co ion levels between manufacturers in the synovial fluid and the range of Co and Cr concentration was 11 to 24,262 mg/l (mean of 4,404 mg/l) and 13 to 185,731 mg/l (mean of 20,593 mg/l). In summary there is a wide variation of Co and Cr levels in synovial fluid and a standardised laboratory method is required to accurately determine metal content.

Although the size of metal particles is smaller, it was suspected that the number of metal particles can be up to 100 times greater than that of polyethylene particles (Doorn et al., 1998). Consequently, the particles can lead to a much higher systemic release of $Co^{2+}$ and $Cr^{3+}$ ions as the total surface area of the metal particle exposed to the corrosive *in vivo* environment is greatly increased leading to a greater propensity for releasing metal ions. Abnormal serum $Co^{2+}$ and $Cr^{3+}$ levels have been widely reported in patients with MOM bearings from numerous studies. This has also been suggested to be associated with the use of large diameter heads (Smith et al. 2012). In 1998, Doorn et al. reported that levels of circulating $Co^{2+}$ ions in serum and blood increased in patients with a metal-on-metal THA and the highest increase was often

observed during the bedding-in phase (median 1.1 μg/l after one year) (Doorn et al., 1998). In a study by Jacobs et al., the circulating $Co^{2+}$ and $Cr^{3+}$ levels at 1 year after THA surgery were increased by 6 and 21 times respectively, compared to the preoperative measurements (Jacobs et al., 2003). Grübl reported the longest (10 years) follow-up of a series of cementless MOM THA and reported a mean serum concentration of cobalt of 0.75 μg/L (range, 0.3–50 μg/L) (Grubl et al., 2007). A further study with a 10-year follow-up of MOM resurfacing patients by De Souza et al also showed that serum $Co^{2+}$ and $Cr^{3+}$ levels increased steeply over the initial 2 years followed by a slow decline for both ions up to 5 years, while there appeared another increase of $Co^{2+}$ and $Cr^{3+}$ levels again in some patients between 5 and 10 years (deSouza et al., 2010). A medical device alert was published to guide the surveillance of metal-on-metal hip arthroplasty by the United Kingdom Medicines and Healthcare products Regulatory Agency (MHRA) in April 2010. It was recommended that more frequent surveillance and further testing should be considered when whole blood levels of $Co^{2+}$ and $Cr^{3+}$ of a patient rise above 7 μg/l equivalent to parts per billion (ppb), which is the so called ‘‘action level’’ (Haddad et al., 2011). However, it was not encouraged to perform revision surgery based on blood metal ion levels alone due to the inadequate sensitivity of the threshold level of 7 μg/L to be used as a screening test for implant failure (Haddad et al., 2011). It also confirmed that blood metal ion levels can serve as a useful tool for diagnosis of failed metal-on-metal total hip arthroplasties.

2.2.5 Modular taper junction and metal ions/particles release

2.2.5.1 Introduction of modular taper junction

With the aim of reproducing the natural biomechanics of the hip to maximise both function and longevity in total hip replacement, changes have been made in a range of design features, including the introduction of modular junctions. The dimensions, materials as well as surface finish of the taper can vary with the manufacturer. The design of a Morse taper refers back to the 1800s when Morse invented a number of basic machining tools. This taper design has been

widely adopted in dental implant, humeral components, intramedullary rods as well as THAs. These modular junctions include the modular femoral head–neck junction and neck-stem junction. In a modular neck-stem junction, there is a 'double taper' as the trunnion of the distal part of the neck engages with a bore created within the stem, as well as the proximal engagement of the neck with the head as illustrated in Figure 2.3.

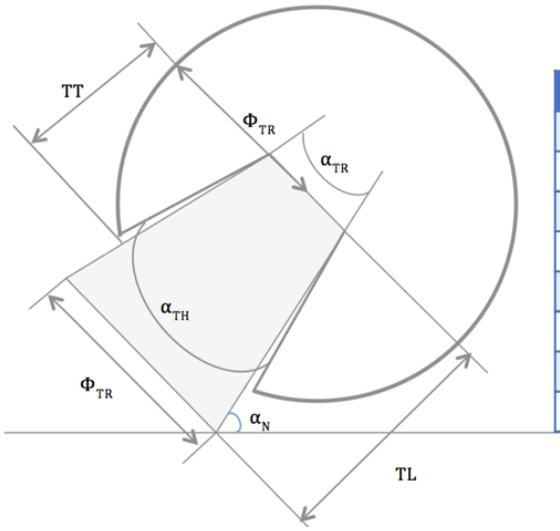


| Symbol | Design variable |
|---|---|
| $\alpha_{TH}$ | Head taper (female taper) angle |
| $\alpha_{TR}$ | Trunnion (male taper) angle |
| $\alpha_N$ | Neck angle |
| HO | Head offset* |
| TL | Trunnion length |
| Rz | Trunnion roughness |
| TT | Taper thickness |
| $\Phi_{TR}$ | Taper diameter |

Figure 2.3 Illustration of the design of a modular head-neck taper junction.

Modular necks offer the surgeon many intra-operative options, which are useful both in difficult primary and revision situations. The design of modularity at the head–neck junction was developed by Weber in 1961, with the original design having a 'little channel' through the head, which allow fluid ingress to lubricate the bearing surface as well as the head–neck taper interface (Weber, 1970). Over the following 5 decades, along with improvement in materials, an increasing number of taper junction designs have been introduced.

2.2.5.2 Advantages of modular taper junctions

With the use of modular taper junction, the surgeon is able to optimise implant stability and range of motion because the implant's geometry can be varied to optimize soft tissue tension. Furthermore, it is also useful in the prevention of impingement between the socket and neck, and bony and muscular impingement (Weber, 1970), as the stem version can be chosen intraoperatively according to patient's individual anatomy.

The most commonly used hip replacement device materials are the cobalt based alloys, or more specifically the cobalt–chromium–molybdenum (CoCrMo) system. The dominant implant alloy used is the ASTM F75 CoCrMo, details of its and other orthopedic alloy compositions are listed in Table 2.4. These alloys have shown to be a suitable choice of material for bearing surfaces due to their mechanical properties such as high strength (yield strength: 448–841 MPa; ultimate strength: 655–1277 MPa and excellent wear resistance including hardnesses ranging from 300 HVN to 400 HVN (Patel, 2012). However high levels of material loss have been reported to have occurred in some patients causing adverse tissue reactions because of the synergistic effect of wear and corrosion. Titanium and its alloys are also widely applied as hip implant material. But unlike high modulus CoCr stem, which is susceptible to fatigue fracture, titanium alloys exhibit a lower stiffness (Young's modulus at 110 GPa vs. 210-253 GPa for CoCr Alloys) enable more physiological transmission of loads to the femur, reducing proximal stress shielding and thus prevent bone resorption in the proximal femur and failure of the cement mantel if cement is used (Yan, 2013). Modularity of the taper has made it possible to combine these materials in order to optimise fixation, resistance to fracture and improve the wear performance of bearing surfaces.

Table 2.4 Weight percent of different metals in orthopedic alloys (Ratner et al., 2012).

| Alloy | Ni | N | Co | Cr | Ti | Mo | Al | Fe | Mn | Cu | W | C | Si | V |
|---|---|---|---|---|---|---|---|---|---|---|---|---|---|---|
| Stainless steel (ASTM F138) | 10–15.5 | <0.5 | * | 17–19 | * | 2–4 | * | 61–68 | * | <0.5 | <2.0 | <0.06 | <1.0 | * |
| Co–Cr–Mo alloys (ASTM F75) | <2.0 | * | 61–66 | 27–30 | * | 4.5–7.0 | * | <1.5 | <1.0 | * | * | <0.35 | <1.0 | * |
| (ASTM F90) | 9–11 | * | 46–51 | 19–20 | * | * | * | <3.0 | <2.5 | * | 14–16 | <0.15 | <1.0 | * |
| (ASTM F562) | 33–37 | * | 35 | 19–21 | <1 | 9.0–11 | * | <1 | <0.15 | * | * | * | <0.15 | * |
| Ti alloys | | | | | | | | | | | | | | |
| CPTi (ASTM F67) | * | * | * | * | 99 | * | * | 0.2–0.5 | * | * | * | <0.1 | * | * |
| Ti-6Al-4V (ASTM F136) | * | * | * | * | 89–91 | * | 5.5–6.5 | * | * | * | * | <0.08 | * | 3.5–4.5 |
| 45TiNi | 55 | * | * | * | 45 | * | * | * | * | * | * | * | * | * |
| Zr Alloy (95% Zr, 5% Nb) | * | * | * | * | * | * | * | * | * | * | * | * | * | * |

A further advantage of introducing modularity occurs at the point of a revision surgery; these are simplified as the device's modularity enables the head component to be removed while leaving a well-fixed femoral stem undisturbed thereby preserving proximal femoral bone stock. This is relevant when just the head is exchanged at the head–neck junction, such as changing the bearing surfaces for wear, adjusting the neck length, offset, head diameter and revision of the socket.

2.2.5.3 Metal ions/particles release from the modular taper junction

Although modular hip prostheses have many advantages in comparison to single component hip prostheses, the concerns about fretting and corrosion damage at the taper junction have become increasingly prominent. The idea that corrosion might occur at the head-neck taper of the femoral component was first described by Lucas (1981) in the early 1980s, and the concept that these taper junctions are susceptible to mechanically assisted crevice corrosion (MACC), a combination of fretting and crevice corrosion, was subsequently introduced (Gilbert et al., 1994). Since that time, there have been numerous reports of corrosion at this taper interface, documented primarily in retrieval studies. The most significant problem regarding corrosion of the modular taper junction is that metal ions and particles can be generated from the taper interface due to corrosion (Brown et al., 1995, Garbuz et al., 2010, Mistry et al., 2016) which may stay bound to local tissues or circulate in the bloodstream and lymphatics and therefore, to remote organs (Woodman et al., 1984). Numerous researchers have documented the material

loss based on measurement at the surface of the femoral head taper (Matthies et al., 2013, Langton et al., 2017b, Langton et al., 2017a, Hothi et al., 2017). Severe taper corrosion is often characterised by obvious black deposits present on the taper surface. The severity of corrosion at the taper junction of MOM THAs has been related to the whole blood metal ion levels of these patients (Hothi et al., 2016). It has been established that the highest median Co/Cr ratio are measured in patients with THA hips that showed severe corrosion of tapers junction, indicating that greater amount of Co ions were released into the blood from the taper corrosion byproducts. Vendittoli et al. measured the blood Co and Cr levels in the patients with large-diameter head THAs (LDH-THA) to investigate the effects of modular junction on metal ions release. They found that the open femoral head design displayed higher Co concentrations (3.0 μg/L) than the closed design (1.8 μg/L, $p = 0.037$). Moreover, the Co levels of LDH-THA were significantly higher than those with same bearing articulations from previously published data (Vendittoli et al., 2011), suggesting that a larger head size could be associated with increased taper corrosion and metal ions release. Intra-articular Co and Cr levels have also been measured in patients undergoing revision THA who had symptomatic taper corrosion. It was reported that in patients with mechanically assisted taper crevice corrosion, intra-articular Co level (940 ppb) was significantly higher than serum Co (5.1 ppb) and intra-articular Cr (491 ppb) was also significantly higher than serum Cr (1.3 ppb) (McGrory et al., 2017).

Metal corrosion products from the taper junction have also been widely reported in the periprosthetic tissues of patients with MOP implants. Gill et al., performed a study of a series of 35 patients who underwent THA with dual-modular short stem with MOP bearing surfaces (Gill et al., 2012). They reported that the mean blood levels of cobalt in patients with taper junctions were raised at 50.75 nmol/l (5-145) compared with 5.6 nmol/l (2-13) in control patients (who had an identical prosthesis and articulating surface without modular taper junctions). Cooper et al. reported a cohort study of 10 patients with failed MOP THA resulted

from corrosion at the femoral head-neck junction (Cooper et al., 2012). Increased serum metal levels, especially the distinctive elevation of $Co^{2+}$ with respect $Cr^{3+}$ levels are also found in these patients.

## 2.3 Effects of CoCr wear particles and ions

### 2.3.1 Local effects of CoCr wear particles and ions

The deposition of CoCr wear particles and associated ions in peri-prosthetic tissues lead to a wide spectrum of necrotic and inflammatory reactions. These soft-tissue reactions have been variously interpreted and termed, including metallosis (Korovessis et al., 2006), aseptic lymphocytic vasculitis-associated lesions (ALVAL) (Willert et al., 2005), adverse reaction to metal debris (ARMD) (Matharu et al., 2016) and pseudotumours (Pandit et al., 2008). Although these soft tissue responses are not malignant or infectious, they can lead to catastrophic local tissue destruction (Pandit et al., 2008) and higher incidence of major complications after revision arthroplasty (Grammatopoulos et al., 2009). Metallosis is used to describe the macroscopic staining of the soft tissues by abnormal wear or corrosion products from the bearing surface or taper junction. Histologically, the soft tissue damages are often characterized by lymphocytes, macrophages, and necrosis with metallic and corrosion deposits (Willert et al., 2005). Campbell et al., 2010 suggested a histologic scoring system which analyzed the presence of lymphocyte-predominant infiltration in the tissues, which is known as ALVAL (Campbell et al., 2010). It is believed to outcome of a type IV hypersensitivity response (Willert et al., 2005) that typically occurs in patients with low grade of metal wear (Langton et al., 2011). Pseudotumour is used to describe a mass, which could be solid or cystic or as a combination, which is usually diagnosed according to cross-sectional imaging or operative observations. Histological analysis of pseudotumours tends to show features described as ALVAL as well as tissue necrosis. ALTR was first proposed by Schmalzried et al., 2009 for describing all kinds of adverse reactions (metallosis, ALVAL and pseudotumours) induced by wear/corrosion

products. Indeed there is no explicit consensus in the literature defining the boundaries of these terms. One study described the histopathology of adverse reactions to metal debris in association with failed metal on metal MOM hip arthroplasties of 123 patients (Natu et al., 2012a). They found that 103 cases showed ALVAL, with 60 cases of the 103 patients also demonstrating a diffuse chronic lymphocytic synovitis, and 40 cases showing lymphoid aggregates with the remaining 17 cases demonstrating pure metallosis (Natu et al., 2012a). Campbell et al., 2010 examined the synovial tissues from MOM hips revised for suspected high wear related and suspected metal hypersensitivity cases, including 32 revised THAs. The ALVAL was scored by examination of synovial lining, inflammatory cell infiltration and tissue structure. High ALVAL scores were found to be associated with patients revised for pain and suspected metal sensitivity. They also observed considerable variability regarding the amount and distribution of metal particles and presence of inflammatory cells. Macrophages and lymphocytes were seen in all cases, while typical histologic features of high wear cases often displayed a diffuse, extensive infiltration of macrophages with a small aggregate of lymphocytes. Patients with a MOP hip prosthesis who underwent revision surgery for corrosion at the modular head-neck junction also showed large soft-tissue masses and surrounding tissue damage with dense infiltration of lymphocytes and macrophages (Jennings et al., 2016, Cooper et al., 2013), which is similar to the adverse local tissue reactions reported in patients with a MOM bearing.

In general, it is believed that these soft tissue reactions may be attributed to two aetiologies: particle/ion-related cellular cytotoxicity and hypersensitivity (Campbell et al., 2010). Wear debris is mainly phagocytosed by macrophages and giant cells. Once the cells take in the particles, they corrode in the acidic intramedullary environment of the lysosomes and produce high intracellular levels of metal ions, particularly cobalt, which can cause cell death. When produced in excess, those particles may induce a response within the tissue and subsequent

inflammation, osteolysis that leads to pain, limited range of motion and even failure of the implants.

### 2.3.2 Cellular response to CoCr wear particles and ions

The nature of the adverse tissue lesion has inevitably necessitated the study of the effects of metal wear particles on cells *in vitro*. Many studies on the effects of metal particles and associated ions on cells *in vitro* are of importance and clinical relevance because they take into account the size of the particles (in nano range) and the tendency of the CoCr particulates to dissociate metal ions into solution. The size of wear and corrosion products is critical as it affects the cellular uptake and even more, the bioactivity of the debris. Many cell lines have previously been used to investigate the effects of CoCr wear particles and ions including macrophages, lymphocytes, fibroblasts and osteoblasts.

#### 2.3.2.1 Macrophages response to CoCr wear particles and ions

Macrophages are widely distributed immune cells that originate from monocytes, derived from the myeloid progenitor cells in the bone marrow and circulate in the blood stream. Upon infection, after toxic or mechanical injury or tissue damage, for example, at the early stage after implantation of a prosthesis, monocytes are rapidly recruited to the tissue and differentiate into tissue macrophages after a series of changes. Macrophages play an indispensable role in tissue homeostasis and defense by engulfing apoptotic cells, cell and tissue debris following tissue injury. Tissue macrophages and recruited monocytes also release numerous growth factors, such as platelet-derived (PDGF), insulin-like (IGF-1), and vascular endothelial (VEGF-α) growth factors to promote cell proliferation and angiogenesis, which help alleviate the local hypoxia induced by injury (Figure 2.4) and restore tissue homeostasis.

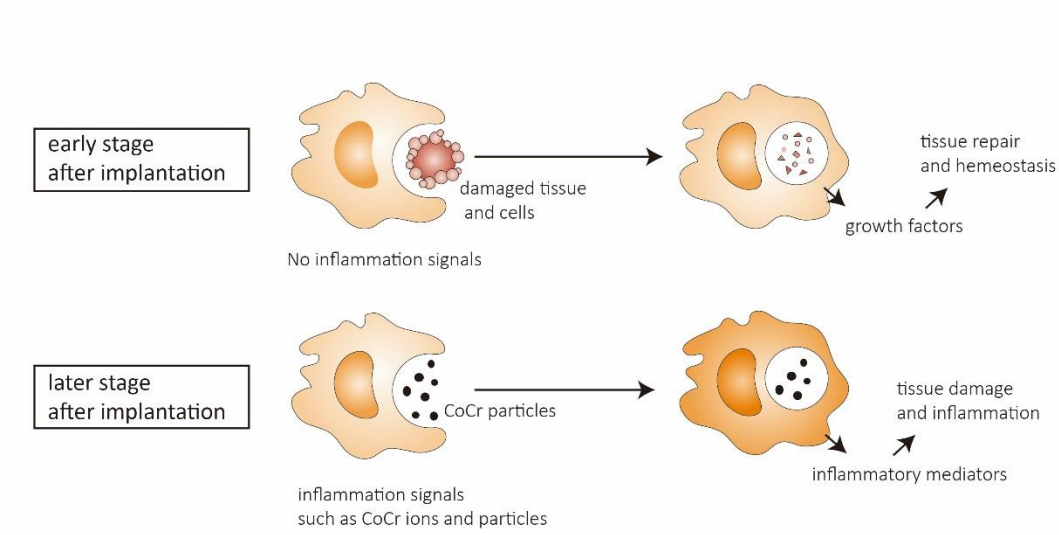


Figure 2.4 Proposed roles of macrophages at different stages after implantation of a prosthesis.

Besides their critical regulatory activity at all stages of tissue injury and repair, they are also regarded as the primary contributors to potentially pathological inflammatory processes (Wynn et al., 2013). Innate immune implant particle and ion induced inflammation is caused predominantly by macrophages (Figure 2.4). Macrophages can effectively respond to implanted materials and able to engulf various biomaterial particles (Tondravi et al., 1997). Phagocytosis of CoCr wear particles by macrophages is a crucial step in the degradation of wear particulates and involves the activation of macrophages. Early *in vitro* studies of CoCr particles involved micron sized particles. Garrett et al., 1983 used the particles ranged from 30 nm to 1.3μm, which were generated by milling in water or serum (Garrett et al., 1983). Mouse macrophages were exposed to these particles at a concentration of 30 μg/ml and noted that cell viability was reduced and the cell morphology was altered. In addition, these metal particles were shown to inhibit the phagocytic activity of macrophages at 5μg/mL (the lowest tested dose). Interestingly, they also noted that the CoCr particles that were produced in serum remained dispersed in the medium solution, whereas the particles that were produced in distilled water or balance salt solution tended to agglomerate, which could affect the

phagocytosis activity of macrophage and internalisation of the particles. Moreover, by using CoCr particles at equal weight, many *in vitro* studies compared the cellular responses to particles of different size and demonstrated that CoCr nanoparticles are more toxic than their micron-sized counterparts (Papageorgiou et al., 2007, Raghunathan et al., 2013, Posada et al., 2014). However, differences in toxicity are often absent when concentration is expressed as total surface area for nano and micron sized particles of the same element according to some other studies in nanotoxicology (Oberdorster et al., 2005, Duffin et al., 2007, Monteiller et al., 2007, Stoeger et al., 2006). Germain et al., 2003 showed that nano-sized CoCr particles ranging from 5-200 nm decreased the viability of human macrophages at 0.5 $\mu m^3$/cell while micro-sized CoCr particles (> 10 μm) did not significantly reduce cell viability. In order to better understand the cellular response to CoCr wear debris, nanoparticles containing different species of Co and Cr were also examined *in vitro*. Both Lucarelli et al., and Kwon et al., reported that Co nanoparticles and soluble Co ions significantly reduced macrophage viability in a dose-dependent manner (Lucarelli et al., 2004, Kwon et al., 2009). On the other hand, Cr nanoparticles did not display a similar cytotoxic effect on macrophages as for Co nanoparticles. Lee et al. showed that $CrPO_4$ particles did not induce a significant decrease in macrophage cell viability compared with unstimulated cells (Lee et al., 1997). VanOs et al., 2014 reported that $Cr_2O_3$ nanoparticles have minimal cytotoxic effects on macrophages and concluded that Cr nanoparticles particles are not the main cause of the inflammatory tissues reaction seen in patients with implants utilising CoCr alloys.

Several mechanisms have been suggested to be associated with cobalt/chromium-induced cell damage. For example, Cr and Co have been shown to induce the intracellular reactive oxygen species formation that leads to oxidative damage (Raghunathan et al., 2013). It is well established that excessive production of ROS can induce a wide range of deleterious effects and irreversible damage via oxidizing protein, lipid, carbohydrate and DNA (Cannizzo et al.,

2011). It has been found that patients with MOM bearings who present the highest level of blood metal ions often showed the highest levels of protein carbonylation due to oxidative stress (Scharf et al., 2014), which helps to explain the tissue necrosis and formation of pseudotumors observed in patients with MOM implants. Cr and Co are thought to enhance ROS generation by promoting the conversion of hydrogen peroxide ($H_2O_2$) into reactive hydroxyl radicals (HO•) (Beyersmann and Hartwig, 2008) or directly binding to proteins to induce oxidation leading to the loss of biological function (Tkaczyk et al., 2010). Furthermore, some studies of the toxic effects of Co/Cr have revealed that it can hinder cellular $Ca^{2+}$ entry, $Ca^{2+}$ signaling and even occupy intracellular $Ca^{2+}$ binding proteins. In addition, various receptors, ion channels and biomolecules can interact with $Co^{2+}$ resulting in the dysfunction of cells.

Once activated, macrophages release a wide array of cytokines, chemokines (Figure 2.5) to modulate the function properties and behaviors of other cell types in the inflammatory milieu. Kaufman et al., 2008 studied the response of primary human macrophages to CoCr particles (mean size of 0.48 μm) and quantify the secretion of 30 different cytokines and chemokines after 24 hours of culture. It was found that CoCr elicited significant increases in tumor necrosis factor-α (TNF-α, 17-fold, $p < 0.05$), Interleukin-6 (IL-6, 2.3-fold, $p < 0.05$), and IL-8 (2.3-fold, $p < 0.05$). Caicedo et al., 2010 reported that both soluble and particulate metal debris could induce monocyte/macrophage inflammatory responses. They found that IL-1β, which has been found to be elevated resulted from inflammasome activation, was upregulated in response to $Co^{2+}$ and CoCrMo alloy particles (2 μm) but not observed for cells treated by nickel or $Cr^{3+}$. The increased release of these cytokines, chemokine and growth-factor can initiate and exacerbate many biological activities of other types of cells. For example, a rise in the level of macrophage derived I-1 can induce neutrophil infiltration, angiogenesis and promote lymphokine synthesis (Dinarello, 2011). In addition, the enhanced release of TNF-α are known

to play an essential role in the metal particles-induced bone-related diseases (Osta et al., 2014). Studies regarding the cytotoxicity and activation of macrophage due to CoCr ions and particles are summarised in Figure 2.5, Tables 2.5 and 2.6.

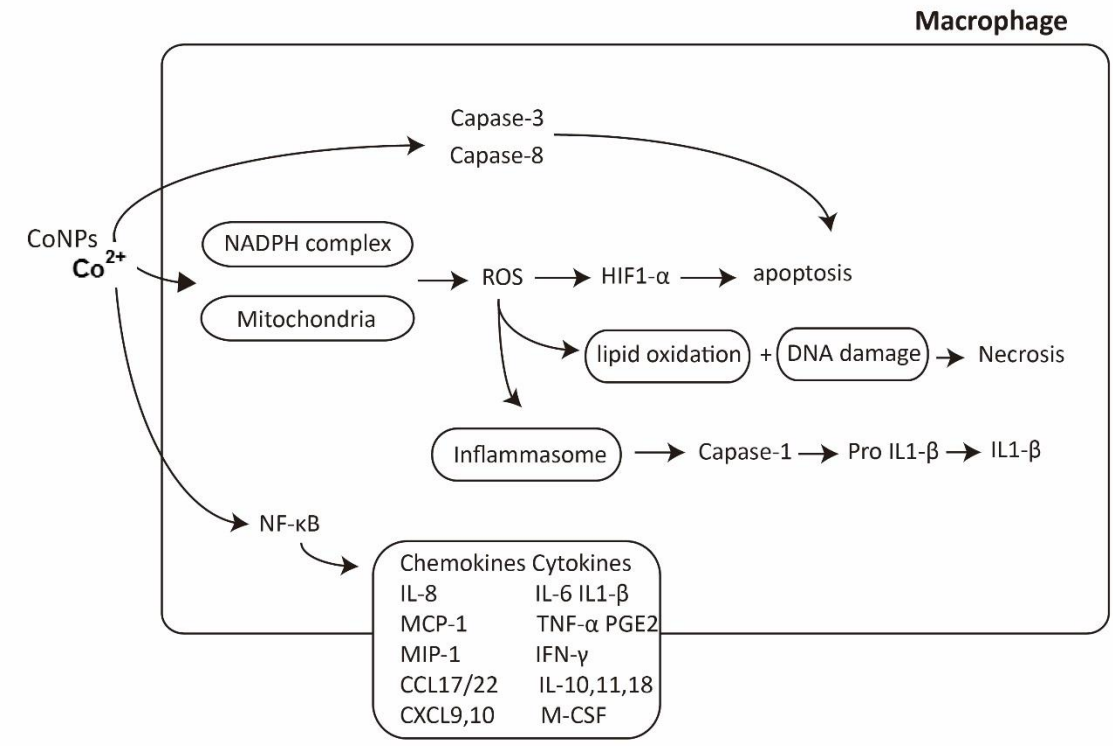


Figure 2.5 Effects of $Co^{2+}$ and CoNPs on oxidative stress mechanism and inflammation in macrophage signaling during ion and particle implant disease.

**Table 2.5 *In vitro* studies of the effect of $Co^{2+}$ and $Cr^{3+}$ on monocytes or macrophage-like cells**

| Study | Dose | Cell Type(s) | Key Findings and Results | Health Endpoint (Assay) |
|---|---|---|---|---|
| **Catelas et al., 2001** | $Co^{2+}$: 0–10 ppm<br>$Cr^{3+}$: 0–500 ppm | J774 mouse macrophages | Both $Co^{2+}$ and $Cr^{3+}$ ions can induce dose-dependent macrophage mortality, and apoptosis with $Co^{2+}$ being more toxic. The apoptosis occurs via a caspase-3 pathway. | Cytotoxicity (MTT)<br>Apoptosis (DNA laddering; western blot) |
| **(Catelas et al., 2003)** | $Co^{2+}$: 0–10 ppm<br>$Cr^{3+}$: 0–500 ppm | J774 mouse macrophages | Both $Co^{2+}$ and $Cr^{3+}$ ions can induce the release of TNF-α and macrophage mortality in a dose- and time-dependent manner. More specifically, $Co^{2+}$ and $Cr^{3+}$ ions induced apoptosis after both 24 and 48 h incubation, although DNA analysis suggested the presence of necrosis at 48 h. | Cytotoxicity (trypan blue exclusion; flow cytometry)<br>Apoptosis (DNA laddering; western blot) |
| **(Huk et al. 2004)** | $Co^{2+}$: 2–10 ppm<br>$Cr^{3+}$: 50–500 ppm | J774 mouse macrophages | The mode of cell death due to $Co^{2+}$ and $Cr^{3+}$ was dependent on the ion concentration and the incubation time. At short incubation times (24 h), the non-inflammatory process of apoptosis was predominant. At longer incubation times (48 h), however, necrosis was predominant at higher ion concentrations. | Cell death ELISA<br>TEM |
| **(Luo et al. 2005)** | $Co^{2+}$: 5–10 ppm<br>$Cr^{3+}$: 100–200 ppm | U937 macrophages | Tyrosine kinases regulate the activation of MMP-1, TIMP-1, and TNF-α by $Co^{2+}$ and $Cr^{3+}$ ions, which may contribute to prosthetic loosening. | Inflammation (western blot, RT-PCR) |
| **(Catelas et al., 2005)** | $Co^{2+}$: 0–10 ppm<br>$Cr^{3+}$: 0–500 ppm | J774 mouse macrophages | Apoptosis was predominant after 24 h induced by both $Co^{2+}$ and $Cr^{3+}$ ions, but high concentrations of those induced mainly necrosis at 48 h, which indicates the potential for these ions of inducing tissue damage by necrosis if present in large concentrations *in vivo*. | Cytotoxicity (flow cytometry)<br>Apoptosis (Cell death ELISA; western blot)<br>TEM |
| **(Petit et al. 2006)** | $Co^{2+}$: 0–10 ppm<br>$Cr^{3+}$: 0–250 ppm | U937 macrophages | $Co^{2+}$ and $Cr^{3+}$ ions induced a time- and dose-dependent protein oxidation, which were inhibited by the antioxidant glutathione monoethyl-ester, suggesting that metal ions from MOM prostheses have the potential to modify the redox state of cells. | Nitration of proteins (Western blot) |
| **(Guo et al. 2006)** | $Co^{2+}$: 0–200 µM | Acute myeloid leukemic cell lines NB4 and U937 macrophages | $Co^{2+}$ induced leukemic cell apoptosis with a loss of mitochondrial transmembrane potentials, the activation of caspase-3/8 and the cleavage of anti-apoptotic protein Mcl-1, together with the accumulation of hypoxia-inducible factor-1 alpha (HIF-1α) protein suggesting a mitochondrial pathway-dependent and HIF-1alpha-independent mechanisms. | Apoptosis assay (RT-PCR; Western blots)<br>Mitochondrial transmembrane potentials (Flow cytometric assays) |

| | | | | |
|---|---|---|---|---|
| **(Colognato et al. 2008)** | $Co^{2+}$:1 0–100 ppm | Human leukocytes | Nano-sized cobalt can be internalized by human leukocytes and can interact with DNA leading to the observed genotoxic effects, which are, however, modulated both by donor's characteristics and/or by $Co^{2+}$ release. | Genotoxicity (Cytokinesis-block micronucleus assay; Comet assay) |
| **(Caicedo et al. 2010)** | $Co^{2+}$: 0–200 µM<br>$Cr^{3+}$: 0–200 µM | Human CD14+ monocytes | Soluble cobalt, chromium, molybdenum, and nickel ions and CoCrMo particles induce stimulate IL-1β secretion in human macrophages that is inflammasome mediated (i.e., NADPH-, caspase-1-, Nalp3-, and ASC-dependent). | Inflammation (ELISA; Stealth RNA Interference) |
| **(Devitt et al. 2010)** | $Co^{2+}$: 10 ppm | Epithelial cells<br>Human neutrophils and monocytes | $Co^{2+}$ enhanced the secretion of IL-8 and MCP-1 in renal epithelial cells, gastric and colon epithelium, monocytes and neutrophils, and small airway epithelial cells but not in alveolar cells. | Inflammation (ELISA) |
| **(Posada et al., 2014)** | $Co^{2+}$: 0.1 µM | U937 human monocytes | Cobalt debris was more effective as an inducer of apoptosis and $NOS_2$ and $BAG_1$gene expression when cells had been pre-treated with $Co^{2+}$. | Cytotoxicity (MTT)<br>Apoptosis assay |

**Table 2.6 *In vitro* studies associated with the effect of CoCr particles on macrophages-like cells**

| Study | Particle characteristics and Source | Dose | Cell Type(s) | Key Findings and Results | Health Endpoint (Assay) |
|---|---|---|---|---|---|
| **(Neale et al.,2000)** | 0.5-3 µm | $4 \times 10^7$ and $1 \times 10^7$particles/mL | Human monocytes | After 14 days, a reduction in the number of CD14+ cells was observed in co-cultures exposed to CoCr particles | CD14+ cell reduction (CD14 staining) |
| **(Germain et al. 2003)** | CoCr 29.5 nm | 50, 5, 0.5 and 0.05µm$^3$ per cell | U937 L929 | The CoCr wear nanoparticles reduced the viability of U937 cell lines, whereas the micronsized commercial CoCr particles did not affect the viability of either cell lines. At equivalent particle volumes, CoCr wear particles were more toxic than the alumina ceramic wear particles. | Cytotoxicity (ATP level, cell counts |
| **(Williams et al., 2003)** | CoCr <40 nm pin-on-plate | 50, 5, 0.5 and 0.05µm$^3$ per cell | U937 L929 | The surface engineered bearings had lower wear compared to the CoCr bearings. The wear particles generated from surface engineered bearings showed decreased cytotoxicity compared to the wear particles generated by CoCr couples. | Cytotoxicity (ATP level) |
| **(Germain et al. 2003)** | CoCr 9.87 µm | 50, 5, 0.5 and 0.05µm3 per cell | U937 L929 | Micron sized CoCr particles did not have significant effect on the viability of U937 and L929 cells over 5 days at any of the tested concentrations. | Cytotoxicity (ATP level, cell count) |
| **(Lucarelli et al. 2004)** | Co 50-200 nm | Co (50 µg/$10^6$ cells) | U937 | CoNPs showed significant toxicity at doses higher than 100 µg/$10^6$ cells and had a pro-inflammatory effect on macrophages | Cell viability (MTT) Inflammation (cytokine level, TLR expression) |
| **(Kaufman et al., 2008)** | CoCr micron-sized | 853 particles per cell | Primary human macrophages | Macrophages cultured with CoCr particles released significant levels of cytokines. | Inflammation (protein level) |
| **(Caicedo et al. 2009)** | CoCr 2 µm | 5, 10, 20 particles per cell | Primary human monocytes THP-1 | Soluble and particulate metal implant debris induced monocyte/macrophage proinflammatory responses. | Inflammation (cytokine level) |
| **(Kwon et al. 2009)** | Co 30 nm, Cr 30 nm | $1 \times 10^{12}$ particles ml$^{-1}$ | RAW 264.7 | CoNPs and ions induced dose-dependent cytotoxic effects on the macrophages. CrNPs showed no significant reduction in cell viability at day 1 and 4. | Cytotoxicity (Alamar Blue) |

| | | | | | |
|---|---|---|---|---|---|
| **(Dalal et al., 2012)** | CoCr 1.1 µm | 5, 10, 50, 100 particles per cell | MG-63<br>L929<br>THP-1 | CoCr particles induced a significant decrease in viability in all cell types. | Cytotoxicity (MTT, LDH)<br>Inflammation (cytokines) |
| **(Caicedo et al., 2013)** | CoCr (1.1-7.3 µm) | 6 µM | THP-1 | Size and shape of CoCr particles influence phagocytosis, lysosomal destabilization, and inflammasome activation. Spherical, smooth CoCr particles did not significantly affect cytokine production whereas irregular CoCr particles of similar size induced significant cytokine production. Larger particles induced higher increase in cytokine production compared to the smaller particles. Larger, irregular particles induced greater intracellular lysosomal damage and cytokine release. | Inflammation (cytokine level) |
| **(VanOs et al., 2014)** | $Cr_2O_3$<br>60nm and 700 nm | 500, 10000, 1500, 2000 particles per cell | J774A.1 | Although the results displayed low overall cytotoxicity, $Cr_2O_3$ nanoparticles at high concentrations induced significant decrease in total cell numbers and significant increase in necrosis. The study also showed low levels of cytokine production from exposures to these particles. 60 nm and 700 nm particles caused similar responses to macrophages when the doses were normalized by volumes. | Cytotoxicity (cell count)<br>Inflammation (cytokine level) |
| **(Posada et al., 2014)** | CoCr (150 nm - 6.5 µm) | 2.5 mg /1 × $10^6$ cells | U937 | Cytotoxicity was observed after 48 hours of exposure. Apoptosis was also observed at 48 hours. | Cytotoxicity (MTT, Neutral Red) |

THP-1: human monocyte cell line; U937: human histiocyte cell line; L929: mouse lung fibroblast cell line; MG-63: human osteoblast-like cell line; RAW 264.7: mouse macrophage cell line; J774A.1: mouse macrophage cell line.

2.3.2.2 Fibroblast response to CoCr wear particles and ions

The *in vitro* response to foreign material has been described as an altered process similar to wound healing, during which the body initiates a cascade of events to resolve injury including inflammatory, proliferative repair and tissue remodeling (Akay, 2006). This is often refered to as the "foreign body response" in the field of biomaterials. The process of the foreign body response is a delicate orchestration of signaling involving the participation from numerous cell types including immune cells, endothelial cells, epithelium and fibroblasts in the appropriate spatial and temporal order. Fibroblasts are one of the central participants during wound healing and inflammation. They play a positive role in promoting the recovery of functional tissue but equally are capable of driving it towards chronic inflammation, fibrosis or even tissue necrosis depending on the biochemical cues they are exposed to.

For a typical foreign body response to implanted materials, the acute inflammation phase is initiated by macrophages. Macrophages phagocytose the foreign body and release a wide range of cytokines, which stimulate the proliferation of fibroblasts and recruit fibroblasts to deposit extracellular matrix (ECM) proteins such as collagen and fibronectin around the biomaterial to form granulation tissues. Fibroblasts actively and dynamically shape the structure of extra cellular microenvironments by contracting ECM matrices and secreting ECM proteins such as collagen and fibronectin (Tracy et al., 2016). In addition, fibroblasts are known to modulate immune cell behaviour by conditioning the local cytokine microenvironment in order to balance the inflammatory repair and tissue damage. For example, during remodeling of the ECM, fibroblasts enhance the release of various kinds of small peptides, such as Pro-Gly-Pro (acetyl-PGP) and tenascin C isoform that have diverse effects on cellular immune responses (Vaday and Lider, 2000, Sorokin, 2010). The inappropriate production of these regulatory molecules by the activated fibroblasts can prevent the resolution of inflammation, resulting instead in persistent chronic inflammation, fibrosis and tissue damage (Buckley et al., 2001).

Furthermore, in some pathological settings, fibroblasts can express the smooth muscle isoform of α-actin (αSMA) that is normally expressed only in smooth muscle cells and become a more contractile phenotype: myofibroblasts with enhanced ECM protein synthesis capacities (Sappino et al., 1990).

Understanding of the fibroblast response to wear/corrosion materials is essential to achieve desirable long-term outcomes of implanted materials or tissue homeostasis considering the indispensable role of fibroblasts play in the biological response to implanted materials. A few studies have investigated the effect of CoCr particles and ions on fibroblasts. Papageorgiou et al., 2007 exposed primary human dermal fibroblast to CoCr particles in order to study their effects on cell viability, integrity and cytokines release. They found that nanoparticles could promote free radical formation thus inducing DNA damage and decrease cell viability (Table 2.7); the CoCr particles were also shown to stimulate the release of IL-6 and TNF-α from fibroblasts. Tsaousi et al., 2010 also showed a dose-dependent cytotoxicity and genotoxicity of CoCr particles (0.56-4.74 μm). Bhabra et al., 2009 revealed that CoCr nanoparticles (29.5 ± 6.3 nm) can induce DNA damage and chromosome aberration in human fibroblasts without significant cell death mediated by a novel mechanism involving transmission of purine nucleotides (such as ATP) and some other intercellular signaling(Bhabra et al., 2009). Although these studies provide useful insights into the cellular response to metal products, they mainly focused on the deleterious effects of CoCr particles on fibroblasts. How CoCr particles and ions affect fibroblast activation and its functional properties at sub-toxic level remains largely unknown. Given the complex and essential role fibroblasts play in the *in vitro* response to foreign materials, further studies regarding the interplay of CoCr and fibroblast is required.

**Table 2.7 *In vitro* studies of the effect of $Co^{2+}$ and $Cr^{3+}$ and CoCr particles on fibroblast**

| Study | Ions/particles | Dose | Cell Type(s) | Key Findings and Results | Health Endpoint (Assay) |
|---|---|---|---|---|---|
| **(Germain et al., 2003)** | CoCr 29.5±6.3 nm | 50, 5, 0.5 and 0.05µm3 per cell | L929 fibroblasts | CoCr wear particles reduced the viability of L929 cells | Cytotoxicity (bioluminescent assay) |
| **(Papageorgiou et al., 2007)** | CoCr 29.5 nm | 0.0005 to 5000 $\mu m^3$/cell | Human fibroblast cell line | CoCr nanoparticles induced DNA damage and cytotoxicity. | Cytotoxicity (MTT, LDH)<br>DNA damage (comet assay)<br>Inflammation (cytokine) |
| **(Bhabra et al., 2009)** | CoCr 30 nm | 0.036 mg $cm^{-2}$ | Primary human fibroblast | CoCr nanoparticles can cause DNA damage across a cellular barrier. | DNA damage (comet, FISH) |
| **(Kovacik et al., 2008)** | CoCr micron-sized | 1.25, 2.5, 5, 10 µm3 $cell^{-1}$ | Primary human synovial fibroblast | CoCr powders resulted in reduction in cell viability. | Cytotoxicity (Trypan Blue)<br>Apoptosis (acridine orange) |
| **(Tsaousi et al., 2010)** | CoCr 0.56-4.74 µm | 0.1 to 10 mg per T-75 flask | Primary human fibroblasts | CoCr particles showed dose-dependent cytotoxicity and genotoxicity. | Cytotoxicity (Trypan Blue)<br>DNA damage (micronucleus test) |
| **(Behl et al., 2013)** | CoCr 40-49 nm | 47.6, 23.8, 2.38, 0.238 and 0.0238 mg/ml | Porcine fibroblast | $Co^{2+}$ and CoCr nanoparticles induced intracellular ROS. | Cytotoxicity (ATP level)<br>Intracellular ROS (DCF)<br>Inflammation (cytokines) |
| **(Raghunathan et al., 2013)** | CoCr 213-241 nm | 0.0005 $\mu m^3$/cell to 500 $\mu m^3$/cell | Primary human fibroblast | CoCr significant increase in intracellular ROS level and induce chromosomal aberrations. | DNA damage (FISH)<br>ROS (DCF) |
| **(Smith et al., 2014)** | $Co^{2+}$, Cobalt oxide 0.27-3.56 µm | $Co^{2+}$: 100-500 µM<br>Cobalt oxide: 1-5 µg/$cm^2$ | Human lung fibroblast cell line | Particulate and soluble cobalt are cytotoxic and genotoxic to human lung cells. | Cytotoxicity (crystal violet)<br>DNA damage (Clastogenicity assay) |

## 2.4 Aims of the present study

Previous studies show that CoCr metal wear debris and dissociated ions induce cytotoxicity and inflammation in human macrophage and fibroblast. This involves the activation of ROS, MMPs and the release of cytokines such as IL-1β and TNF-α, which leads to tissue damage and implant loosening.

The present study aims to examine how $Co^{2+}$, $Cr^{3+}$, CoNPs and CrNPs from CoCr alloys influence the behaviour of the local cell populations and related mechanisms.

Objectives:

1. The effects of $Co^{2+}$, $Cr^{3+}$, CoNPs and CrNPs on macrophage.

- To determine their toxicity on macrophage viability *in vitro*.
- To assess their effects on macrophage motility *in vitro* and *in vivo* and underlying mechanisms.

2. The effects of $Co^{2+}$and $Cr^{3+}$ on fibroblast.

- To determine their toxicity on human fibroblast viability *in vitro*.
- To identify their effects on fibroblast function in ECM modelling and associated mechanisms.
- To identify the effects on fibroblast activities in the presence of macrophages.

3. To histologically examine the peri-prosthetic synovial tissues from patients with MOM implants and evaluate the activation of synovial fibroblasts from these patients *in vitro*.

# Chapter 3. The effects of $Co^{2+}$, $Cr^{3+}$, CoNPs and CrNPs on macrophage behaviour

## 3.1 Introduction

CoCr wear particles and associated ions produced in peri-prosthetic tissues would trigger a wide spectrum of necrotic and inflammatory reactions. The soft-tissue reactions have been interpreted and termed, for example, adverse reaction to metal debris (ARMD) (Matharu et al., 2016). It occurs as a result of prolonged inflammation at the site of an implant, which normally includes a bearing component. Initially, wear particles and corrosion products are detected and phagocytosed mainly by tissue-resident macrophages (Sutphen et al., 2016). When phagocytosis of these wear particles occurs in sufficient number, macrophages are activated to release an array of cytokines and chemokines to initiate the leucocyte response (Nich et al., 2013). The leukocytes infiltrate the inflamed tissue, promote recruitment of inflammatory neutrophils or monocytes that differentiate locally into macrophages and potentiate the pro-inflammatory environment. This response has also be shown to mediated and exacerbated by the $Co^{2+}$ and $Cr^{3+}$ found in the serum and synovial fluid of patients with MoM hip implants (Jennings et al., 2016, Davda et al., 2011).

Cell migration plays a central role in the maintenance of multicellular functions as well as the development of many diseases (Franz et al., 2002). Several studies have investigated the effects of nanoparticles on cell migration. $TiO_2$-NPs were shown to reduce fibroblast migration by around 59% (Pan et al., 2009). Au-NPs were shown to reduce migration of prostate carcinoma (PC3) cells while the migration of HDF was associated with the surface charge and shape of Au nanoparticles (Yang et al., 2013).

Silica nanoparticles have been reported to be capable of suppressing migration of normal human keratinocytes (Wang et al., 2012). However, none of these studies have provided a direct mechanistic explanation and the effect of CoNPs on cell migration remains unknown.

The physiological response to a MoM implant has been reported to be either a macrophage predominant or a mixed macrophagic and lymphocytic infiltration of soft tissue (Sutphen et al., 2016). Macrophages play a decisive role in the innate immunity as the first-line immune defense. They are highly motile cells that react rapidly *in vivo* to wounding or inflammatory signals migrating at speeds of over 10 μm/min compared with fibroblasts or epithelial cells (~0.1–0.5 μm/min) (Grabher et al., 2007). It is equally important that the inflammatory macrophages can migrate out from an inflamed site in a controlled and effective manner to prevent undesired macrophage-induced tissue damage, granuloma tissue formation and the development of chronic inflammation due to excessive macrophage accumulation.

$Co^{2+}$ have been shown to enhance inflammatory cells migration *in vitro*, including monocytes and lymphocytes. For example, both $Co^{2+}$ and $Cr^{3+}$ have been shown to enhance the migration of T lymphocytes independently of circulating cytokines or chemokines, but have no effect on B cell motility, resulting in the accumulation of more T than B lymphocytes in periprosthetic tissues of some patients with CoCr-based implants (Baskey et al., 2017). However, the effect of $Co^{2+}$ and CoNPs on the macrophages' migration ability, which plays an essential role in the homeostasis of the extra cellular environment and inflammation progression and resolution, remains largely unknown.

This study aims to reveal the correlation of local exposure to cobalt and chromium particulates and ions with the clinical manifestation of a chronic inflammatory response. The present study investigate the effect of $Co^{2+}$, $Cr^{3+}$, CoNPs and CrNPs on the migration of macrophages.

## 3.2 Methods

### 3.2.1. Particles and ions

CoNPs and CrNPs purchased from American Elements (Los Angeles, CA, USA). CoNPs were composed of 90% cobalt and 10% cobalt (II, III) oxide with a molecular weight of 58.93 with a diameter of 2-60 nm (data from the company). CrNPs were in the form of chromium oxide ($Cr_2O_3$) nanoparticles with a diameter of 10-30 nm (manufacturer data).

Prior to use, the nanoparticles were washed in 100% ethanol for sterilisation and resuspended in sterile $H_20$ at a concentration of 1 mg/ml using a sonicator (pulsed mode, 3 min). Stock solutions (0.1 M) of $Co^{2+}$ and $Cr^{3+}$ ions were freshly prepared by dissolving $CoCl_2 \cdot 6H_2O$ (99.5% purity; Sigma Aldrich) and $CrCl_3 \cdot 6H_2O$ (98% purity; Sigma Aldrich) in sterile $H_20$. These solutions were sterilized by filtration through 0.2 μm pore size sterile syringe filter (Merck Millipore). Stock solutions of cobalt and chromium nanoparticles and ions were further diluted in cell culture medium prior to experiments.

### 3.2.2. Characterization of the CoNPs and CrNPs

Transmission Electron Microscopy (TEM; JEOL JEM-2010, Japan) was employed to observe the morphology of CoNPs and CrNPs as shown in Figure 3.1. CoNPs and

CrNPs were suspended in pure ethanol and a drop of particle suspension was placed onto a carbon coated grid prior to imaging.

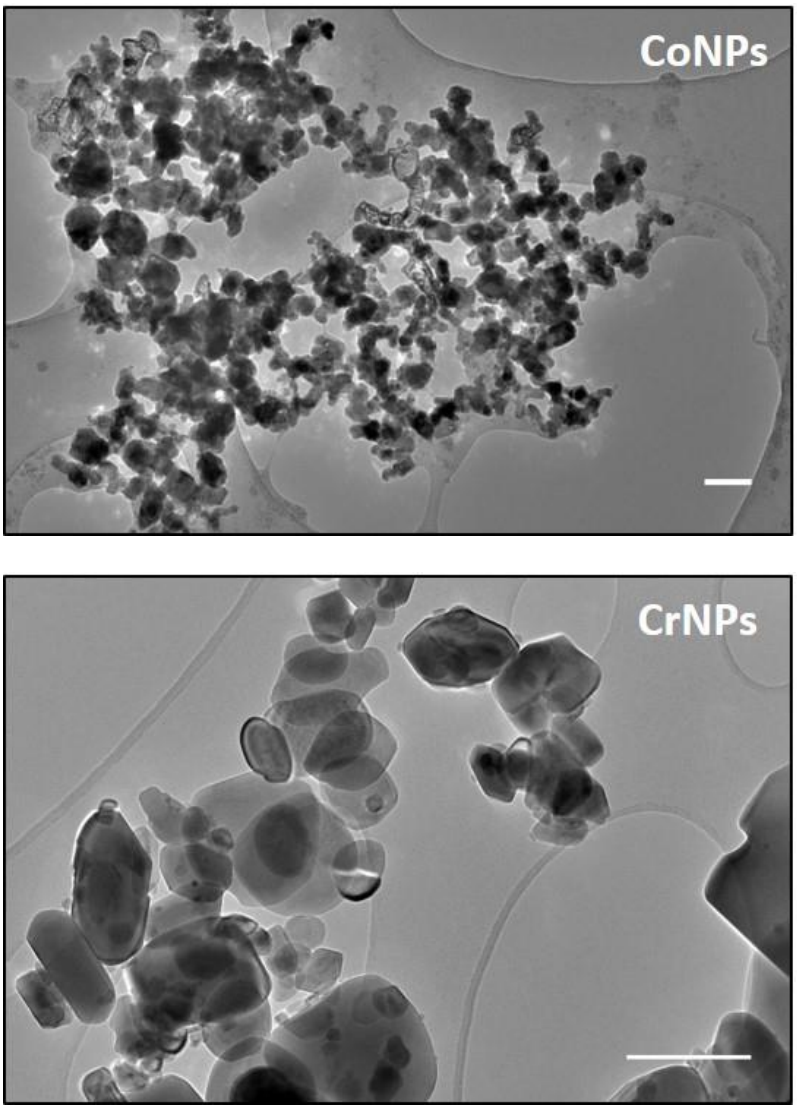


Figure 3.1 Transmission electron microscopy image of cobalt and chromium nanoparticles. Scale bar=100 µm.

### 3.2.3. Cell lines and culture preparation

3.2.3.1 Human U937 monocytic cell line

Cells from the U937 cell line (passage 6-25, donation from Dr Akihisa Mitani, Imperial College London, UK) were cultured in RPMI 1640 medium (ThermoFisher, USA)

supplemented with 10% FBS (Sigma, USA), 1.9 mM L-glutamine, 96 U/ml penicillin, 96 µg/ml streptomycin, 19 mM 2-[4-(2-hydroxyethyl)piperazin-1-yl] ethanesulfonic acid (HEPES) buffer, in a humidified atmosphere with 5% $CO_2$ at 37°C. To induce differentiation into adherent macrophage-like cells, cells were treated with 50 ng/ml 12-tetradecanoate-13-acetate (PMA, Sigma Aldrich) for 48 h, followed by rest for a further 24 h in complete RPMI 1640 medium prior to further experiments.

3.2.3.2 Isolation and differentiation of bone marrow-derived macrophages

Bone marrow-derived macrophages (BMDMs) (Weischenfeldt and Porse, 2008) were isolated and differentiated according to established standard protocols. All mice were cared for according to the UK Animal Scientific Procedures Act (1986) and by the Institutional Committee for Use and Care of Laboratory Animals. Experiments were performed under the UK Home Office Personal licence number I56EDA266 and the groups UK Home Office Project Licence number 70/7266.

Femurs were obtained from 6–12 week old C57BL/6 mice. After euthanasia, the mice were sprayed with 70% ethanol and the femurs were dissected using scissors, cutting through the tibia below the knee joints as well as through the pelvic bone close to the hip joint. Muscles connected to the bone were removed using clean gauze, and the femurs were placed into polypropylene tubes containing sterile PBS on ice. In a tissue culture hood, the bones were soaked in 70% ethanol for 1 minute, then washed in sterile RPMI 1640 medium. The epiphyses were removed by using sterile scissors and forceps, the bones were flushed with a 1ml syringe with 25g x 16mm needle (BD Biosciences, USA) filled with RPMI 1640 medium to extrude the bone marrow into a 15 mL sterile polypropylene tube. The cell suspension generated was fresh bone marrow cells. The cells were resuspended in 10 ml bone marrow differentiation media, which is

RPMI1640 supplemented with 10% fetal bovine serum (Gibco, cat. 12657-029), 100 U/ml penicillin, 100mg/ml streptomycin, 2 mM Lglutamine and M-CSF (50 ng/ml, R&D Systems, USA). The cells were seeded in non-tissue culture treated petri dishes (BD Biosciences, USA) and incubated at 37°C in a 5% $CO_2$ atmosphere. Four days after seeding the cells, an additional 10 ml of fresh medium were added per plate and incubated for an additional 3 days. To obtain the BMDM, the supernatants were discarded and the attached cells were washed with 10 ml of sterile PBS. 10 ml of ice-cold PBS was added to each plate and incubated at 4 ° C for 10 minutes. The differentiated bone marrow macrophages were detached by gently pipetting the PBS across the dish. The cells were then centrifuged at 1200 rpm for 5 minutes and resuspended in 10 ml of BMDM cultivation media. The cells were counted, seeded and cultivated in tissue culture plates for a further 12 hours before any further experimental procedure was carried out.

### 3.2.4 Cytotoxicity assay

A colourimetric assay, MTS, was performed to assess the effect $Co^{2+}$, $Cr^{3+}$, CoNPs and CrNPs on macrophage viability using the CellTiter 96® Aqueous One Solution Cell Proliferation Assay (Promega, Southampton, UK). Cells were seeded at a concentration of $5\times10^4$/well in 96-well plates and exposed to $Co^{2+}$, $Cr^{3+}$, CoNPs or Cr NPs. The doses ranged from 50 – 350 μM for $Co^{2+}$, 20 – 200 μM for CoNPs, 200-800 μM for $Cr^{3+}$ and 200 – 800 μM for CrNP. For vehicle control, cells were stimulated with complete RMPI 1640 medium.

After incubation for 6 and 24 h, the medium was aspirated and 100 μl of serum-free RPMI medium containing 10% MTS reagent was added to each well. Plates were subsequently incubated for 3 h at 37°C and the absorbance was read at 490 nm using

an Infinite F50 plate reader (Tecan, Switzerland). Five replicates of each exposure were tested and the entire assay was repeated for three separate experiments. The cell viability was determined as a percentage of control cell viability.

### 3.2.5 Cell motility and migration assays

3.2.5.1 Single cell motility monitoring

The macrophage migratory ability was investigated using live cell imaging. An inverted microscope (Lumascope 720, Etaluma, USA) connected to a cell culture incubator was used for live cell imaging to visualise macrophage migration. Time-lapse images of migrating U937 macrophages at a seeded density of $2\times10^4$ cells/cm$^2$ in a 24-well plate were collected after 12 h incubation with $Co^{2+}$ (200 µM), $Cr^{3+}$ (400 µM), CoNPs (100 µM) or CrNPs (400 µM). Images were captured every 5 min for 6 h.

Migratory properties of individual cells (n=25 cells / condition) were identified from the time-lapse images and analysed using ImageJ software with "Manual Tracking" plugin and Chemotaxis and Migration Tool (ibidi, USA).

3.2.5.2 Transwell cell migration assay

Cell migration was also investigated using 6.5 mm Transwell chambers with 8 µm pores (Costar, Corning, NY, USA). Briefly, $2\times10^5$ harvested U937 macrophages or BMDMs in serum free RPMI 1640 medium were added to the upper chamber of the insert. The lower chamber was filled with 600 µl RPMI 1640 medium with 10% FBS to encourage cell migration down the FBS chemotactic gradient. Cells migration was analysed over a 6-hour period in the presence of $Co^{2+}$ or $Cr^{3+}$ or following 2-hour pretreatment with CoNPs or CrNPs (Table 3.1).

Table 3.1 Concentration of cobalt and chromium applied for the migration tests

| Treatment | Cell type | |
|---|---|---|
| | U937 macrophages | BMDMs |
| $Co^{2+}$ | 200 µM | 50 µM |
| $Cr^{3+}$ | 400 µM | 200 µM |
| CoNPs | 100 µM | 20 µM |
| CrNPs | 400 µM | 200 µM |

### 3.2.6 *In vivo* macrophage efflux model

To demonstrate the *in vivo* effect of cobalt on mouse macrophage migration, 20 WT C57BL/6 mice were first injected intraperitoneally with 1 ml of 4% thioglycollate (Sigma, USA) to recruit macrophages into the peritoneal cavity. Thioglycollate solution was wrapped with aluminum foil and placed at room temperature to age for 3 weeks by when it turned to brown in color. This aging process is essential to enable the thioglycollate solution to effectively induce peritonitis. After 4 days, the mice were injected intraperitoneally with 5 µg of CoNPs (10 mice) or PBS (10 control mice). After 12 h, peritoneal cells from 5 mice from each group were harvested to quantify the number of macrophages. The remaining 5 mice from each group were injected with LPS (250 µl; 5 µg/ml) to induce macrophages migration/efflux towards regional lymph nodes. After 4 h, the peritoneal cells were harvested by lavage and counted.

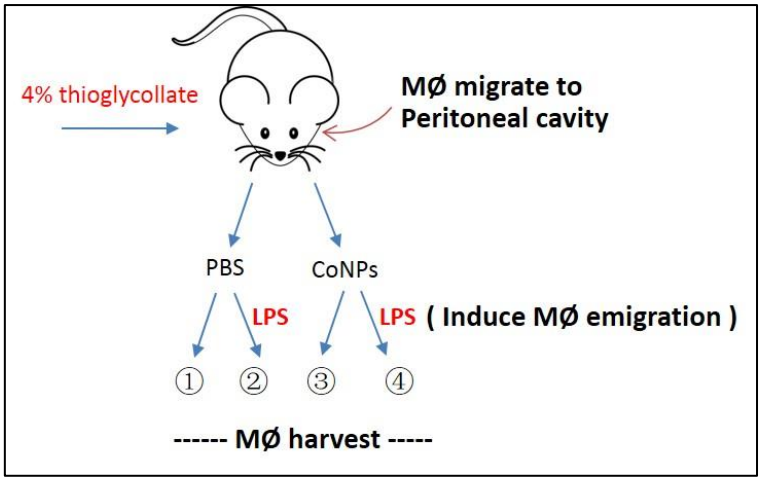


Figure 3.2 Illustration of *in vivo* macrophage migration model.

### 3.2.7 Fluorescence-activated cell sorting (FACS) analysis

The macrophages harvested as described in 3.2.3.2 were quantified by flow cytometry. The collected cell suspensions were transferred to FACS tubes (BD Biosciences; Oxford, UK), centrifuged for 5min at 350g and the supernatant was then aspirated. Cell suspensions were pre-incubated with anti–CD16/CD32 mAb (BD Pharmingen) in FACS buffer to block Fcγ R II/III receptors, which bind antibody-antigen immune complexes, on ice for 15 min to identify any non-specific binding. All the tubes were then gently vortexed and left for 15 min in the dark at room temperature. After centrifugation and washing, cells were stained with PE/Cy5 anti-mouse CD11b antibody (Abcam, UK) and FITC anti-mouse F4/80 antibody (Abcam, UK). Stained cells were washed and re-suspended in 200 µl of PBS and analysed using a flow cytometer (BD ACCURI C6) and FlowJo software (TreeStar).

Table 3.2 Monoclonal antibodies used to assess murine macrophages.

| **Antibody** | **Purpose** |
|---|---|
| anti-mouse CD11b-PE/Cy5 | Expressed on leukocytes |
| anti-mouse F4/80-FITC | Expressed on murine macrophage |

### 3.2.8 Data analysis

Normality testing (Kolmogorov-Smirnov test) was performed for all experimental data. All data are expressed as the median or mean ± SEM from separate experiments. The number of replicates per experiment (n) is indicated in the figure. Statistical analysis was conducted with SPSS (Inc., Chicago, IL, USA) for each assays are listed in Table 3.3.

Table 3.3 Statistics methods for each assays.

| **Experiments** | **Statistics methods** |
|---|---|
| Cell viability test | one-way ANOVA with Bonferroni post-hoc t-test |
| Random migration assays | one-way ANOVA with Bonferroni post-hoc t-test |
| Transmigration assays | one-way ANOVA with Bonferroni post-hoc t-test |
| *In vivo* migration assay | one-way ANOVA with Bonferroni post-hoc t-test |

## 3.3 Results

### 3.3.1 Activation of U937 cells with PMA

In this study, U937 cells were exposed to 50 ng/ml PMA for 2 days with the medium changed and then left for one more day to recover from PMA treatment. The alteration in cell aggregation and adhesion, recorded every 24 hours by imaging the culture cells, are shown in Figure 3.3 Although U937 cells are non-adherent cells, they tend to sediment and sit at the bottom of the well forming a homogenous layer (Figure 3.3A). It can be seen that when cells were treated with PMA for 2 days (Figure 3.3B), cell aggregates, characteristic of the differentiation of U937 cells, were formed.

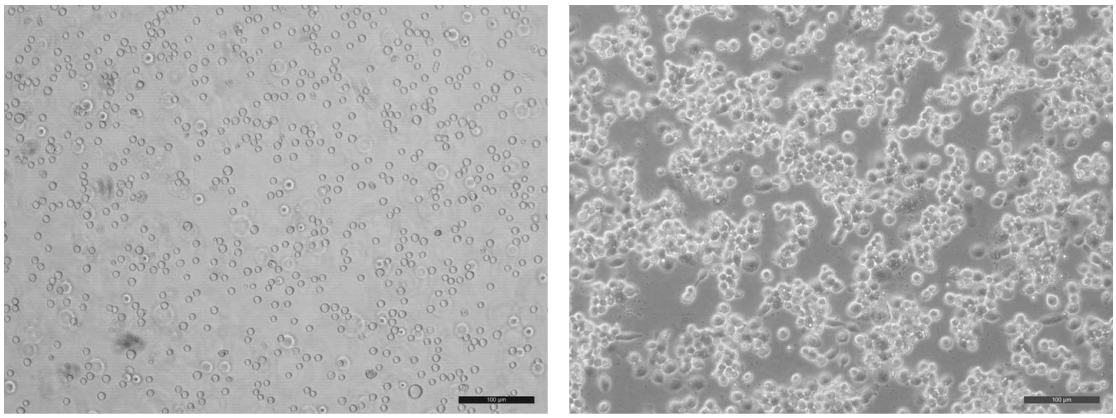


Figure 3.3 Differentiation of U937 cells. A: Untreated U937; B: U937 cells activated with PMA for two days. Images acquired using an optical microscope (DCF420, Leica, Germany) with a 10X lens. Bar: 100 µm.

### 3.3.2 The effects of $Co^{2+}$, $Cr^{3+}$, CoNPs and CrNPs on U937 macrophages viability

The viability of differentiated U937 cells following exposure to $Co^{2+}$ and CoNPs over 6 and 24 hours measured with MTS assay are shown in Figure 3.4. $Co^{2+}$, in concentrations ranging from 50 to 350 µM, had no significant effect on U937 cell viability after 24 hours of treatment. CoNPs cytotoxicity evaluated in concentrations ranging from 20 to 100 µM had no obvious effect on U937 macrophages viability (Figure 3.4). While CoNPs started to show an effect on U937 macrophages at a concentration of 150 µM, which reduced cell viability by approximately 25%. However, this reduction was not visible after 24 hours. 200 µM of CoNPs caused an approximately 30% reduction in cell viability at 6 hour and this effect remained significant after 24 hours. In addition, $Cr^{3+}$ and CrNPs up to 800 µM had limited effect on U937 cell viability.

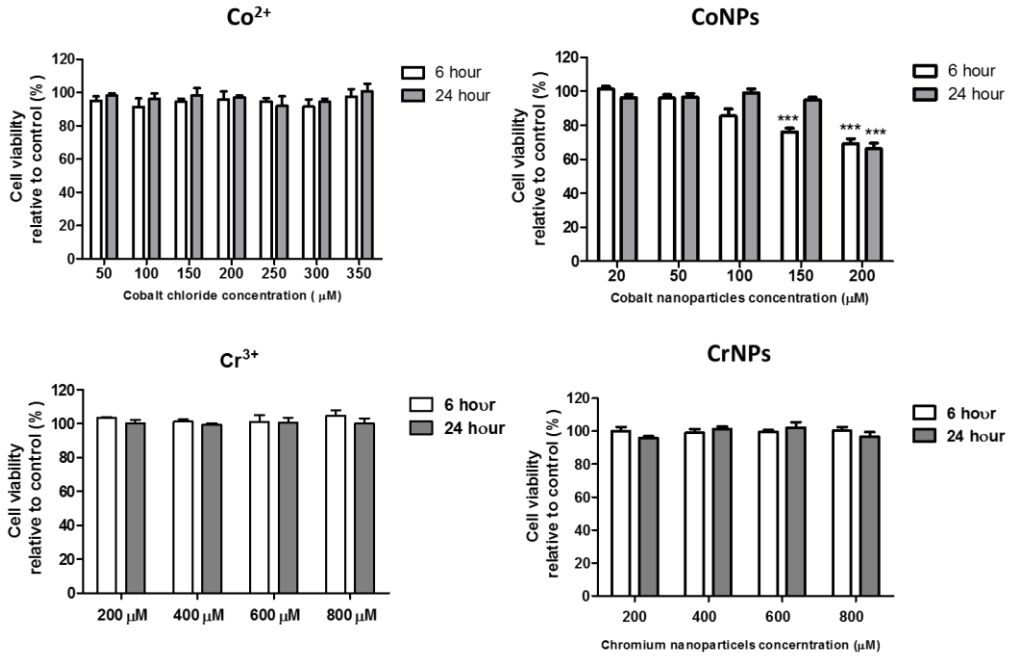


Figure 3.4 Effect of $Co^{2+}$ and CoNPs on U937 cell viability at 6 and 24 hours with the MTS assay. Data represents mean +SEM, n=9 from 3 independent experiments. Statistically significant differences are indicated relative to untreated control; ***p<0.001.

### 3.3.2 The effects of $Co^{2+}$, $Cr^{3+}$, CoNPs and CrNPs on BMDMs viability

In general, $Co^{2+}$ and CoNPs caused a concentration-dependent cytotoxicity in the BMDMs (Figure 3.5). $Co^{2+}$ at concentrations below 100 µM and CoNPs less than 40 µM had no significant effect on the BMDMs viability over 24 hours, which was thereby deemed to be non-toxic. 150 µM of $Co^{2+}$ and 60 µM of CoNPs induced a significant decrease in cell viability, to approximately 80% after 24 hours, falling to approximately 60% at the highest concentrations applied (200 µM Co or 80 µM CoNPs). Therefore, the cytotoxicity results indicate that $Co^{2+}$ and CoNPs at high doses could cause early, or acute adverse cell response and cell death. Similarly, $Cr^{3+}$ and CrNPs did not shown any significant effect on BMDMs viability.

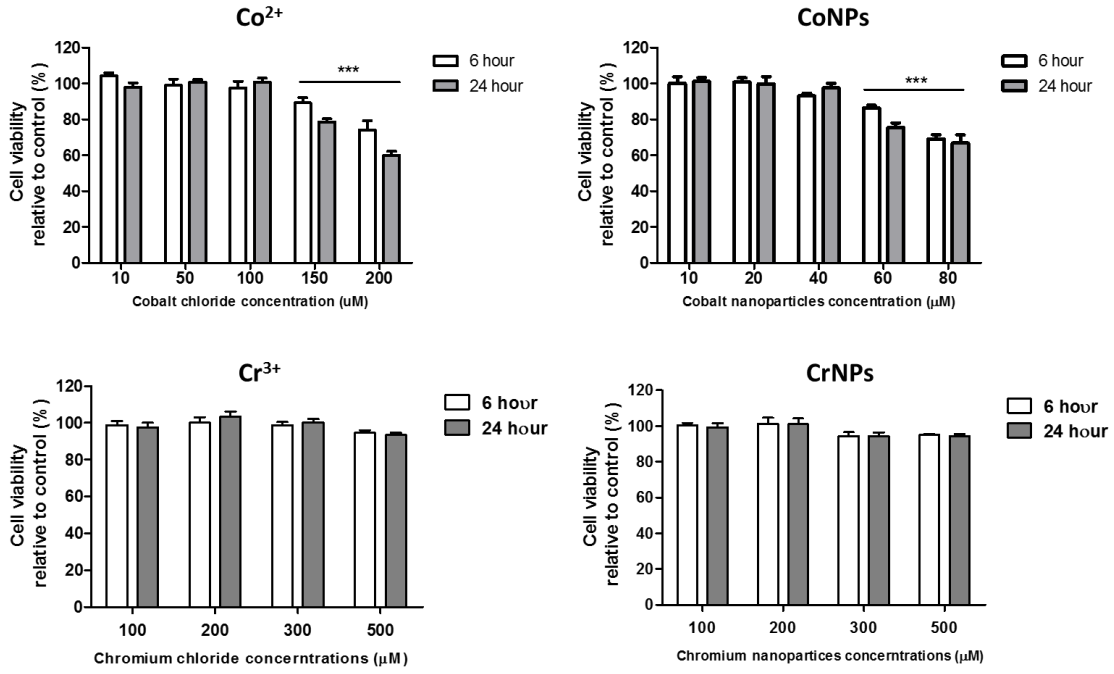


Figure 3.5 Cytotoxic effect of $Co^{2+}$ and CoNPs on the BMDMs viability at 6 and 24 hours. Data represents mean +SEM, n=9 from 3 independent experiments. Statistically significant differences are indicated relative to untreated control; ***p<0.001.

### 3.3.4 $Co^{2+}$ and CoNPs inhibit U937 macrophage random migration

To directly measure the impact of cobalt and chromium on macrophage motility *in vitro*, time-lapse imaging of U937 macrophages after 6 hours of cobalt or chromium treatment using non-cytotoxic concentrations (Table 3.1) based on cell viability testing (Figure 3.4) was performed. Figure 3.6 A-E shows the migration paths for 25 individual cells in each treatment group over 6 hours of observation. The total path length of cells treated with $Co^{2+}$ and CoNPs was significantly shorter than those for untreated control cells ($p<0.001$, Figure. 3.6F). Treatment with $Cr^{3+}$ or CrNPs had no significant effect on macrophage migration length.

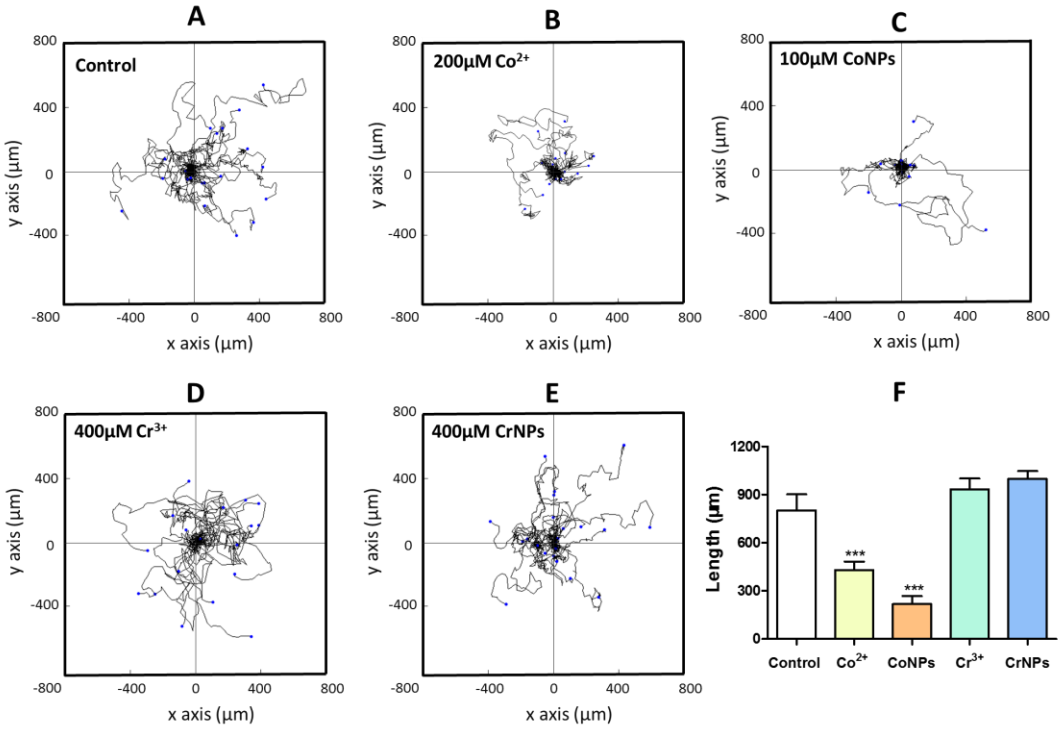


Figure 3.6 $Co^{2+}$ and CoNPs reduce U937 macrophage random migration. (A-E): Detailed migration trajectories of cells (n=25) over a 6-hour period following treatment with cobalt or chromium. Individual tracks were transposed so that each of the cells started at the same origin. (F) Net cell migration length for each treatment with values indicating mean +SEM from 3 independent experiments (n=75 cells/condition). Statistically significant differences are indicated relative to untreated control; ***P<0.001.

### 3.3.5 $Co^{2+}$ and CoNPs inhibits U937 macrophages transmigration

Using the transwell migration assay, the results observed from the cell random migration assay (Figure 3.6) were confirmed. The ability of U937 macrophages to migrate through the porous transwell membrane was significantly impaired by pre-treatment with either $Co^{2+}$ or CoNPs (Figure. 3.7). Exposure to $Co^{2+}$ and CoNPs, reduced the number of transmigrating cells by approximately 62% and 55%, respectively. While CoNPs caused a slightly reduction in cell migration, the difference was not statistically significant. Incubation with $Cr^{3+}$ had no obvious effect on the cell migration relative to untreated controls for U937 macrophages.

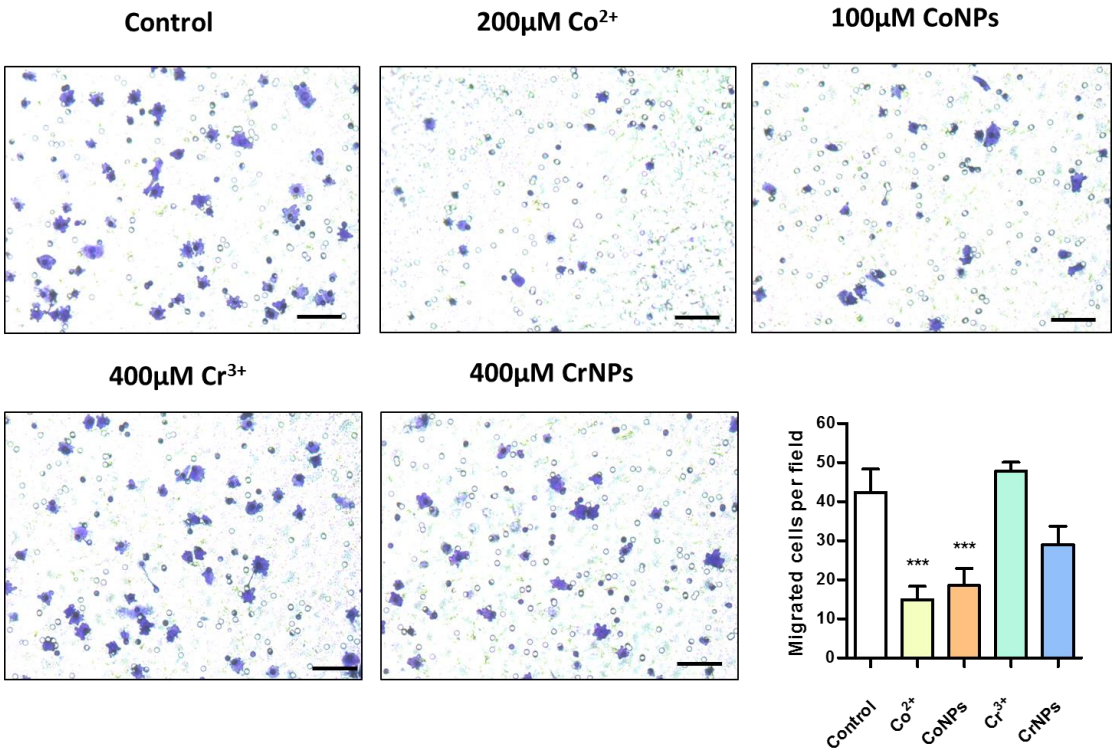


Figure 3.7 $Co^{2+}$ and CoNPs reduce transmigration of U937 macrophages. Representative images of migrated U937 macrophages treated by $Co^{2+}$, CoNPs, $Cr^{3+}$ and CrNPs (Scale bar = 100 µm) and quantifications of the migration assay based on three independent experiments. Values represent mean + SEM. n=30 from 3 independent experiments; 10 random fields were imaged for each treatment in each experiment. Statistically significant differences are indicated relative to untreated control; ***P<0.001.

### 3.3.6 Cobalt inhibits BMDMs transmigration

In BMDMs, the corresponding reduction in migration was approximately 45% and 53% for $Co^{2+}$ and CoNPs, respectively (Figure 3.8). In addition, incubation with $Cr^{3+}$ and CrNPs had no statistically significant effect on the cell migration relative to untreated controls.

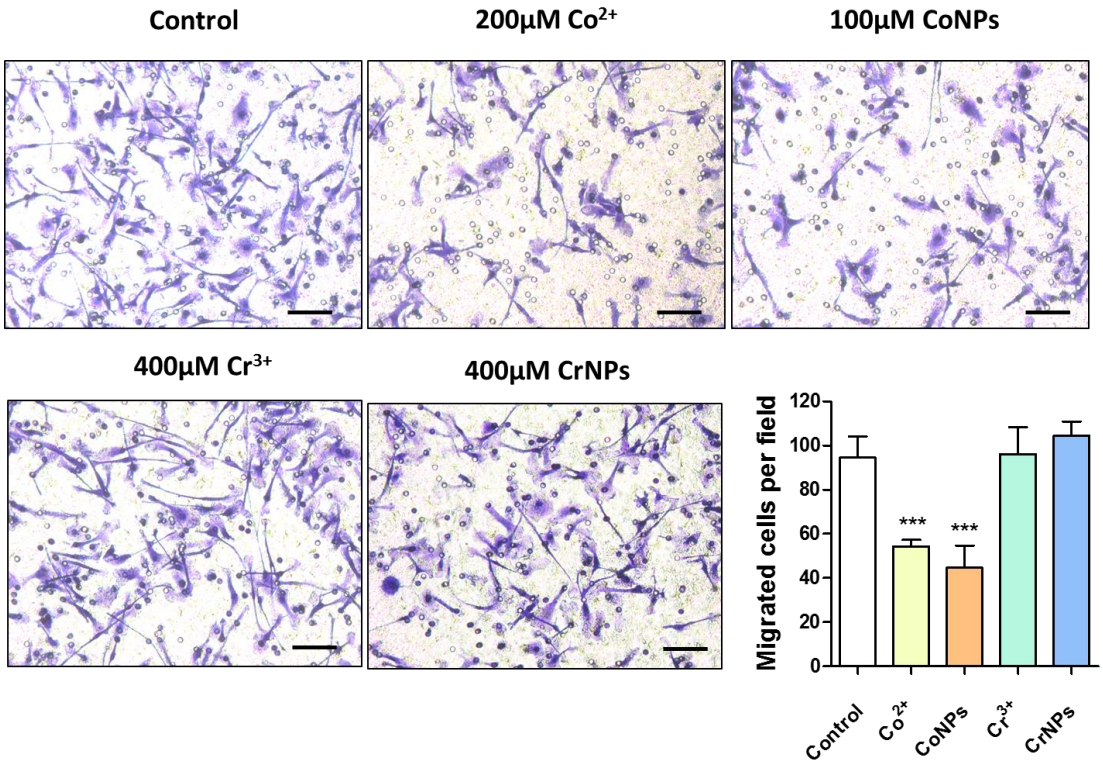


Figure 3.8 $Co^{2+}$ and CoNPs reduce transmigration of BMDMs. Representative images of migrated BMDMs treated by $Co^{2+}$, CoNPs, $Cr^{3+}$ and CrNPs (Scale bar = 100 µm) and quantifications of the migration assay based on three independent experiments. Values represent mean + SEM. n=30 cells from 3 independent experiments (10 random fields were imaged for each treatment in each experiment). Statistically significant differences are indicated relative to untreated control; ***P<0.001.

### 3.3.6 CoNPs inhibit macrophage migration *in vivo*

To study the effect of CoNPs on macrophage migration *in vivo*, the number of macrophages in the mouse peritoneal cavity before and after LPS stimulation with or without 5 µg CoNPs treatment were quantified. Harvested peritoneal macrophages were identified by a flow cytometry gating strategy according to their size and granularity (Figure 3.9A), CD11b and F4/80 surface marker expression (Figure 3.9B).

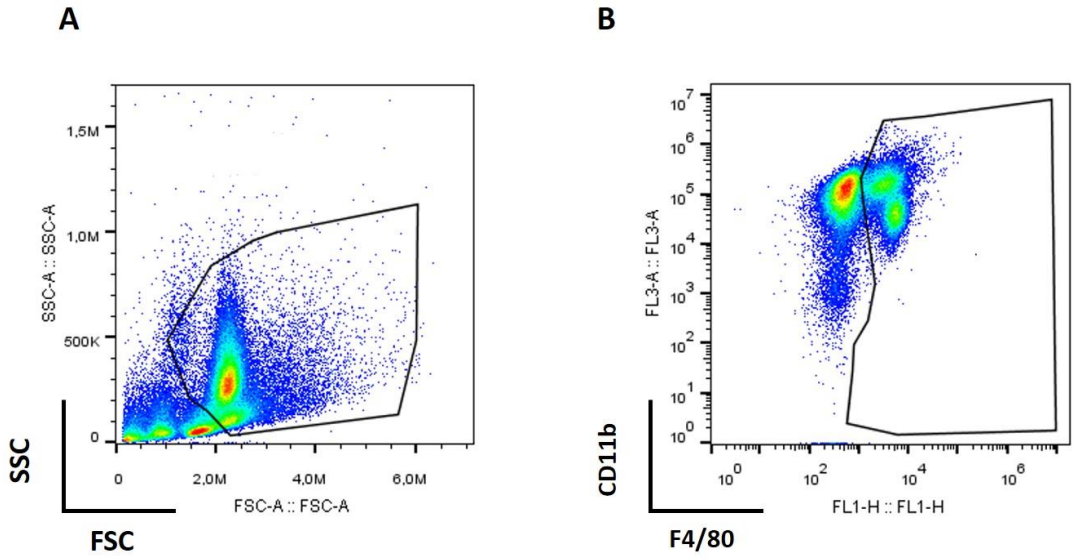


Figure 3.9 Gating strategy of FACS analysis to identify mouse peritoneal macrophages. Representative FACS analysis images showing the gating strategy to identify the peritoneal macrophages based on (A) cell size, cell granularity, (B) CD11b and F4/80 surface markers expression.

In the absence of LPS stimulation, no any significant change to the number of peritoneal macrophages following 12 hours of CoNPs pre-treatment when compared to the PBS control was observed. In control mice (PBS-treatment), LPS stimulation significantly increased the efflux of peritoneal macrophages (Figure 3.10) from the cavity, with a reduction of the number of macrophages to 40% of the control, consistent with previously published work (Park et al., 2009). Following CoNPs pre-treatment, the number of macrophages was not greatly affected by LPS stimulation (95% of the control) and remained at similar levels to the CoNPs pre-treatment alone (115%). In summary, CoNPs inhibited murine peritoneal macrophages migrating out from the cavity.

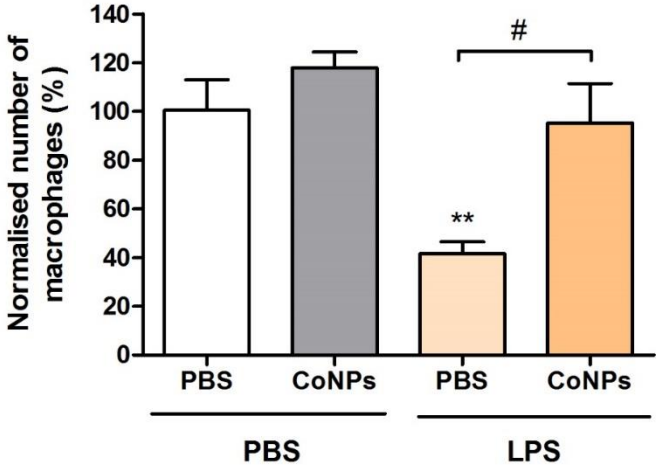


Figure 3.10 Macrophage migration *in vivo* is inhibited by CoNPs. Figure showing the number of harvested macrophages from treated mouse from each group. Data normalised to PBS control. n = 5 mice per treatment, ** indicates difference from PBS control $P < 0.01$; # indicates difference between CoNPs treatment and corresponding PBS control both in the presence of LPS, $P<0.05$).

### 3.4 Discussion

A wide range of in *vivo* and *in vitro* studies have been conducted to elucidate the contributing factors and mechanism underline the pathogenesis of ALTRs due to CoCr exposure. This chapter has described a combined *in vitro* and *in vivo* approach to examine the differential response of macrophages to both cobalt and chromium ions and associated nanoparticles. Here, rather than focusing on what doses of $Co^{2+}$ and CoNPs induce cell apoptosis or trigger inflammatory response, this study has focused on how metal ions and particles exposure alter macrophages migration at relatively modest levels.

It has been well established that both CoCr ions and nanoparticles are cytotoxic and able to trigger apoptosis or necrosis in a dose and time-dependent manner (Papageorgiou et al., 2007, Nyga et al., 2015, Petit et al., 2006, Catelas et al., 2005, Posada et al., 2014). Metallic debris has been shown to promote macrophage activation and trigger the release of an array of proinflammatory mediators, such as TNF-α, IL-1β, IL-6, IL-8 and interferon (IFN)-γ (Caicedo et al., 2010, Kaufman et al., 2008).

The present *in vitro* results revealed that both $Co^{2+}$ and CoNPs markedly inhibit the random migration and chemotaxis of both U937 macrophages as well as murine bone marrow derived macrophages (BMDMs), while $Cr^{3+}$ and CrNPs had no statistically significant effect. These results were further confirmed *in vivo.* Previously, *in vivo* studies have generally been performed by directly injecting micro-size CoCr particles into knees or muscles of rats and/or guinea pigs from a few days to months and investigating the tumor formation or abnormal findings during gross examination of the animals (Brown et al., 2007). For the first time, a peritoneal macrophage efflux model was applied in this study and revealed that, in the presence of CoNPs, macrophage

emigration from the cavity triggered by LPS was significantly inhibited (Figure 3.10), supporting the *in vitro* findings. These findings suggest that the extensive clinical issues associated with implants manufactured from CoCr alloys could be associated with macrophage retention in the peri-prostheses area due to impaired cell migratory ability.

Cell migration plays a critical role in many cellular process, such as embryogenesis, wound healing or immune response (Mayor and Etienne-Manneville, 2016). It has been reported that metal ions and NPs are able to alter the speed of the cell motility. $Co^{2+}$ and $Cr^{3+}$ have been shown to enhance the migration of T lymphocytes. Beryllium ($Be^{2+}$), known as a metal sensitizer, can also stimulate lymphocyte migration (Klein et al., 2006). The contributing factors for the enhanced cell migration was not provided in these studies. Also, one study examined the chemotactic effects of $Co^{2+}$ and $Cr^{3+}$ on human neutrophils via monitoring cell movement through agarose gels (Williams, 1989). Their results suggested that cobalt and chromium ions are not chemotactic for human neutrophils. On the other hand, a variety of NPs are showed to have an effect on cell motility. For example, the speed of A549 cell movement was reduced by $SiO_2$ NP treatment due to the disruption of cytoskeleton structure (Gonzalez et al., 2015). In addition, $SiO_2$ and $TiO_2$ treatments have been shown to increased cell adhesion, cell traction and reduce migration of TR146 cells in a dose-dependent manner, which is also associated with alteration in cytoskeleton (Tay et al., 2014a). However, treatment of MSC cells with $TiO_2$ have been shown to impair cell adhesion and lead to reduced cell migration, as, without proper adhesion, cells are not be able to exert sufficient traction force to pull the cells forward in order to initiate migration (Hou et al., 2013). In all, the effects of metal ions and NPs on cytoskeleton organization and cell-ECM interaction play essential roles in promoting or hampering cell migration. In the light of this, whether $Co^{2+}$, $Cr^{3+}$, CoNPs and CrNPs mediate changes in cytoskeleton and associated

molecular signalling pathway will be investigated in the next chapter to elucidate the mechanisms of macrophages retention caused by $Co^{2+}$ and CoNPs.

# Chapter 4. Cytoskeleton remodelling and associated signalling pathway activation resulting from $Co^{2+}$, $Cr^{3+}$, CoNPs and CrNPs treatment

## 4.1 Introduction

By applying a range of *in vitro* and *in vivo* migration assays, chapter 3 demonstrated that $Co^{2+}$ and CoNPs, reduced macrophage migration capacity, while $Cr^{3+}$ and CrNPs had limited effects. In response to tissue damage or infection, macrophages have the ability to quickly change their shape and move. To initiate cell migration, internal forces are developed by the actin cytoskeleton and transmitted through cell-substrate adhesion sites coupled with the dynamic turnover of adhesion complexes (Mayor and Etienne-Manneville, 2016). Generally, cell migration includes the steps illustrated schematically in Figure 4.1.

1. In response to the guidance cue in the extracellular environment, cells form short surface protrusions, termed filopodia or microspike supported by a core of bundled actin filaments (microfilaments) at the front. In macrophages, filopodia support a thin sheet of membrane-enclosed cytoplasm, known as lamellipodia, containing a meshwork of myosin II-associated microfilaments.
2. New adhesion points are then formed in the front of cell for attachment to the ECM.
3. Actomyosin activity is enhanced to promote the retraction of the rear.
4. Finally, the whole cell body is enable to move forward via disassembly of the adhesions at the rear part of cell.

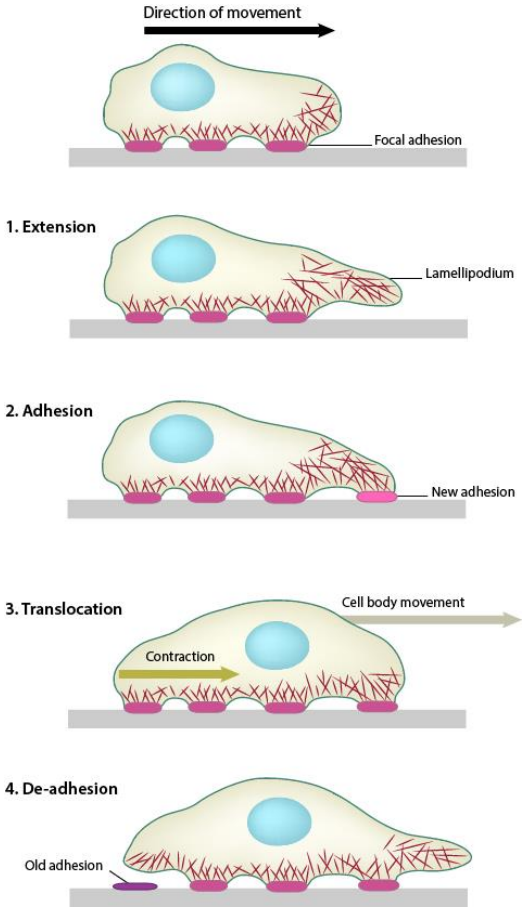


Figure 4.1 Illustration of the basic steps during 2D cell migration. (Adapted from https://www.mechanobio.info).

While the actin cytoskeleton provides the driving force for cell migration, the microtubule network is known to play a critical role in regulating cell polarity (Ridley et al., 2003). Studies concerning the correlation between the actin and microtubule structure have also indicated that these two polymers are closely connected via signalling molecules and intermediate proteins either directly or indirectly (Etienne-Manneville, 2004).

Therefore, in this chapter, a wide range of techniques were applied to unravel the effects of $Co^{2+}$ and CoNPs on macrophage cytoskeleton organization and associated signalling pathway that regulate the retention of macrophages after treatment with cobalt.

## 4.2 Method

### 4.2.1 Immunofluorescence confocal and super resolution microscopy

Cobalt and chromium-treated U937 macrophages and BMDMs were fixed with 4% paraformaldehyde (Sigma, USA) and washed and permeabilized with 0.5% Triton X-100 and rinsed 3 times with PBS. Nonspecific binding sites were blocked by adding PBS with 1% BSA. The adhesion protein, vinculin, was labelled by incubation at 4°C, overnight with mouse monoclonal anti-vinculin primary antibody, clone hVIN-1 (1:400, Sigma, USA). Cells were then washed and incubated for 1 h at room temperature in Alexa 488 conjugated anti-Mouse IgG as Secondary Antibody (1:1000, Invitrogen, USA). In separate samples, cellular α-tubulin and acetylated α-tubulin were labelled using rabbit polyclonal anti-α tubulin antibody (1:200, Abcam, UK) and mouse anti-acetylated tubulin, clone 611B-1 (1:2000; Sigma-Aldrich, USA) respectively with Alexa 488 secondary antibodies as above.

To simultaneously label the F-actin, the samples were incubated for 30 mins with 200 µl of rhodamine-conjugated phalloidin (Molecular Probes, USA) in a humidified chamber at room temperature in the dark. Cell nuclei were stained by incubation with 5 µg/ml DAPI (Dojindo) followed by two PBS rinses. Slides were then visualized with a fluorescence microscope (Leica SP2) with x63 objective. Slides were also imaged on a microscope (Zeiss 710 ELYRA PS.1) with a ×63/1.4 NA objective for structural illumination microscopy.

### 4.2.2 Protein extraction and Immunoblotting

All lysis buffers were supplemented with 1% protease inhibitor (Sigma Aldrich, USA). Protein extracts were resolved using gradient precast SDS – polyacrylamide gel electrophoresis (Biorad Laboratories Inc, USA), and then electro-transferred onto a

nitrocellulose membrane by using Trans-Blot® Turbo™ Transfer System (Biorad Laboratories Inc, USA) for immunoblot analysis. Antibody probing was performed as per manufacturers' instructions. Secondary antibodies either IRDye® 800CW Goat anti-Mouse IgG (LI-COR, USA) or IRDye® 800CW Goat anti-Rabbit IgG (LI-COR, USA) were used with dilution of 1:10000. Specific protein bands were detected using Odyssey® CLx Imaging System (LI-COR, USA). Images of protein bands were analysed as depicted in Appendix I.

### 4.2.3 Scanning electron microscope (SEM) analysis

U937 macrophages treated by $Co^{2+}$ (200 µM), CoNPs (100 µM), $Cr^{3+}$ (400 µM) or CrNPs (400 µM) for 12 hours were fixed in 2.5% glutaraldehyde (Sigma, USA) for 2 h and dehydrated in graded ethanol (50%, 70%, 80%, 90%, 95%, and 100%; 10 min for each). The samples were transferred to critical-point drying with hexamethyldisilazane (Sigma, USA) then coated with a 5 nm thick layer of gold–palladium alloy. The SEM images were obtained with a scanning electron microscope (FEI Quanta 200) at a low voltage (~1 kV).

### 4.2.4 Immunofluorescent images analysis

Immunofluorescent images were analysed by using imageJ (NIH, USA) (Schindelin et al., 2012). To quantify cell area, the original image (Figure 4.2A) for the F-actin channel was converted to 8 bits and binary images (Figure 4.2B). Individual cells were defined as region of interest (ROI) to measure cell area using Analyze Particles tool in imageJ. For quantification of podosomes, the image (Figure 4.2D) was first smoothed to reduce the background noise (Figure 4.2E). The images were similarly converted to binary (Figure 4.2F) with adjacent objects segmented using the Watershed function. The circular areas of F-actin dots corresponding to podosomes were defined using the

Analyze Particles tool and counted with the Find Maxima tool in ImageJ (Cervero et al., 2013).

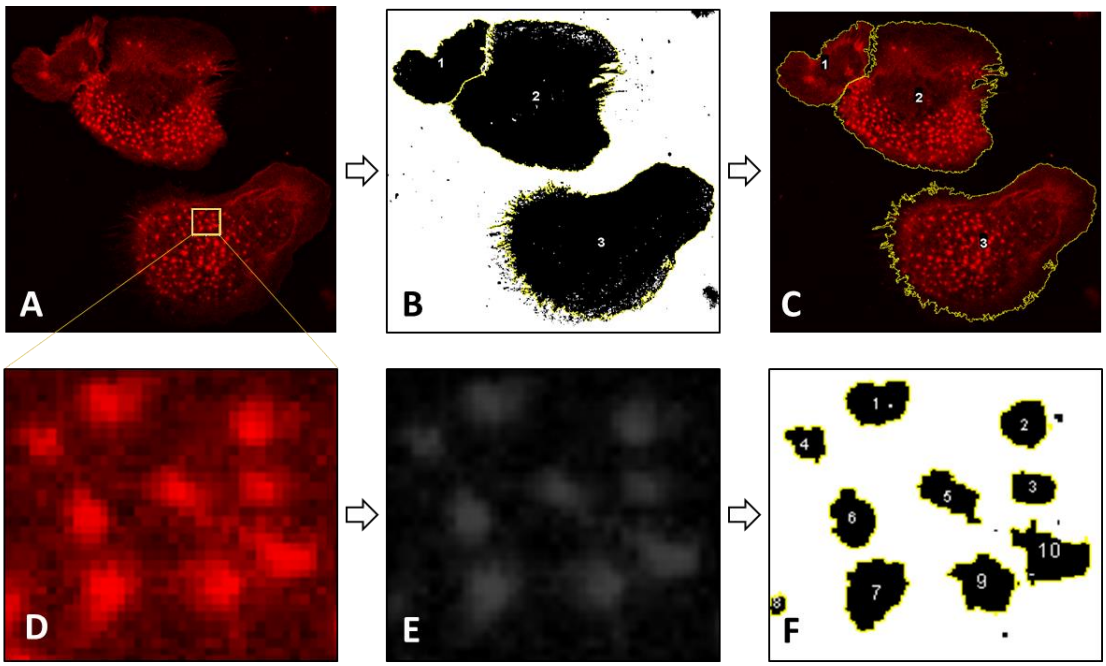


Figure 4.2 Fluorescence images showing the method applied to quantify cell area and podosomes in individual cell with ImageJ step by step.

### 4.2.5 Cell adhesion assay

U937 macrophages were seeded at a concentration of $2\times10^5$ cells/well into a 24-well plastic cell culture plate coated with 2% gelatin and treated with 100 µM, 200 µM or 300 µM $Co^{2+}$. After 30 min of incubation, cell culture medium in each well was aspirated and gently rinsed twice with warm PBS. Adherent cells were then imaged (10 fields of each well were randomly selected) with an inverted microscope (DCF420, Leica, Germany) and counted.

### 4.2.6 *In vitro* ECM degradation assay

*Preparation of glass coverslips and coating with fluorescently-conjugated gelatin*

Cells were seeded onto coverslips that were coated with FITC-conjugated gelatin as part of an *in vitro* ECM degradation assay, as described in Figure 4.3. Briefly, glass coverslips were coated with 0.2 mg/ml FITC-gelatin (Molecular Probes) in PBS and fixed with 0.5 % glutaraldehyde, washed six times with PBS, then washed once with 70% ethanol/PBS and once with medium.

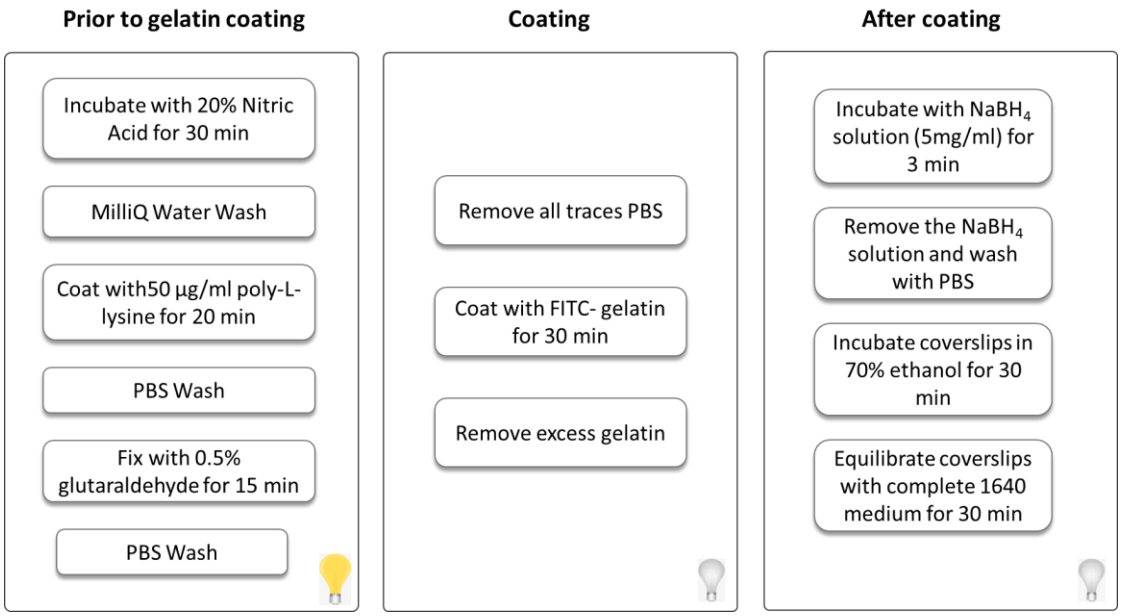


Figure 4.3 Schematic demonstrating the individual steps involved in preparing glass coverslips for gelatin matrix coating. Steps conducted in the light (lit bulb) and in the dark (non-illuminated bulb) are cartoon indicated. Steps conducted in the dark help prevent photobleaching of the fluorescent matrices.

*Matrix degradation activity quantification*

U937 macrophages ($1 \times 10^5$) were plated onto the coverslips and incubated at 37 °C for 24 h, then fixed, processed for F-actin staining with rhodamine-conjugated phalloidin, and observed as described above. The coverslips were examined using a Leica SP2 confocal microscope and the total area that was degraded was measured using ImageJ software [17]. The matrix degradation index was calculated as the ratio between the

areas of gelatin matrix degraded by treated cells to the area of gelatin matrix degraded by untreated cells.

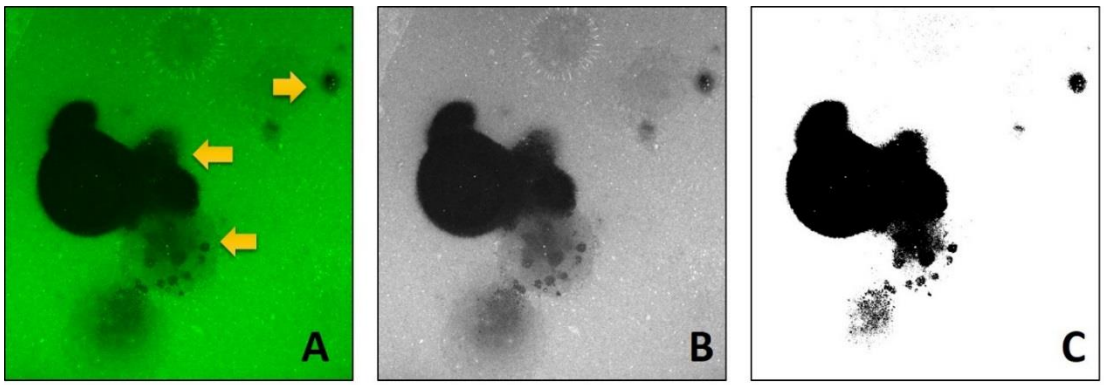


Figure 4.4 Images demonstrating key steps in computational-assisted quantification of normalized gelatin degradation. (A) Image of FITC-conjugated gelatin, showing dark areas (arrows) where degradation has occurred. (B) 8-bit image converted from A. (C) Thresholded gelatin image highlighting areas of degradation, which would be measured by imageJ software.

### 4.2.7 Gelatin zymography

Conditioned media collected from cells treated by $Co^{2+}$ and CoNPs were used for gelatin zymography to measure MMPs activities. The supernatants were subjected to electrophoresis in an 8% SDS-PAGE gel co-polymerized with gelatin (1 mg/ml, Sigma, USA). The gelatinolytic activities were detected as transparent bands against the background of Coomassie Brilliant Blue-stained gelatin and quantified using ImageJ software.

### 4.2.8 ROS measurements

ROS formation was measured using 5-(and 6-)-chloromethyl-2’7’-dichlorodihydrofluorescein diacetate (CM-$H_2$DCFDA, Life technologies, USA). Cells were cultured in black 96-well plates with a clear bottom. After exposure, the supernatant was removed and cells were briefly washed with warmed PBS. CM-

H2DCFDA was dissolved in anhydrous DMSO to a final concentration of 1 mM and diluted further in Hank's balanced salt solution (HBSS, ThermoFisher, USA). Cells were exposed to 1 μM CM-H2DCFDA for 30 min at 37 °C in the dark. Fluorescence was read at excitation 485/20 nm with emission 528/20 nm using a microplate reader (Synergy HT Multi-Mode).

### 4.2.9 Data analysis

Normality testing (Kolmogorov-Smirnov test) was performed for all experimental data. All data are expressed as the median or mean ± SEM from independent repeat experiments (N=3). The number of repeat measurement per experiment (n) is indicated for each figure. Statistics analysis conducted with SPSS (Inc., Chicago, IL, USA) for each assays are listed in Table 4.1.

Table 4.1 Statistics methods for each assays.

| **Experiments** | **Statistics methods** |
|---|---|
| Fluorescent signal intensity measurement | one-way ANOVA with Bonferroni post-hoc t-test |
| Protein expression analysis via western blot | one-way ANOVA with Bonferroni post-hoc t-test |
| Transmigration assays | one-way ANOVA with Bonferroni post-hoc t-test |
| Quantification of podosome number and podosome density. | Kruskal-Wallis test and Dunn's post-test |
| Podosome formation in $Co^{2+}$-treated cells with or without NAC | Mann-Whitney U test |
| Percentages of cells forming podosomes projected cell area quantification | one-way ANOVA with Bonferroni post-hoc t-test |
| Cell adhesion analysis | one way ANOVA and Bonferroni post-hoc t-test |
| Zymography assay | one-way ANOVA with Bonferroni post-hoc t-test |
| ROS production analysis | one-way ANOVA with Bonferroni post-hoc t-test |

## 4.3 Results

### 4.3.1 Modulation of cobalt and chromium on microtubule acetylation in U937 macrophages

4.3.1.1 Influence of $Co^{2+}$ and CoNPs on microtubule acetylation in U937 macrophages

Uptake of metal particles are known to impede the force balance between the microtubule and F-actin by inhibiting MT polymerization (Mayor and Etienne-Manneville, 2016). Therefore whether the inhibition of macrophage migration is caused by microtubule or cytoskeletal impairment was investigated.

The structure of the microtubules for the untreated and treated cells are shown in Figure 4.5A. It is evident that exposure to $Co^{2+}$ and CoNPs induced a substantial increase in U937 macrophage tubulin acetylation based on the fluorescent signal of immuolabeled acetylated-α-tubulin (Ac-tubulin, Figure 4.5A), the basic component for microtubule biopolymer (Akhmanova and Steinmetz, 2015). Further quantification of the fluorescent intensity of acetylated α-tubulin relative to α-tubulin (Figure 4.5B) showed a significant increase in the acetylation of tubulin when macrophages were treated by $Co^{2+}$ and CoNPs (~90% and ~50% increase respectively). Cr and CrNPs did not have an obvious effect on the acetylation of tubulin in macrophages (Figure 4.5). Tubastatin A (5μM) was applied as a positive control to induce hyper-acetylation of α-tubulin.

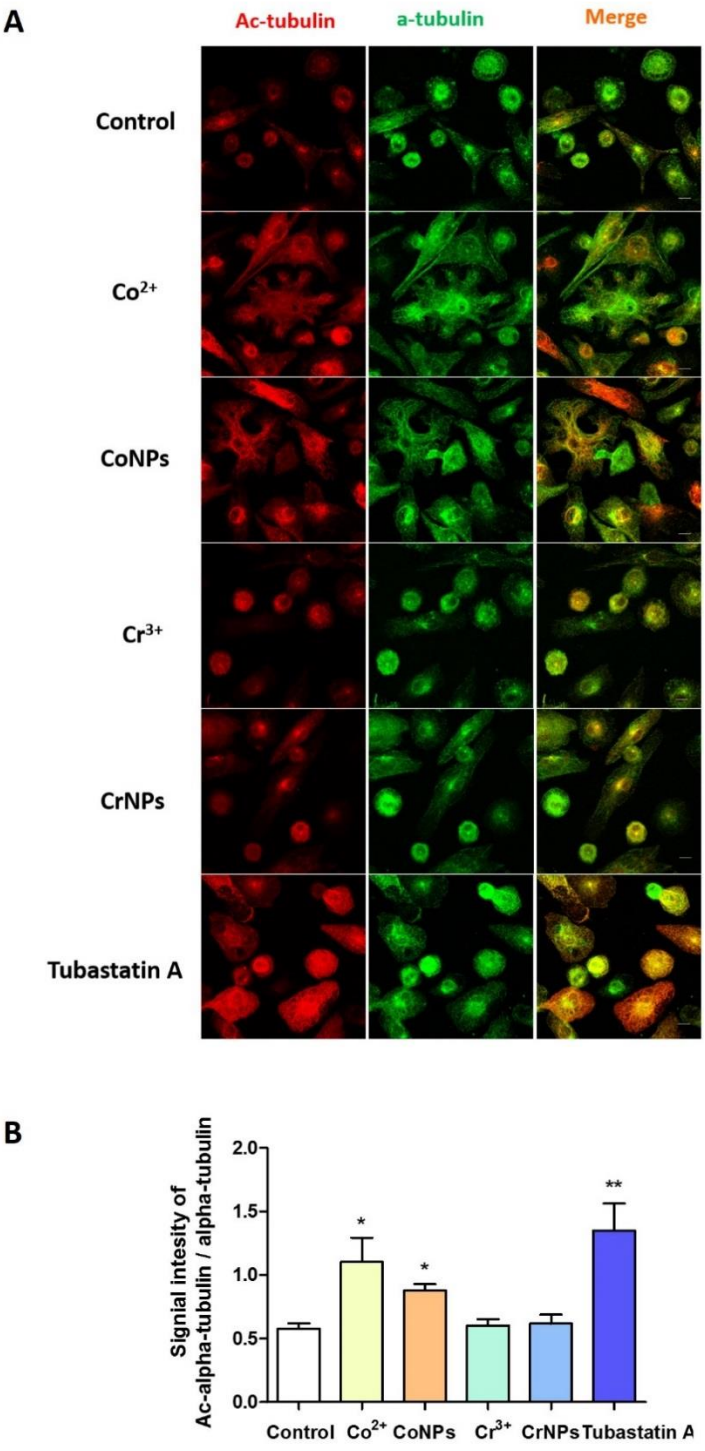


Figure 4.5 Cobalt induces hyper-acetylation of alpha tubulin. (A) Representative immunofluorescence confocal images of U937 macrophages treated with $Co^{2+}$, CoNPs, $Cr^{3+}$, CrNPs and Tubastatin A. Cells were stained for acetylated α-tubulin (red) and α-tubulin (green). Scale bar represents 20 µm. Integrated fluorescent signal intensity for acetylated and non-acetylated tubulin in each cell was quantified and shown in (B); values represent mean +SEM; n=75 cells for $Co^{2+}$, CoNPs, $Cr^{3+}$, CrNPs and Tubastatin A treatment from 3 independent experiments (25 cells/experiment); *$p < 0.05$; **$p < 0.01$.

Further protein expression analysis revealed a consistent increase in acetylated a-tubulin of $Co^{2+}$ and CoNPs-treated cell (Figure 4.6). By contrast, chromium had no significant effect on microtubule organisation or acetylation.

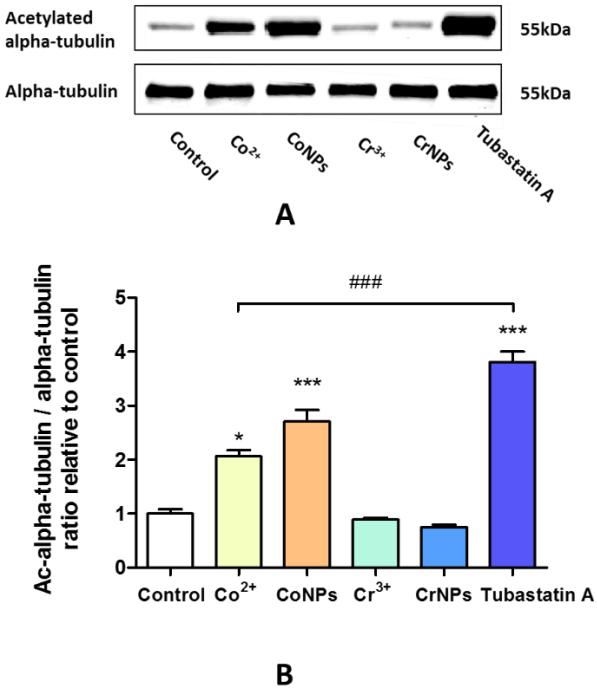


Figure 4.6 Cobalt induces hyper-acetylation of alpha tubulin at protein level. (A) Western blots results for acetylated α-tubulin and α-tubulin for cells treated with cobalt, chromium, Tubastatin A and (B) the corresponding quantification demonstrating increased total α-tubulin acetylation. Values represent mean +SEM; n=6 replicates for $Co^{2+}$, CoNPs, $Cr^{3+}$ and CrNPs treatment from 3 independent experiments (2 replicates/experiment); n=4 replicates for Tubastatin A treatment from 2 independent experiments (2 replicates/experiment); */*** indicate difference from control, $p < 0.05$/$p < 0.001$; ### indicate difference between $Co^{2+}$ and Tubastatin A, $p < 0.001$.

4.3.1.2 The effect of microtubule acetylation on U937 macrophages migration

Overexpression of HDAC6 (Histone deacetylase 6), which induces a global deacetylation of alpha-tubulin, promotes NIH-3T3 cell chemotactic migration (Hubbert et al., 2002). Similarily, Tubastatin A treatment caused a statistically significant reduction in the number of migrated U937 macrophages quantified using the transwell migration assay, which partially replicated the effect of cobalt treatment (Figure 4.7). However, while Tubastatin A induced a greater degree of increase in tubulin acetylation compared to exposure to $Co^{2+}$ (Figure 4.6B, $p< 0.001$), it did not have a parallel impact on macrophage migration (Figure 4.7). This suggests that cobalt-mediated tubulin acetylation in macrophages does not play a decisive role in downregulation of cell migration resulted from cobalt challenge.

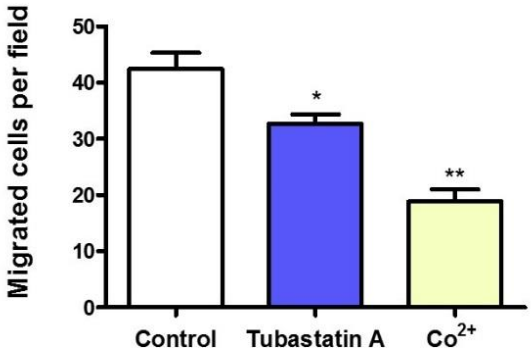


Figure 4.7 The effect of Tubastatin A on macrophage migration compared with $Co^{2+}$ treatment. Increased tubulin acetylation with Tubastatin A significantly reduced macrophage transwell migration partially replicating the effect of cobalt treatment. Values represent mean+SEM; 10 random fields were imaged for each treatment in each experiment. n=30 from 3 independent experiments; *$p<0.05$, **$p< 0.01$.

### 4.3.2 Cobalt promotes F-actin cytoskeleton remodelling of U937 macrophages

Unlike some other adherent cell lines, instead of forming actin stress fibres, macrophages produce podosomes, which comprise of a F-actin core, surrounded by a ring of adhesion receptors and actin-associated proteins (Evans and Matsudaira, 2006). U937 macrophages were shown to express characteristic podosome-like punctate adhesion structures, characterised by an actin-rich core surrounded adhesion proteins, for example, vinculin. Treatment with both $Co^{2+}$ and CoNPs dramatically enhanced podosome formation. (Figure. 4.8).

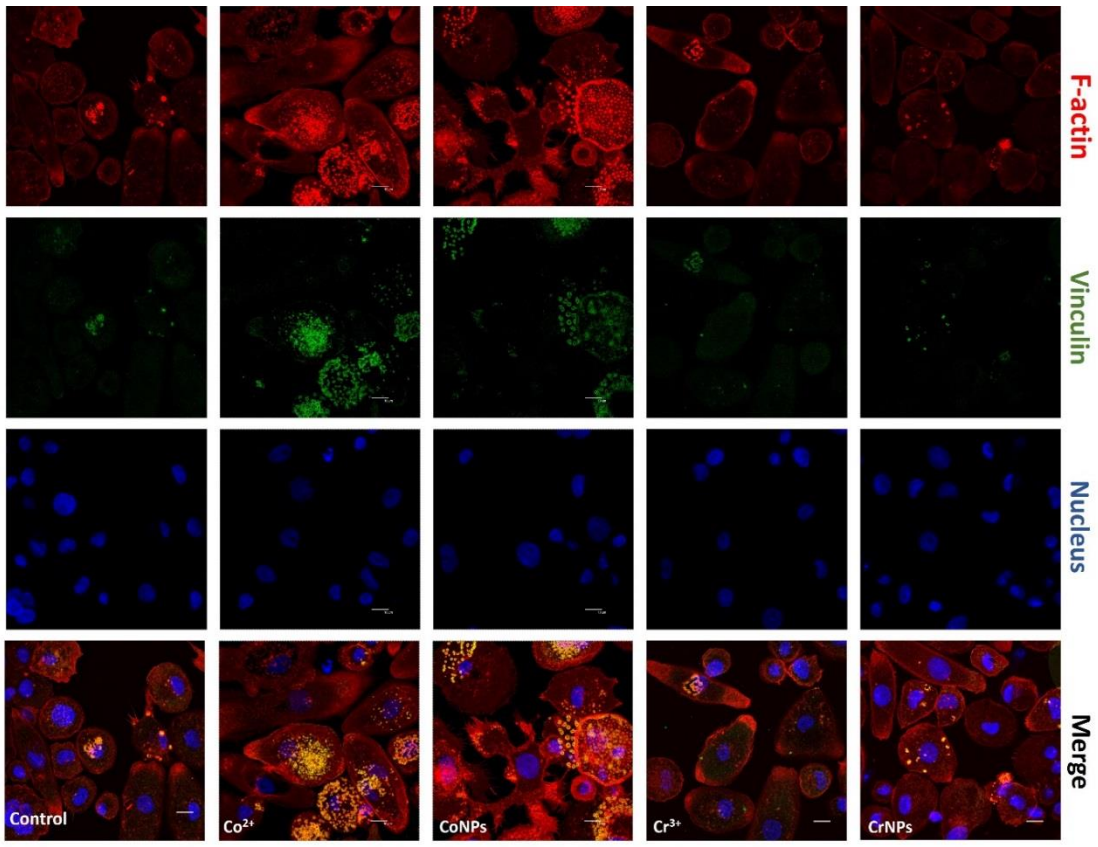


Figure 4.8 $Co^{2+}$ and CoNPs promote podosome formation. Representative confocal microscopy images showing appearance of punctate podosome adhesion structures consisting of actin core (red) and surrounded by vinculin (green) in U937 macrophages following treatment with cobalt or chromium. Scale bar indicate 10 µm.

Treatment with both $Co^{2+}$ and CoNPs significantly increased the number podosome (Figure 4.9A), the density within individual cells (Figure 4.9B) and the percentage of cell showing podosomes (Figure 4.9C). Quantification of cell projected area revealed that $Co^{2+}$ and CoNPs also led to marked cell spreading with a significant increase ($p<0.001$) in cell size (Figure 4.9D).

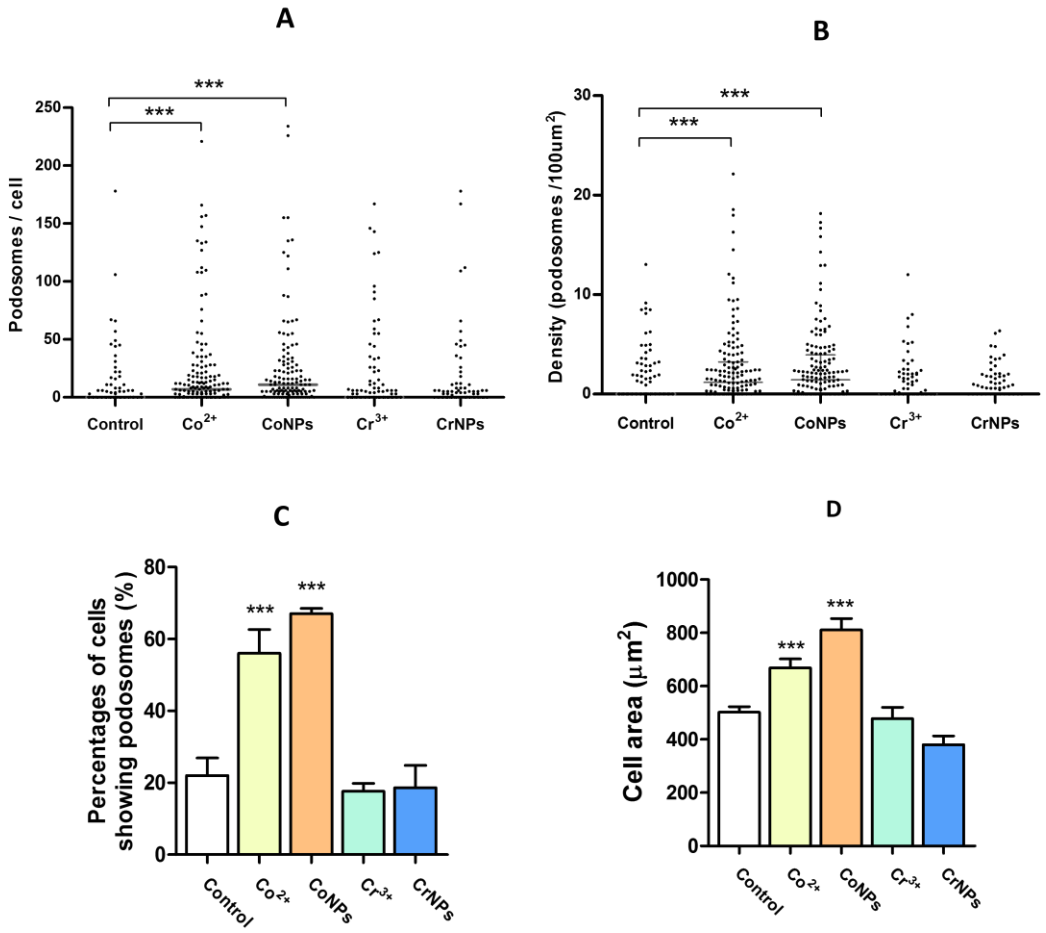


Figure 4.9 $Co^{2+}$ and CoNPs promote podosome formation. Quantification of (A) Podosome number/cell; (B) Podosome density; data with median shown from one representative experiment out of three; n=200; ***$p < 0.001$. (C) Percentages of cells forming podosomes in different group and (D) Projected cell area for each treatment. Vales represent mean + SEM, n=600 cells from 3 independent experiments (200 cells/experiment); ***$p < 0.001$.

### 4.3.3 Cobalt induces macrophage morphology change

Consistent with F-actin cytoskeleton labelling, as shown by SEM images, $Co^{2+}$ and CoNPs promoted drastic changes in the U937 macrophage morphology with marked cell spreading and increased lamellipodia protrusions projected around the cell periphery (Fig. 4.10).

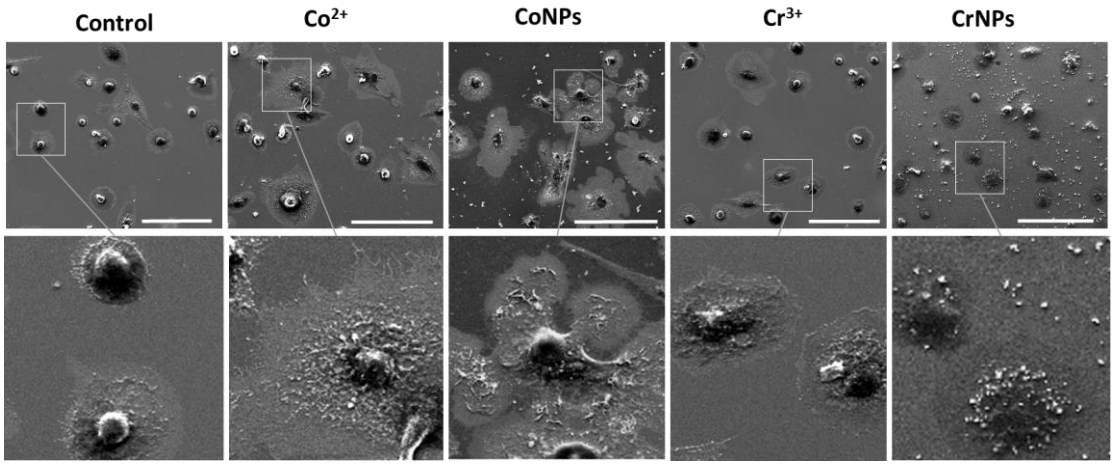


Figure 4.10 Representative SEM images of U937 macrophages incubated for 12 h with $Co^{2+}$ (200 µM), CoNPs (100 µM), $Cr^{3+}$ (400 µM) or CrNPs (400 µM) and untreated control. Scale bar indicates 100 µm.

### 4.3.4 Cobalt promotes podosome formation in BMDMs

While cell area is not statistically different among different treatment groups (Figure 4.11A), treatment with both $Co^{2+}$ and CoNPs significantly increased the percentages of cells showing podosomes. While around 24% of untreated BMDMs presented podosome structure, $Co^{2+}$ and CoNPs exposure induced approximately 46% and approximately 40% BMDMs respectively to form podosomes (Figure 4.11 B,C). Similarly, neither $Cr^{3+}$ nor CrNPs showed an obvious effect on cytoskeleton organization of BMDMs.

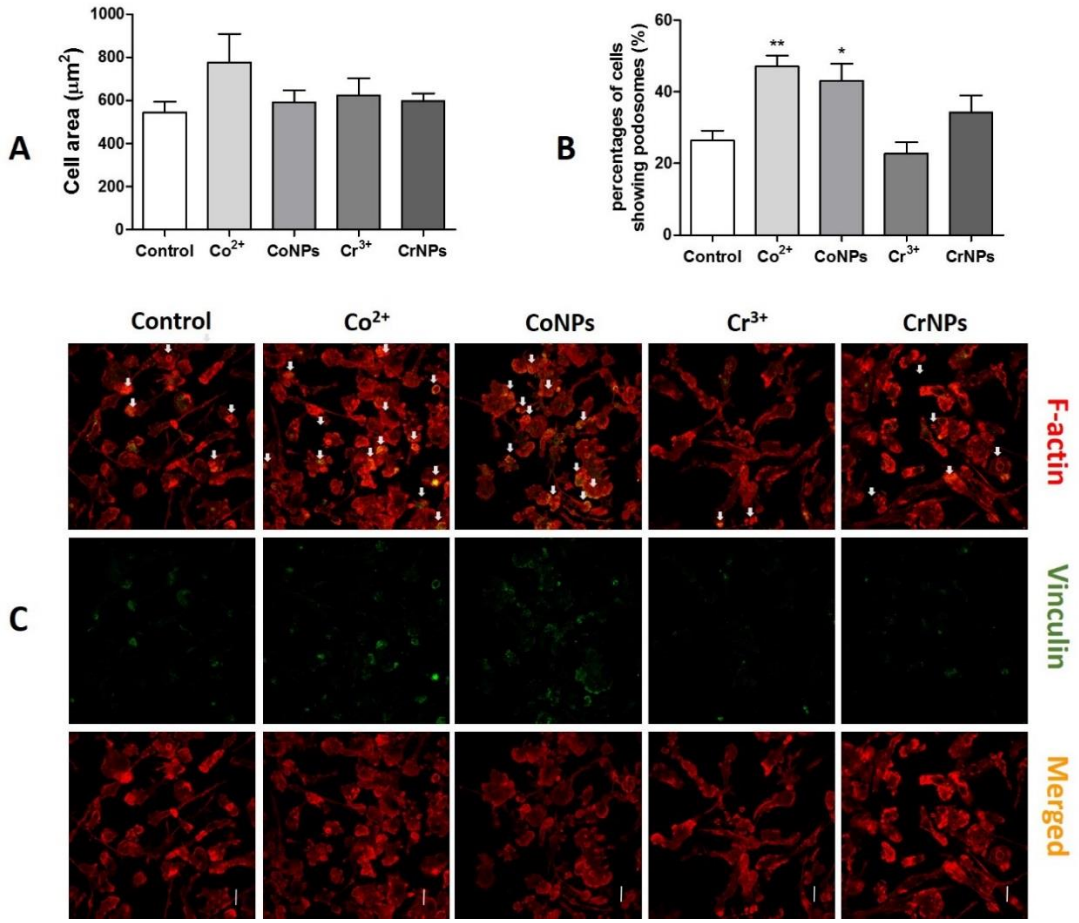


Figure 4.11 Cobalt increases the percentages of cells forming podosomes in BMDMs, (A) Quantification of alteration in cell area. (B) Percentages of cell forming podosmes in BMDMs after treatments; arrows: podosomes in BMDMs; Vales represent mean + SEM, n=300 cells from 3 independent experiments (100 cells/experiment); *$p < 0.05$, **$p < 0.01$. (C) Staining and of podosome formation; arrows: podosome structure. Scale bar indicates 10 µm.

### 4.3.5 $Co^{2+}$ enhance cell adhesion in a dose-dependent manner

It is known that an excessive formation of adhesion complexes could result in the strong anchorage of cells to the underlying substrate, which can lead to inhibited cell migration (Osma-Garcia et al., 2016). Thus, whether changes in morphology and podosome formation due to cobalt treatment, were associated with alterations in cell adhesion was examined. Treatment with $Co^{2+}$ enhanced U937 macrophage adhesion, to extracellular matrix as shown by a dose-dependent increase in the number of adhered macrophages

(Figure 4.12). Collectively, these results indicated that the cobalt-induced reduction in migration were associated with cytoskeletal reorganisation, podosome formation and increased cell adhesion.

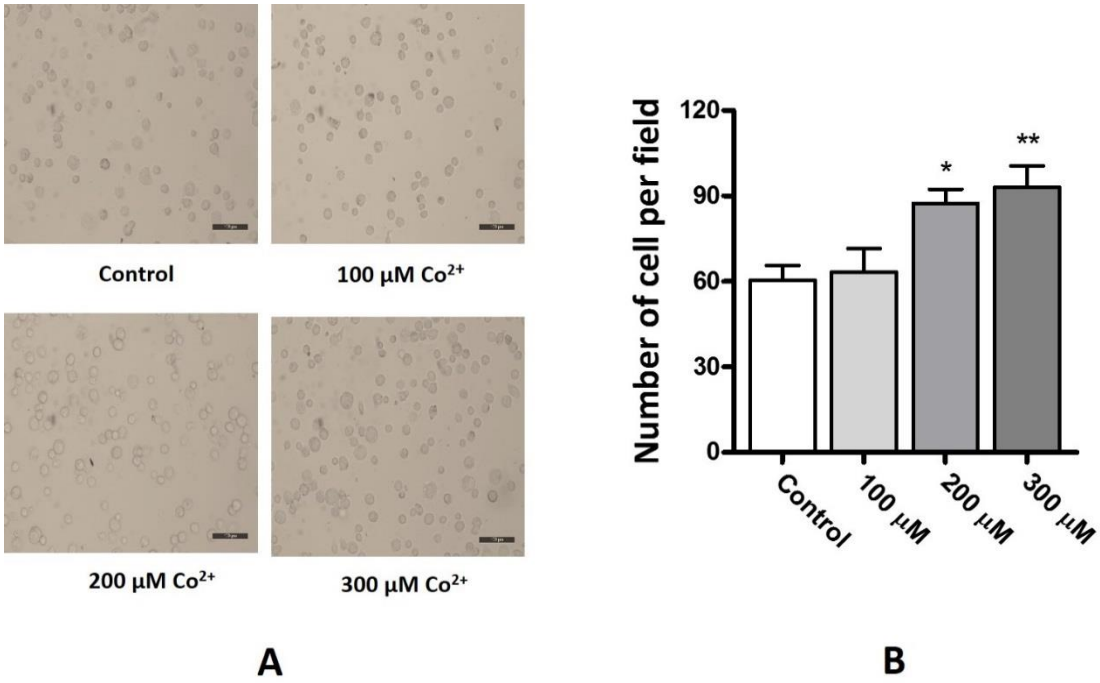


Figure 4.12 (A) Representative bright-field of view images showing that cobalt increased cell adhesion to ECM in a dose-dependent manner, where the scale bar indicates 100 µm, as quantified in (B) by significantly increased numbers of adherent cells per field of view at 200 µM and 300 µM. Values represent mean + SEM. n=30 from 3 independent experiments; 10 random fields were imaged for each treatment in each experiment; *$p < 0.05$, **$p < 0.01$.

### 4.3.6 Cobalt-induced podosome formation in U937 macrophages stimulates ECM degradation

#### 4.3.6.1 Cobalt enhance ECM degradation by U937 macrophages

Podosomes promote adhesion to the substrate and degrade the components of the extracellular matrix. To determine whether cobalt-induced podosomes are able to locally degrade the extracellular matrix, an *in vitro* matrix degradation assay based on

loss of FITC-conjugated gelatin was performed. Macrophages induced localised degradation as shown by dark areas in the fluorescent-tagged gelatin matrix (indicated by arrows in Figure 4.13A). The degradation of gelatin were closely associated with cells expressing podosomes. In some cases, the podosomes were located directly over the degraded matrix based on confocal images (Figure 4.13A) and fluorescent intensity measurement (Figure 4.13B).

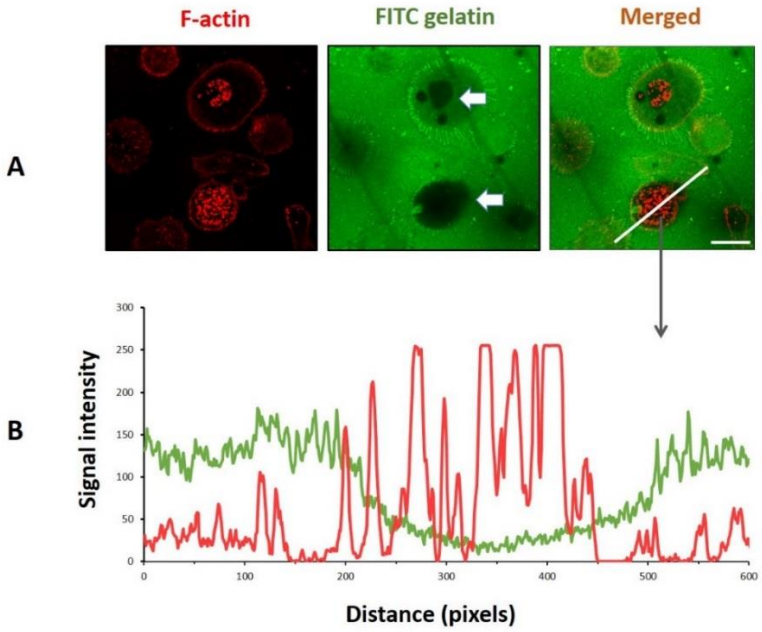


Figure 4.13 Podosome formation in U937 macrophages is associated with ECM degradation. (A) Representative fluorescence microscopy image showing FITC-conjugated gelatin (green) degraded by U937 macrophages counter stained for F-actin (red) podosomes. (B) Associated fluorescence intensity measurement demonstrates the co-localization of areas of gelatin degradation and the F-actin podosomes. Scale bar indicates 10 µm.

Both $Co^{2+}$ and CoNPs promoted matrix degradation as shown by representative images in Figure 4.14A, with associated statistically significant differences in matrix degradation index (Figure 4.14B). Treatment with $Cr^{3+}$ and CrNPs had limited effects on degradation.

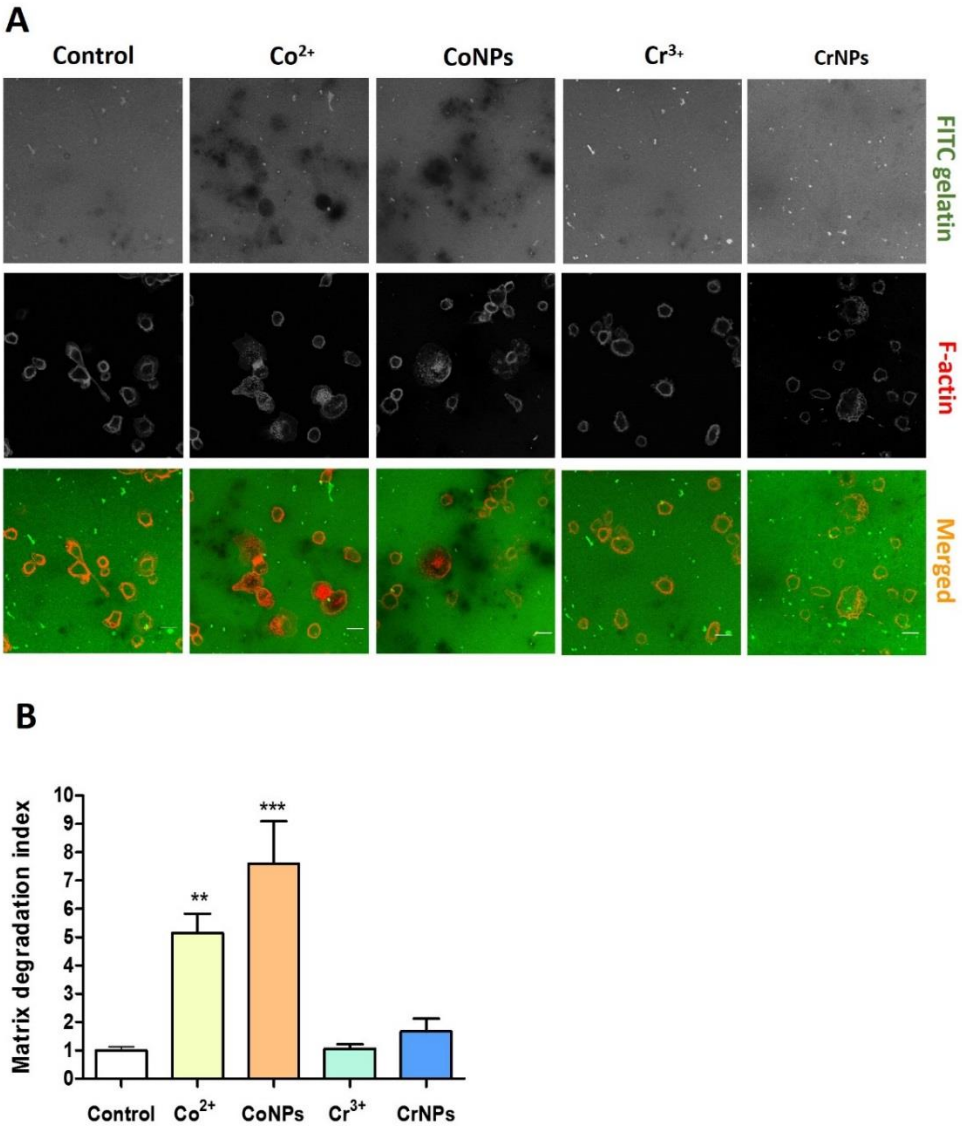


Figure 4.14 Enhanced ECM degradation is induced by $Co^{2+}$ and CoNPs. (A) Representative images showing FITC-conjugated gelatin degradation following 24 h treatment with $Co^{2+}$ (200 µM), CoNPs (100 µM), $Cr^{3+}$ (400 µM) or CrNPs (400 µM) and untreated control. (B) Associated measurements of degradation area quantified as degradation index normalized to control group show significantly increased degradation following cobalt treatments. Values represent mean + SEM. n=30 from 3 independent experiments; 10 random fields were imaged for each treatment in each experiment. $^{**}p < 0.01$, $^{***}p < 0.001$.

4.3.6.2 Cobalt stimulates MMP9 release and activation in U937 macrophages, which is co-localized with podosome formation

The matrix degradation by podosomes involves the recruitment and activation of matrix metalloproteinases (MMPs) (Linder and Aepfelbacher, 2003). Using a zymography assay, the release and activation of MMP2 and MMP9 was measured. It was observed that the release of MMP9 (bands at a molecular weight of 82-92 kDa) was increased after cobalt stimulation (Figure 4.15A). Additionally, a lower band of 82 kDa molecular weight was observed indicating an active form of MMP9 cleaved from pro-MMP9. Pro-MMP9 release was not dose-dependent, while both $Co^{2+}$ and CoNPs induced a dose-dependent increase in the formation of active MMP9 (Figure 4.15B, C). Cobalt exposure had no significant effect on MMP2 release (Figure 4.15B, C).

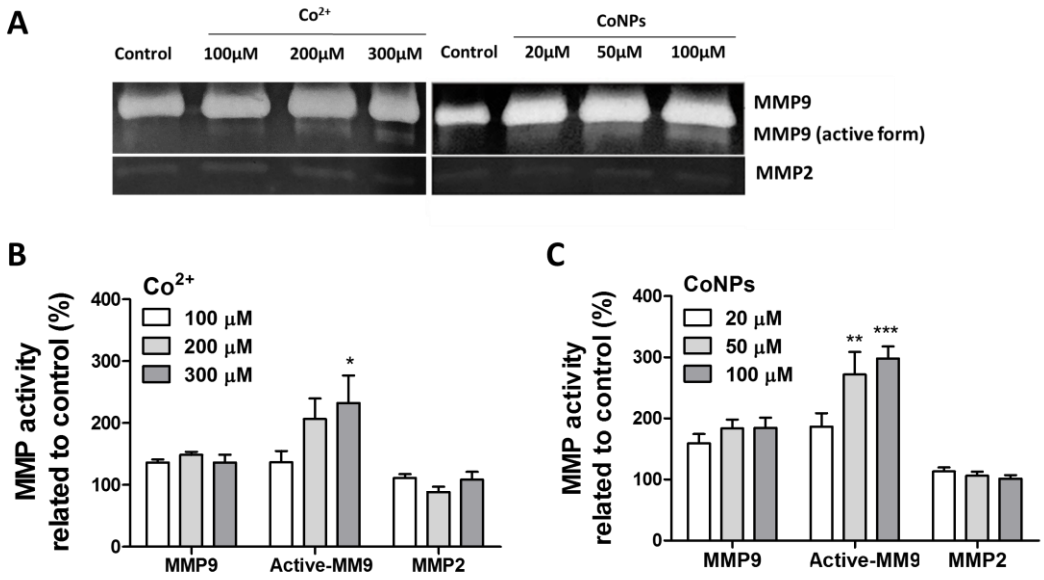


Figure 4.15 Enhanced ECM degradation induced by cobalt is associated with the release and activation of MMP9, which co-localizes with podosomes. (A) Zymography gels showing the release and activation of MMP9 by U937 cells due to cobalt treatment. (B & C) Quantification of the formation of pro-MMP9, active MMP9 and MMP2 based on gelatin zymography results, Values represent mean+SEM; n=6 replicates for each treatment from 3 independent experiments (2 replicates/experiment). $*p < 0.05$, $**p < 0.01$, $***p < 0.001$.

Immunofluorescent staining revealed that intracellular MMP9 frequently co-localised with cobalt-induced podosomes (Figure 4.16).

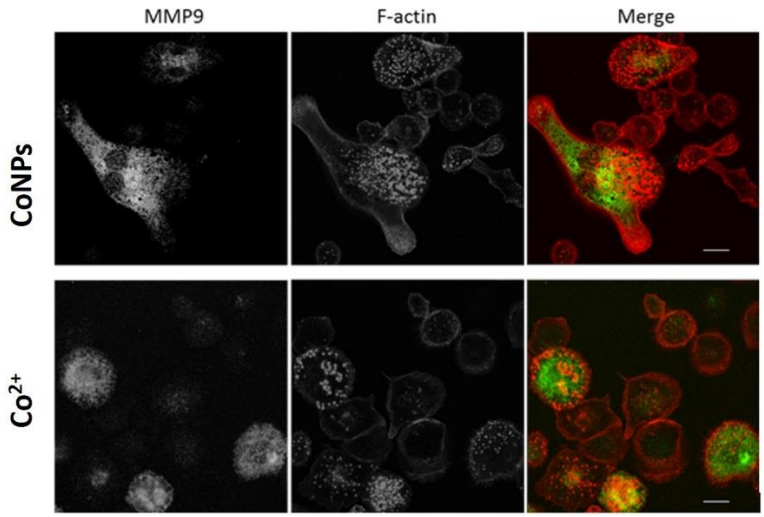


Figure 4.16 Confocal immunofluorescence localisation of MMP-9 (green) in U937 macrophages after cobalt treatment (200 µM $Co^{2+}$ and 100 µM CoNPs) reveal co-localisation with F-actin podosomes (red). Scale bar indicates 20 µm.

### 4.3.7 Cobalt promotes macrophage cytoskeleton remodelling and inhibits cell migration via down-regulating RhoA expression, which is mediated by reactive oxygen species (ROS) formation

#### 4.3.7.1 $Co^{2+}$ and CoNPs induce ROS production U937 macrophages

Heavy metal ions and nanoparticles can provoke cellular stress, which may lead to alterations in cellular structure and function, and potentially loss of cell viability. Both $Co^{2+}$ and CoNPs induce ROS in a concentration-depended manner in U937 macrophages, which occurs at non-cytotoxic concentrations (Figure 4.17A). The maximum increase in ROS production of approximately 90% compared to unstimulated cells, occurred within the first 30 minutes. This significant increase persisted for 4 hours of treatment but decreased after 6 hours. Exposure to CoNPs at 100-150 µM induced a transient upregulation in ROS measured at 2 hours, with an increase of approximately

75% at 150 µM (Figure 4.17B). Cobalt-treatment with ROS scavenger and antioxidant, NAC (N-acetyl-L-cysteine), abolished the cobalt-induced ROS production in cells (Figure 4.17A, B).

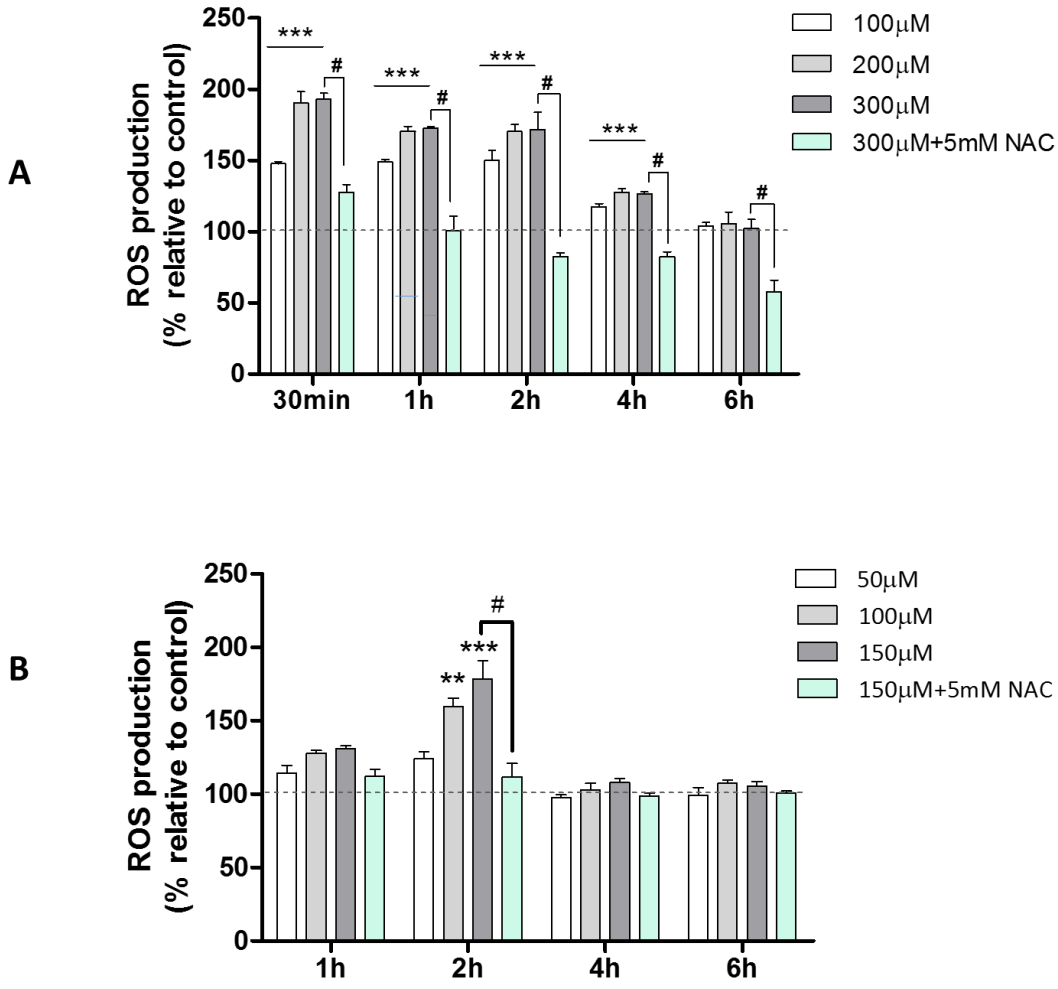


Figure 4.17 ROS production induced by $Co^{2+}$ and CoNPs. Values represent mean+SEM; n=12 replicates for control, 100µM, 200µM, 300µM $Co^{2+}$ and 100µM, 50µM, 100µM CoNPs treatment from 4 independent experiments (3 replicates/experiment) and n=9 for 300 µM $Co^{2+}$ + 5mM NAC treatment and 150 µM CoNPs + 5mM NAC treatment from 2 independent experiments (2 replicates/experiment). (A: *** indicates significant upregulation for all of the three concentrations; B: **$p < 0.01$; ***$p < 0.001$; # indicates significant difference between cells treated with cobalt only and cells treated with both cobalt and NAC.)

4.3.7.2 U937 macrophages cytoskeleton reorganization induced by cobalt was associated with ROS production.

Further experiments were performed to determine whether ROS generation was responsible for the cobalt-induced podosome formation and the consequent inhibition of U937 macrophage migration. 200 µM $Co^{2+}$-treated cells with NAC (5 mM) resulted in a significant reduction in the cobalt-induced podosome formation in individual cells as showed in Figure 4.18A and B.

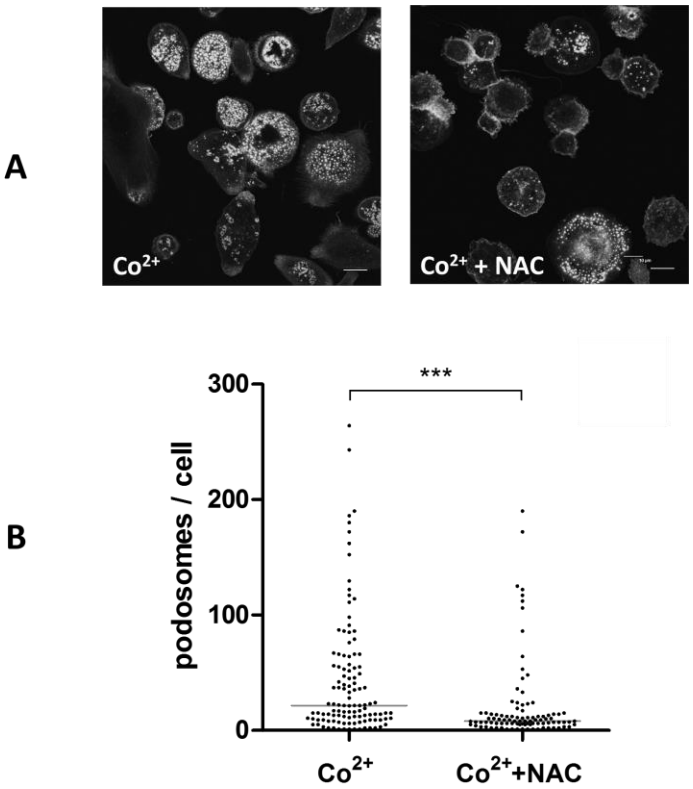


Figure 4.18 Cobalt-induced ROS production stimulates podosome formation and impedes macrophage migration. (A) Fluorescence images showing that the ROS inhibitor, NAC (5 mM, 12 h) prevents $Co^{2+}$ induced upregulation of podosome formation as shown by F-actin labelling with phalloidin and quantified in (B), n=150 cells from 3 independent experiments.***$p < 0.001$; Scale bars represents 10 µm.

4.3.7.3 Inhibited U937 macrophages migration by cobalt was associated with ROS production.

NAC treatment also induced a significant increase in macrophage transmigration exposed to cobalt (Figure 4.19). As mitochondria and NADPH oxidases are the main sources of cellular ROS, the effect of a NADPH oxidase inhibitor apocynin (5 μM, 10 μM and 50 μM) was also tested. However, apocynin was not able to inhibit cobalt-mediated ROS generation nor to restore macrophage migration (data not shown), which suggested that cobalt-mediated ROS increases are mainly mitochondria-derived.

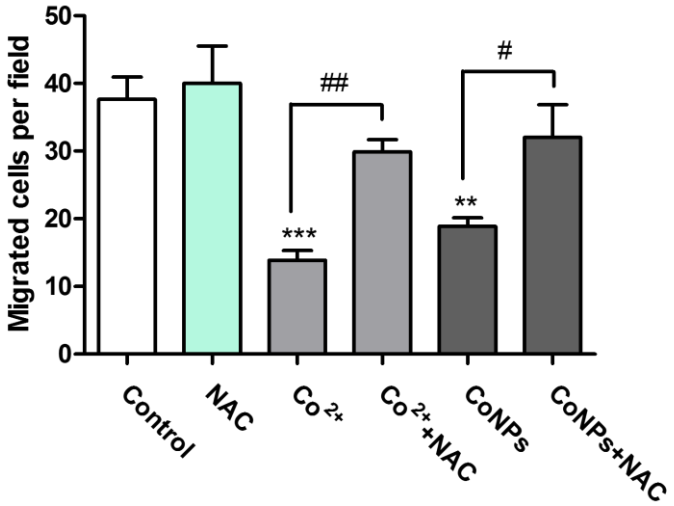


Figure 4.19 Macrophage migration inhibited by cobalt is rescued by treatment with NAC. Values represent mean + SEM. n=30 from 3 independent experiments; 10 random fields were imaged for each treatment in each experiment. #$p < 0.05$, ##/**$p < 0.01$; ###/***$p < 0.001$.

4.3.7.4 Cobalt downregulates RhoA GTPase expression in U937 macrophages

Actin organisation and podosome turnover are tightly regulated by the Rho GTPase, such as RhoA (Ras homolog gene family, member A), Rac1 (Ras-related C3 botulinum toxin substrate 1) and Cdc42 (Cell division control protein 42 homolog), whose activity is determined by their guanine nucleotide-bound state (Jomova and Valko, 2011). To determine if cobalt-induced ROS acts as an upstream regulator to activate Rho GTPases, the expression of RhoA, Cdc42 and Rac1 after U937 macrophages were treated by $Co^{2+}$ (200 µM) and CoNPs (100 µM) was investigated. As shown in Figure 4.20A and B, cobalt did not affect the Rac1 and Cdc42 levels, but caused decreased RhoA expression indicating that $Co^{2+}$ and CoNPs negatively regulate RhoA signalling. This was further confirmed by down-regulation of the downstream proteins of RhoA signalling, such as pMLC (phospho-myosin Light Chain) and pMYPT (phospho-myosin-binding subunit of myosin phosphatase).

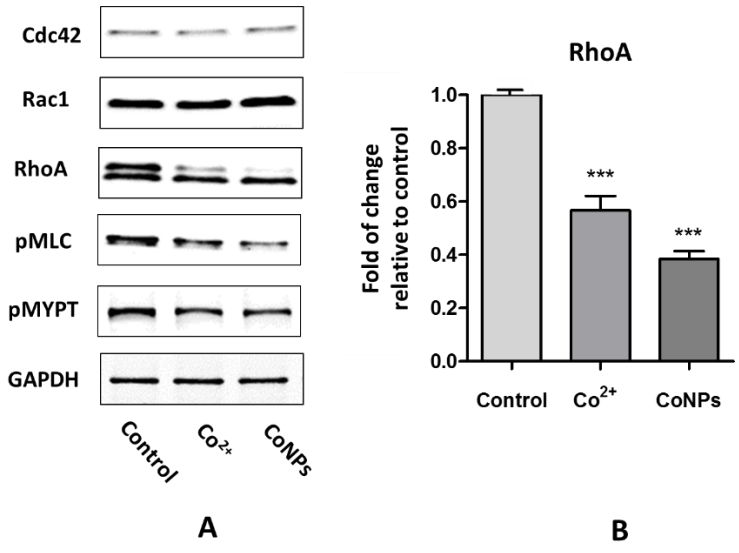


Figure 4.20 Cobalt do not affect the Rac1 and Cdc42 levels, but down-regulated RhoA expression. (A) Western blots results for untreated cell and cells treated with $Co^{2+}$ and CoNPs. (B) The corresponding quantification demonstrating decreased RhoA expression. Values represent mean+SEM; n=12 replicates (4 replicates/experiment) for control, n=6 rerplicates (2 replicates/experiment) for $Co^{2+}$ and CoNPs treatment from 3 independent experiments; *** indicate difference from control, $p < 0.001$.

4.3.7.5 Inhibition of RhoA signalling promotes U937 macrophage cytoskeleton change and reduces macrophage migration

In addition, the treatment of macrophages with the RhoA-specific inhibitor C3 Transferase (2 µg/ml) and RhoA/ROCK1 pathway inhibitor Y-27632 (20 µM) also led to intensive cell spreading and increased podosome formation (Fig. 4.21A) as observed in cobalt-treated cells. Accordingly, the migration of U937 macrophages were also significantly impaired when RhoA signalling was inhibited by inhibitor C3 Transferase and Y-27632 (Figure. 4.21A, B).

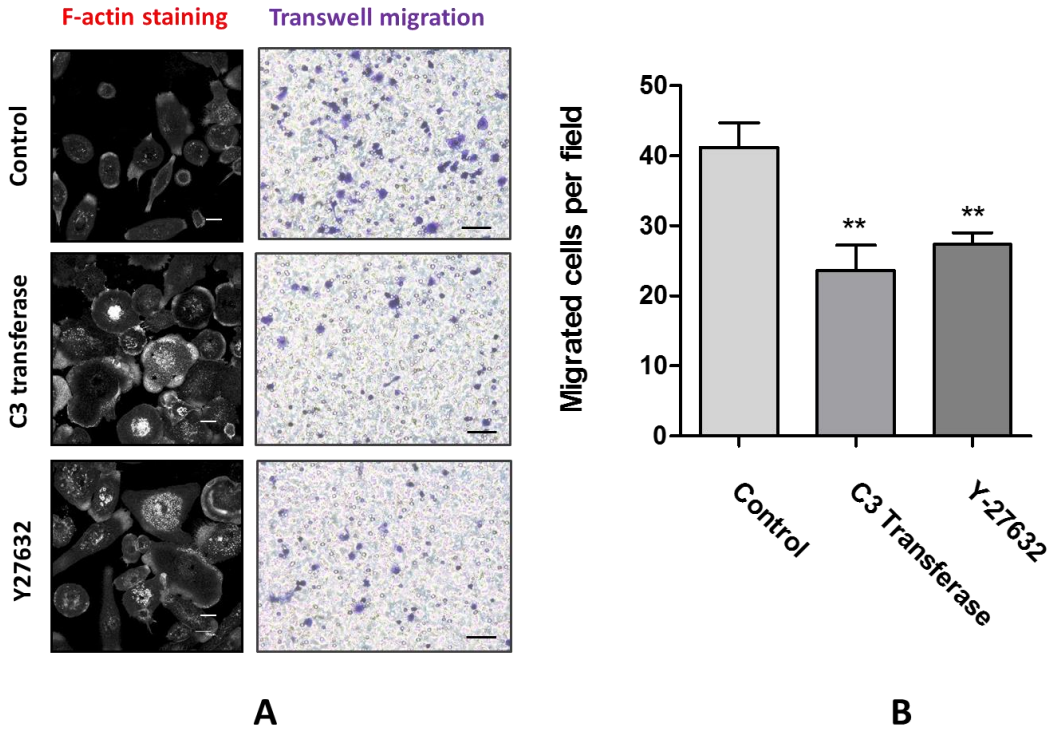


Figure 4.21 Inhibition of RhoA signalling promotes U937 macrophage cytoskeleton change and reduces macrophage migration. (A) Representative images showing the effects of inhibitor C3 Transferase and Y-27632 on U937 macrophage cytoskeleton organization and migration. (B) Quantification of the effects of C3 Transferase and Y-27632 on U937 macrophage organization. Values represent mean + SEM. n=30 from 3 independent experiments; 10 random fields were imaged for each treatment in each experiment. **P < 0.01.

4.3.7.6 Inhibition of ROS generation by NAC partially restores RhoA activity.

Furthermore, the reduced expression of RhoA level caused by $Co^{2+}$ and CoNPs was significantly reversed by using the NAC (Figure. 4.22 A, B), which has showed to suppress the cobalt-induced ROS generation and be capable of partially restore the migration ability of U937 macrophages. These data suggest that cobalt-induced ROS production lies upstream of the RhoA signalling and down-regulation of RhoA expression results in remodelling of macrophage cytoskeleton and impaired migration.

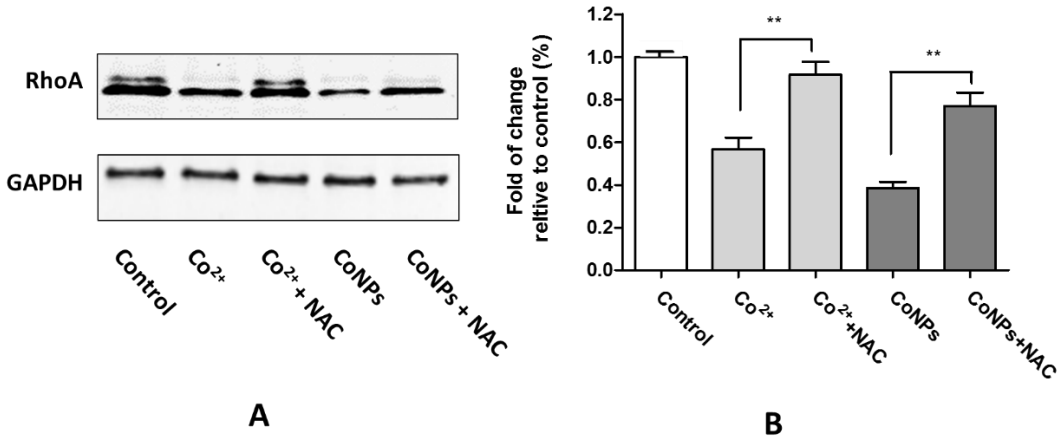


Figure 4.22 Inhibition of ROS generation via NAC restores RhoA activity. (A) Western blots results showing RhoA level reduced by $Co^{2+}$ and CoNPs could be partially restored by inhibition of ROS with NAC (5 mM). (B) The corresponding quantification of cellular RhoA level with treatment by $Co^{2+}$, CoNPs and NAC. Values represent mean+SEM; n=6 replicates (2 replicates/experiment) for each treatment from 3 independent experiments. ** $P < 0.01$;

# 4. Discussion

The mechanism of cell migration is controlled by a coordinated turnover of the actin and microtubule cytoskeletal network (Le Clainche and Carlier, 2008). Migration is regulated by actin polymerization with actin/myosin interactions forming contractile forces to retract the cell, while microtubules specify migration directionality (Ridley et al., 2003). When studying the effect of cobalt and chromium on these critical components of the cell migration machinery, it was observed a slightly decrease in the acetylation of α-tubulin in response to CrNPs occurred without affecting cell motility (Figure 4.5). In contrast, cobalt increased α-tubulin acetylation as well as inhibiting cell migration. To test whether increased acetylation initiates the inhibition of macrophage migration, cells were treated with Tubastatin A, a potent HDAC6 inhibitor. Tubastatin A treatment resulted in higher levels of α-tubulin acetylation than cobalt, and a reduction in macrophage migration, but to a smaller extend than cobalt (Figure. 4.6 and 4.7). These results indicated that cobalt-induced tubulin acetylation was not the main cause of inhibited cell migration.

Apart from tubulin modifications, it was found that cobalt induced alterations in macrophage morphology in the form of increased cell spreading as well as an increase in the number and density of podosomes (Figure. 4.8, 4.9 and 4.10). Both cell spreading and podosomes formation involve the deformation of a cell membrane and the strengthening of cell–substrate attachment (McGrath, 2007, Murphy and Courtneidge, 2011). Podosome-type adhesions are rich in vinculin and other types of adhesion proteins, and regulate cell adhesion to the ECM (Murphy and Courtneidge, 2011). Cell spreading and short-lived podosome formations with their adhesion structures are associated with enhanced macrophage migration and invasion (Linder and

Aepfelbacher, 2003). When either process is uncontrolled, cell migration can be hindered (Ilic et al., 1995). For example, the inflammatory mediator PGE2 has been shown to promote macrophage migration in response to chemotactic signals, but at high doses, it reduces macrophage chemotaxis by enhancing cell-substratum adhesion (Osma-Garcia et al., 2016). In the current study, it was confirmed that the non-toxic concentrations of $Co^{2+}$ led to a concentration-dependent increase in cell adhesion to the ECM substrate (Figure. 4.12). These results suggest that the reduction in macrophage migration induced by cobalt is due to both the increased cell spreading and the enhanced podosome formation.

The current study established that the molecular mechanisms through which cobalt regulates podosome adhesion and reduced migration, involves the formation of ROS (Figure. 4.17). Both $Co^{2+}$ and CoNPs have been shown to promote generation of the oxidative stress and increase ROS levels *in vitro* (Kamiya et al., 2008). ROS is generated as a by-product during cellular oxidative metabolism, although its overproduction enhances cellular oxidative stress, transforming cells so they are unable to maintain normal physiological functions (Sauer et al., 2001, Bigarella et al., 2014). ROS are also the key signalling molecules during the progression of inflammatory disorders (Mittal et al., 2014), by modulating the production of inflammatory chemokines and expression of leukocyte adhesion receptors to accumulate circulating monocytes at affected sites (Mittal et al., 2014). Oxygen radicals produced by local macrophages may further facilitate macrophage accumulation and their activation, resulting in prolonged inflammation. The current findings indicate that the mechanism behind ROS role in the retention of infiltrated macrophages at the inflamed sites is through regulating the cytoskeleton reorganization, a finding that has not been suggested previously.

The cytoskeleton reorganization in presence of ROS is driven by the ability of ROS to induce reversible oxidation of proteins, which involves direct modification of protein kinases and transcription factors (Meng et al., 2002). Major regulators of macrophage motility and cytoskeleton organization are influenced by Rho family GTPase (Jones et al., 1998, Konigs et al., 2014, Ridley, 2015), F-actin regulation pathways (Linder et al., 1999) and tyrosine phosphorylation (Dwyer et al., 2016, Jones, 2000). The Rho family of GTPases play critical roles in cell motility by affecting actin organization and microtubule dynamics, myosin activity, and cell–ECM and cell–cell interactions (Hanna and El-Sibai, 2013). In this study, it was showed for the first time that cobalt-induced ROS formation acts as an upstream regulator to directly inactivate the RhoA, leading to a reorganization of the macrophage cytoskeleton and impaired cell migration (Fig. 4.19, 4.20, 4.21 and 4.22). Small GTPase Rho is known to stimulate stress fiber formation and hamper the cell migration in many types of cells (Tojkander et al., 2012). It is even reported that inactivation of Rho in transformed fibroblasts by dominant negative RhoA or the C3 exoenzyme would disrupt podosome structure (Berdeaux et al., 2004), but also that podosome formation in Src-transformed fibroblasts could be promoted by limiting Rho activation (Schramp et al., 2008). In addition, it was recently revealed that podosome disassembly is associated with the activation of Rho and blockade of RhoA signalling, and could promote actin core assembly and podosome formation in macrophages (Rafiq et al., 2017).

Underlying mechanisms through which biomaterials-induced ROS formation modulates macrophage behaviour are of considerable importance. Despite emerging advances in materials science, biomaterials do not behave like native biological components and frequently incite adverse tissue reactions, which may lead to ultimate failure of the implants. Therefore accurate and facile approaches for screening and

evaluating the biocompatibility of biomaterials are of critical interest, especially understanding the cellular behaviour of macrophages because of their decisive role in the long term survival of implanted biomaterials in addition to orchestrating inflammatory processes.

# Chapter 5. The effects of $Co^{2+}$ and $Cr^{3+}$ on ECM remodelling, fibroblast mechanical properties and fibroblast-macrophage interplay

## 5.1 Introduction

Local effects of CoCr metal ions in the periprosthetic tissue have been demonstrated to induce cytotoxicity, apoptosis, and necrosis with secretion of various cytokines and chemokines (Petit et al., 2004, Catelas et al., 2001, Fleury et al., 2006, Queally et al., 2009). The released ions ($Co^{2+}$ and $Cr^{3+}$) that were reported to cause an issue in MoM implants, are now also frequently reported in patients with MoP bearings; the effects that have been increasingly reported include adverse local tissue reactions and pseudotumours (Plummer et al., 2016, Dimitriou et al., 2016, Kwon et al., 2016, Jennings et al., 2016). Histological evaluation of the synovial tissues from revision hips utilizing CoCr alloys frequently reveal features with extensive tissue reaction, which is characterised by abundant tissue necrosis and fibrosis with infiltration of immune cells (Campbell et al., 2010). Although it is evident that the by-products generated in total joint replacements are associated with the aberrant tissue remodelling (Campbell et al., 2010, Willert et al., 2005), few studies have investigated how the cell processes are driven by cobalt and chromium.

The extra cellular matrix (ECM) contains a diverse range of dynamic structures built from a complex web of secreted molecules. The ECM not only provides cells with structural support, but also regulates cellular function, cell fate and disease progression via chemical/mechanical cues and cell-matrix interactions (Iskratsch et al., 2014). For example, during chronic inflammation, aberrant ECM production and ECM protein fragments generated from tissue-remodelling processes, can impact immune cell

activation and survival, thereby interfering with the resolution of inflammatory responses at these sites (Sorokin, 2010).

Fibroblasts are the primary cell type responsible for collagen synthesis and the maintenance of collagen network tension (Eckes et al., 1999). Investigations into the biological response to metal debris and released ions have largely focused on whether certain types of cells would be able to survive when exposed to the material or how the profile of secreted cytokines are altered when immune cells are treated by cobalt and chromium (Madl et al., 2015b). However, how cobalt and chromium affect the functional properties of fibroblasts in terms of their cell-matrix interaction and ECM synthesis has not been fully elucidated. Tissues surrounding metal total hip implants obtained at revision operations are frequently characterised with massive infiltration of macrophages (Natu et al., 2012b); thus macrophages may also play an important role in mediating the fibrotic response of fibroblasts in the presence of cobalt and chromium.

Therefore, the aim of this study was to investigate the effects of $Co^{2+}$ and $Cr^{3+}$ on human fibroblast-matrix interaction by utilising a 3D collagen culture systems to mimic the physiological ECM features. The effect of these ions on the fibrotic response of fibroblasts were also studied with a macrophage and fibroblast co-culture model.

## 5.2. Method

### 5.2.1 Preparation of $Co^{2+}$ and $Cr^{3+}$ ions solution

Stock solutions (0.1 M) of $Co^{2+}$ and $Cr^{3+}$ ions were freshly prepared as described in section 3.2.1.

### 5.2.2 Primary culture of human fibroblasts and U937 cells

*Human dermal fibroblasts (HDFs)*

Normal adult HDFs (PromoCell, UK) were grown in DMEM (4.5g/L glucose, Gibco, ThermoFisher Scientific) supplemented with 10% foetal calf serum (FCS, Sigma), 0.625 μg/mL amphotericin B (Sigma), 100 IU/mL penicillin and 100 μg/mL streptomycin (Sigma). The medium was changed every 3 days until the cells reached 80% confluency. HDFs between passages 3 and 8 were used for all experiments.

*U937 cell line*

U937 cell line (passage 6-25, donation from Dr. Akihisa Mitani, Imperial College London, UK) were cultured in RPMI 1640 medium as previously described in section 3.2.3.

*Co-culture*

Porous plasma-treated polycarbonate inserts (pore size: 3 μm, Transwell, Corning, USA) were used for non-contact co-culture of fibroblasts. HDFs ($0.4\times10^5$/well) were cultured at the bottom of the well (24-well tissue culture plate) and U937 macrophages ($2\times10^5$) were added to the top of the Transwell® insert.

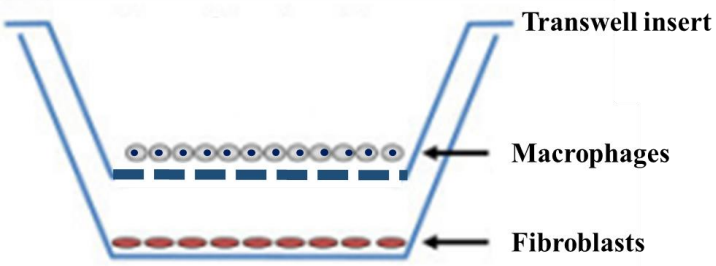


Figure 5.1 Illustration showing the macrophages-fibroblasts co-culture system.

*3D culture*

Rat tail collagen type I (2mg/ml, Firstlink) was used to fabricate three-dimensional matrix by collagen fibril self-assembly. Solution (8:2) containing collagen (final collagen concentration: 1mg/ml) and 10X MEM (ThermoFisher Scientific) was adjusted to pH 7.4 using 1M NaOH, and by observing colour change from yellow to salmon pink. The required cell suspension was then added and the cell-containing collagen mixture was polymerised at 37 °C for 30 min in cell culture plates. Following this step, serum-free DMEM medium was added to the wells. For fibroblasts-containing gels, $2\times10^5$ cells/ml were used.

### 5.2.3 Cell viability and proliferation test

*Cytotoxicity Assay*

A LIVE-DEAD® Cytotoxicity Assay Kit (ThermoFisher Scientific) was used to measure cell viability in the presence of $Co^{2+}$ and $Cr^{3+}$. HDFs in 96-well tissue culture plates at $5\times10^3$ cells/well for 2D and $2\times10^4$ cells/well for 3D, were exposed for 6h to 200, 300 or 500 µM $Co^{2+}$ or 200, 400, or 800 µM $Cr^{3+}$. Following exposure, supernatants were removed and a 200 µL solution of 1 µM calcein AM and 2 µM ethidium homodimer in PBS was added to each well for 20 min. Fluorescence images were then captured using 10× magnification on a SP2 confocal microscope. Viable cells

were stained green with calcein AM (ex 495nm, em 530 ± 12.5 nm), while dead cells red with ethidium homodimer (ex 528nm, em 645 ± 20 nm). Three replicates of each condition were tested with the entire assay repeated in three separate experiments.

*Proliferation test*

HDF proliferation was measured using CellTiter 96® Aqueous One Solution Cell Proliferation Assay (MTS assay, Promega) according to the manufacturer's instructions. HDFs in 96-well tissue culture plates at $5\times10^3$ cells/well for 2D and $2\times10^4$ cells/well for 3D studies. The cells were exposed for up to 96h to $Co^{2+}$ or $Cr^{3+}$ at concentrations of 100 - 500 µM or 100 - 800 µM respectively. Following exposures, supernatants were aspirated and 100 µL of serum-free DMEM medium containing 10% CellTiter reagent was added to each well. Plates were incubated for 2h at 37°C and the absorbance was read at 490 nm using an Infinite F50 plate reader (Tecan). Five replicates of each exposure were tested and the entire assay was repeated in three separate experiments. The cell viability was determined as a percentage of control cell viability.

### 5.2.4 3D Collagen Gel Assays

*Collagen gel contraction*

To measure collagen contraction by fibroblasts, 0.5 mL fibroblast-containing solution was added to 24-well cell culture plates and polymerized for 30 min at 37°C. Then 0.5 mL of serum-free cell culture medium was added and the gels were incubated for 12h. Following the incubation, gels containing fibroblasts were gently detached from the wells using fine straight and curved forceps. The medium was aspirated and replaced with culture media containing $Co^{2+}$ (100, 200 or 300 µM) or $Cr^{3+}$ (100, 200 or 400 µM). The gel contraction was recorded by time-lapse imaging over 6h.

*Collagen gel stiffness*

Gel stiffness was evaluated for untreated samples or samples exposed to 200 μM $Co^{2+}$ as described in the previous section. Shear rheology of fibroblast-containing gels was measured with a strain rotational rheometer (T.A. Instruments, UK). Storage modulus was measured over a strain range of 0.2 - 2% at a fixed angular frequency of 0.5 rad/s and a temperature of 21°C.

### 5.2.5 Immunofluorescence

$Co^{2+}$ and $Cr^{3+}$ -treated fibroblasts were fixed with 4% paraformaldehyde (Sigma, UK), washed and permeabilized with 0.5% Triton X-100 (Sigma, UK) then rinsed 3 times with PBS. Nonspecific binding sites were blocked with 1% BSA in PBS. Cells were labelled for α-Smooth Muscle Actin (α-SMA) by incubating the cells at 4°C overnight with a mouse monoclonal anti-α SMA primary antibody (1:400, Abcam, UK). Cells were then washed and incubated for 1h at room temperature in Alexa 488 conjugated anti-Mouse IgG as Secondary Antibody (1:1000, ThermoFisher, UK). To label the cellular F-actin, fixed fibroblasts in collagen gel were incubated for 30 min with 200 μL of rhodamine-conjugated phalloidin (Molecular Probes, UK) in a humidified chamber at room temperature in the dark. Before imaging, cell nuclei were stained by incubation with 5 μg/mL DAPI (Dojindo, UK) followed by three PBS rinses. Slides were visualized with a fluorescence microscope (Leica SP2, Germany) utilising a x10 and x63 objective.

### 5.2.6 Fibroblast mechanical properties measurement

Many studies have linked the changes in fibroblast mechanical properties, such as cell stiffness and cellular contractile force to its activation. Cell mechanical properties are closely associated with cell behaviour. A variety of approaches have been applied to study to study cell mechanics including micropipette aspiration, magnetic tweezers,

cytoindentation and atomic force measurements (AFM) and traction force measurements (TFM). Here AFM and TFM were used to monitor changes in fibroblast mechanical properties.

### 5.2.6.1 *Atomic force microscopy*

Atomic force microscopy (AFM) is an invaluable tool to determine certain physical properties of specimens, especially their mechanical properties. Investigations of an sample is performed by using a fine tip attached to a cantilever to scan over the sample surface, The interplay between tip and sample causes the cantilever to bend while the bending of the cantilever can be detected by the deflection of a laser beam focused on the end of the cantilever. Then the force applied to the sample can be calculated via the cantilever bending, In addition, the bending of the cantilever is recorded as a function of its distance from the surface in the form of force-distance curves. As the tip approaches and retracts from the sample, the long-range attractive or repulsive forces between the tip and sample surfaces can be detected, which allows measurements of mechanical properties such as adhesion or elasticity on a nanometre scale.

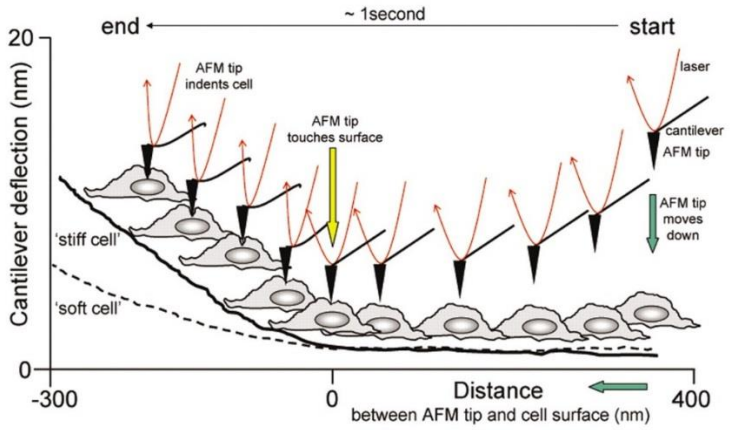


Figure 5.2 Principle of cell stiffness measurements (force-distance curves) performed on living human endothelial cells with an atomic force microscope (AFM).

The stiffness of human dermal fibroblasts was measured using Advanced Quantitative Imaging mode on a JPK NanoWizard 4 system in combination with an inverted microscope (Axio Observer Z1, Zeiss). Cantilevers (HYDRA6R, AppNano) were calibratedby first measuring the sensitivity against a stiff polystyrene substrate, and then fitting the resonance peak in the thermal noise spectrum to determine the spring constant (i.e. 0.07 ~ 0.08 N/m). A ROI of 100 µm × 100 µm was selected to cover an entire cell. Indentations were performed in a format of 32 × 32 at a loading/unloading speed of 50 µm/s, to minimize cell movement during scanning without compromising the resolution. All the AFM experiments were carried out at 37°C in FBS-free medium with or without $Co^{2+}$. Force-indentation curves were further processed in JPK data processing software, which was through background subtraction, height correction and fitting with a modified hertz model. The poisson's ratio is assumed to be 0.5. Young's modulus values ranging from 1kPa to 200 kPa were extracted and averaged to determine the overall stiffness of a cell.

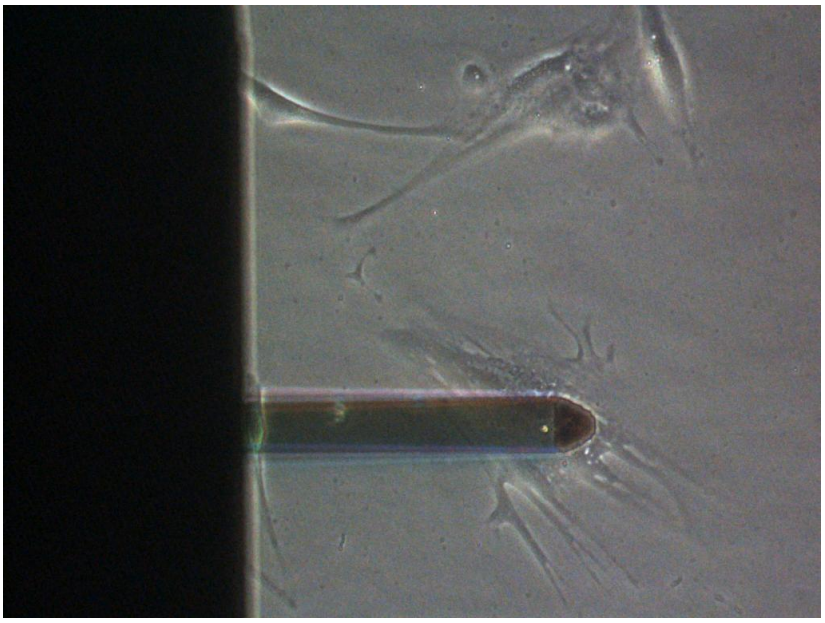

Figure 5.3 An optical image from the top-view camera integrated with the AFM system used showing the indentation of the cantilever over a fibroblast.

*5.2.6.2 Traction force measurement*

Forces generated by cells are key regulators of cellular signalling and function. Contractile forces are generated by a cell via actomyosin contraction, which transmits to the ECM or neighbouring cells. It is very demanding to directly measure the cellular tractions as they are very small (piconewtons to nanonewtons) and occur across limited length scales (nanometers to micrometers). However, cell tractions can be determined through quantifying shape change or deformation of soft materials caused by the forces applied to it. Over the past two decades, many techniques have been developed to measure and map the forces generated by cells.

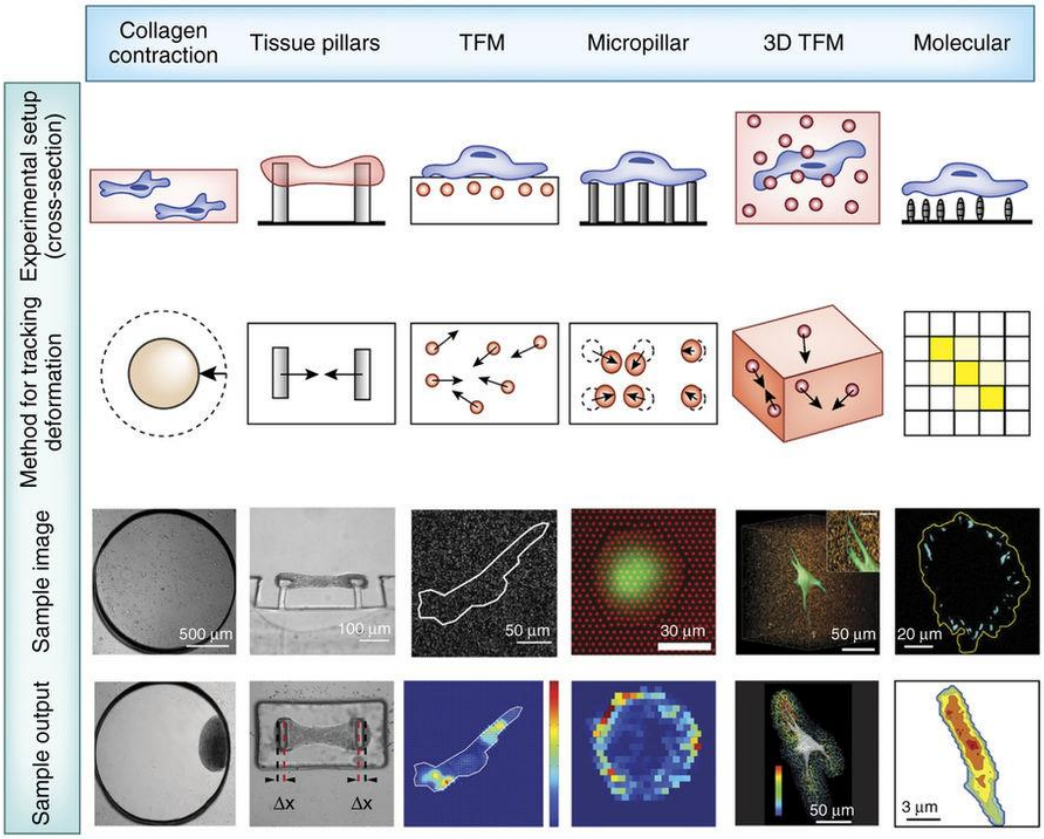


Figure 5.4 Methods for measuring cellular forces (Posada et al., 2015).

As the most widely used technique for measuring cell force, cellular traction force microscopy (TFM) involves tracking the deformations of synthetic elastic polymer substrates induced by the exertion of cellular traction. Briefly, small fluorescent beads are integrated into deformable synthetic substrates, which can be tracked in time and space using optical microscopy. In general, it involves the following steps: 1) Imaging of the distribution of fluorescent beads in a stressed state; 2) Releasing cell tractions via cell lysis; 3) Imaging of the beads to record their positions in the unstressed state; 4) Computational algorithms are applied to analyse the two sequence images (before and after lysis) to determine the displacement of the beads, that the forces needed to induce such displacement exerted by the cells can be acquired.

Detailed steps performed in the TFM experiment were as followed. Firstly, 22 mm coverslips (Corning) were first treated with Hexamethyldisilazane (HMDS, VWR) overnight, rinsed in distilled water, and air dried. A gel solution containing 5% acrylamide (Biorad), 0.25% bis-acrylamide (Biorad), ammonium persulfate (10% APS, Sigma), 1, 2-Bis (dimethylamino) ethane (TEMED, Sigma, USA) and carboxylate-modified beads (fluorescent red, diameter 0.2 μm, 1% v/V, ThermoFisher) was added to the hydrophobic coverslips. After polymerization for 15 min at room temperature, the gel was activated with heterobifunctional cross-linker 1mg/ml Sulfo-SANPAH (Sigma) under UV light for 30 min and rinsed 5 times with distilled water. The coated coverslips were then conjugated with type I collagen (0.2 mg/ml). Fibroblasts, at a density of $3 \times 10^4$ cells/well, were plated on the coverslips in serum-free DMEM and subjected to $Co^{2+}$ treatment (200 μM) for 6 hours prior to imaging (LS720 Microscope, Lumascope) in a humid incubator. Bright-field and 525 nm image stacks were acquired for each position. After imaging, fibroblasts were lysed with 1% SDS and the positions were re-imaged. Images were analysed using Fiji software. Pre- and post-lysis stack

images were first aligned to correct the experimental shift in the z-position. Traction-induced bead displacement and gel deformation were determined utilsing particle image velocitometry (PIV) using the iterative PIV plugin as described (Martiel et al., 2015). A FTTC (Fourier transform traction cytometry) plugin was used to determine the traction forces and vectors.

### 5.2.7 Transwell cell migration assay

Cell migration was investigated using 6.5 mm Transwell chambers with 8 μm pores (Costar, Corning, NY, USA). Briefly, $5\times10^4$ harvested fibroblasts in serum free DMEM medium were added to the upper chamber of the insert. The lower chamber was filled with 600 μl DMEM medium with 10% FBS to encourage cell migration down the FBS chemotactic gradient. Cell migration was analysed over a 6-hour period in the presence of 200 μM $Co^{2+}$. After 6 hours treatment, cells remaining on the membrane were fixed, stained with crystal violet and counted.

### 5.2.8 Reactive oxygen species measurement

ROS formation was measured using CM-$H_2$DCFDA (ThermoFisher). HDFs in collagen gels ($2\times10^4$ cells/gel) were cultured in black 96-well cell culture plates with a clear bottom. Following up to 6h exposure to 100-300 μM $Co^{2+}$, the supernatant was aspirated and cells were washed with warmed PBS. 1μM (100 μl) CM-$H_2$DCFDA in HBBS was added to the gels and they were incubated for 30 min at 37°C in the dark. Fluorescence was read at excitation 485/20 nm with emission 528/20 nm using a Synergy HT Multi-Mode microplate reader.

### 5.2.9 Hydroxyproline content measurement

To measure the amount of hydroxyproline released in the cell culture medium, HDFs were exposed to 200 μM $Co^{2+}$ or 400 μM $Cr^{3+}$ with or without U937 macrophages presence for 24h. The culture medium was collected and hydrolyzed in 6N HCl for 24h at 105 °C. The amount of 4-hydroxy proline in the hydrolyzate was determined at the wavelength of 570 nm using a microplate reader (BMG Nova Star, BMG LABTECH) using the conventional colorimetric method (Reddy and Enwemeka, 1996).

### 5.2.10 Protein extraction and Immunoblotting

Protein extraction and immunoblotting were performed as described in section 4.2.2. Anti-myosin light chain (phospho S20) antibody (1:1000, Abcam) and anti-GAPDH antibody (1:2000, Abcam) were used.

### 5.2.11 Data analysis and statistics

Normality testing (Kolmogorov-Smirnov test) was performed for all experimental data. All data are expressed as the median or mean ± SEM from independent repeat experiments (N=3). The number of repeat measurement per experiment (n) is indicated for each figure. Statistics analysis conducted with SPSS (Inc., Chicago, IL, USA) for each assays are listed in Table 5.1.

| **Experiments** | **Statistics methods** |
|---|---|
| Cell viability assay | one-way ANOVA with Bonferroni post-hoc t-test |
| Cell proliferation assay | one-way ANOVA with Bonferroni post-hoc t-test |
| Cell length measurement | one-way ANOVA with Bonferroni post-hoc t-test |
| Collagen gel contraction measurement | one-way ANOVA with Bonferroni post-hoc t-test |
| Collagen gel stiffness comparison | paired Student's t-test (two- tailed). |
| Transmigration assays | unpaired Student's t test |
| Cell elastic modulus comparison | unpaired Student's t test |
| Cell fibroblast contractile force | unpaired Student's t test |
| Protein expression analysis via western blot | one-way ANOVA with Bonferroni post-hoc t-test |
| ROS production analysis | one-way ANOVA with Bonferroni post-hoc t-test |
| Hydroxyproline measurement | one-way ANOVA with Bonferroni post-hoc t-test |
| α-SMA positive fibroblasts analysis | one-way ANOVA with Bonferroni post-hoc t-test |

## 5.3 Results

### 5.3.1 Human Dermal Fibroblast viability following exposure to $Co^{2+}$ and $Cr^{3+}$

A live/dead assay was first applied to assess the acute effects of $Co^{2+}$ and $Cr^{3+}$ on the viability of fibroblasts. Figure 5.5A shows images of fibroblasts in 2D tissue culture plates and 3D type I collagen matrix from the live/dead fluorescence assay taken at 20× magnification. Quantitatively, $Co^{2+}$ (200, 300 and 500 µM, Figure 5.5B) and $Cr^{3+}$ (200, 400, 800 µM, Figure 5.5C) showed little or no evidence of toxicity on fibroblasts in 2D and 3D matrices following 6 hours of exposure.

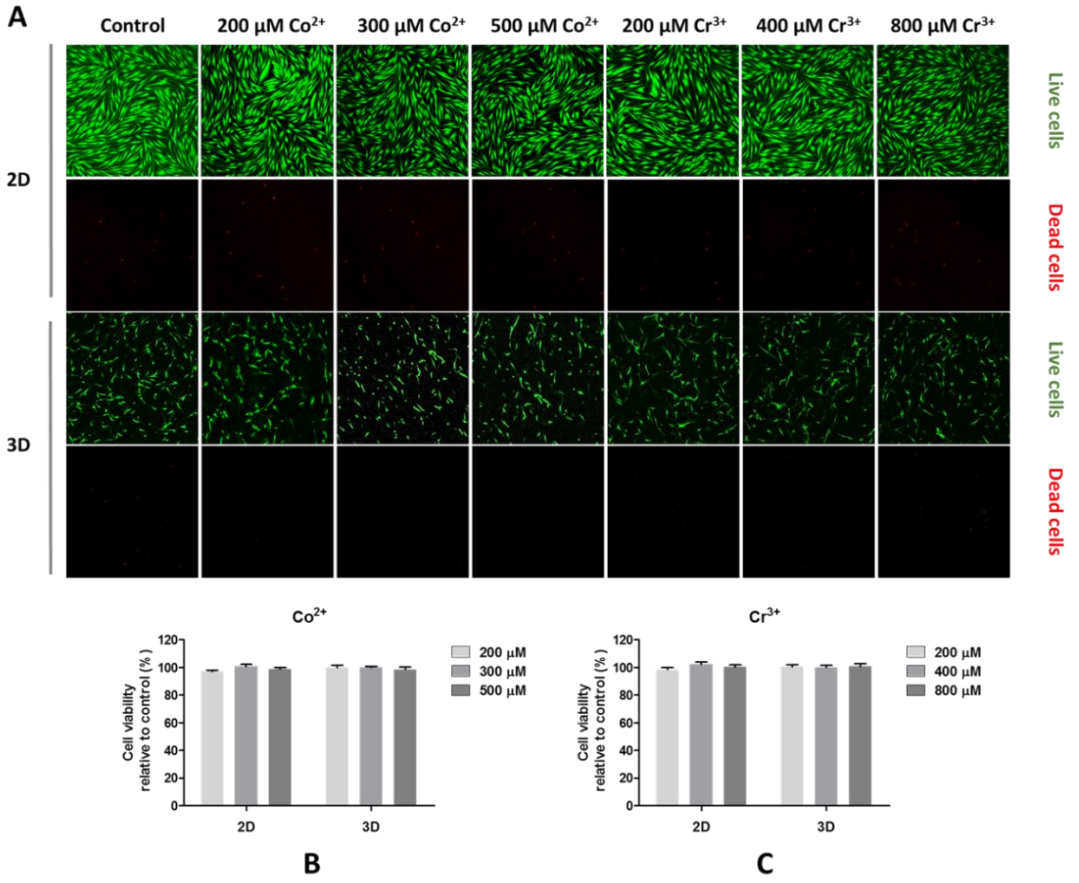


Figure 5.5 Images of human fibroblasts in the Live/Dead cell assay taken under 20× magnification. A. fluorescent staining of live and dead cells exposed to $Co^{2+}$ and $Cr^{3+}$, B. Quantification of cell viability when treated by $Co^{2+}$ (200, 300 and 500 µM); C. Quantification of cell viability when treated by $Cr^{3+}$ (200, 400, 800 µM). Data represents mean +SEM, n=9 from 3 independent experiments.

### 5.3.2 Fibroblast proliferation during exposure to $Co^{2+}$ and $Cr^{3+}$

The effect of $Co^{2+}$ and $Cr^{3+}$ on the proliferative capacity of fibroblasts was also investigated by using an MTS assay. When cultured on TCP, $Co^{2+}$ had no obvious effects on fibroblast proliferation over the first 24 hrs of treatment (Figure 5.6A). After 48 hrs of exposure, $Co^{2+}$ from 100, 200 and 300 µM transiently increased the number of fibroblasts by around 5, 5 and 8% respectively before returning to control levels, while the increase was not statistically different. In addition, $Co^{2+}$ at 500 µM significantly decreased the fibroblast proliferation by around 20% compared with untreated cells at day 2 and 3. Similarly, $Co^{2+}$ also supressed cell proliferation in 3D collagen matrices after 72 hours. On the other hand, $Cr^{3+}$ ranging from 200-800 µM had no statistically significant effect on fibroblast proliferation ability over 3 days of treatment (Figure 5.6B).

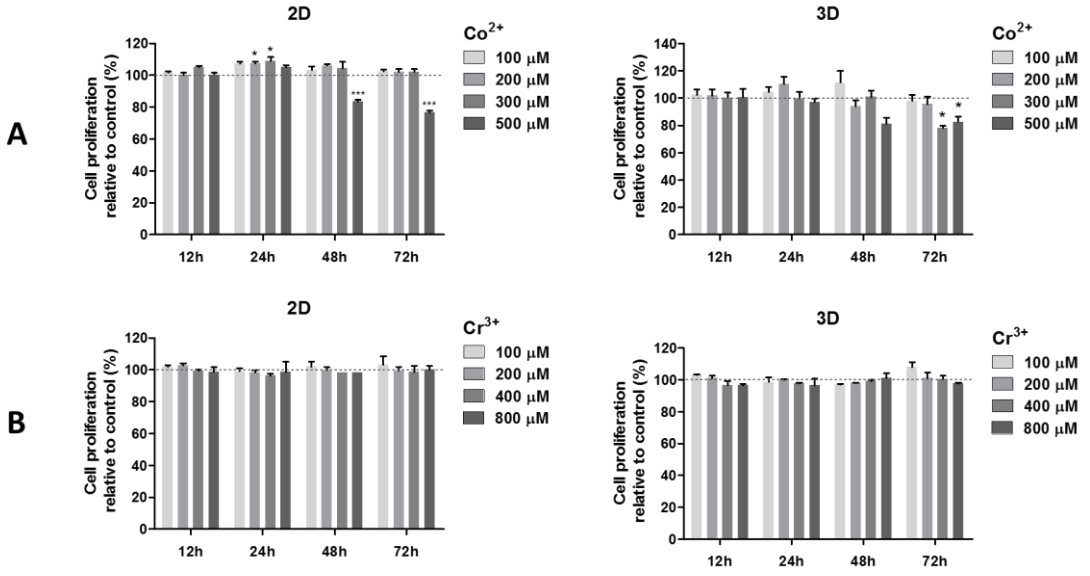


Figure 5.6 Effects of $Co^{2+}$ (A) and $Cr^{3+}$ (B) on HDFs proliferation capacity when grown in 2D tissue culture plates and 3D type I collagen matrix. Data represents mean +SEM, n=9 from 3 independent experiments.

### 5.3.3 Morphology of fibroblasts when cultured in type I collagen matrices when exposed to $Co^{2+}$ and $Cr^{3+}$

The direct impact of $Co^{2+}$ on fibroblast activation and function still remains poorly understood. To investigate this, fibroblasts in type I collagen matrices were incubated and their cell morphology was evaluated. As shown in Fig 5.7A, $Co^{2+}$ treatment induced a contracted morphology and the reduced fibroblast's length, while untreated cells and $Cr^{3+}$-treated cells remained with an elongated spindle-like appearance in the collagen matrices. An increased formation of actin stress fibres was also observed in $Co^{2+}$-treated cells.

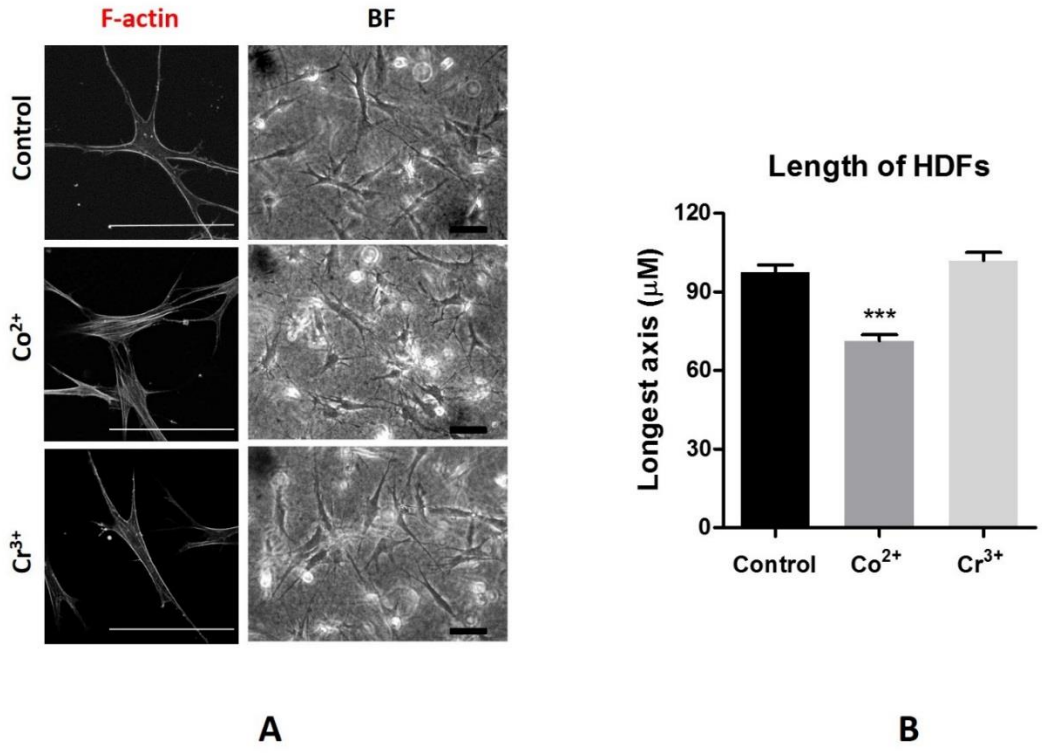


Figure 5.7 $Co^{2+}$ induces fibroblasts morphology change in collagen gel. (A) F-actin staining of human fibroblasts grown in 3D collagen I. Right: Bars show quantification of the longest distance of fibroblast grown in 3D collagen I. Bars represent mean + SEM; n = 50 individual cells from three experimental repeats. Statistically significant difference is indicated relative to untreated control. ***$p < 0.001$. Scale bar: 100 μm.

### 5.3.4 Remodelling of HDF-seeded collagen gels following exposure to $Co^{2+}$

5.3.4.1 Contraction of HDF-seeded collagen gels following exposure to $Co^{2+}$

The effect of cobalt on the fibroblasts ability to contract and remodel their surrounding matrix was subsequently investigated. Over 6h exposure, $Co^{2+}$ enhanced collagen gel contraction by fibroblasts in a time-dependent manner whilst untreated cells showed negligible contraction (Figure 5.8A, B). The collagen gels were contracted by nearly 50% within the first hour following exposure to $Co^{2+}$ (100-300 µM). The higher dose of $Co^{2+}$ (300 µM) triggered a faster contraction of the collagen matrices with significant differences at 30 min compared to 100 µM $Co^{2+}$. By contrast, $Cr^{3+}$ treatment from 100-400 µM showed no statistically significant effect on collagen gel contraction (Figure 5.8 – data only shown for 400 µM $Cr^{3+}$).

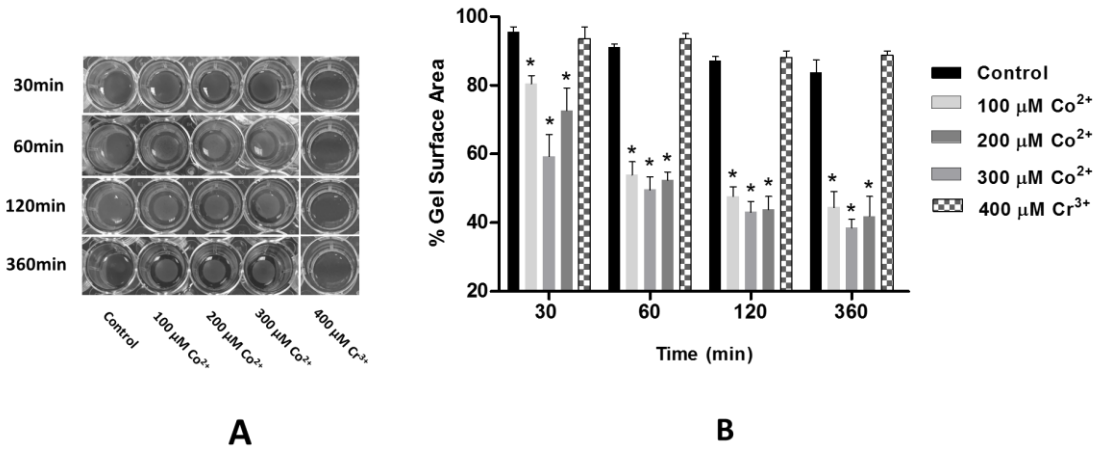


Figure 5.8 $Co^{2+}$ triggers fibroblasts-populated collagen gel contraction. (A) HDFs-induced gel contraction assay. Images show HDFs-induced contraction of collagen I matrices remodelling over 6 h of treatment; (B) quantification of $Co^{2+}$/$Cr^{3+}$-induced collagen gel contraction relative to control; bars indicate mean ± SEM; n=6 from three experimental repeats. Statistically significant difference is indicated relative to untreated control. *$p < 0.001$.

5.3.4.2 Stiffening of HDF-seeded collagen gels following exposure to $Co^{2+}$

Shear rheology indicated that storage modulus of the cell seeded collagen gels was independent of strain (Figure 5.9A). Cells treated with $Co^{2+}$ remodelled their collagen matrix resulting in a statistically significant increase in storage modulus from a mean value of 6.9 ± 0.74 Pa in untreated constructs to 12.5 ± 1.3 Pa following 6h treatment with 200 µM $Co^{2+}$ (Figure 5.9B). In addition, $Cr^{3+}$ had no significant effect on fibroblasts-populated collagen gel (data not showed).

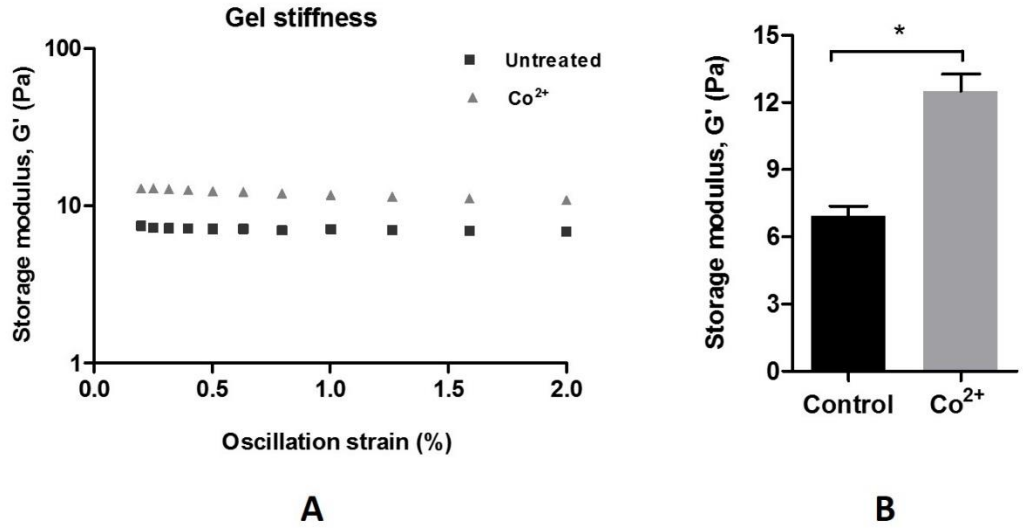


Figure 5.9 Stiffening of collagen gels following treatment of $Co^{2+}$. (A) Left: Matrix stiffness of collagen gel with or without 200 µM $Co^{2+}$ treatment. The storage modulus (G') of collagen I was measured by shear rheology after 6h of fibroblasts remodelling; Scatter plot indicates storage modules from 3 matched testing. (B) Comparison of collagen gel stiffness before and after treating by $Co^{2+}$. Bars indicate mean ± SEM; n=6 from three experimental repeats. Statistically significant difference is indicated relative to untreated control. *$p < 0.05$.

### 5.3.6 HDF-seeded collagen gels remodelling treated by $Co^{2+}$ is not caused by enhanced cell migration

The effect of $Co^{2+}$ on cell migration was examined as previous studies suggested that collagen gel contraction may be due to an enhanced cell motility (Andujar et al., 1992). However, no significant effect of $Co^{2+}$ (200 µM) on fibroblast 3D migration when using a transwell migration assay (Fig. 5.10A and B) was observed.

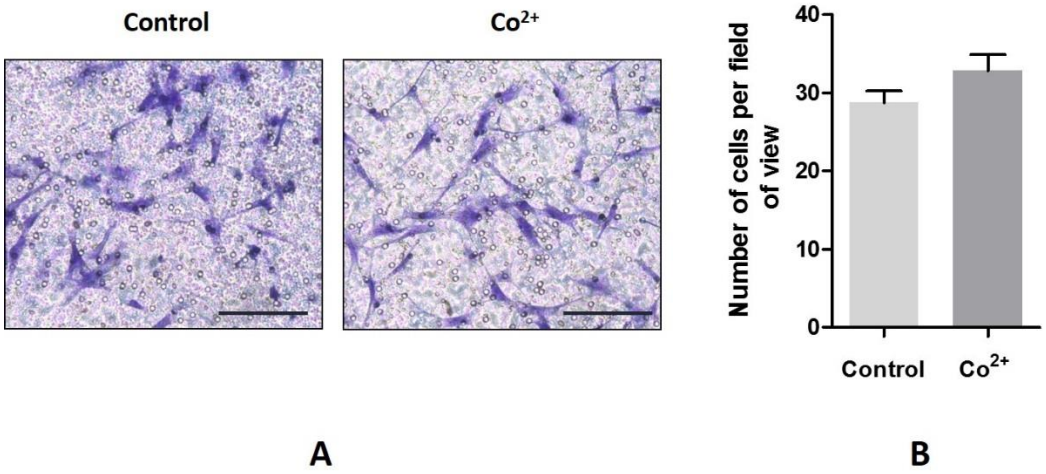


Figure 5.10 The effect of $Co^{2+}$ on fibroblast migratory ability. (A) Representative images of migrated cells stained after migration assays for untreated cells and $Co^{2+}$-treated cells. (B) Results of the migration assays for the two group. Quantifications of the migration assay based on three independent experiments. Values represent mean + SEM. n=30 from three independent experiments; for each experiment, 10 random fields were imaged for each treatment.

### 5.3.7 $Co^{2+}$-induced fibroblast contractility is associated with altered biomechanical **properties**

#### 5.3.7.1 $Co^{2+}$ affects fibroblast elastic modulus

Firstly, the cell stiffness was assessed by using atomic force microscopy. According to the AFM images and analysis (Fig. 5.11A, B), the stiffest part of the fibroblast corresponds to the periphery of the cell, which indicates the higher density, cross-link content and better alignment of the actin at the edge of the cell. Compared with untreated cells, $Co^{2+}$-treated fibroblasts showed increased stiffness, which was characterised by the statistically significant differences in elastic moduli compared to untreated controls ($p < 0.001$, Figure 5.11C).

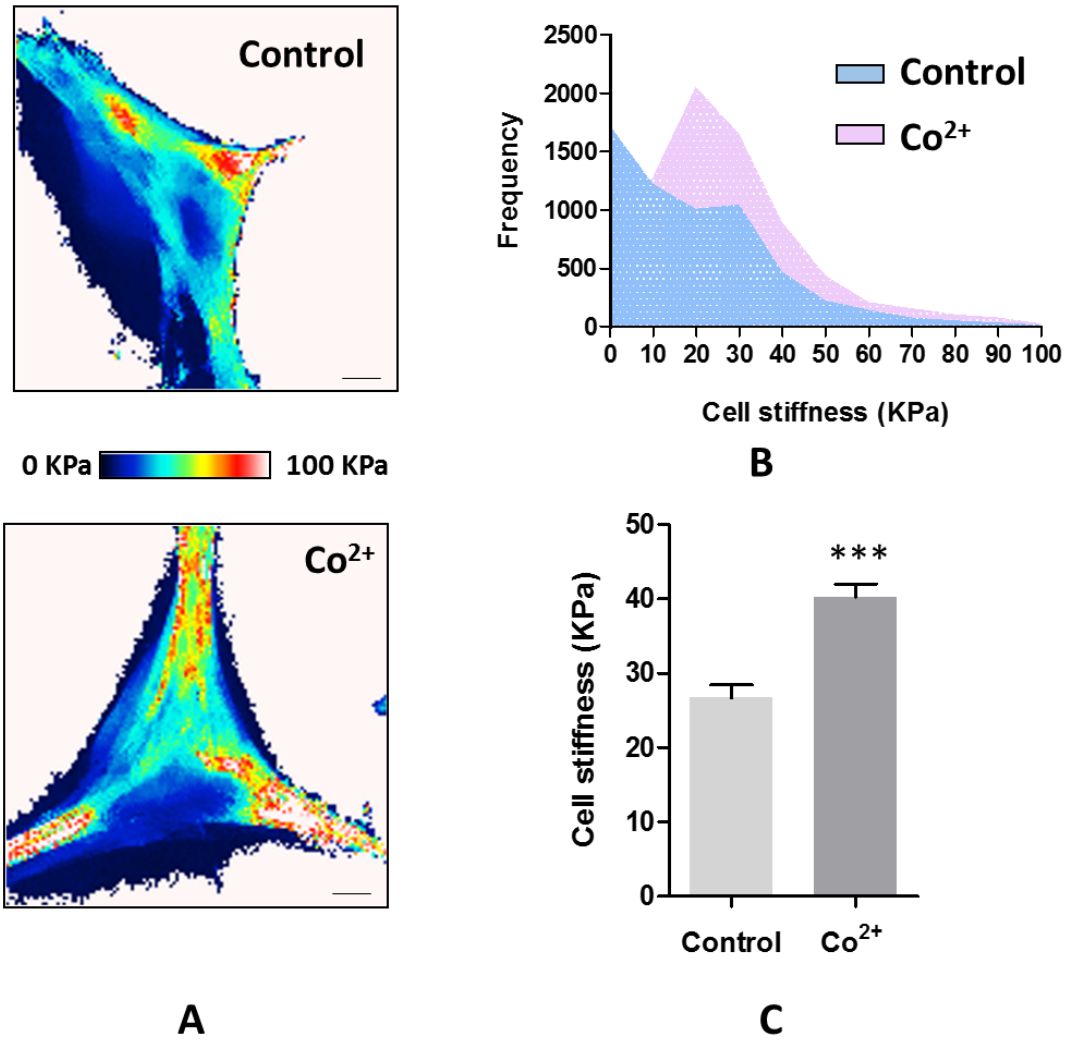


Figure 5.11 Altered cell stiffness of fibroblasts due to $Co^{2+}$ treatment. (A) Representative images showing the Young's modulus of the control and of Co-treated fibroblasts and associated density plot (B) showing distribution of the measured stiffness for values of individual locations of measurement within the physiological range of 0 kPa to 100 kPa,. (C): Quantification of mean cell stiffness of control and of $Co^{2+}$-treated fibroblasts; n=30 from 3 independent experiments; ***p< 0.001.

5.3.7.2 $Co^{2+}$ treatment increases fibroblast contractile force

Fibroblasts exposed to $Co^{2+}$ exhibited a nearly 80% increase in cellular contractile force ($p < 0.01$, Figure 5.12A and B). Traction forces in $Co^{2+}$-treated cells were found to be higher at the edge of a cell as well as underneath the cell body. Collectively, the increase in the Young's modulus and cellular contractile force of Co-treated cells correlated with the alterations in their morphological and ECM-modulating capability.

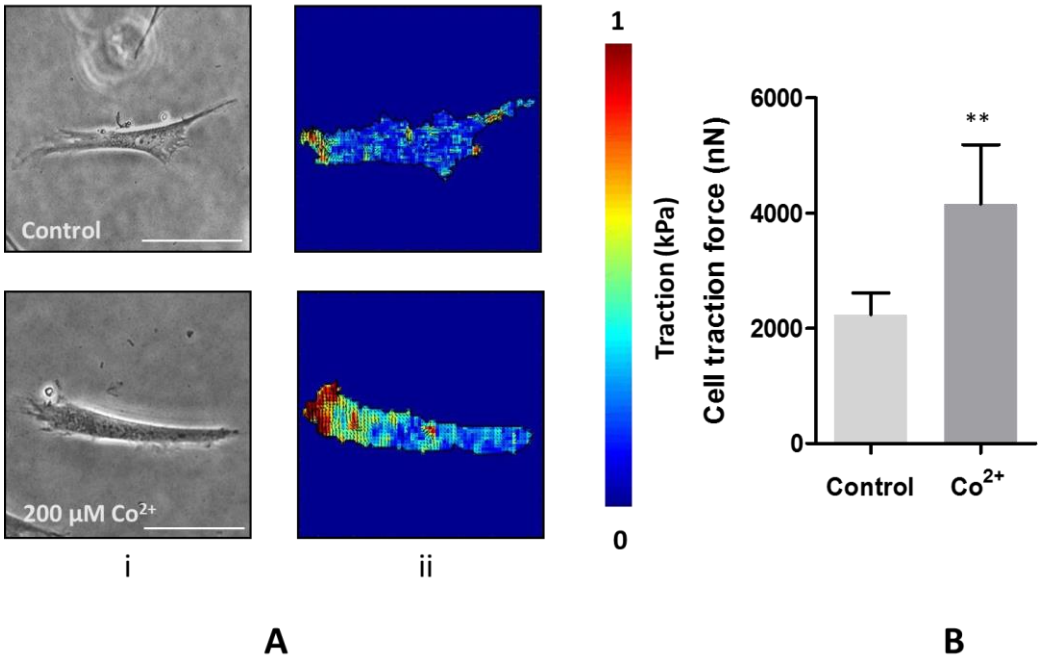


Figure 5.12 Contractile forces of a representative control and $Co^{2+}$-treated fibroblast. (A) Bright field images of individual cell (i) and corresponding stress magnitude maps (ii). Scale bar indicates 50 µm. (B): Quantification cellular contractile force of fibroblasts from control and untreated cells; n=30 from three independent experiments; **$p < 0.01$.

### 5.3.7 $Co^{2+}$ promotes phosphorylation of myosin light chain (MLC) and ROS production.

5.3.7.1 $Co^{2+}$ promotes phosphorylation of myosin light chain (MLC)

Cellular contractile state is governed by the actin-myosin-mediated motor activity (Ennomani et al., 2016). Non-muscle myosins are regulated by the cyclic phosphorylation and activation of myosin light chain (MLC) (Vicente-Manzanares et al., 2009, Moussavi et al., 1993). In the present study, $Co^{2+}$ (200 µM) induced a sustained enhancement in phosphorylation of MLC over 6 hours of treatment. The increase of approximately 80% occurred within 10 min following the initiation of $Co^{2+}$ treatment (Fig 5.13A).

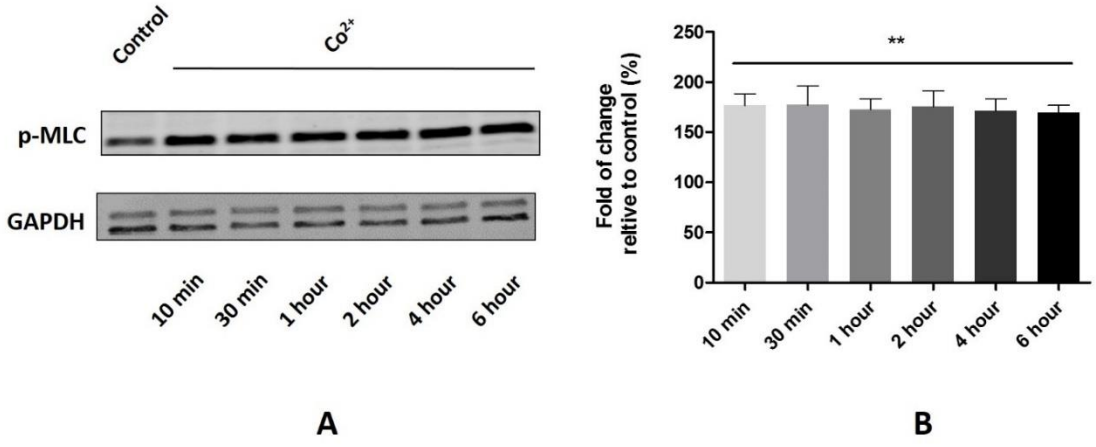


Figure 5.13 $Co^{2+}$ induced phosphorylation of myosin light chain (MLC). (A) Phosphorylation of MLC stimulated by 200 µM $Co^{2+}$over 6 hours of treatment. (B) Quantification of the phosphorylation of myosin light chain (MLC) stimulated by 200 µM $Co^{2+}$ over time. Values represent mean + SEM; ** $p < 0.01$; n=6 from three independent experiments.

### 5.3.7.2 $Co^{2+}$-induced phosphorylation of MLC requires ROCK activity and depends on ROS formation

Phosphorylation of myosin is known to be catalyzed either by Myosin Light Chain Kinase (MLCK) or by Rho-associated coiled-coil–forming kinase (ROCK) (Fukata et al., 2001). By applying the MLCK inhibitor ML-7 (10 µM, Sigma) and ROCK1 inhibitor Y-27632 (10 µM, Sigma), we found that ML-7 did not have an inhibitory effect, while Y-27632 pre-treatment completely prevented the collagen gel contraction by fibroblasts. ROCK1 is activated by small GTPase RhoA (Tang et al., 2012), therefore the activity of RhoA was inhibited by treating fibroblast during cobalt exposure with the cell permeable RhoA inhibitor, C3 transferase (2 µg/ml, Cytoskeleton). However, supressing RhoA activity did not prevent the collagen gel contraction (Figure 5.14A). Hence, cobalt did not induce fibroblast contraction via the RhoA/ROCK1 signalling pathway although ROCK activity is required during this process.

It has been reported previously that exposure to $Co^{2+}$ induced reactive oxygen species (ROS) formation (Chandel et al., 1998, Zou et al., 2001, Harris and Shi, 2003). When cells were treated with a ROS inhibitor in the form of the antioxidant, NAC (5mM, Sigma), $Co^{2+}$ -induced fibroblast contractility was completely prevented (Figure 5.14B). Further, treatment with NAC reduced the phosphorylation of MLC to base levels similar to that in untreated cells (Figure 5.14C and D). In summary, these results suggest that $Co^{2+}$ induces activation of the fibroblast contractile phenotype by promoting MLC phosphorylation mediated through the generation of ROS.

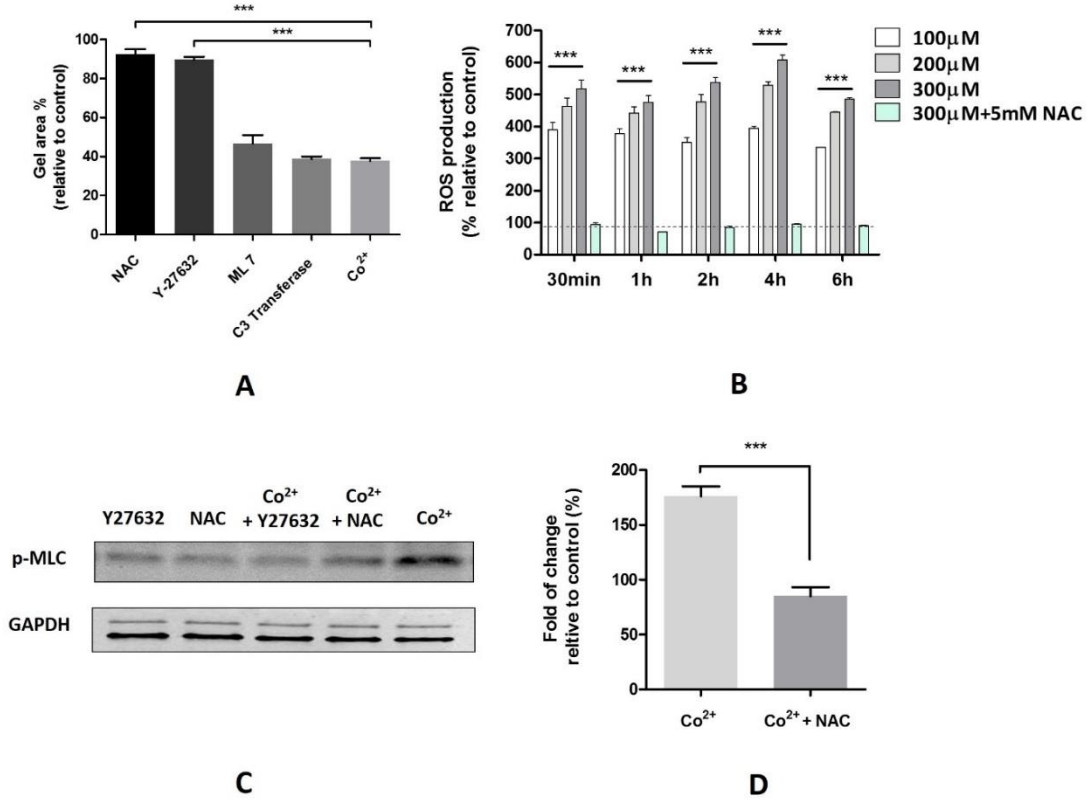


Figure 5.14 $Co^{2+}$-induced fibroblast activation is dependent on ROS production. (A) The effects of antioxidant NAC, ROCK1 inhibitor Y-27632, MLCK inhibitor ML-7 and RhoA inhibitor C3 transferase on cobalt-mediated collagen gel contraction by fibroblast. Values represent mean + SEM; *** indicate difference from cell only treated by $Co^{2+}$, n= 6 from 3 independent experiments (2 replicates/experiment); *** $P < 0.01$; (B) ROS formation stimulated by 100 - 300 µM $Co^{2+}$over 6 hours of treatment and inhibition of ROS formation by NAC. Values represent mean + SEM; n= 9 from 3 independent experiments (3 replicates/experiment); *** indicate difference from untreated cells, $P < 0.001$. (C) The effects of antioxidant NAC and ROCK1 inhibitor Y-27632 on the phosphorylation of MLC. (D) Quantification of the phosphorylation of MLC when NAC was added; n= 6 from 3 independent experiments (2 replicates/experiment); Values represent mean + SEM; ***$p < 0.001$.

### 5.3.7 $Co^{2+}$ stimulates the release of pro-fibrotic signals from macrophages

To investigate whether $Co^{2+}$ -induced fibroblast contraction is accompanied with enhanced collagen production, the amount of hydroxyproline secreted by the fibroblasts following different treatments (Myllyharju and Kivirikko, 2004) was measured. As shown in Figure 5.15A, $Co^{2+}$ or $Cr^{3+}$ alone did not have any obvious effect on pro-collagen production. However, when U937 macrophages were exposed to $Co^{2+}$ or $Cr^{3+}$ the amount of hydroxyproline content in the culture medium was significantly increased. Interestingly, for co-cultures of fibroblasts and macrophages, treatment with $Co^{2+}$ induced a synergistic response with an increase in hydroxyproline release of nearly 5 times that seen in macrophages alone (Figure 5.15A). Co-cultures treated with $Cr^{3+}$ did not exhibit this synergistic effect.

The degree of α-SMA expression, a marker of contractile and collagen-producing fibroblasts (Hinz, 2010), was also determined to assess the activation of cells exposed to cobalt and chromium. The number of α-SMA positive fibroblasts were significantly upregulated when macrophages and fibroblasts were co-cultured in the presence of $Co^{2+}$, as quantified in Figure 5.14B and shown in Figure 14C. These results indicate that $Co^{2+}$ stimulated the release of pro-fibrotic signals from macrophages, which enhance the fibrotic response of fibroblasts. In contrast $Cr^{3+}$ had no significant effects.

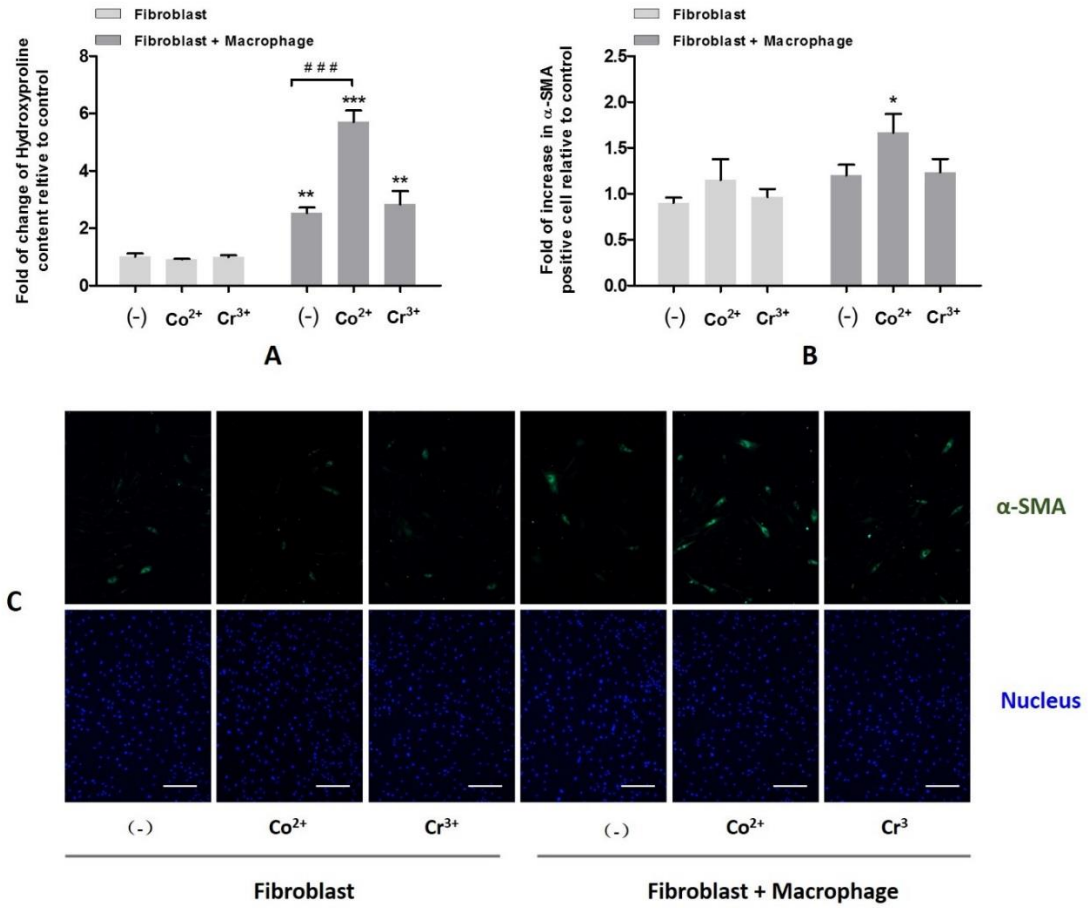


Figure 5.15 $Co^{2+}$ stimulated the release of pro-fibrotic signals from macrophages. (A) Fold of change in the amount of hydroxyproline content measured in the culture medium from fibroblast when treated by $Co^{2+}$ (200 µM), $Cr^{3+}$(400 µM) with or without U937 macrophages or co-culture without treatments. Values represent mean + SEM; n= 9 from 3 independent experiments (3 replicates/experiment). (B) Fold of change in the percentages of α-SMA positive fibroblasts with different treatments as described in (A). n=30 from 3 independent experiments; 10 random fields were imaged for each treatment in each experiment. (C) Representative Images of fibroblasts with α-SMA marker stained in each group; green: α-SMA; blue: nucleus; scale bar indicates 200 µm. *$p < 0.05$, **$p < 0.01$ and ***$p < 0.001$.

## 5.4 Discussion

Clinical reports highlight the presence of a soft tissue response and soft tissue destruction in patients with MoM implants showing abundant tissue necrosis, fibrosis and an inflammatory response (Campbell et al., 2010). How the metal debris, whether in particulate or ionic form, causes the destruction of soft tissue remains unclear. To elucidate this mechanism we investigated the effect of cobalt and chromium on human fibroblasts, the key cells involved in ECM remodelling.

The results showed that $Co^{2+}$ but not $Cr^{3+}$ significantly enhanced the capability of HDFs to contract extracellular matrix (ECM), in our case collagen type I gels. The enhanced contractility was associated with an alteration in the cytoskeleton and biomechanical properties. Furthermore, $Co^{2+}$ stimulated the release of pro-fibrotic signals from macrophages, which subsequently promoted the collagen synthesis and increase in α-SMA positive fibroblasts.

In our study we used both 2D and 3D models to study the effect of $Co^{2+}$ or $Cr^{3+}$ at non-cytotoxic concentrations on human fibroblasts. We observed increased contraction of fibroblast-populated collagen gels after treatment with $Co^{2+}$. This response associated with changes in fibroblast cytoskeleton, which gradually led to a stiffer collagen matrices. Using atomic force microscopy and traction force microscopy, we found that altered fibroblast contractility was associated with changes in the mechanical properties. Cobalt exposure caused a significant increase in cell stiffness and enhanced contractile forces. This is in line with previous observations that the biomechanical properties of fibroblasts serve as a key regulator of the cell's ability to organize the ECM (Rhee, 2009, Rhee and Grinnell, 2007, Humphrey et al., 2014). For example, fibroblasts are

able to dynamically shape the ECM due to alteration their cytoskeleton, in result mediating the progression of tumor growth (Alkasalias et al., 2017).

It was found that $Co^{2+}$ drives the contraction of fibroblasts by regulating MLC phosphorylation, which could be abrogated by ROS scavenger. $Co^{2+}$ is known to lead to the generation of reactive oxygen species (ROS) in a range of cell types (Leonard et al., 1998). Our results indicate for the first time that this cobalt-induced ROS formation also plays a critical role in ECM modulation by fibroblasts.

Following fibroblasts' activation they differentiate into myofibroblasts (MFs), this is widely observed in conditions requiring tissue remodelling, such as wound healing and fibrosis. MFs form contractile stress fibers and express de novo α-smooth muscle actin (α -SMA) (Tomasek et al., 2002). In the current work cobalt exposure led to the differentiation of HDFs by enhancing α -SMA expression, however this was only observed during co-culture with macrophages. Also only during fibroblast-macrophage co-culture, cobalt promoted the release of collagen (in the form of hydroxyproline) from fibroblasts. Macrophage plays a critical role in disease progression and in mediating the interplay between tissue and biomaterials. Previous studies showed that immune cells are affected by the matrix stiffness, e.g. stiffer substrates enhanced neutrophil transmigration (Stroka and Aranda-Espinoza, 2011) and release of pro-inflammatory cytokines by macrophages stimulated with LPS (Blakney et al., 2012). These findings indicate that immune cells probe and sense the alteration in the mechanical properties of the extracellular environment, hence could interact with the altered matrices by contractile fibroblasts. This could explain the enhanced pro-fibrotic response of cobalt-treated fibroblasts during macrophage co-culture.

Macrophages are capable of not only directly activating fibroblasts by releasing TGFβ1 (transforming growth factor-β1) and PDGF (platelet-derived growth factor) (Bonner et al., 1991, Wahl et al., 1990), but also control ECM turnover by regulating the balance of matrix metalloproteinases and their inhibitors (Fallowfield et al., 2007, Madala et al., 2010, Hironaka et al., 2000). Moreover, macrophages exacerbate fibrogenesis by producing chemokines that recruit fibroblasts and other inflammatory cells (Wynn, 2007). Furthermore, cobalt-treated macrophage also promote the cellular α-SMA expression, which is associated with upregulated collagen synthesis ability of fibroblasts compared with α-SMA (-) fibroblasts. Moreover, cobalt stimulates macrophages to release a range of inflammatory mediators, such as IL-1β and TNF-α (Goodman, 2007), which can also affect ECM turnover and tissue homeostasis. In summary, there is a link between cobalt-induced fibroblast activation, ROS production and the enhanced response in the presence of macrophages.

Total joint replacements may trigger unusual tissue remodelling (Campbell et al., 2010, Willert et al., 2005), activated by the release of metal, and in particular $Co^{2+}$. Understanding these mechanisms through the study of fibroblasts and the co-culture with macrophages has provided an indication that the control of ROS could influence implant-induced fibrosis and matrix remodelling and thereby enhance implant performance.

# Chapter 6. Investigation of the synovial fibroblasts and tissues and from patients with CoCr metal-on-metal hip implants and primary THA patients

## 6.1 Introduction

Tissue changes are often observed following the use of cobalt chromium implants. Soft tissue reactions including pseudotumour, ALVAL and metallosis (usually defined as aseptic fibrosis and local necrosis) are believed to be the sequelae of large amounts of metal debris released from MoM hip bearings due to wear and corrosion. The spectrum of these tissue reactions is extensive and ranges from small asymptomatic cysts to formation of destructive periprosthetic soft-tissue masses (Campbell et al., 2010). Histological methods have been used to observe and investigate the synovial lining integrity, inflammatory cell (lymphocytes, macrophages, plasma cells and giant cells) infiltrates to examine the degree of ALVAL (Willert et al., 2005). Also, numerous studies have documented the role of immune cells in the initiation and progression of the tissue reactions (Matharu et al., 2016, Pandit et al., 2008). However, few studies have examined the alteration of fibroblasts and tissue/ECM organization when subjected to wear and corrosion products *in vivo*. Fibroblasts have been reported as cells supplying ECM proteins such as collagen and fibronectin (Tracy et al., 2016). However, in addition to this essential function, they also play an important role in modulating inflammation progress. It has been suggested that some of the chronic inflammation occurs because of the activated fibroblasts, which result in the inappropriate survival and retention of immune cells within inflamed tissue (Buckley et al., 2001).

In the chapter 5 it was shown that $Co^{2+}$ ions promote fibroblasts contraction and stimulate the release of pro-fibrotic signals from macrophages thus leading to the fibrotic reactions and matrix remodelling. In order to verify these events *in vivo*, the synovial fibroblasts and periprosthetic synovial tissues from patients with metal-on-metal hip implants at their revision operation and patients undergoing a primary hip replacement operation were analysed to elucidate cellular and histological changes.

## 6.2 Method

### 6.2.1 Tissue collection

6.2.1.1 Ethical approval and patient selection

Ethical approval was obtained from the West London Research Ethics Committee 3 [07/Q0401/25]. Signed and written consent for the use of tissue samples (synovial membranes) removed during surgery was obtained from the patients. Soft tissue samples were collected from patients undergoing either a primary hip replacement surgery (control) or a revision surgery of MoM hip implant during surgery performed by Prof. Alister Hart at the Royal National Orthopaedic Hospital and the London Clinic. All tissue specimens were anonymised.

6.2.1.2 Inclusion and exclusion criteria

All patients with unilateral or bilateral total hip replacement were included in this study. Patients with prostheses made of components other than MoM, such as metal-on-polyethylene and metal-on-ceramic, were excluded from this study. The selection criteria for failed MoM were: unexplained pain, implant loosening and high cobalt and chromium levels in the blood (Table 6.1). The exclusion criteria were infection, mechanical instability or prosthesis malalignement.

Table 6.1 Patient demographics.

| | No. | Sex (M/F) | Age (year) | Time from primary to revision (year) |
|---|---|---|---|---|
| **Primary THA** | 1 | F | 53 | / |
| | 2 | F | 53 | / |
| | 3 | F | 54 | / |
| | 4 | F | 53 | / |
| | 5 | M | 49 | / |
| | 6 | F | 58 | / |
| | 7 | F | 62 | / |
| | 8 | F | 55 | / |
| **Revision THA** | 1 | F | 28 | 3 |
| | 2 | F | 59 | 15 |
| | 3 | F | 83 | 10 |
| | 4 | F | 64 | 5 |
| | 5 | M | 61 | 14 |
| | 6 | F | 88 | 7 |
| | 7 | F | 49 | 1 |
| | 8 | M | 73 | 6 |

6.2.1.3 Tissue harvest and storage

Tissues were collected from patient's synovial membrane enclosing the acetabulofemoral joint cavity, where the hip prostheses were implanted. Tissues from the control group were obtained from patients undergoing primary total hip replacement. Tissues harvested from patients were immediately collected, processed and stored appropriately in -80 °C. For histology, tissues were fixed in 10% Neutral Buffered Formalin (Sigma, UK) at room temperature before processing.

### 6.2.2 Isolation and Culture of synovial Fibroblasts

Primary fibroblasts were isolated immediately from biopsies obtained from the patients. First, harvested tissues were transferred into a 10 cm tissue culture dish in DMEM medium using a sterile forceps and finely minced into approximately 1 $mm^3$pieces using sterile scalpels. Then the pieces of tissues were placed in a 15 mL centrifuge tube containing 10 mL of digestion solution (0.1% collagenase in DMEM medium, Sigma,

UK) and incubated at 37°C in a horizontal orientation for 2 hours. 15 mL DMEM medium was subsequently added to dilute the collagenase which was passed through a 70 μm cell strainer (BD) to obtain a single-cell suspension. The cell suspension was centrifuged for 5 min at 200 x g at room temperature, the supernatant was discarded and the pellet resuspended in 1 mL DMEM medium. Harvested cells were counted and seeded at approximately 4,000 cells/$cm^2$ in a T75 flask. The human synovial fibroblasts were cultured at 37°C and 5% $CO_2$, with a first medium change 24-48 hours later. The medium was changed every 2-3 days.

### 6.2.3 Cell metabolic activity measurement

Synovial fibroblast proliferation was measured using CellTiter 96® Aqueous One Solution Cell Proliferation Assay (Promega) according to the manufacturer's instructions as described in section 5.2.3.

### 6.2.4 Collagen contraction

Fibroblast-mediated matrix contraction was assessed using collagen gel lattices, as described in section 5.2.4. Moreover, to determine fibroblast response to cytokines and growth factors, gels were made using serum free (SF) medium with the addition of one of the following factors: IL-1β (10 ng/ml, Peprotech, UK), PDGF-BB (10 ng/ml, Peprotech, UK) or TGF-β 1 (5 ng/ml, Peprotech, UK).

### 6.2.5. Fibroblast mechanical properties measurement

Fibroblast contractile force and stiffness was measured as described in section 5.2.6.

### 6.2.6 Collagen production measurements

The amount of hydroxyproline released in the cell culture medium was measured as described in section 5.2.9.

### 6.2.7 Immunohistochemical staining

6.2.7.1 Tissue embedding and cutting

Tissues, fixed in 10% neutral buffer formalin, were processed using the Histology department facilities at the Blizard Institute Core Pathology, Queen Mary School of Medicine and Dentistry. Briefly, fixed tissues were dehydrated through a series of graded ethanol baths (70%, 90%, absolute ethanol) to displace the water, cleared in xylene (Sigma, UK) bath and finally embedded in paraffin and placed on ice at -20°C overnight. After incubation tissue in the wax blocks were trimmed and placed again overnight. Finally, wax blocks were cut on an Accu-Cut® SRMTM 200 rotary microtome (Torrance, CA, USA) into 5 μm sections. Sections were placed into a hot water bath (40°C) to smooth the sections and were removed using glass microscope slides. Sections were left to drain and placed in an oven to soften the paraffin wax (60°C).

6.2.7.2 Sample staining

Slides were first deparaffinized by washing in 2 changes of xylene and graded ethanol baths (absolute ethanol, 90%, 70%). Antigen retrieval was performed to unmask the antigenic epitope of the tissue sample by boiling the deparaffinized sections in citrate buffer at pH 6.0. Endogenous peroxidase activity was locked by incubating sections in 3% $H_2O_2$ solution (Sigma, UK) in PBS at room temperature for 10 min followed by 2 rinses in PBS. To reduce background staining and any other immunostaining application, the samples were incubated with normal goat serum (5% in PBS) to block nonspecific binding sites in a humidified chamber at room temperature for 1 hour before staining. After draining the blocking buffer, 100µl of diluted primary antibody (in 1% goat serum in PBS) was added to the sections on the slides and incubated in a

humidified chamber at room temperature for 1 hour, after which the slides were washed twice in PBS. Then 100 µl of diluted biotinylated secondary antibody (in 1% goat serum in PBS) was applied to the sections on the slides and incubated in a humidified chamber at room temperature for 30 min with the slides washed in PBS after that. Amplification of antigen was achieved using an Elite® ABC-HRP Kit (Vector Laboratories, UK) and positive staining was visualized by using a DAB Peroxidase (HRP) Substrate Kit (Vector laboratories, UK).

### 6.2.8 Image analysis

Images were acquired on a Nikon Eclipse upright microscope. For image quantification, the mean percentage area positive for 10× randomly selected high powered fields (×10 magnification) was calculated using ImageJ analysis software as described (Jensen, 2013).

### 6.2.9 Data analysis and statistics

Statistical analysis was conducted with SPSS (Inc., Chicago, IL, USA) for each assays are listed in Table 6.2.

Table 6.2 Statistics methods for each assays.

| **Experiments** | **Statistics methods** |
|---|---|
| Cell proliferation assay | unpaired Student's t test |
| Collagen gel contraction measurement | Mann–Whitney U test |
| Cell fibroblast contractile force | unpaired Student's t test |
| Cell elastic modulus comparison | unpaired Student's t test |
| Hydroxyproline measurement | unpaired Student's t test |
| Collagen deposition comparison | unpaired Student's t test |
| α-smooth muscle actin expression cells analysis | unpaired Student's t test |

## 6.3 Results

### 6.3.1 Synovial fibroblast proliferation

The proliferative capacity of human synovial fibroblasts from patients in the control group (primary THA) and patients with a MoM implant (MoM) were investigated with an MTS assay. Proliferation of fibroblasts from MoM patients was not significantly different to cells cultured from primary THA patients over 72 hours (Figure 6.1).

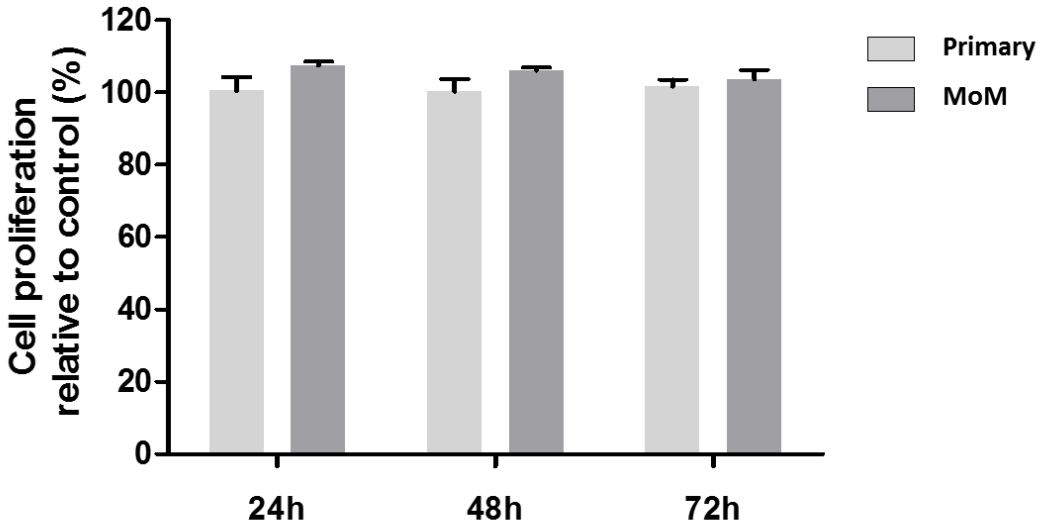


Figure 6.1 Synovial fibroblasts proliferation capacity over 3 days of culture. Bars represent mean + SEM; n = 72 from three independent experiment; 3 replicates/cell for each experiment from MoM (8) or primary THA (8).

### 6.3.2 Fibroblasts from patients with metal-on-metal implant exhibit a higher ability to contract 3D collagen matrices

An *in vitro* collagen gel contraction assay was applied to determine the contractile profile of fibroblasts from MoM and primary THA, in the presence of serum (10%) or cytokines and growth factors. When cultured in serum-free medium without any stimulating factors, fibroblasts from the two groups showed similar ability to contract the collagen gel (Figure 6.2). Fibroblasts from MoM patients were generally more contractile than fibroblasts from primary THA patients in most conditions, this trend was significant for serum ($p < 0.05$), PDGF ($p < 0.01$) and TGF-β ($p < 0.01$) stimulation (Figure 6.2 B-D). Fibroblasts from both groups responded well to TGFβ1 and PDGF, but the response to IL-1β was limited (Figure 6.2E). When stimulated by PDGF and TGFβ1 1, fibroblasts from MoM patients induced 56.9 ± 3.8% and 59.5 ± 3.7% contraction of the collagen matrices after 48 hours of treatment respectively, while fibroblasts from primary THA patients merely showed 31.7 ± 3.1% and 40.3 ± 2.9% reduction in gel area.

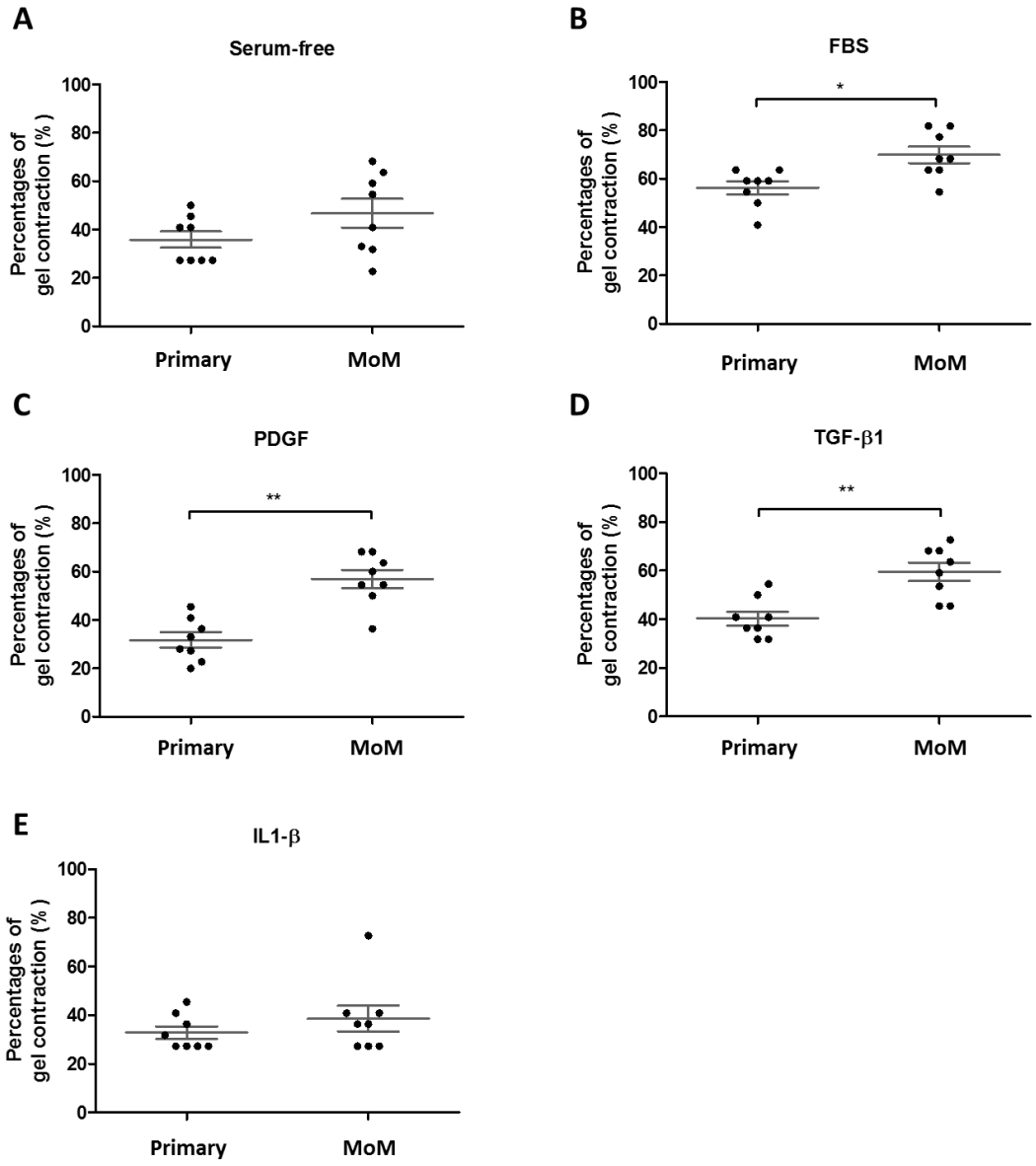


Figure 6.2 Synovial fibroblasts from patients with MoM implant display increased matrix contraction abilities. Fibroblasts from MoM and primary THA were embedded in collagen matrix and contraction was measured after 48 hrs, in serum-free medium (A), medium with 10% serum (B), or with cytokines (PDGF 10 μg/mL, TGF-β1 5 μg/mL and IL-1β 10 ng/mL). (A-E) fibroblasts from MoM patients exhibited higher contraction compared to fibroblasts from primary THA patients in the presence of serum (* $p = 0.0108$, two-tailed t-test), PDGF-BB (** $p = 0.0023$), TGF-β1 (** $p = 0.0053$). Shown is mean ± SEM for gel contraction after 48 hrs of culture. n = 6 from three independent experiment; 2 replicates/patient for each experiment from MoM (8) or primary THA (8).

### 6.3.3 Fibroblasts from patients with metal-on-metal implant display altered contraction force

It was shown in chapter 5 that there was a relationship between fibroblast's contraction potential and their mechanical properties. To determine whether the higher capacity of fibroblasts from MoM patients to contract collagen matrices was also associated with upregulated intrinsic cellular force level, the cellular contractile force of both groups at resting state (after 24 hours starvation in serum-free medium) was measured. According to the results showed in Figure 6.3, fibroblasts indeed displayed different levels of cell contraction force in the resting state. Fibroblasts from MoM patients presented a nearly 60% increase in cellular contractile force ($P < 0.05$) compared with fibroblasts from primary THA patients.

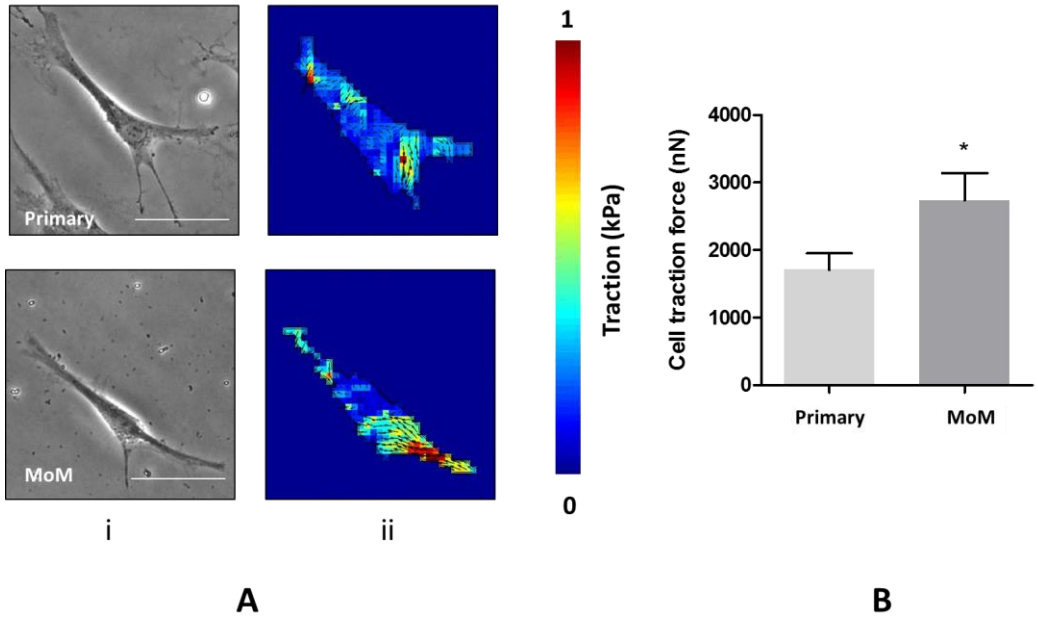


Figure 6.3 Contractile forces of fibroblasts from primary THA patients and patients with MoM implant. (A) Bright field images of individual cell (i) and corresponding stress magnitude maps (ii); (B) Quantification of cellular contractile force of fibroblasts from the cells of individual group; n = 120 from three independent experiment; 5 cells/patient were quantified for each experiment for MoM (8) or primary THA (8); *p < 0.05.

### 6.3.4 Fibroblasts from each group display similar cell elastic modules

Cell stiffness has been suggested as an indicator of cell phenotype alteration and multiple cellular process, for example, cell differentiation. Therefore, we further examined the cell elastic modules from the two groups of fibroblasts using an AFM technique. According to the results from the AFM study, the stiffness of fibroblasts from MoM patients (38.5 ± 1.9) was slightly higher than that of primary THA patients (33.3 ± 5.0), although the difference was not statistically different.

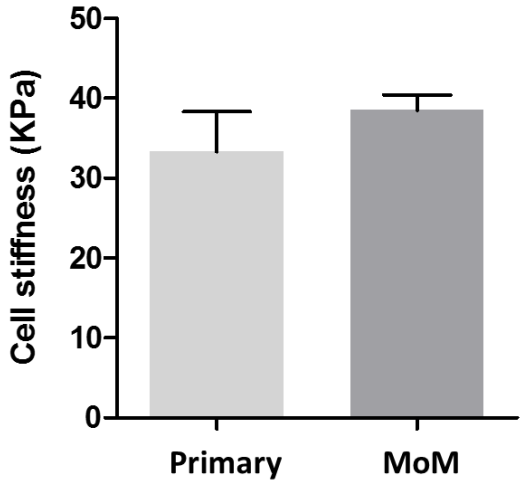


Figure 6.4 Quantification of cell stiffness of fibroblasts from primary THA patients and patients with MoM implant; n = 120 from three independent experiment; 5 cells/patient were quantified for each experiment for MoM (8) or primary THA (8).

### 6.3.5 Increased collagen production of fibroblasts from metal-on-metal revision patients

To quantify the ability of matrix production of fibroblasts from primary and MoM revision patients, hydroxyproline content was measured as a surrogate to determine levels of collagen. A significant increase was observed in the concentration of pro-collagen released from fibroblasts from MoM patients compared with that of patients with a primary THA (Figure 6.5).

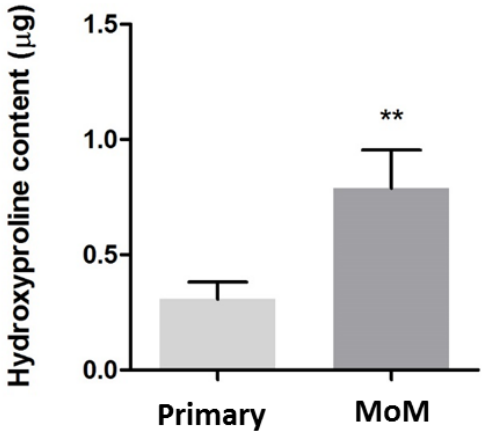


Figure 6.5 Increased collagen production of synovial fibroblasts from patients with MoM implant. Collagen released by cultured synovial fibroblasts into the cell culture medium after 48 hrs. Bars represent mean + SEM; n = 72 from three independent experiment; 3 replicates/cell were quantified for each experiment for MoM (8) or primary THA (8); ** $p < 0.01$.

### 6.3.6 Macroscopic appearance of the synovial tissues from patients with metal-on-metal hip implants and patients undergoing primary hip replacement

Macroscopically, the synovial membrane collected from primary total hip replacement patients generally appeared to be homogenous, fatty tissue (Figure 6.6 A, B). In contrast, tissues from patients with MoM implants undergoing a revision operation (Figure 6.6 C, D) appeared to be dense, pigmented and fibrotic tissues. In addition, the primary tissues floated in the digesting media whereas MoM revision tissue, for the majority of samples, sunk indicating a higher density. Tissues from patients with metal-on-metal hip were infiltrated with metal wear/corrosion products in some cases, which appeared a dark-grey or green (Figure 6.6 C, D).

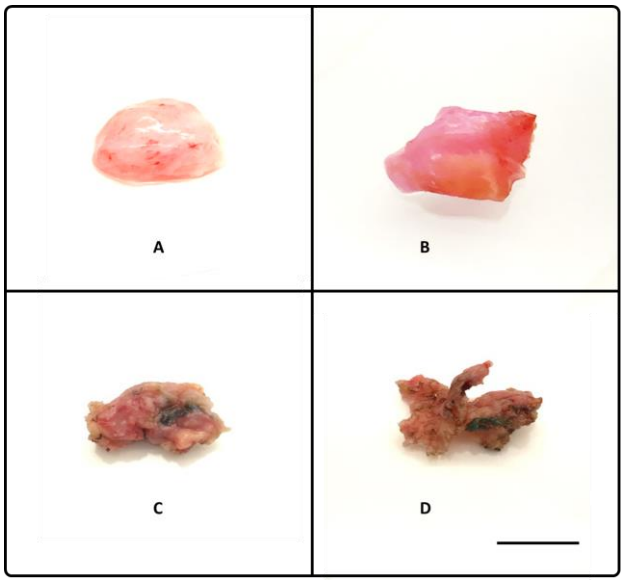


Figure 6.6 Macroscopic evaluation of tissue from primary and revision MoM THA. Synovial membrane were isolated from patients undergoing primary THA (A and B), patients undergoing revision MoM THA (C and D). Both tissues from primary THA patients appeared to be homogenous, fatty, non-fibrotic tissue. In contrast, tissue from revision THA patients appeared to be dense, pigmented, fibrotic tissue. Scale bar indicates 10 mm.

### 6.3.7 Increased collagen deposition in patients with metal-on-metal hip implants

Picrosirius red staining for collagen and immunohistochemistry for collagen I were used to confirm the increase in collagen in MoM patients and to investigate its distribution within the tissue. The synovial membranes from primary THA patients were characterised by a homogenous distribution of fat cells (adipocytes) with a small quantity of collagen (Figure 6.7A) or collagen I (Figure 6.7D) distributed surrounding adipocytes or throughout the tissue. For patients with MoM implants, there was evidence of extensive tissue remodelling characterised by the loss of adipocytes and the deposition of large quantities of densely packed collagen (Figure 6.7B) and collagen I fibres (Figure 6.7E). There was a significant increase in the percentage positive staining for picrosirius red (Figure 6.7 C) and collagen 1 (Figure 6.7F) in patients undergoing MoM revision THA.

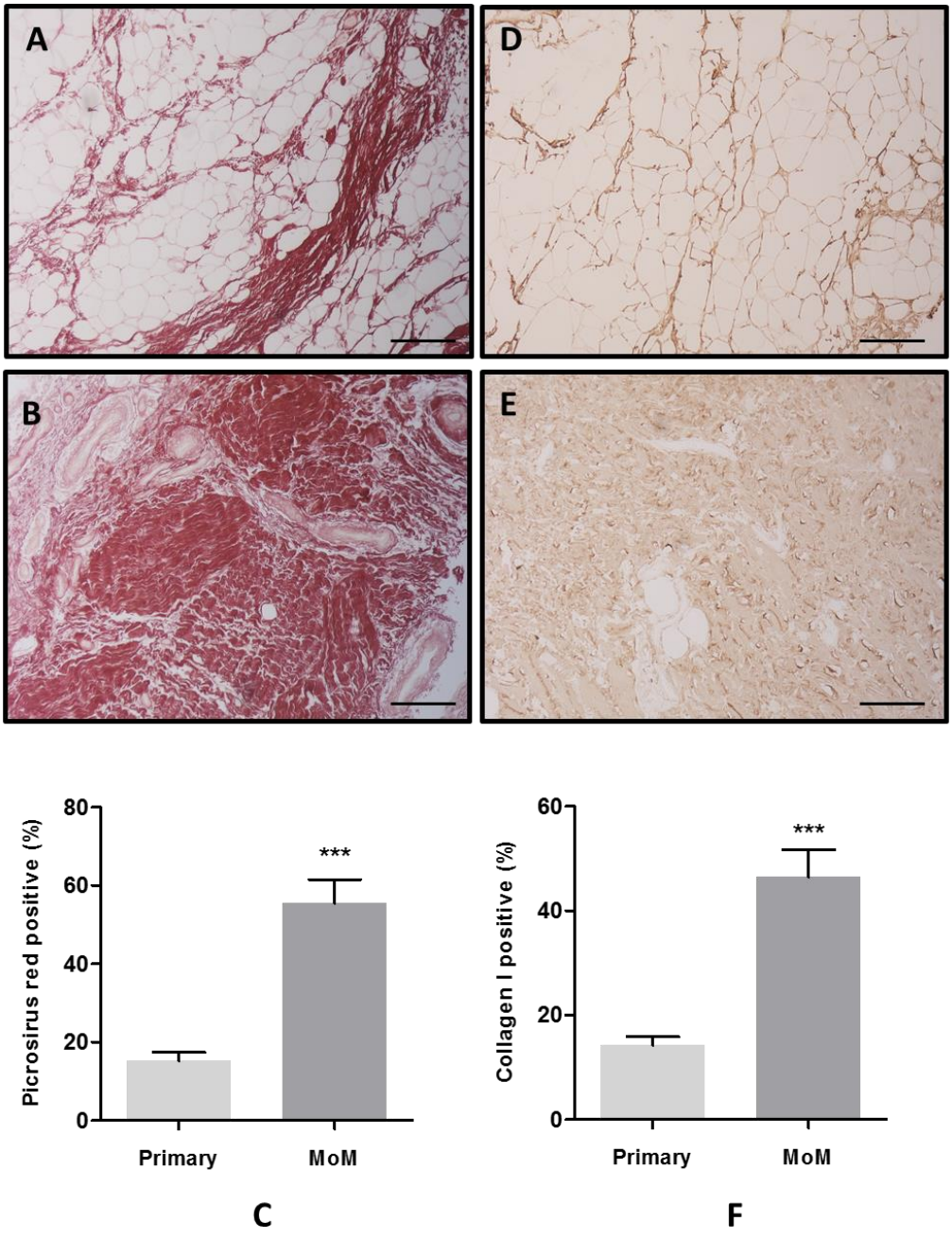


Figure 6.7 Significant tissue remodelling in collagen deposition and increased collagen I expression in revision MoM THA tissue. Picrosirius red staining was used to stain collagen (A and B) and immunohistochemistry staining was applied to visualize collagen I (D and E) with quantification showed in (C) and (F). Representative images of synovial membrane tissues from primary THA patients (A, D) and patients with metal-on-metal hip implants (B, E). Bars represent mean + SEM; n = 80 from two independent experiment; 5 random fields/patient were imaged and quantified for each experiment for MoM (8) or primary THA (8); *** $p < 0.001$; scale bar indicates 100 µm.

### 6.3.8 Increased α-smooth muscle actin expression in patients with metal-on-metal hip implants

Fibroblasts are cells of distinct morphology that are responsible for the maintenance and deposition of extracellular matrix throughout human body. However fibroblasts, in particular α -SMA positive myofibroblasts, have been identified as one of the major effector cells in tissue repair and, in some cases, the subsequent development of pathologic tissue reaction in multiple tissues/organs. Therefore, synovial membrane from primary (Figure 6.8A) and revision MoM (Figure 6.8B) patients were stained to determine the the levels of myofibroblasts present. Following quantification, Figure 6.8 C, the amount of α-SMA positive fibroblasts was significantly increased in revision MoM THA tissue.

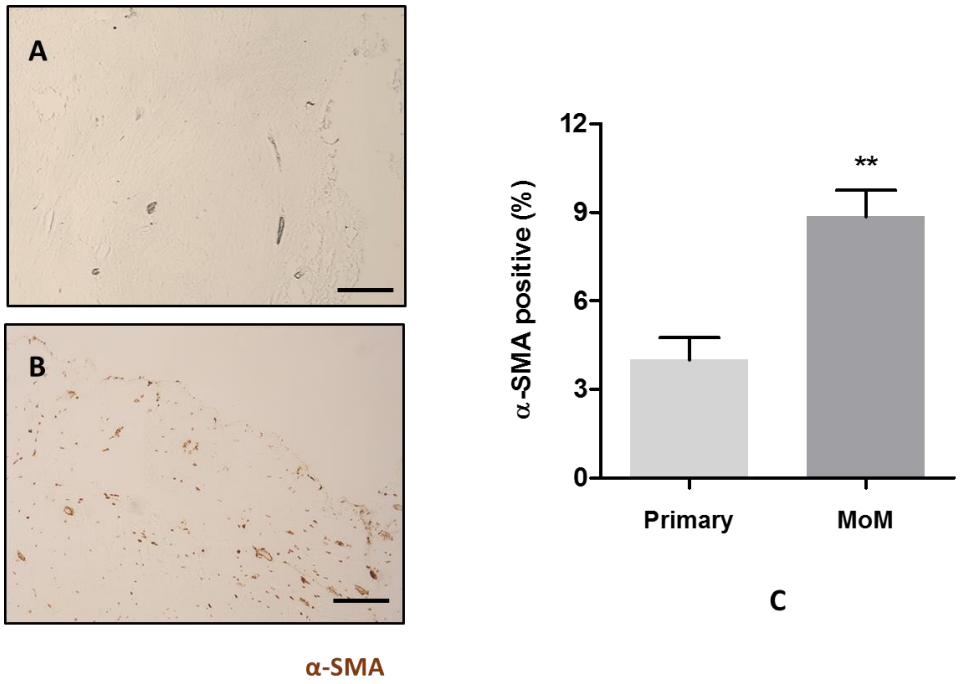


Figure 6.8 Increased amount of α-SMA positive fibroblasts in revision MoM THA tissues. Representative images of synovial membrane tissues from primary THA patients (A) and patients with metal-on-metal hip implants (B) with quantification showed in (C). Bars represent mean + SEM; n = 80 from two independent experiment; 5 random fields/patient were imaged and quantified for each experiment for MoM (8) or primary THA (8); ** $p < 0.01$; scale bar indicates 100 µm.

## 6.4 Discussion

Despite being one of the most significant issues in the field of arthroplasty, the mechanism related to adverse tissue reactions to wear and corrosion debris, responsible for the devastating failure of MoM implants remains relatively limited. The research to date has largely focused on the complex inflammatory responses of immune cells triggered by the CoCr metal products (Papageorgiou et al., 2007, Papis et al., 2007, Behl et al., 2013, Smith et al., 2014), with little attention being paid to the local tissue homeostasis mediated by the fibroblasts. Previous work from others have shown DNA damage and ROS production in human fibroblasts after exposure to the CoCr micron sized particles (Papageorgiou et al., 2007, Behl et al., 2013). In chapter 5, the effects of $Co^{2+}$ and $Cr^{3+}$ ions on human fibroblast-matrix interaction were investigated by utilising a 3D collagen culture systems and found that $Co^{2+}$ had a marked impact on the cytoskeleton, contractile forces and mechanical properties of the fibroblast without any detectable cytotoxic effects, inducing a profibrotic state, which were further enhanced by the presence of macrophages.

In this chapter, *in vitro* assays were applied to characterise some of the key features of synovial fibroblasts to investigate their contribution to the tissue response and disease progression. The data demonstrated that fibroblasts isolated from patients undergoing a MoM revision THA were more efficient at contracting collagen gels (Figure 6.2) and were more responsive to stimuli such as cytokines and growth factors. They are also found to display altered cell force responses (Figure 6.3) compared to the control primary cells. Moreover, synovial tissue from patients undergoing MoM revision THA is macroscopically and histologically different from tissue isolated from patients undergoing primary THA, with evidence of extensive tissue remodelling characterised by loss/replacement of adipocytes with dense areas of collagen. In addition, we

observed an obvious enhancement of synovial fibroblasts activation with significant increase in the number of myofibroblasts in the tissues (Figure 6.8). Our data highlights a significant enhancement of the activation of fibroblast and its important potential role in the undesired cellular response to wear and corrosion products.

The response to an inflammatory lesion involves a complex interplay of diverse cellular and tissue elements that restrain tissue invasion and ultimately establish normal tissue integrity (Buckley et al., 2013). It has also become increasingly clear that the remodelling of the extracellular matrix has profound effects on cellular immune responses (Sorokin, 2010). Instead of being a passive player in the immune system, fibroblasts are showed to actively define the organization of tissue microenvironments and modulate cell activities by conditioning the local cellular and cytokine microenvironment (Jordana et al., 1994, Buckley et al., 2001). The inappropriate activation of fibroblasts prevents the resolution of acute inflammation thereby leading to chronic persistent inflammation (Buckley et al., 2001).

The phenotypic changes of synovial fibroblasts are associated with dramatic functional alteration. How their ability to influence immune cells survival, differentiation and accumulation within synovium when exposed to CoCr metal and associated ions remains unknown. Addressing these questions in future studies will greatly improve our understanding of the development of tissue lesions following THA.

# Chapter 7 Discussion and future work

## 7.1 Discussion

The use of metal on metal total hip replacements has almost ceased, however implants containing CoCr alloys are still being widely utilized in THAs, in the modular femoral heads in MoP couplings as well as in dental prosthesis (Kuhta et al., 2009, Dimitriou et al., 2016). Significant increases in the measured metal ions released into the saliva of patients with dental metallic materials has been reported (Downarowicz and Mikulewicz, 2017). In addition, many retrieval studies have recently documented the adverse tissue reactions and pseudotumour formation adjacent to taper junctions in many total hip replacement designs (Plummer et al., 2016, Kwon et al., 2016), which are clinically and histologically similar to ALTRs previously reported in failed MoM bearings. The etiology of this soft-tissue damage has been linked to release of metal ions and debris from the modular taper junctions. A series of studies have examined the inflammatory response to CoCr ions and particulates which reveal that CoCr metallic debris promotes cell death and triggers the release of an array of proinflammatory mediators (Petit et al., 2006, Tsaousi et al., 2010, Posada et al., 2015, Kanaji et al., 2009, Dalal et al., 2012). However, how CoCr ions and particulates affect cell behaviour and modulate their activities remains largely unknown.

When tissue damage occurs or foreign insults are detected, circulating monocytes are attracted to adhere to and penetrate the endothelia walls. Through a series of morphological and functional changes, they become macrophages in order to target cells and foreign bodies that need eliminating (Shi and Pamer, 2011). After phagocytosis, the usual fate of inflammatory macrophages is to migrate from the inflamed site to the draining lymphatics (Buckley et al., 2013). Therefore, migration of

monocytes/macrophages play a critical role in the initiation and resolution of inflammatory response. In this thesis, using *in vitro* and *in vivo* approaches, it has been revealed that at moderate levels, cobalt ions and nanoparticles could prevent the efflux of macrophages, which would result in the accumulation of these inflammatory cells and subsequent prolonged inflammation. The mechanisms that underline this observation were clarified in chapter 4. To the best of our knowledge, this is the first study using an *in vivo* model to investigate the effects of the cobalt ions on immune cell's motility. It was found that cobalt nanoparticles inhibit macrophages efflux *in vivo*, which is consistent with the results of live time cell motility monitoring and cell transmigration assays. This phenomenon suggests that macrophage accumulation and subsequent prolonged inflammation in the peri-prosthetic tissues could be partially explained by the fact that their migratory ability was impaired after phagocytosis of CoCr wear particles or exposed to ionic cobalt. As monocytes are recruited to the inflamed site by a gradient of chemokines and other signalling factors secreted by local cells, they could be trapped in the area and exacerbate the tissue damage. A similar phenomenon has been previously revealed for the lipid-laden macrophages in the arterial intima during the development of atherosclerosis (Park et al., 2009).

The cytoskeleton consists of protein microfilaments, intermediate filaments, and microtubules (Fletcher and Mullins, 2010). The cytoskeleton serves, not only as a framework that helps cells maintain their morphology and internal organization, but additionally provides mechanical support that enables cells to carry out a wide range of functions such as division and movement (Fletcher and Mullins, 2010). Cellular responses to extracellular signals frequently includes changes in cell movement and cell shape. Nano particles (NPs) have previously been found to have a disruptive impact on cytoskeletal integrity according to *in vitro* studies of the interaction of actin/tubulin

with NPs, which showed destabilization and degradation of actin filaments or tubulin structure in cells exposed to NPs (Gonzalez et al., 2015, Tay et al., 2014b, Wang et al., 2012). Additionally NPs have been shown to influence MT network polymerization and further induce MT destabilization leading to straightening, thickening or shortening of MT structure (Tay et al., 2014a). Pernodet et al. showed that Au NPs induced aberrant F-actin formation and significantly decrease cell area while it was considered to be bioinert (Pan et al., 2009). Another study indicated that RAW 264.7 macrophages exposed to zinc oxide (ZnO) resulted in F-actin depolymerization and a decrease in the level of F-actins (Pati et al., 2016). It was speculated that the binding of $Zn^{2+}$ to the actin network led to this perturbation as it is known that actin contain $Zn^{2+}$ binding sites and the self-assembly of actin microfilaments could be disturbed by this binding (Garcia-Hevia et al., 2016). Impairments of F-actin could induce destabilization of the cytoskeleton and furthermore lead to permanent cell injury or even cell death (Franklin-Tong and Gourlay, 2008). However, in this current study it was shown that, in contrast to the detrimental effects of some other nanoparticles on cytoskeleton networks, CoNPs could actively promote cytoskeleton remodelling to modify macrophages' behaviour without affecting the cytoskeleton integrity or cell viability, which was triggered by the down-regulation of RhoA expression caused by ROS formation.

Fibroblasts and their activated phenotype known as myofibroblasts are the most common cell types in connective tissue. Because of their prevalence and the critical role they play in determining extracellular environment, fibroblasts also serve as one of the most frequently used cell types for *in vitro* toxicity tests for biomaterials. Numerous studies have examined the effects of Co and Cr ions and particles on fibroblasts in proliferation, cytotoxicity and DNA damage in 2D culture condition (Tsaousi et al., 2010, Parry et al., 2010, Kovacik et al., 2008). However, how Co and Cr affect

fibroblasts functionality and behaviour at sub-toxic level has not been previously reported. Fibroblasts are the primary cell type responsible for ECM proteins synthesis to build up the connective tissue. Moreover, they promote ECM remodelling via transmitting force to contract and compact the surrounding matrices to achieve tensional homoeostasis, which have a significant impact on other cells' behaviour. To analyse the fibroblasts' functional and biomechanical response to both Co and Cr under conditions that resemble an *in vivo*-like environment, a 3 dimensional (3D) matrix-cell culture system was applied in this thesis. It was demonstrated that $Co^{2+}$ promotes fibroblast contraction to induce ECM remodelling through its effect on fibroblast biomechanical properties. Cobalt exposure was found to cause a significant increase in cell stiffness and enhanced contractile forces. This is in agreement with previous observations that the biomechanical properties of fibroblasts serve as a key regulator of cell's ability to organize the ECM (Alkasalias et al., 2017). We found that $Co^{2+}$ drives the contraction of fibroblasts by regulating MLC phosphorylation, which could be abrogated by ROS scavenger (Figure 5.14). CoCr particles are known to lead to the generation of reactive oxygen species (ROS) in a range of cell types (Samelko et al., 2013, Behl et al., 2013, Raghunathan et al., 2013). The results indicated, for the first time, that this cobalt-induced ROS formation also plays a critical role in ECM modulation by fibroblasts. Furthermore, it was shown in chapter 5 that cobalt exposure also led to differentiation of fibroblasts into myofibroblasts in the presence of macrophages, which could secret multiple signalling factors, such as TGFβ1 (transforming growth factor-β1) and PDGF (platelet-derived growth factor), to enhance the activation of fibroblasts along with cobalt. This is consistent with the histology findings that the immune cells infiltrated peri-prosthetic area often showed concurrent aberrant tissue remodelling (Cooper et al., 2013).

More importantly, the synovial fibroblasts from patients with MoM implanted were successfully isolated and compared with fibroblasts from primary THA patients in this thesis. It was found that fibroblasts isolated from patients undergoing MoM revision THA were more efficient at contracting collagen matrices with altered cell traction forces (Figure 6.2 and 6.3). Also, MoM fibroblasts were shown to be more responsive to stimuli such as cytokines and growth factors compared to their normal counterparts.

The activation of fibroblasts and subsequent alteration in ECM mechanical properties have many implications. For example, immune cells are able to probe and sense the alteration in the mechanical properties of the extracellular environment. Previous studies have shown that immune cells are affected by the matrix stiffness, e.g. stiffer substrates enhanced neutrophil transmigration (Stroka and Aranda-Espinoza, 2011) and release of pro-inflammatory cytokines by macrophages (Blakney et al., 2012). This in turn could further promote tissue reactions that result in fibrosis as showed in Figure 6.6 or even tissue necrosis as reported in some patients. The retention of macrophages demonstrated in chapters 3 and 4 could further exacerbate this scenario. In addition, cobalt has been showed to activate macrophages to release a range of inflammatory mediators, which can affect ECM turnover and tissue homeostasis. For example, as a pleiotropic inflammatory factor, sustained IL-1β production in macrophages has been implicated in inducing tissue pathology and promoting the release of profibrogenic mediators (Daheshia and Yao, 2008, Negash et al., 2013). TNF-α was showed to stimulate collagen synthesis, increased expression of TIMP-1 (tissue inhibitor of metalloproteinases), and decreased activity of MMP-2 (matrix metalloproteinase 2) of Intestinal myofibroblast (Theiss et al., 2005). It also promotes the formation of TGF via ERK-dependent pathways in Swiss 3T3 fibroblasts and primary mouse fibroblasts

(Sullivan et al., 2005). Further studies are required for improved understanding of the interplay between fibroblasts and macrophages in the presence of cobalt.

In conclusion, this study has identified new downstream effects of cobalt-induced ROS production. Cobalt was found to reduce RhoA expression in modulating macrophage migration and cytoskeleton organization. The effects of this signalling cascade lead to an enhancement in macrophage spreading, adhesion and inhibition of migration, which could lead to a prolonged immune cell retention thereby propagating the chronic inflammation. The increased podosome formation in macrophages is also associated with enhanced activation of MMP9 and associated increased matrix degradation. On the other hand, cobalt-induced production of reactive oxygen species mediated the alteration of the mechanical properties of fibroblast leading to aberrant tissue remodelling *in vitro* and *in vivo*. Moreover, the profibrotic effect could be further enhanced due to the retention of macrophages. The effects of cobalt on macrophages and fibroblast and associated mechanisms are summarized in Figure 7.1. The identification of these new mechanisms through which cobalt, but not chromium, ions and nanoparticles induce macrophage retention and ECM remodeling provides a novel insight into the metal-associated periprosthetic tissue lesions.

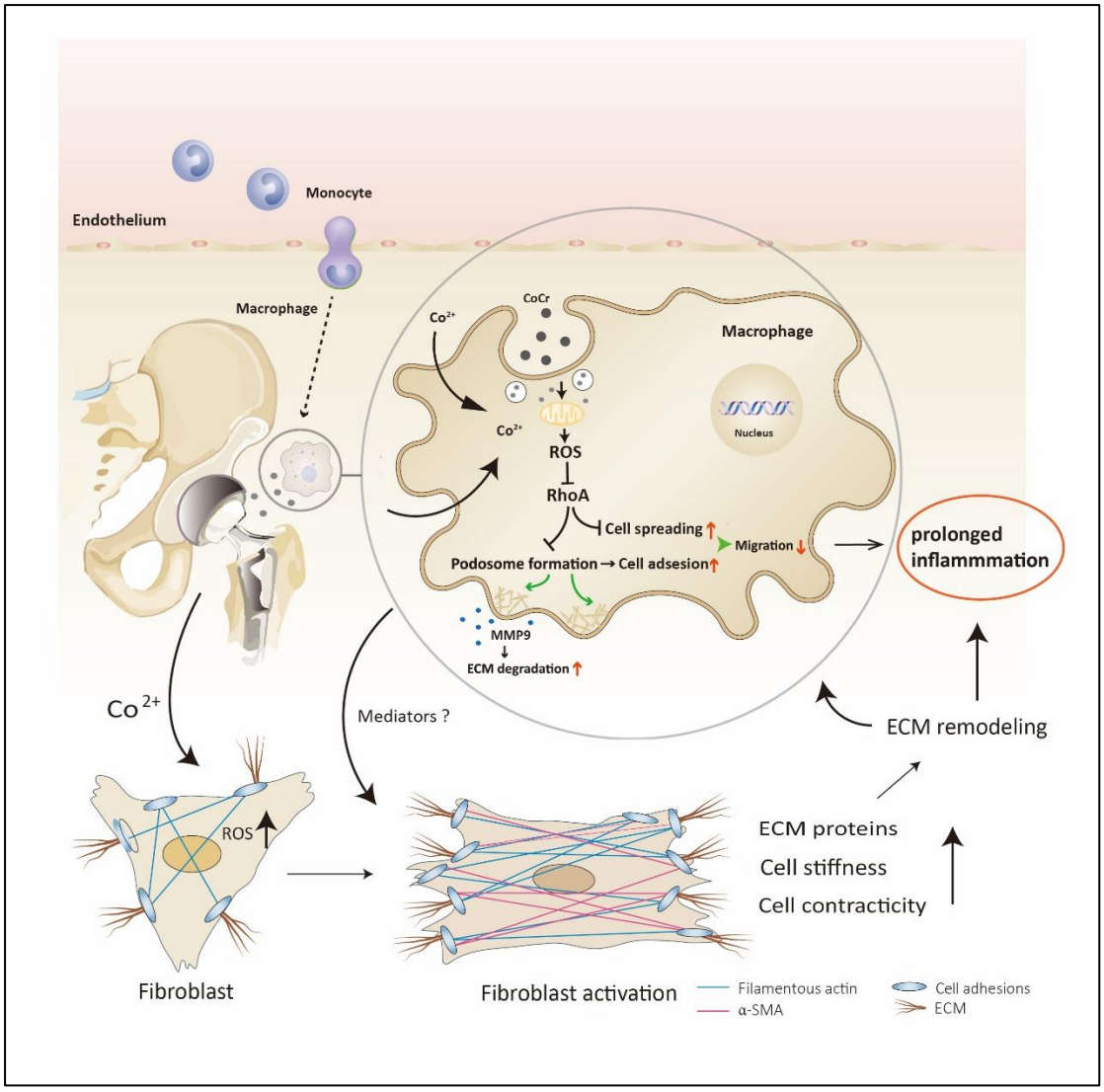


Figure 7.1 Illustration showing the proposed mechanisms of how $Co^{2+}$ and CoNPs from CoCr hip replacement implant affect macrophage and fibroblast functionality and lead to prolonged inflammation and aberrant tissue remodeling

## 7.2 Future work

### 7.2.1 The use of wear debris from MoM implants

The use of commercially available nanoparticles, while they could be chemically and physically different from the wear particles generated *in vivo,* allowed the individual role of the two primary elements from this alloy to be deciphered in the cellular response. It would be interesting to investigate wear debris from MoM implants, with all the challenges that this would introduce, to provide some further clinically relevant answers in future studies.

### 7.2.2 The effects of physical properties of metal particles on cellular response

It has been previously suggested that NPs are more bioactive than micron size particles (Papageorgiou et al., 2007) for the CoCr alloy. In this thesis, it was revealed that, similar to Co NPs, $Co^{2+}$ showed comparable effects on macrophages for both cell migration and cytoskeleton organization. It remains unknown if larger CoCr particles, of micron size, would also have such effects. In addition, there are reports that cellular response to metallic particles could be affected by their physical properties, such as surface roughness, tomography and density. Given the complexity of the physical properties of metal particles generated *in vivo,* it is of clinical relevance and importance to investigate how the physical properties of larger metal particles would impact cellular responses.

### 7.2.3 The role of fibroblast activation on immune cells recruitment and accumulation

Besides their capacity in tissue remodelling, fibroblasts are also known to play an important role in regulating the switch from acute resolving to chronic persistent inflammation. For example, the activation of fibroblasts results in the rapid production

and release of various cytokines, chemokines and prostanoids (Buckley et al., 2001). Moreover, fibroblasts also mediate the behaviour of immune cells that infiltrate the damaged tissue. Therefore, it is necessary to elucidate whether the activation of fibroblasts by cobalt is accompanied by signalling factors that regulate the activation and recruitment of inflammatory cells, which could ultimately lead to the identification of potential new therapeutic targets.

### 7.2.4 The effects of CoCr on bone cells and bone homeostasis

Many studies have revealed that cobalt and chromium have negative effects on bone formation and suggested that this may be associated with its detrimental effects on bone cells (Orhue et al., 2011, Kanaji et al., 2009). However, the molecular mechanisms that contributes to this dysregulated bone homeostasis has not been identified. Osteoclasts that derived from monocytes also play an essential role in bone homeostasis due to their osteolytic activity. As demonstrated in chapter 3 and 4, cobalt has significant effects on monocyte-derived macrophages behaviour. It would be helpful to uncover the influence of both Co and Cr ions and particles on the activities of osteoblasts and osteoclasts for preventing wear particles-related osteolysis in patients with CoCr containing implants.

### 7.2.5 ARMDs in patients treated with MoM total knee arthroplasty (TKA)

Although it is well established that MoM hip replacements leading to elevated levels of metal ions and ARMDs, there is little information available concerning the prevalence of these adverse reactions in patients with TKA implants containing CoCr alloys. It would be useful to analyse the extent of cobalt released from CoCr knee implant and investigate whether it would cause similar cellular/tissue response as reported in THA patients with CoCr bearing surface and the contributing factors for the possible discrepancy between THA and TKA.

# 8. Publications and presentations

## 8.1 Publications

Xu, J., Yang, J., Nyga, A., Ehteramyan, M., Moraga, A., Wu, Y., Zeng, L., Knight, M.M. and Shelton, J.C., 2018. Cobalt (II) ions and nanoparticles induce macrophage retention by ROS-mediated down-regulation of RhoA expression. *Acta biomaterialia*, *72*, pp.434-446.

Jing Xu, Agata Nyga, Weiqi Li, Xiaoli Zhang, Núria Gavara, Martin M Knight, Julia C Shelton., (2018). Cobalt ions (II) stimulate a fibrotic response through matrix remodelling, fibroblast contraction and the release of pro-fibrotic signals from macrophages. *Eur Cell Mater*. (Under review)

## 8.2 Presentations

**ORS (Orthopaedic Research Society) 2017 Annual Meeting**

Response To Cobalt Release From Joint Replacements: Enhancement in Fibroblast Proliferation, Motility And Contractility. Jing Xu, Martin Knight, Julia Shelton. (Poster No.1028)

Response To Cobalt Release From Joint Replacements: Enhancement in Macrophage Invasiveness through the Remodeling of Actin Cytoskeleton & Cell-matrix Interaction. Jing Xu, Martin Knight, Julia Shelton. (Poster No.1089)

**ISTA (International Society for Technology in Arthroplasty) 2017 Annual Congress**

Cobalt Released from Total Joint Replacement Leads to Accumulation of Macrophages by Inhibition of Cell Migration. Jing Xu, Lingfang Zeng, Martin Knight, Julia Shelton. (Oral Presentation)

# 9. References


AKAY, M. 2006. *Wiley Encyclopedia of Biomedical Engineering, 6 Volume Set*, Wiley.

AKHMANOVA, A. & STEINMETZ, M. O. 2015. Control of microtubule organization and dynamics: two ends in the limelight. *Nat Rev Mol Cell Biol,* 16**,** 711-26.

ALKASALIAS, T., ALEXEYENKO, A., HENNIG, K., DANIELSSON, F., LEBBINK, R. J., FIELDEN, M., TURUNEN, S. P., LEHTI, K., KASHUBA, V., MADAPURA, H. S., BOZOKY, B., LUNDBERG, E., BALLAND, M., GUVEN, H., KLEIN, G., GAD, A. K. & PAVLOVA, T. 2017. RhoA knockout fibroblasts lose tumor-inhibitory capacity in vitro and promote tumor growth in vivo. *Proc Natl Acad Sci U S A,* 114**,** E1413-E1421.

ANDUJAR, M. B., MELIN, M., GUERRET, S. & GRIMAUD, J. A. 1992. Cell-Migration Influences Collagen Gel Contraction. *Journal of Submicroscopic Cytology and Pathology,* 24**,** 145-154.

BARSOUM, K. E. C. A. H. A. K. K. W. K. 2010. Evolution of bearing surfaces in total hip arthroplasty: a review. *Current Orthopaedic Practice***,** 198-208.

BASKEY, S. J., LEHOUX, E. A. & CATELAS, I. 2017. Effects of Cobalt and Chromium Ions on Lymphocyte Migration. *Journal of Orthopaedic Research,* 35**,** 916-924.

BEHL, B., PAPAGEORGIOU, I., BROWN, C., HALL, R., TIPPER, J. L., FISHER, J. & INGHAM, E. 2013. Biological effects of cobalt-chromium nanoparticles and ions on dural fibroblasts and dural epithelial cells. *Biomaterials,* 34**,** 3547-58.

BERAUDI, A., CATALANI, S., MONTESI, M., STEA, S., SUDANESE, A., APOSTOLI, P. & TONI, A. 2013. Detection of cobalt in synovial fluid from metal-on-metal hip prosthesis: correlation with the ion haematic level. *Biomarkers,* 18**,** 699-705.

BERDEAUX, R. L., DIAZ, B., KIM, L. & MARTIN, G. S. 2004. Active Rho is localized to podosomes induced by oncogenic Src and is required for their assembly and function. *Journal of Cell Biology,* 166**,** 317-323.

BEYERSMANN, D. & HARTWIG, A. 2008. Carcinogenic metal compounds: recent insight into molecular and cellular mechanisms. *Arch Toxicol,* 82**,** 493-512.

BHABRA, G., SOOD, A., FISHER, B., CARTWRIGHT, L., SAUNDERS, M., EVANS, W. H., SURPRENANT, A., LOPEZ-CASTEJON, G., MANN, S., DAVIS, S. A., HAILS, L. A., INGHAM, E., VERKADE, P., LANE, J., HEESOM, K., NEWSON, R. & CASE, C. P. 2009. Nanoparticles can cause DNA damage across a cellular barrier. *Nat Nanotechnol,* 4**,** 876-83.

BIGARELLA, C. L., LIANG, R. & GHAFFARI, S. 2014. Stem cells and the impact of ROS signaling. *Development,* 141**,** 4206-4218.

BLAKNEY, A. K., SWARTZLANDER, M. D. & BRYANT, S. J. 2012. The effects of substrate stiffness on the in vitro activation of macrophages and in vivo host response to poly(ethylene glycol)-based hydrogels. *J Biomed Mater Res A,* 100**,** 1375-86.

BONNER, J. C., OSORNIOVARGAS, A. R., BADGETT, A. & BRODY, A. R. 1991. Differential Proliferation of Rat Lung Fibroblasts Induced by the Platelet-Derived Growth Factor-Aa, Factor-Ab, and Factor-Bb Isoforms Secreted by Rat Alveolar Macrophages. *American Journal of Respiratory Cell and Molecular Biology,* 5**,** 539-547.

BROWN, C., WILLIAMS, S., TIPPER, J. L., FISHER, J. & INGHAM, E. 2007. Characterisation of wear particles produced by metal on metal and ceramic on metal hip prostheses under standard and microseparation simulation. *J Mater Sci Mater Med,* 18**,** 819-27.

BROWN, S. A., FLEMMING, C. A., KAWALEC, J. S., PLACKO, H. E., VASSAUX, C., MERRITT, K., PAYER, J. H. & KRAAY, M. J. 1995. Fretting corrosion accelerates crevice corrosion of modular hip tapers. *J Appl Biomater,* 6**,** 19-26.

BUCKLEY, C. D., GILROY, D. W., SERHAN, C. N., STOCKINGER, B. & TAK, P. P. 2013. The resolution of inflammation. *Nat Rev Immunol,* 13**,** 59-66.

BUCKLEY, C. D., PILLING, D., LORD, J. M., AKBAR, A. N., SCHEEL-TOELLNER, D. & SALMON, M. 2001. Fibroblasts regulate the switch from acute resolving to chronic persistent inflammation. *Trends Immunol,* 22**,** 199-204.

BUCKWALTER, J. A. & MANKIN, H. J. 1998. Articular cartilage: degeneration and

osteoarthritis, repair, regeneration, and transplantation. *Instr Course Lect,* 47**,** 487-504.

BUSCHER, R., TAGER, G., DUDZINSKI, W., GLEISING, B., WIMMER, M. A. & FISCHER, A. 2005. Subsurface microstructure of metal-on-metal hip joints and its relationship to wear particle generation. *J Biomed Mater Res B Appl Biomater,* 72**,** 206-14.

CAICEDO, M. S., PENNEKAMP, P. H., MCALLISTER, K., JACOBS, J. J. & HALLAB, N. J. 2010. Soluble ions more than particulate cobalt-alloy implant debris induce monocyte costimulatory molecule expression and release of proinflammatory cytokines critical to metal-induced lymphocyte reactivity. *J Biomed Mater Res A,* 93**,** 1312-21.

CALLAGHAN, J. J., ROSENBERG, A. G. & RUBASH, H. E. 2007. *The Adult Hip*, Lippincott Williams & Wilkins.

CAMPBELL, P., EBRAMZADEH, E., NELSON, S., TAKAMURA, K., DE SMET, K. & AMSTUTZ, H. C. 2010. Histological features of pseudotumor-like tissues from metal-on-metal hips. *Clin Orthop Relat Res,* 468**,** 2321-7.

CAMPBELL, P., URBAN, R. M., CATELAS, I., SKIPOR, A. K. & SCHMALZRIED, T. P. 2003. Autopsy analysis thirty years after metal-on-metal total hip replacement. A case report. *J Bone Joint Surg Am,* 85-A**,** 2218-22.

CANNIZZO, E. S., CLEMENT, C. C., SAHU, R., FOLLO, C. & SANTAMBROGIO, L. 2011. Oxidative stress, inflamm-aging and immunosenescence. *J Proteomics,* 74**,** 2313-23.

CATELAS, I., PETIT, A., VALI, H., FRAGISKATOS, C., MEILLEUR, R., ZUKOR, D. J., ANTONIOU, J. & HUK, O. L. 2005. Quantitative analysis of macrophage apoptosis vs. necrosis induced by cobalt and chromium ions in vitro. *Biomaterials,* 26**,** 2441-53.

CATELAS, I., PETIT, A., ZUKOR, D. J. & HUK, O. L. 2001. Cytotoxic and apoptotic effects of cobalt and chromium ions on J774 macrophages - Implication of caspase-3 in the apoptotic pathway. *Journal of Materials Science-Materials in Medicine,* 12**,** 949-953.

CERVERO, P., PANZER, L. & LINDER, S. 2013. Podosome reformation in macrophages: assays and analysis. *Methods Mol Biol,* 1046**,** 97-121.

CHANDEL, N. S., MALTEPE, E., GOLDWASSER, E., MATHIEU, C. E., SIMON, M. C. &

SCHUMACKER, P. T. 1998. Mitochondrial reactive oxygen species trigger hypoxia-induced transcription. *Proceedings of the National Academy of Sciences of the United States of America,* 95**,** 11715-11720.

CHARNLEY, J. 1961. Arthroplasty of the hip. A new operation. *Lancet,* 1**,** 1129-32.

COHEN, D. 2012. How safe are metal-on-metal hip implants? *BMJ*.

COOPER, H. J., DELLA VALLE, C. J., BERGER, R. A., TETREAULT, M., PAPROSKY, W. G., SPORER, S. M. & JACOBS, J. J. 2012. Corrosion at the head-neck taper as a cause for adverse local tissue reactions after total hip arthroplasty. *J Bone Joint Surg Am,* 94**,** 1655-61.

COOPER, H. J., URBAN, R. M., WIXSON, R. L., MENEGHINI, R. M. & JACOBS, J. J. 2013. Adverse local tissue reaction arising from corrosion at the femoral neck-body junction in a dual-taper stem with a cobalt-chromium modular neck. *J Bone Joint Surg Am,* 95**,** 865-72.

COWIN, S. C. 2001. *Bone Mechanics Handbook, Second Edition*, Taylor & Francis.

DAHESHIA, M. & YAO, J. Q. 2008. The interleukin 1beta pathway in the pathogenesis of osteoarthritis. *J Rheumatol,* 35**,** 2306-12.

DALAL, A., PAWAR, V., MCALLISTER, K., WEAVER, C. & HALLAB, N. J. 2012. Orthopedic implant cobalt-alloy particles produce greater toxicity and inflammatory cytokines than titanium alloy and zirconium alloy-based particles in vitro, in human osteoblasts, fibroblasts, and macrophages. *J Biomed Mater Res A,* 100**,** 2147-58.

DAVDA, K., LALI, F. V., SAMPSON, B., SKINNER, J. A. & HART, A. J. 2011. An analysis of metal ion levels in the joint fluid of symptomatic patients with metal-on-metal hip replacements. *J Bone Joint Surg Br,* 93**,** 738-45.

DE PASQUALE, D., STEA, S., SQUARZONI, S., BORDINI, B., AMABILE, M., CATALANI, S., APOSTOLI, P. & TONI, A. 2014. Metal-on-metal hip prostheses: correlation between debris in the synovial fluid and levels of cobalt and chromium ions in the bloodstream. *Int Orthop,* 38**,** 469-75.

DE STEIGER, R. N., HANG, J. R., MILLER, L. N., GRAVES, S. E. & DAVIDSON, D. C.

2011. Five-year results of the ASR XL Acetabular System and the ASR Hip Resurfacing System: an analysis from the Australian Orthopaedic Association National Joint Replacement Registry. *J Bone Joint Surg Am,* 93**,** 2287-93.

DESOUZA, R. M., PARSONS, N. R., ONI, T., DALTON, P., COSTA, M. & KRIKLER, S. 2010. Metal ion levels following resurfacing arthroplasty of the hip: serial results over a ten-year period. *J Bone Joint Surg Br,* 92**,** 1642-7.

DIMITRIOU, D., LIOW, M. H. L., TSAI, T. Y., LEONE, W. A., LI, G. A. & KWON, Y. M. 2016. Early Outcomes of Revision Surgery for Taper Corrosion of Dual Taper Total Hip Arthroplasty in 187 Patients. *Journal of Arthroplasty,* 31**,** 1549-1554.

DINARELLO, C. A. 2011. Interleukin-1 in the pathogenesis and treatment of inflammatory diseases. *Blood,* 117**,** 3720-32.

DOORN, P. F., CAMPBELL, P. A., WORRALL, J., BENYA, P. D., MCKELLOP, H. A. & AMSTUTZ, H. C. 1998. Metal wear particle characterization from metal on metal total hip replacements: transmission electron microscopy study of periprosthetic tissues and isolated particles. *J Biomed Mater Res,* 42**,** 103-11.

DOWNAROWICZ, P. & MIKULEWICZ, M. 2017. Trace metal ions release from fixed orthodontic appliances and DNA damage in oral mucosa cells by in vivo studies: A literature review. *Adv Clin Exp Med,* 26**,** 1155-1162.

DOWSON, D. & WRIGHT, V. 1981. *Introduction to the Biomechanics of Joints and Joint Replacement*, Wiley.

DUFFIN, R., TRAN, L., BROWN, D., STONE, V. & DONALDSON, K. 2007. Proinflammogenic effects of low-toxicity and metal nanoparticles in vivo and in vitro: highlighting the role of particle surface area and surface reactivity. *Inhal Toxicol,* 19**,** 849-56.

DWYER, A. R., MOUCHEMORE, K. A., STEER, J. H., SUNDERLAND, A. J., SAMPAIO, N. G., GREENLAND, E. L., JOYCE, D. A. & PIXLEY, F. J. 2016. Src family kinase expression and subcellular localization in macrophages: implications for their role in CSF-1-induced macrophage migration. *J Leukoc Biol,* 100**,** 163-75.

ECKES, B., KESSLER, D., AUMAILLEY, M. & KRIEG, T. 1999. Interactions of fibroblasts with the extracellular matrix: implications for the understanding of fibrosis. *Springer Semin Immunopathol,* 21**,** 415-29.

ENNOMANI, H., LETORT, G., GUERIN, C., MARTIEL, J. L., CAO, W. X., NEDELEC, F., DE LA CRUZ, E. M., THERY, M. & BLANCHOIN, L. 2016. Architecture and Connectivity Govern Actin Network Contractility. *Current Biology,* 26**,** 616-626.

ETIENNE-MANNEVILLE, S. 2004. Actin and microtubules in cell motility: which one is in control? *Traffic,* 5**,** 470-7.

EVANS, J. G. & MATSUDAIRA, P. 2006. Structure and dynamics of macrophage podosomes. *Eur J Cell Biol,* 85**,** 145-9.

FALLOWFIELD, J. A., MIZUNO, M., KENDALL, T. J., CONSTANDINOU, C. M., BENYON, R. C., DUFFIELD, J. S. & IREDALE, J. P. 2007. Scar-associated macrophages are a major source of hepatic matrix metalloproteinase-13 and facilitate the resolution of murine hepatic fibrosis. *Journal of Immunology,* 178**,** 5288-5295.

FLETCHER, D. A. & MULLINS, R. D. 2010. Cell mechanics and the cytoskeleton. *Nature,* 463**,** 485-92.

FLEURY, C., PETIT, A., MWALE, F., ANTONIOU, J., ZUKOR, D. J., TABRIZIAN, M. & HUK, O. L. 2006. Effect of cobalt and chromium ions on human MG-63 osteoblasts in vitro: Morphology, cytotoxicity, and oxidative stress. *Biomaterials,* 27**,** 3351-3360.

FRANKLIN-TONG, V. E. & GOURLAY, C. W. 2008. A role for actin in regulating apoptosis/programmed cell death: evidence spanning yeast, plants and animals. *Biochem J,* 413**,** 389-404.

FRANZ, C. M., JONES, G. E. & RIDLEY, A. J. 2002. Cell migration in development and disease. *Dev Cell,* 2**,** 153-8.

FUKATA, Y., AMANO, M. & KAIBUCHI, K. 2001. Rho-Rho-kinase pathway in smooth muscle contraction and cytoskeletal reorganization of non-muscle cells. *Trends in Pharmacological Sciences,* 22**,** 32-39.

GARBUZ, D. S., TANZER, M., GREIDANUS, N. V., MASRI, B. A. & DUNCAN, C. P. 2010.

The John Charnley Award: Metal-on-metal hip resurfacing versus large-diameter head metal-on-metal total hip arthroplasty: a randomized clinical trial. *Clin Orthop Relat Res,* 468**,** 318-25.

GARCIA-HEVIA, L., VALIENTE, R., MARTIN-RODRIGUEZ, R., RENERO-LECUNA, C., GONZALEZ, J., RODRIGUEZ-FERNANDEZ, L., AGUADO, F., VILLEGAS, J. C. & FANARRAGA, M. L. 2016. Nano-ZnO leads to tubulin macrotube assembly and actin bundling, triggering cytoskeletal catastrophe and cell necrosis. *Nanoscale,* 8**,** 10963-73.

GARRETT, R., WILKSCH, J. & VERNON-ROBERTS, B. 1983. Effects of cobalt-chrome alloy wear particles on the morphology, viability and phagocytic activity of murine macrophages in vitro. *Aust J Exp Biol Med Sci,* 61 (Pt 3)**,** 355-69.

GERMAIN, M. A., HATTON, A., WILLIAMS, S., MATTHEWS, J. B., STONE, M. H., FISHER, J. & INGHAM, E. 2003. Comparison of the cytotoxicity of clinically relevant cobalt-chromium and alumina ceramic wear particles in vitro. *Biomaterials,* 24**,** 469-79.

GILBERT, J. L., BUCKLEY, C. A., JACOBS, J. J., BERTIN, K. C. & ZERNICH, M. R. 1994. Intergranular corrosion-fatigue failure of cobalt-alloy femoral stems. A failure analysis of two implants. *J Bone Joint Surg Am,* 76**,** 110-5.

GILL, I. P., WEBB, J., SLOAN, K. & BEAVER, R. J. 2012. Corrosion at the neck-stem junction as a cause of metal ion release and pseudotumour formation. *J Bone Joint Surg Br,* 94**,** 895-900.

GONZALEZ, L., DE SANTIS PUZZONIA, M., RICCI, R., AURELI, F., GUARGUAGLINI, G., CUBADDA, F., LEYNS, L., CUNDARI, E. & KIRSCH-VOLDERS, M. 2015. Amorphous silica nanoparticles alter microtubule dynamics and cell migration. *Nanotoxicology,* 9**,** 729-36.

GOODE, A. E., PERKINS, J. M., SANDISON, A., KARUNAKARAN, C., CHENG, H., WALL, D., SKINNER, J. A., HART, A. J., PORTER, A. E., MCCOMB, D. W. & RYAN, M. P. 2012. Chemical speciation of nanoparticles surrounding metal-on-metal hips.

*Chem Commun (Camb),* 48**,** 8335-7.

GOODMAN, S. B. 2007. Wear particles, periprosthetic osteolysis and the immune system. *Biomaterials,* 28**,** 5044-8.

GRABHER, C., CLIFFE, A., MIURA, K., HAYFLICK, J., PEPPERKOK, R., RORTH, P. & WITTBRODT, J. 2007. Birth and life of tissue macrophages and their migration in embryogenesis and inflammation in medaka. *J Leukoc Biol,* 81**,** 263-71.

GRAMMATOPOULOS, G., PANDIT, H., KWON, Y. M., GUNDLE, R., MCLARDY-SMITH, P., BEARD, D. J., MURRAY, D. W. & GILL, H. S. 2009. Hip resurfacings revised for inflammatory pseudotumour have a poor outcome. *J Bone Joint Surg Br,* 91**,** 1019-24.

GRUBL, A., MARKER, M., BRODNER, W., GIUREA, A., HEINZE, G., MEISINGER, V., ZEHETGRUBER, H. & KOTZ, R. 2007. Long-term follow-up of metal-on-metal total hip replacement. *J Orthop Res,* 25**,** 841-8.

HADDAD, F. S., THAKRAR, R. R., HART, A. J., SKINNER, J. A., NARGOL, A. V., NOLAN, J. F., GILL, H. S., MURRAY, D. W., BLOM, A. W. & CASE, C. P. 2011. Metal-on-metal bearings: the evidence so far. *J Bone Joint Surg Br,* 93**,** 572-9.

HANNA, S. & EL-SIBAI, M. 2013. Signaling networks of Rho GTPases in cell motility. *Cell Signal,* 25**,** 1955-61.

HARRIS, G. K. & SHI, X. L. 2003. Signaling by carcinogenic metals and metal-induced reactive oxygen species. *Mutation Research-Fundamental and Molecular Mechanisms of Mutagenesis,* 533**,** 183-200.

HENDRIX, R. W., WIXSON, R. L., RANA, N. A. & ROGERS, L. F. 1983. Arthrography after total hip arthroplasty: a modified technique used in the diagnosis of pain. *Radiology,* 148**,** 647-52.

HINZ, B. 2010. The myofibroblast: Paradigm for a mechanically active cell. *Journal of Biomechanics,* 43**,** 146-155.

HIRONAKA, K., SAKAIDA, I., MATSUMURA, Y., KAINO, S., MIYAMOTO, K. & OKITA, K. 2000. Enhanced interstitial collagenase (matrix metalloproteinase-13) production of Kupffer cell by gadolinium chloride prevents pig serum-induced rat liver fibrosis.

*Biochemical and Biophysical Research Communications,* 267**,** 290-295.

HOTHI, H. S., BERBER, R., WHITTAKER, R. K., BLUNN, G. W., SKINNER, J. A. & HART, A. J. 2016. The Relationship Between Cobalt/Chromium Ratios and the High Prevalence of Head-Stem Junction Corrosion in Metal-on-Metal Total Hip Arthroplasty. *J Arthroplasty,* 31**,** 1123-7.

HOTHI, H. S., KENDOFF, D., LAUSMANN, C., HENCKEL, J., GEHRKE, T., SKINNER, J. & HART, A. 2017. Clinically insignificant trunnionosis in large-diameter metal-on-polyethylene total hip arthroplasty. *Bone Joint Res,* 6**,** 52-56.

HOU, Y., CAI, K., LI, J., CHEN, X., LAI, M., HU, Y., LUO, Z., DING, X. & XU, D. 2013. Effects of titanium nanoparticles on adhesion, migration, proliferation, and differentiation of mesenchymal stem cells. *Int J Nanomedicine,* 8**,** 3619-30.

HUBBERT, C., GUARDIOLA, A., SHAO, R., KAWAGUCHI, Y., ITO, A., NIXON, A., YOSHIDA, M., WANG, X. F. & YAO, T. P. 2002. HDAC6 is a microtubule-associated deacetylase. *Nature,* 417**,** 455-8.

HUMPHREY, J. D., DUFRESNE, E. R. & SCHWARTZ, M. A. 2014. Mechanotransduction and extracellular matrix homeostasis. *Nat Rev Mol Cell Biol,* 15**,** 802-12.

ILIC, D., FURUTA, Y., KANAZAWA, S., TAKEDA, N., SOBUE, K., NAKATSUJI, N., NOMURA, S., FUJIMOTO, J., OKADA, M. & YAMAMOTO, T. 1995. Reduced cell motility and enhanced focal adhesion contact formation in cells from FAK-deficient mice. *Nature,* 377**,** 539-44.

ISKRATSCH, T., WOLFENSON, H. & SHEETZ, M. P. 2014. Appreciating force and shape-the rise of mechanotransduction in cell biology. *Nat Rev Mol Cell Biol,* 15**,** 825-33.

JACOBS, J. J., HALLAB, N. J., SKIPOR, A. K. & URBAN, R. M. 2003. Metal degradation products: a cause for concern in metal-metal bearings? *Clin Orthop Relat Res***,** 139-47.

JENNINGS, J. M., DENNIS, D. A. & YANG, C. C. 2016. Corrosion of the Head-neck Junction After Total Hip Arthroplasty. *Journal of the American Academy of Orthopaedic Surgeons,* 24**,** 349-356.

JENSEN, E. C. 2013. Quantitative Analysis of Histological Staining and Fluorescence Using

ImageJ. *Anatomical Record-Advances in Integrative Anatomy and Evolutionary Biology,* 296**,** 378-381.

JOMOVA, K. & VALKO, M. 2011. Advances in metal-induced oxidative stress and human disease. *Toxicology,* 283**,** 65-87.

JONES, G. E. 2000. Cellular signaling in macrophage migration and chemotaxis. *J Leukoc Biol,* 68**,** 593-602.

JONES, G. E., ALLEN, W. E. & RIDLEY, A. J. 1998. The Rho GTPases in macrophage motility and chemotaxis. *Cell Adhes Commun,* 6**,** 237-45.

JORDANA, M., SARNSTRAND, B., SIME, P. J. & RAMIS, I. 1994. Immune-inflammatory functions of fibroblasts. *Eur Respir J,* 7**,** 2212-22.

KAMIYA, T., HARA, H., YAMADA, H., IMAI, H., INAGAKI, N. & ADACHI, T. 2008. Cobalt chloride decreases EC-SOD expression through intracellular ROS generation and p38-MAPK pathways in COS7 cells. *Free Radical Research,* 42**,** 949-956.

KANAJI, A., CAICEDO, M. S., VIRDI, A. S., SUMNER, D. R., HALLAB, N. J. & SENA, K. 2009. Co-Cr-Mo alloy particles induce tumor necrosis factor alpha production in MLO-Y4 osteocytes: a role for osteocytes in particle-induced inflammation. *Bone,* 45**,** 528-33.

KAUFMAN, A. M., ALABRE, C. I., RUBASH, H. E. & SHANBHAG, A. S. 2008. Human macrophage response to UHMWPE, TiAlV, CoCr, and alumina particles: analysis of multiple cytokines using protein arrays. *J Biomed Mater Res A,* 84**,** 464-74.

KLEIN, A. B., WITONSKY, S. G., AHMED, S. A., HOLLADAY, S. D., GOGAL, R. M., JR., LINK, L. & REILLY, C. M. 2006. Impact of different cell isolation techniques on lymphocyte viability and function. *J Immunoassay Immunochem,* 27**,** 61-76.

KONIGS, V., JENNINGS, R., VOGL, T., HORSTHEMKE, M., BACHG, A. C., XU, Y., GROBE, K., BRAKEBUSCH, C., SCHWAB, A., BAHLER, M., KNAUS, U. G. & HANLEY, P. J. 2014. Mouse macrophages completely lacking Rho subfamily GTPases (RhoA, RhoB, and RhoC) have severe lamellipodial retraction defects, but robust chemotactic navigation and altered motility. *J Biol Chem,* 289**,** 30772-84.

KOROVESSIS, P., PETSINIS, G., REPANTI, M. & REPANTIS, T. 2006. Metallosis after contemporary metal-on-metal total hip arthroplasty. Five to nine-year follow-up. *J Bone Joint Surg Am,* 88**,** 1183-91.

KOVACIK, M. W., MOSTARDI, R. A., NEAL, D. R., BEAR, T. F., ASKEW, M. J., BENDER, E. T., WALKER, J. I. & RAMSIER, R. D. 2008. Differences in the surface composition of seemingly similar F75 cobalt-chromium micron-sized particulates can affect synovial fibroblast viability. *Colloids Surf B Biointerfaces,* 65**,** 269-75.

KUHTA, M., PAVLIN, D., SLAJ, M., VARGA, S., LAPTER-VARGA, M. & SLAJ, M. 2009. Type of archwire and level of acidity: effects on the release of metal ions from orthodontic appliances. *Angle Orthod,* 79**,** 102-10.

KWON, Y. M., KHORMAEE, S., LINCOLN, M. H., TSAI, T. Y., FREIBERG, A. A. & RUBASH, H. E. 2016. Asymptomatic Pseudotumors in Patients with Taper Corrosion of a Dual-Taper Modular Femoral Stem MARS-MRI and Metal Ion Study. *Journal of Bone and Joint Surgery-American Volume,* 98.

KWON, Y. M., XIA, Z., GLYN-JONES, S., BEARD, D., GILL, H. S. & MURRAY, D. W. 2009. Dose-dependent cytotoxicity of clinically relevant cobalt nanoparticles and ions on macrophages in vitro. *Biomed Mater,* 4**,** 025018.

LANGTON, D., AHMED, I., AVERY, P., BONE, M., COOKE, N., DEEHAN, D., DUFFY, P., FOGUET, P., GREEN, S., HOLLAND, J., JAFRI, A., LONGSTAFF, L., LORD, J., LOUGHEAD, J., MEEK, R. M., MURRAY, H., NANU, A., NARGOL, A. V., SCHOLES, S. C., SIDAGINAMALE, R. P., WALLER, S. & JOYCE, T. 2017a. Investigation of Taper Failure in a Contemporary Metal-on-Metal Hip Arthroplasty System Through Examination of Unused and Explanted Prostheses. *J Bone Joint Surg Am,* 99**,** 427-436.

LANGTON, D. J., JOYCE, T. J., JAMESON, S. S., LORD, J., VAN ORSOUW, M., HOLLAND, J. P., NARGOL, A. V. & DE SMET, K. A. 2011. Adverse reaction to metal debris following hip resurfacing: the influence of component type, orientation and volumetric wear. *J Bone Joint Surg Br,* 93**,** 164-71.

LANGTON, D. J., SIDAGINAMALE, R. P., JOYCE, T. J., MEEK, R. D., BOWSHER, J. G., DEEHAN, D., NARGOL, A. V. F. & HOLLAND, J. P. 2017b. A comparison study of stem taper material loss at similar and mixed metal head-neck taper junctions. *Bone Joint J,* 99-B**,** 1304-1312.

LAVIGNE, M., BELZILE, E. L., ROY, A., MORIN, F., AMZICA, T. & VENDITTOLI, P. A. 2011. Comparison of whole-blood metal ion levels in four types of metal-on-metal large-diameter femoral head total hip arthroplasty: the potential influence of the adapter sleeve. *J Bone Joint Surg Am,* 93 Suppl 2**,** 128-36.

LE CLAINCHE, C. & CARLIER, M. F. 2008. Regulation of actin assembly associated with protrusion and adhesion in cell migration. *Physiological Reviews,* 88**,** 489-513.

LEE, S. H., BRENNAN, F. R., JACOBS, J. J., URBAN, R. M., RAGASA, D. R. & GLANT, T. T. 1997. Human monocyte/macrophage response to cobalt-chromium corrosion products and titanium particles in patients with total joint replacements. *J Orthop Res,* 15**,** 40-9.

LEONARD, S., GANNETT, P. M., ROJANASAKUL, Y., SCHWEGLER-BERRY, D., CASTRANOVA, V., VALLYATHAN, V. & SHI, X. 1998. Cobalt-mediated generation of reactive oxygen species and its possible mechanism. *J Inorg Biochem,* 70**,** 239-44.

LINDER, S. & AEPFELBACHER, M. 2003. Podosomes: adhesion hot-spots of invasive cells. *Trends Cell Biol,* 13**,** 376-85.

LINDER, S., NELSON, D., WEISS, M. & AEPFELBACHER, M. 1999. Wiskott-Aldrich syndrome protein regulates podosomes in primary human macrophages. *Proc Natl Acad Sci U S A,* 96**,** 9648-53.

LUCARELLI, M., GATTI, A. M., SAVARINO, G., QUATTRONI, P., MARTINELLI, L., MONARI, E. & BORASCHI, D. 2004. Innate defence functions of macrophages can be biased by nano-sized ceramic and metallic particles. *Eur Cytokine Netw,* 15**,** 339-46.

MADALA, S. K., PESCE, J. T., RAMALINGAM, T. R., WILSON, M. S., MINNICOZZI, S., CHEEVER, A. W., THOMPSON, R. W., MENTINK-KANE, M. M. & WYNN, T. A. 2010. Matrix Metalloproteinase 12-Deficiency Augments Extracellular Matrix

Degrading Metalloproteinases and Attenuates IL-13-Dependent Fibrosis. *Journal of Immunology,* 184**,** 3955-3963.

MADL, A. K., KOVOCHICH, M., LIONG, M., FINLEY, B. L., PAUSTENBACH, D. J. & OBERDORSTER, G. 2015a. Toxicology of wear particles of cobalt-chromium alloy metal-on-metal hip implants Part II: Importance of physicochemical properties and dose in animal and in vitro studies as a basis for risk assessment. *Nanomedicine,* 11**,** 1285-98.

MADL, A. K., LIONG, M., KOVOCHICH, M., FINLEY, B. L., PAUSTENBACH, D. J. & OBERDORSTER, G. 2015b. Toxicology of wear particles of cobalt-chromium alloy metal-on-metal hip implants Part I: physicochemical properties in patient and simulator studies. *Nanomedicine,* 11**,** 1201-15.

MARTIEL, J. L., LEAL, A., KURZAWA, L., BALLAND, M., WANG, I., VIGNAUD, T., TSENG, Q. & THERY, M. 2015. Measurement of cell traction forces with ImageJ. *Methods Cell Biol,* 125**,** 269-87.

MATHARU, G. S., PANDIT, H. G., MURRAY, D. W. & JUDGE, A. 2016. Adverse reactions to metal debris occur with all types of hip replacement not just metal-on-metal hips: a retrospective observational study of 3340 revisions for adverse reactions to metal debris from the National Joint Registry for England, Wales, Northern Ireland and the Isle of Man. *BMC Musculoskelet Disord,* 17**,** 495.

MATTHIES, A. K., RACASAN, R., BILLS, P., BLUNT, L., CRO, S., PANAGIOTIDOU, A., BLUNN, G., SKINNER, J. & HART, A. J. 2013. Material loss at the taper junction of retrieved large head metal-on-metal total hip replacements. *J Orthop Res,* 31**,** 1677-85.

MAYOR, R. & ETIENNE-MANNEVILLE, S. 2016. The front and rear of collective cell migration. *Nat Rev Mol Cell Biol,* 17**,** 97-109.

MCGRATH, J. L. 2007. Cell spreading: the power to simplify. *Curr Biol,* 17**,** R357-8.

MCGRORY, B. J., PAYSON, A. M. & MACKENZIE, J. A. 2017. Elevated Intra-Articular Cobalt and Chromium Levels in Mechanically Assisted Crevice Corrosion in Metal-on-Polyethylene Total Hip Arthroplasty. *J Arthroplasty,* 32**,** 1654-1658.

MENG, T. C., FUKADA, T. & TONKS, N. K. 2002. Reversible oxidation and inactivation of protein tyrosine phosphatases in vivo. *Molecular Cell,* 9**,** 387-399.

MISTRY, J. B., CHUGHTAI, M., ELMALLAH, R. K., DIEDRICH, A., LE, S., THOMAS, M. & MONT, M. A. 2016. Trunnionosis in total hip arthroplasty: a review. *J Orthop Traumatol,* 17**,** 1-6.

MITTAL, M., SIDDIQUI, M. R., TRAN, K., REDDY, S. P. & MALIK, A. B. 2014. Reactive Oxygen Species in Inflammation and Tissue Injury. *Antioxidants & Redox Signaling,* 20**,** 1126-1167.

MONTEILLER, C., TRAN, L., MACNEE, W., FAUX, S., JONES, A., MILLER, B. & DONALDSON, K. 2007. The pro-inflammatory effects of low-toxicity low-solubility particles, nanoparticles and fine particles, on epithelial cells in vitro: the role of surface area. *Occup Environ Med,* 64**,** 609-15.

MORLOCK, M. M., BISHOP, N., ZUSTIN, J., HAHN, M., RUTHER, W. & AMLING, M. 2008. Modes of implant failure after hip resurfacing: morphological and wear analysis of 267 retrieval specimens. *J Bone Joint Surg Am,* 90 Suppl 3**,** 89-95.

MOUSSAVI, R. S., KELLEY, C. A. & ADELSTEIN, R. S. 1993. Phosphorylation of Vertebrate Nonmuscle and Smooth-Muscle Myosin Heavy-Chains and Light-Chains. *Molecular and Cellular Biochemistry,* 128**,** 219-227.

MURPHY, D. A. & COURTNEIDGE, S. A. 2011. The 'ins' and 'outs' of podosomes and invadopodia: characteristics, formation and function. *Nat Rev Mol Cell Biol,* 12**,** 413-26.

MYLLYHARJU, J. & KIVIRIKKO, K. I. 2004. Collagens, modifying enzymes and their mutations in humans, flies and worms. *Trends in Genetics,* 20**,** 33-43.

NATIONAL JOINT REGISTRY FOR ENGLAND, W. A. N. I. 2010. 7th annual report, 2010.

NATIONAL JOINT REGISTRY FOR ENGLAND, W. A. N. I. 2017. 14th annual report, 2017.

NATU, S., SIDAGINAMALE, R. P., GANDHI, J., LANGTON, D. J. & NARGOL, A. V. 2012a. Adverse reactions to metal debris: histopathological features of periprosthetic soft tissue reactions seen in association with failed metal on metal hip arthroplasties. *J Clin*

*Pathol,* 65**,** 409-18.

NATU, S., SIDAGINAMALE, R. P., GANDHI, J., LANGTON, D. J. & NARGOL, A. V. F. 2012b. Adverse reactions to metal debris: histopathological features of periprosthetic soft tissue reactions seen in association with failed metal on metal hip arthroplasties. *Journal of Clinical Pathology,* 65**,** 409-418.

NEGASH, A. A., RAMOS, H. J., CROCHET, N., LAU, D. T., DOEHLE, B., PAPIC, N., DELKER, D. A., JO, J., BERTOLETTI, A., HAGEDORN, C. H. & GALE, M., JR. 2013. IL-1beta production through the NLRP3 inflammasome by hepatic macrophages links hepatitis C virus infection with liver inflammation and disease. *PLoS Pathog,* 9**,** e1003330.

NICH, C., TAKAKUBO, Y., PAJARINEN, J., AINOLA, M., SALEM, A., SILLAT, T., RAO, A. J., RASKA, M., TAMAKI, Y., TAKAGI, M., KONTTINEN, Y. T., GOODMAN, S. B. & GALLO, J. 2013. Macrophages-Key cells in the response to wear debris from joint replacements. *Journal of Biomedical Materials Research Part A,* 101**,** 3033-3045.

NYGA, A., HART, A. & TETLEY, T. D. 2015. Importance of the HIF pathway in cobalt nanoparticle-induced cytotoxicity and inflammation in human macrophages. *Nanotoxicology,* 9**,** 905-17.

OBERDORSTER, G., OBERDORSTER, E. & OBERDORSTER, J. 2005. Nanotoxicology: an emerging discipline evolving from studies of ultrafine particles. *Environ Health Perspect,* 113**,** 823-39.

ORHUE, V., KANAJI, A., CAICEDO, M. S., VIRDI, A. S., SUMNER, D. R., HALLAB, N. J., JAHR, H. & SENA, K. 2011. Calcineurin/nuclear factor of activated T cells (NFAT) signaling in cobalt-chromium-molybdenum (CoCrMo) particles-induced tumor necrosis factor-alpha (TNFalpha) secretion in MLO-Y4 osteocytes. *J Orthop Res,* 29**,** 1867-73.

OSMA-GARCIA, I. C., PUNZON, C., FRESNO, M. & DIAZ-MUNOZ, M. D. 2016. Dose-dependent effects of prostaglandin E2 in macrophage adhesion and migration. *Eur J Immunol,* 46**,** 677-88.

OSTA, B., BENEDETTI, G. & MIOSSEC, P. 2014. Classical and Paradoxical Effects of TNF-alpha on Bone Homeostasis. *Front Immunol,* 5**,** 48.

PAN, Z., LEE, W., SLUTSKY, L., CLARK, R. A., PERNODET, N. & RAFAILOVICH, M. H. 2009. Adverse effects of titanium dioxide nanoparticles on human dermal fibroblasts and how to protect cells. *Small,* 5**,** 511-20.

PANDIT, H., GLYN-JONES, S., MCLARDY-SMITH, P., GUNDLE, R., WHITWELL, D., GIBBONS, C. L., OSTLERE, S., ATHANASOU, N., GILL, H. S. & MURRAY, D. W. 2008. Pseudotumours associated with metal-on-metal hip resurfacings. *J Bone Joint Surg Br,* 90**,** 847-51.

PAPAGEORGIOU, I., BROWN, C., SCHINS, R., SINGH, S., NEWSON, R., DAVIS, S., FISHER, J., INGHAM, E. & CASE, C. P. 2007. The effect of nano- and micron-sized particles of cobalt-chromium alloy on human fibroblasts in vitro. *Biomaterials,* 28**,** 2946-58.

PAPIS, E., GORNATI, R., PRATI, M., PONTI, J., SABBIONI, E. & BERNARDINI, G. 2007. Gene expression in nanotoxicology research: analysis by differential display in BALB3T3 fibroblasts exposed to cobalt particles and ions. *Toxicol Lett,* 170**,** 185-92.

PARK, Y. M., FEBBRAIO, M. & SILVERSTEIN, R. L. 2009. CD36 modulates migration of mouse and human macrophages in response to oxidized LDL and may contribute to macrophage trapping in the arterial intima. *J Clin Invest,* 119**,** 136-45.

PARRY, M. C., BHABRA, G., SOOD, A., MACHADO, F., CARTWRIGHT, L., SAUNDERS, M., INGHAM, E., NEWSON, R., BLOM, A. W. & CASE, C. P. 2010. Thresholds for indirect DNA damage across cellular barriers for orthopaedic biomaterials. *Biomaterials,* 31**,** 4477-83.

PATEL, B., GREGORY FAVARO, FAWAD INAM, MICHAEL J. REECE, ARASH ANGADJI, WILLIAM BONFIELD, JIE HUANG, AND MOHAN EDIRISINGHE 2012. Cobalt-based orthopaedic alloys: Relationship between forming route, microstructure and tribological performance. *Materials Science and Engineering: C*.

PATI, R., DAS, I., MEHTA, R. K., SAHU, R. & SONAWANE, A. 2016. Zinc-Oxide

Nanoparticles Exhibit Genotoxic, Clastogenic, Cytotoxic and Actin Depolymerization Effects by Inducing Oxidative Stress Responses in Macrophages and Adult Mice. *Toxicol Sci,* 150**,** 454-72.

PETIT, A., MWALE, F., TKACZYK, C., ANTONIOU, J., ZUKOR, D. J. & HUK, O. L. 2006. Cobalt and chromium ions induce nitration of proteins in human U937 macrophages in vitro. *J Biomed Mater Res A,* 79**,** 599-605.

PETIT, A., MWALE, F., ZUKOR, D. J., CATELAS, I., ANTONIOU, J. & HUK, O. L. 2004. Effect of cobalt and chromium ions on bcl-2, bax, caspase-3, and caspase-8 expression in human U937 macrophages. *Biomaterials,* 25**,** 2013-2018.

PLUMMER, D. R., BERGER, R. A., PAPROSKY, W. G., SPORER, S. M., JACOBS, J. J. & DELLA VALLE, C. J. 2016. Diagnosis and Management of Adverse Local Tissue Reactions Secondary to Corrosion at the Head-Neck Junction in Patients With Metal on Polyethylene Bearings. *Journal of Arthroplasty,* 31**,** 264-268.

POSADA, O. M., GILMOUR, D., TATE, R. J. & GRANT, M. H. 2014. CoCr wear particles generated from CoCr alloy metal-on-metal hip replacements, and cobalt ions stimulate apoptosis and expression of general toxicology-related genes in monocyte-like U937 cells. *Toxicol Appl Pharmacol,* 281**,** 125-35.

POSADA, O. M., TATE, R. J. & GRANT, M. H. 2015. Effects of CoCr metal wear debris generated from metal-on-metal hip implants and Co ions on human monocyte-like U937 cells. *Toxicol In Vitro,* 29**,** 271-80.

QUEALLY, J. M., DEVITT, B. M., BUTLER, J. S., MALIZIA, A. P., MURRAY, D., DORAN, P. P. & O'BYRNE, J. M. 2009. Cobalt Ions Induce Chemokine Secretion in Primary Human Osteoblasts. *Journal of Orthopaedic Research,* 27**,** 855-864.

RAFIQ, N. B. M., LIEU, Z. Z., JIANG, T. T., YU, C. H., MATSUDAIRA, P., JONES, G. E. & BERSHADSKY, A. D. 2017. Podosome assembly is controlled by the GTPase ARF1 and its nucleotide exchange factor ARNO. *Journal of Cell Biology,* 216**,** 181-197.

RAGHUNATHAN, V. K., DEVEY, M., HAWKINS, S., HAILS, L., DAVIS, S. A., MANN, S., CHANG, I. T., INGHAM, E., MALHAS, A., VAUX, D. J., LANE, J. D. & CASE, C.

P. 2013. Influence of particle size and reactive oxygen species on cobalt chrome nanoparticle-mediated genotoxicity. *Biomaterials,* 34**,** 3559-70.

RATNER, B. D., HOFFMAN, A. S., SCHOEN, F. J. & LEMONS, J. E. 2012. *Biomaterials Science: An Introduction to Materials in Medicine*, Elsevier Science.

REDDY, G. K. & ENWEMEKA, C. S. 1996. A simplified method for the analysis of hydroxyproline in biological tissues. *Clin Biochem,* 29**,** 225-9.

RHEE, S. 2009. Fibroblasts in three dimensional matrices: cell migration and matrix remodeling. *Exp Mol Med,* 41**,** 858-65.

RHEE, S. & GRINNELL, F. 2007. Fibroblast mechanics in 3D collagen matrices. *Adv Drug Deliv Rev,* 59**,** 1299-305.

RIDLEY, A. J. 2015. Rho GTPase signalling in cell migration. *Curr Opin Cell Biol,* 36**,** 103-12.

RIDLEY, A. J., SCHWARTZ, M. A., BURRIDGE, K., FIRTEL, R. A., GINSBERG, M. H., BORISY, G., PARSONS, J. T. & HORWITZ, A. R. 2003. Cell migration: integrating signals from front to back. *Science,* 302**,** 1704-9.

SAMELKO, L., CAICEDO, M. S., LIM, S. J., DELLA-VALLE, C., JACOBS, J. & HALLAB, N. J. 2013. Cobalt-alloy implant debris induce HIF-1alpha hypoxia associated responses: a mechanism for metal-specific orthopedic implant failure. *PLoS One,* 8**,** e67127.

SAPPINO, A. P., SCHURCH, W. & GABBIANI, G. 1990. Differentiation repertoire of fibroblastic cells: expression of cytoskeletal proteins as marker of phenotypic modulations. *Lab Invest,* 63**,** 144-61.

SAUER, H., WARTENBERG, M. & HESCHELER, J. 2001. Reactive oxygen species as intracellular messengers during cell growth and differentiation. *Cellular Physiology and Biochemistry,* 11**,** 173-186.

SCHARF, B., CLEMENT, C. C., ZOLLA, V., PERINO, G., YAN, B., ELCI, S. G., PURDUE, E., GOLDRING, S., MACALUSO, F., COBELLI, N., VACHET, R. W. & SANTAMBROGIO, L. 2014. Molecular analysis of chromium and cobalt-related

toxicity. *Sci Rep,* 4**,** 5729.

SCHINDELIN, J., ARGANDA-CARRERAS, I., FRISE, E., KAYNIG, V., LONGAIR, M., PIETZSCH, T., PREIBISCH, S., RUEDEN, C., SAALFELD, S., SCHMID, B., TINEVEZ, J. Y., WHITE, D. J., HARTENSTEIN, V., ELICEIRI, K., TOMANCAK, P. & CARDONA, A. 2012. Fiji: an open-source platform for biological-image analysis. *Nat Methods,* 9**,** 676-82.

SCHRAMP, M., YING, O., KIM, T. Y. & MARTIN, G. S. 2008. ERK5 promotes Src-induced podosome formation by limiting Rho activation. *Journal of Cell Biology,* 181**,** 1195-1210.

SHI, C. & PAMER, E. G. 2011. Monocyte recruitment during infection and inflammation. *Nat Rev Immunol,* 11**,** 762-74.

SMITH, L. J., HOLMES, A. L., KANDPAL, S. K., MASON, M. D., ZHENG, T. & WISE, J. P., SR. 2014. The cytotoxicity and genotoxicity of soluble and particulate cobalt in human lung fibroblast cells. *Toxicol Appl Pharmacol,* 278**,** 259-65.

SOROKIN, L. 2010. The impact of the extracellular matrix on inflammation. *Nat Rev Immunol,* 10**,** 712-23.

STOEGER, T., REINHARD, C., TAKENAKA, S., SCHROEPPEL, A., KARG, E., RITTER, B., HEYDER, J. & SCHULZ, H. 2006. Instillation of six different ultrafine carbon particles indicates a surface area threshold dose for acute lung inflammation in mice. *Environ Health Perspect,* 114**,** 328-33.

STROKA, K. M. & ARANDA-ESPINOZA, H. 2011. Endothelial cell substrate stiffness influences neutrophil transmigration via myosin light chain kinase-dependent cell contraction. *Blood,* 118**,** 1632-40.

SULLIVAN, D. E., FERRIS, M., POCIASK, D. & BRODY, A. R. 2005. Tumor necrosis factor-alpha induces transforming growth factor-beta1 expression in lung fibroblasts through the extracellular signal-regulated kinase pathway. *Am J Respir Cell Mol Biol,* 32**,** 342-9.

SUTPHEN, S. A., MACLAUGHLIN, L. H., MADSEN, A. A., RUSSELL, J. H. & MCSHANE,

M. A. 2016. Prevalence of Pseudotumor in Patients After Metal-On-Metal Hip Arthroplasty Evaluated with Metal Ion Analysis and MARS-MRI. *Journal of Arthroplasty,* 31**,** 260-263.

TANG, A. T., CAMPBELL, W. B. & NITHIPATIKOM, K. 2012. ROCK1 feedback regulation of the upstream small GTPase RhoA. *Cell Signal,* 24**,** 1375-80.

TAY, C. Y., CAI, P., SETYAWATI, M. I., FANG, W., TAN, L. P., HONG, C. H., CHEN, X. & LEONG, D. T. 2014a. Nanoparticles strengthen intracellular tension and retard cellular migration. *Nano Lett,* 14**,** 83-8.

TAY, C. Y., CAI, P. Q., SETYAWATI, M. I., FANG, W. R., TAN, L. P., HONG, C. H. L., CHEN, X. D. & LEONG, D. T. 2014b. Nanoparticles Strengthen Intracellular Tension and Retard Cellular Migration. *Nano Letters,* 14**,** 83-88.

THEISS, A. L., SIMMONS, J. G., JOBIN, C. & LUND, P. K. 2005. Tumor necrosis factor (TNF) alpha increases collagen accumulation and proliferation in intestinal myofibroblasts via TNF receptor 2. *J Biol Chem,* 280**,** 36099-109.

TKACZYK, C., HUK, O. L., MWALE, F., ANTONIOU, J., ZUKOR, D. J., PETIT, A. & TABRIZIAN, M. 2010. Investigation of the binding of Cr(III) complexes to bovine and human serum proteins: a proteomic approach. *J Biomed Mater Res A,* 94**,** 214-22.

TOJKANDER, S., GATEVA, G. & LAPPALAINEN, P. 2012. Actin stress fibers--assembly, dynamics and biological roles. *J Cell Sci,* 125**,** 1855-64.

TOMASEK, J. J., GABBIANI, G., HINZ, B., CHAPONNIER, C. & BROWN, R. A. 2002. Myofibroblasts and mechano-regulation of connective tissue remodelling. *Nat Rev Mol Cell Biol,* 3**,** 349-63.

TONDRAVI, M. M., MCKERCHER, S. R., ANDERSON, K., ERDMANN, J. M., QUIROZ, M., MAKI, R. & TEITELBAUM, S. L. 1997. Osteopetrosis in mice lacking haematopoietic transcription factor PU.1. *Nature,* 386**,** 81-4.

TOPOLOVEC, M. & MILOSEV, I. 2014. A comparative study of four bearing couples of the same acetabular and femoral component: a mean follow-up of 11.5 years. *J Arthroplasty,* 29**,** 176-80.

TRACY, L. E., MINASIAN, R. A. & CATERSON, E. J. 2016. Extracellular Matrix and Dermal Fibroblast Function in the Healing Wound. *Adv Wound Care (New Rochelle),* 5**,** 119-136.

TSAOUSI, A., JONES, E. & CASE, C. P. 2010. The in vitro genotoxicity of orthopaedic ceramic (Al2O3) and metal (CoCr alloy) particles. *Mutat Res,* 697**,** 1-9.

VADAY, G. G. & LIDER, O. 2000. Extracellular matrix moieties, cytokines, and enzymes: dynamic effects on immune cell behavior and inflammation. *J Leukoc Biol,* 67**,** 149-59.

VENDITTOLI, P. A., AMZICA, T., ROY, A. G., LUSIGNAN, D., GIRARD, J. & LAVIGNE, M. 2011. Metal Ion release with large-diameter metal-on-metal hip arthroplasty. *J Arthroplasty,* 26**,** 282-8.

VICENTE-MANZANARES, M., MA, X. F., ADELSTEIN, R. S. & HORWITZ, A. R. 2009. Non-muscle myosin II takes centre stage in cell adhesion and migration. *Nature Reviews Molecular Cell Biology,* 10**,** 778-790.

WAHL, S. M., MCCARTNEYFRANCIS, N., ALLEN, J. B., DOUGHERTY, E. B. & DOUGHERTY, S. F. 1990. Macrophage Production of Tgf-Beta and Regulation by Tgf-Beta. *Annals of the New York Academy of Sciences,* 593**,** 188-196.

WANG, B., CHEN, D., GUO, W., LI, Z., LI, Y., ZHOU, X., HUANG, P. & SUN, Z. 2012. Silica nanoparticles suppress fibronectin-mediated adhesion and migration in normal human keratinocytes. *J Nanosci Nanotechnol,* 12**,** 293-9.

WEBER, B. G. 1970. Total hip replacement with rotation-endoprosthesis. [Trunnion-bearing prosthesis]. *Clin Orthop Relat Res,* 72**,** 79-84.

WEISCHENFELDT, J. & PORSE, B. 2008. Bone Marrow-Derived Macrophages (BMM): Isolation and Applications. *CSH Protoc,* 2008**,** pdb prot5080.

WILLERT, H. G., BUCHHORN, G. H., FAYYAZI, A., FLURY, R., WINDLER, M., KOSTER, G. & LOHMANN, C. H. 2005. Metal-on-metal bearings and hypersensitivity in patients with artificial hip joints. A clinical and histomorphological study. *J Bone Joint Surg Am,* 87**,** 28-36.

WILLIAMS, A. R. F. 1989. Chemotaxis and the inhibition of chemotaxis of human neutrophils

in reponse to metal ions. *Journal of Materials Science: Materials in Medicine,* 1**,** 26-32.

WINGSTRAND, H., WINGSTRAND, A. & KRANTZ, P. 1990. Intracapsular and atmospheric pressure in the dynamics and stability of the hip. A biomechanical study. *Acta Orthop Scand,* 61**,** 231-5.

WOODMAN, J. L., JACOBS, J. J., GALANTE, J. O. & URBAN, R. M. 1984. Metal ion release from titanium-based prosthetic segmental replacements of long bones in baboons: a long-term study. *J Orthop Res,* 1**,** 421-30.

WYNN, T. A. 2007. Common and unique mechanisms regulate fibrosis in various fibroproliferative diseases. *Journal of Clinical Investigation,* 117**,** 524-529.

WYNN, T. A., CHAWLA, A. & POLLARD, J. W. 2013. Macrophage biology in development, homeostasis and disease. *Nature,* 496**,** 445-55.

XIA, Z., KWON, Y. M., MEHMOOD, S., DOWNING, C., JURKSCHAT, K. & MURRAY, D. W. 2011. Characterization of metal-wear nanoparticles in pseudotumor following metal-on-metal hip resurfacing. *Nanomedicine,* 7**,** 674-81.

YAN, Y. 2013. *Bio-Tribocorrosion in Biomaterials and Medical Implants*, Elsevier Science.

YANG, J. A., PHAN, H. T., VAIDYA, S. & MURPHY, C. J. 2013. Nanovacuums: nanoparticle uptake and differential cellular migration on a carpet of nanoparticles. *Nano Lett,* 13**,** 2295-302.

ZOU, W. G., YAN, M. D., XU, W. J., HUO, H. R., SUN, L. Y., ZHENG, Z. C. & LIU, X. Y. 2001. Cobalt chloride induces PC12 cells apoptosis through reactive oxygen species and accompanied by AP-1 activation. *Journal of Neuroscience Research,* 64**,** 646-653.

**Appendix 1: Densitometric Analysis using ImageJ**

1. Convert each TIFF file, scanned from a film at a DPI of >300 to an 8-bit Image, in ImageJ, Figure 1.

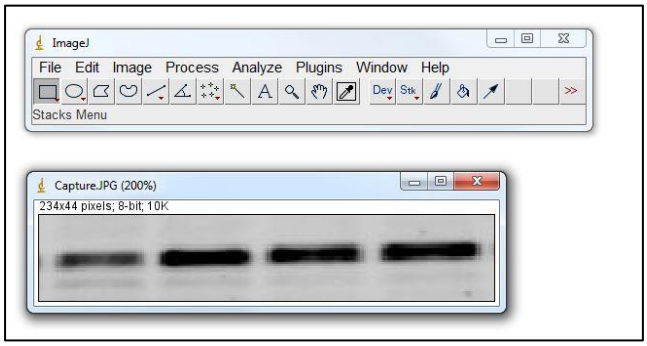


Figure 1

2. Utilising Analyze>Gels>Gel Analyzer Options, select Label with percentages and Invert peaks, Figure 2.

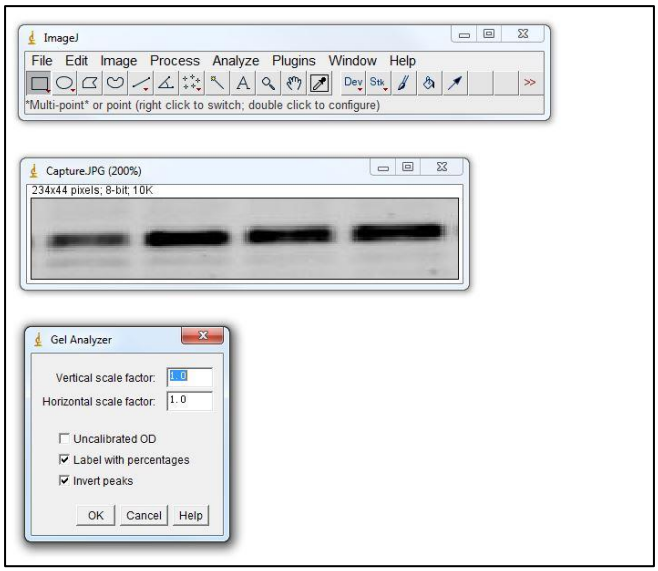


Figure 2

3. Draw a rectangle around the first band and select Analyze>Gels>Select First Lane to designate lane #1. Move the rectangle to the next lane and go to Analyze>Gels>Select Next Lane and continue to do this for each lane (Figures 3 and 4).

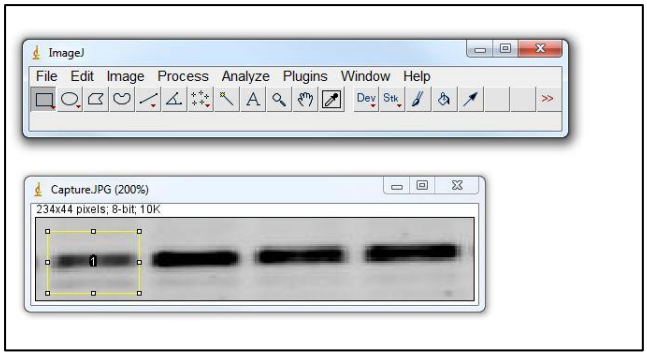


Figure 3

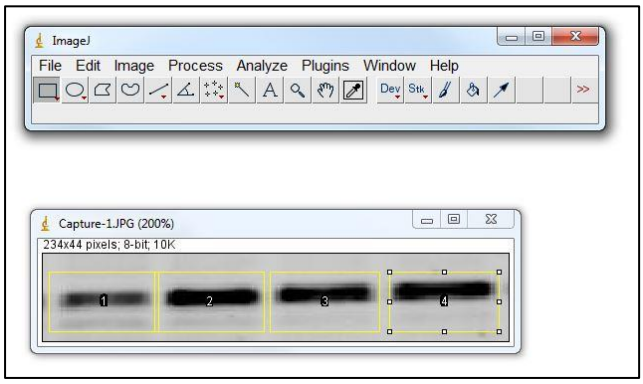


Figure 4

4. When all the lanes have been highlighted, go to Analyze>Gels>plot lanes to bring up a new window displaying a histogram of each lane (Figure 5). Use the line tool to draw a straight line at the bottom of each peak to enclose the area under each peak (Figure 6). When each peak has been enclosed, utilising the magic wand from the tool menu select each peak.

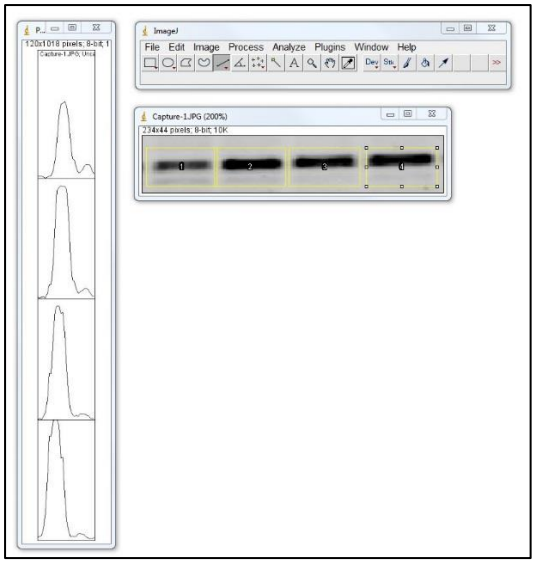


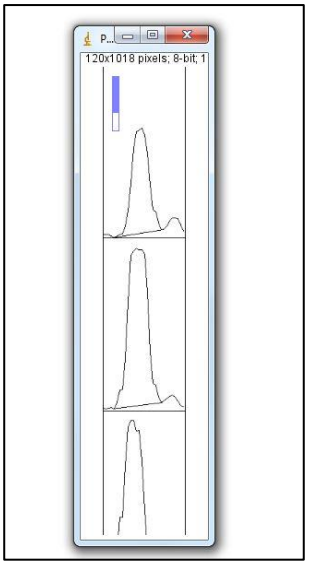


Figure 5 Figure 6

5. Analyse using <u>Analyze>Gels>Label Peaks</u> to provide an area under each peak (Figure 7).

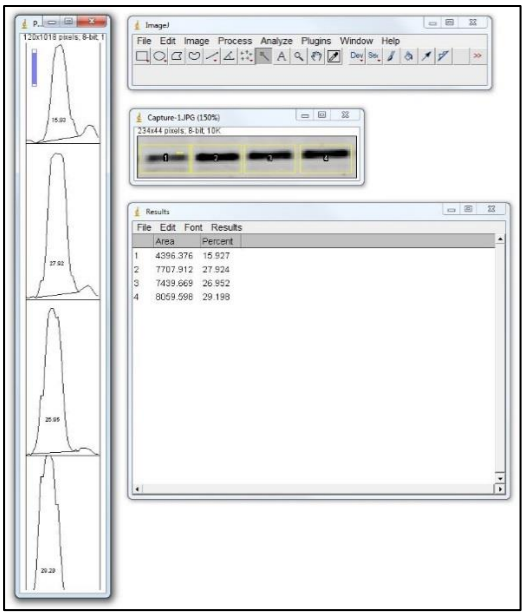


Figure 7

6. Repeat the process for each image before determining the relative density of each band using the control condition.

# Appendix 2: A copy of publication

Acta Biomaterialia 72 (2018) 434–446

Contents lists available at ScienceDirect

Acta Biomaterialia

journal homepage: www.elsevier.com/locate/actabiomat

Full length article

## Cobalt (II) ions and nanoparticles induce macrophage retention by ROS-mediated down-regulation of RhoA expression

Jing Xu [a], Junyao Yang [b], Agata Nyga [c,d], Mazdak Ehteramyan [e], Ana Moraga [e], Yuanhao Wu [a], Lingfang Zeng [e,*], Martin M. Knight [a,*], Julia C. Shelton [a,*]

[a] Institute of Bioengineering, School of Engineering and Materials Science, Queen Mary University of London, London, UK
[b] Department of Laboratory Medicine, Xinhua Hospital, School of Medicine, Shanghai Jiao Tong University, Shanghai 200092, China
[c] Division of Surgery and Interventional Sciences, University College London, London NW3 2QG, United Kingdom
[d] Institute for Bioengineering of Catalonia, 08028 Barcelona, Spain
[e] Cardiovascular Division, Faculty of Life Science and Medicine, King's College London, London SE5 9NU, United Kingdom

ARTICLE INFO

*Article history:*
Received 18 November 2017
Received in revised form 15 March 2018
Accepted 30 March 2018
Available online 9 April 2018

*Keywords:*
Cobalt chromium
Nanoparticles
Wear debris
Macrophage
ROS

ABSTRACT

Histological assessments of synovial tissues from patients with failed CoCr alloy hip prostheses demonstrate extensive infiltration and accumulation of macrophages, often loaded with large quantities of particulate debris. The resulting adverse reaction to metal debris (ARMD) frequently leads to early joint revision. Inflammatory response starts with the recruitment of immune cells and requires the egress of macrophages from the inflamed site for resolution of the reaction. Metal ions ($Co^{2+}$ and $Cr^{3+}$) have been shown to stimulate the migration of T lymphocytes but their effects on macrophages motility are still poorly understood. To elucidate this, we studied *in vitro* and *in vivo* macrophage migration during exposure to cobalt and chromium ions and nanoparticles. We found that cobalt but not chromium significantly reduces macrophage motility. This involves increase in cell spreading, formation of intracellular podosome-type adhesion structures and enhanced cell adhesion to the extracellular matrix (ECM). The formation of podosomes was also associated with the production and activation of matrix metalloproteinase-9 (MMP9) and enhanced ECM degradation. We showed that these were driven by the down-regulation of RhoA signalling through the generation of reactive oxygen species (ROS). These novel findings reveal the key mechanisms driving the wear/corrosion metallic byproducts-induced inflammatory response at non-toxic concentrations.

**Statement of significance**

Adverse tissue responses to metal wear and corrosion products from CoCr alloy implants remain a great challenge to surgeons and patients. Macrophages are the key regulators of these adverse responses to the ions and debris generated. We demonstrated that cobalt, rather than chromium, causes macrophage retention by restructuring the cytoskeleton and inhibiting cell migration via ROS production that affects Rho Family GTPase. This distinctive effect of cobalt on macrophage behaviour can help us understand the pathogenesis of ARMD and the cellular response to cobalt based alloys, which provide useful information for future implant design and biocompatibility testing.
© 2018 Acta Materialia Inc. Published by Elsevier Ltd. This is an open access article under the CC BY-NC-ND license (http://creativecommons.org/licenses/by-nc-nd/4.0/).

### 1. Introduction

Total hip arthroplasty (THA) restores mobility and improves the quality of life in patients suffering from severe osteoarthritis or femoral fractures. In 2015, 83,886 primary hip replacements were conducted in the UK with 8,367 hip revision procedures performed largely due to the aseptic loosening, pain, implant wear and adverse reaction to metal debris (ARMD) [1]. It is expected that these numbers will keep rising due to the ageing of population and an increasing number of implanted prostheses.

Since the mid-1980 s, over one million metal-on-metal (MoM) hip replacement prostheses, made from a cobalt chromium (CoCr) alloy, have been implanted worldwide [2]. These were used for joint replacements in younger, more active patients [3] due to

* Corresponding authors.
*E-mail addresses:* lingfang.zeng@kcl.ac.uk (L. Zeng), m.m.knight@qmul.ac.uk (M.M. Knight), j.shelton@qmul.ac.uk (J.C. Shelton).

https://doi.org/10.1016/j.actbio.2018.03.054
1742-7061/© 2018 Acta Materialia Inc. Published by Elsevier Ltd.
This is an open access article under the CC BY-NC-ND license (http://creativecommons.org/licenses/by-nc-nd/4.0/).

the adverse response to polyethylene particles from the first-generation metal-on-polyethylene (MoP) bearings or from the fracture risk of a ceramic head. However, concerns for these implants became increasingly prominent due to reports of ARMD [4,5]. The metal wear debris and released ions ($Co^{2+}$ and $Cr^{3+}$), which are widely generated in MoM bearings of hip implants, are now also found in patients with MoP bearings due to the mechanically assisted crevice corrosion of modular taper junctions, including head–neck and neck-stem taper interfaces [5–8].

Wear and corrosion particles retrieved from tissues surrounding MoM devices have been shown to be predominantly in the nanometer-size range [4,9]; the particles are generally smaller than 50 nm (range 6–834 nm) with round or irregular morphologies. The wear particles have been generated in hip simulators to have similar size distribution and morphology as recorded clinically, however the *in vitro* studies so far have not established the mechanism behind the adverse local response to these wear products, such as aseptic chronic inflammation and pseudotumour formation [9–12], which is closely associated with pain and implant failure.

Prolonged inflammation results in ARMD at the implant site. First, wear particles and ionic corrosion products are detected and phagocytosed mainly by the tissue-resident macrophages [10] and if phagocytosed in a large number, these wear particles can activate macrophages to release an array of cytokines and chemokines to alarm circulating leucocytes [13]. Leukocytes infiltrating the inflamed tissue, promote recruitment of neutrophils or monocytes that differentiate locally into macrophages, and potentiate the pro-inflammatory environment. At the same time, the resolution of the inflammatory response occurs by removing the dead neutrophils and the egress of inflammatory macrophages from the inflamed tissue to the nearest opening of the draining lymphatics [14]. The undesired response to a MoM implant are frequently found to show soft tissue failure characterized by macrophage predominant infiltration with their massive intake of wear particles [15]. Metal ions ($Co^{2+}$ and $Cr^{3+}$) have been shown to enhance the migration of T lymphocytes independently of circulating cytokines or chemokines resulting in an accumulation of T lymphocytes in the periprosthetic tissues of some patients with CoCr-based implants [16]. However, the mechanism behind the macrophage migration in the presence of both wear debris and ions is largely unknown.

This study aims to reveal the mechanism regulating macrophage migration during exposure to cobalt and chromium compounds, in order to understand the clinical manifestation of a chronic inflammatory response. We have shown that cobalt, but not chromium, affects the migration of macrophages through ROS and RhoA signalling pathways.

## 2. Materials and methods

### 2.1. Particles and ions

Cobalt and chromium nanoparticles were purchased from American Elements (Los Angeles, CA, USA). Cobalt nanoparticles (CoNPs) were composed of 90% cobalt and 10% cobalt (II,III) oxide with a molecular weight of 58.93 and had a diameter of 2–60 nm (data from the company). Chromium nanoparticles (CrNPs) were in the form of chromium oxide ($Cr_2O_3$) nanoparticles with a diameter of 10–30 nm (manufacturer data). Prior to use, the nanoparticles were washed in 100% ethanol for sterilisation and resuspended in sterile $H_20$ at a concentration of 1 mg/ml using a sonicator (pulsed mode, 3 min). Stock solutions (0.1 M) of $Co^{2+}$ and $Cr^{3+}$ ions were freshly prepared by dissolving $CoCl_2{\cdot}6H_2O$ (99.5% purity; Sigma Aldrich) and $CrCl_3{\cdot}6H_2O$ (98% purity; Sigma Aldrich) in sterile $H_20$. These solutions were sterilized by filtration through 0.2 μm pore size sterile syringe filter (Merck Millipore). Stock solutions of cobalt and chromium nanoparticles and ions were further diluted in cell culture medium to achieve the desired concentrations.

### 2.2. Characterization of the cobalt and chromium nanoparticles

Transmission Electron Microscopy (TEM; JEOL JEM-2010, Japan) was employed to observe the morphology of CoNPs and CrNPs as shown in Fig. S1. CoNPs and CrNPs were suspended in pure ethanol and a drop of particle suspension was placed onto the carbon coated grid. The polydispersity index (PDI) and the surface charge of cobalt and chromium nanoparticles in 1640 RPMI medium that were employed in this study were analysed by Zetasizer (Malvern Co., UK).

### 2.3. Cell lines and culture preparation

#### 2.3.1. Human U937 monocytic cell line

Cells from the U937 cell line (passage 6-25, donation from Dr Akihisa Mitani, Imperial College London, UK) were cultured in RPMI 1640 medium (ThermoFisher, USA) supplemented with 10% FBS (Sigma, USA), 1.9 mM L-glutamine, 96 U/ml penicillin, 96 μg/ml streptomycin, 19 mM HEPES buffer, in a humidified atmosphere with 5% $CO_2$ at 37 °C. To induce differentiation into adherent macrophage-like cells, cells were treated with 50 ng/ml PMA (Phorbol 12-myristate 13-acetate, Sigma Aldrich) for 48 h and followed by rest for a further 24 h in complete RPMI 1640 medium prior to further experiments.

#### 2.3.2. Isolation and differentiation of bone marrow-derived macrophages

Bone marrow-derived macrophages (BMDMs) were harvested, pooled and differentiated according to established standard protocols [17]. To review briefly, femurs and tibiae were obtained from 8 of 6–12-week-old C57BL/6 mice. All mice were cared for according to the UK Animal Scientific Procedures Act (1986) and by the Institutional Committee for Use and Care of Laboratory Animals. Experiments were performed under the UK Home Office Personal licence number I56EDA266 and the groups UK Home Office Project Licence number 70/7266. Bone marrow was flushed from femurs and tibiae and bone marrow cells were collected and differentiated in RPMI-1640 complete medium containing macrophage colony-stimulating factor (M-CSF, 50 ng/ml, R&D Systems, Minneapolis, MN, USA) for 7 days.

### 2.4. Cytotoxicity assay

A colourimetric assay, MTS, was performed to assess the effect of cobalt and chromium nanoparticles and ions on macrophage viability using the CellTiter 96® Aqueous One Solution Cell Proliferation Assay (Promega, Southampton, UK). Cells (U937 macrophages or BMDMs) were seeded at a concentration of $5 \times 10^4$ in 96-well plates. For vehicle control, cells were stimulated with complete RMPI medium. After incubation for 6 and 24 h, medium was aspirated and 100 μl of serum-free RPMI medium containing 10% MTS reagent was added to each well. Plates were subsequently incubated for 3 h at 37 °C and the absorbance was read at 490 nm using an Infinite F50 plate reader (Tecan, Switzerland). Five replicates of each exposure were tested and the entire assay was repeated for three separate experiments. The cell viability was determined as a percentage of control cell viability.

### 2.5. Cell motility and migration assays

#### 2.5.1. Single cell motility monitoring

Macrophage migratory ability was first investigated using live cell imaging. Inverted microscope (Lumascope 720, Etaluma, USA) connected to a cell culture incubator was used for live cell imaging to visualise macrophage migration. Time-lapse images of migrating U937 macrophages at a seeded density of $2 \times 10^4$ cells/cm$^2$ in a 24-well plate were collected after 12 h incubation with $Co^{2+}$ (200 μM), $Cr^{3+}$ (400 μM), CoNPs (100 μM) or CrNPs (400 μM). The application of different concentrations of $Co^{2+}$, $Cr^{3+}$, CoNPs and CrNPs, Table 1, was based on the highest concentration that could be delivered whilst maintaining high cell viability, following cell viability tests shown in Fig. S2.

Images were captured every 5 min for 6 h. Migratory properties of individual cells identified from the time-lapse images were then analysed using ImageJ software (n = 25 cells/condition).

#### 2.5.2. Transwell cell migration assay

Cell migration was also investigated using 6.5 mm Transwell chambers with 8 μm pores (Costar, Corning, NY, USA). Briefly, $2 \times 10^5$ harvested U937 macrophages or BMDMs in serum free RPMI 1640 medium were added to the upper chamber of the insert. The lower chamber was filled with 600 μl RPMI 1640 medium with 10% FBS to encourage cell migration down the FBS chemotactic gradient. Cells migration was analysed over a 6-hour period in the presence of $Co^{2+}$ or $Cr^{3+}$ that was added to both the upper and lower well at the required concentration or following 2-hour pretreatment with CoNPs or CrNPs (Table 1). After 6 h treatment, cells remaining on the membrane were fixed with 4% paraformaldehyde (Sigma, USA), stained with crystal violet (Sigma, USA) and counted.

#### 2.5.3. In vivo macrophage migration assay and FACS (flow cytometry) analysis

To demonstrate the validity of the *in vitro* studies, the *in vivo* effect of cobalt ions on mouse macrophage migration was studied. 20 wt C57BL/6 mice were first injected intraperitoneally with 1 ml of 4% thioglycollate (Sigma, USA) to recruit macrophages into the peritoneal cavity. After 4 days, the mice were injected intraperitoneally with 5 μg of CoNPs (10 mice) or PBS (10 control mice). After 12 h, 5 mice from each group were injected with LPS (250 μl; 5 μg/ml) intraperitoneally to induce macrophages migration towards the regional lymph nodes; the remaining 5 mice from each group were injected intraperitoneally with PBS (250 μl) as blank control. After 4 h, the peritoneal cells were harvested by lavage and counted. The macrophages in the lavage were quantified by flow cytometry. Cell suspensions were pre-incubated with anti–CD16/CD32 mAb to block FcγRII/III receptors (BD Pharmingen) on ice for 15 min. After washing the suspension, cells were stained with PE/Cy5 anti-mouse CD11b antibody (Abcam, UK) and FITC anti-mouse F4/80 antibody (Abcam, UK). Stained cells were washed and re-suspended in 200 μl of PBS and analysed using a flow cytometer (BD ACCURI C6) and FlowJo software (TreeStar).

**Table 1**
Concentration of cobalt and chromium applied during the migration tests.

| Treatment | Cell type | |
|---|---|---|
| | U937 macrophages | BMDMs |
| $Co^{2+}$ | 200 μM | 50 μM |
| $Cr^{3+}$ | 400 μM | 200 μM |
| CoNPs | 100 μM | 20 μM |
| CrNPs | 400 μM | 200 μM |

### 2.6. Scanning electron microscope (SEM) analysis

U937 macrophages on the coverslips were fixed in 2.5% glutaraldehyde (Sigma, USA) for 2 h and dehydrated in graded ethanol (50%, 70%, 80%, 90%, 95%, and 100%; 10 min for each). The samples were transferred to critical-point drying with hexamethyldisilazane (Sigma, USA) then coated with a 5 nm thick layer of gold–palladium alloy. The SEM images were obtained with a scanning electron microscope (FEI Quanta 200) at a low voltage (~1 kV).

### 2.7. Immunofluorescence confocal and super resolution microscopy

Treated cells (U937 macrophages or BMDMs) were fixed with 4% paraformaldehyde (Sigma, USA) and washed and permeabilized with 0.5% Triton X-100 and rinsed 3 times with PBS. Nonspecific binding sites were blocked by adding PBS with 1% BSA. The adhesion protein, vinculin, was labelled by incubation at 4 °C, overnight with mouse monoclonal anti-vinculin primary antibody, clone hVIN-1 (1:400, Sigma, USA). Cells were then washed and incubated for 1 h at room temperature in Alexa 488 conjugated anti-Mouse IgG as Secondary Antibody (1:1000, Invitrogen, USA). In separate samples, cellular α-tubulin and acetylated α-tubulin were labelled using rabbit polyclonal anti-α tubulin antibody (1:200, Abcam, UK) and mouse anti-acetylated tubulin, clone 611B-1 (1:2000; Sigma-Aldrich, USA) respectively with Alexa 488 secondary antibodies as above.

To simultaneously label the F-actin, the samples were incubated for 30 mins with 200 μl of rhodamine-conjugated phalloidin (Molecular Probes, USA) in a humidified chamber at room temperature in the dark. Cell nuclei were stained by incubation with 5 μg/ml DAPI (Dojindo, USA) followed by two PBS rinses. Slides were then visualized with a fluorescence microscope (SP2, Leica, Germany) with ×63 objective. Slides were also imaged on a microscope (710 ELYRA PS.1, Zeiss, Germany) with a ×63/1.4NA objective for structural illumination microscopy.

### 2.8. Cell adhesion assay

U937 macrophages were seeded at a concentration of $2 \times 10^5$ cells/well into a 24-well plastic cell culture plate coated with 2% gelatin and treated with 100 μM, 200 μM or 300 μM $Co^{2+}$. After 30 min of incubation, cell culture medium in each well were aspirated and gently rinsed 2 times with warm PBS. Adherent cells of were then imaged (10 fields of each well were randomly selected) with an inverted microscope (DCF420, Leica, Germany) and counted.

### 2.9. Proteolytic activity measurement

#### 2.9.1. In vitro ECM degradation assay

U937 macrophages were seeded onto coverslips coated with FITC-conjugated gelatin, as part of an *in vitro* ECM degradation assay, as previously described [18]. Briefly, glass coverslips were coated with 0.2 mg/ml FITC-gelatin (Molecular Probes, USA) in PBS and fixed with 0.5% glutaraldehyde, washed six times with PBS, then washed once with 70% ethanol/PBS and once with medium. U937 macrophages ($1 \times 10^5$/well) were plated onto the coverslips and incubated at 37 °C in the presence of $Co^{2+}$ (200 μM), CoNPs (100 μM), $Cr^{3+}$ (400 μM) or CrNPs (400 μM) for 24 h, then fixed, processed for F-actin staining with rhodamine-conjugated phalloidin, and observed as described above. The coverslips were examined using a confocal microscope (SP2, Leica, Germany) and the total area that was degraded was measured using ImageJ software [18]. The matrix degradation index was calculated as the ratio between the area of gelatin matrix degraded by treated cells to that degraded by untreated cells.

*2.9.2. Gelatin zymography*

Conditioned media collected from cells treated by cobalt ions (100 μM, 200 μM, 300 μM) and nanoparticles (20 μM, 50 μM and 100 μM) for 24 h were used for gelatin zymography. The supernatants were subjected to electrophoresis in an 8% SDS-PAGE gel co-polymerized with gelatin (1 mg/ml, Sigma, USA). The gelatinolytic activities were detected as transparent bands against the background of Coomassie Brilliant Blue-stained gelatin and quantified using ImageJ software.

*2.10. ROS measurements*

ROS formation was measured using 5-(and 6-)-chloromethyl-2′7′-dichlorodihydrofluorescein diacetate (CM-$H_2$DCFDA, Life technologies, USA). Cells were cultured in black 96-well plates with a clear bottom. After exposure to cobalt, the supernatant was removed and cells were briefly washed with warmed PBS. CM-$H_2$DCFDA was dissolved in anhydrous DMSO to a final concentration of 1 mM and diluted further in Hank's balanced salt solution (HBSS, ThermoFisher, USA). Cells were exposed to 1 μM CM-$H_2$DCFDA for 30 min at 37 °C in the dark. Fluorescence was read at an excitation of 485/20 nm with emission 528/20 nm using a microplate reader (Synergy HT Multi-Mode, Biotek, USA).

*2.11. Protein extraction and immunoblotting*

All lysis buffers were supplemented with 1% protease inhibitor (Sigma Aldrich, USA). Protein extracts were resolved using gradient precast SDS – polyacrylamide gel electrophoresis (Biorad Laboratories Inc, USA), and then electro-transferred onto a nitrocellulose membrane by using Trans-Blot® Turbo™ Transfer System (Biorad Laboratories Inc, USA) for immunoblot analysis. Antibody probing was done as per manufacturers' instructions Antibodies used include anti-RhoA antibody (1:1000, Abcam, UK), anti-CDC42 antibody (1:1000, Abcam, UK), anti-Rac1 antibody (1:1000 Abcam, UK), anti-phospho-MYPT1 (Thr696) antibody (1:1000, Cell Signaling Technology, USA), anti-myosin light chain (phospho S20) antibody (1:1000, Abcam, UK), anti-GAPDH antibody (1:2000, Abcam, UK). Secondary antibodies either IRDye® 800CW Goat anti-Mouse IgG (LI-COR, USA) or IRDye® 800CW Goat anti-Rabbit IgG (LI-COR, USA) were used with dilution of 1:15000. Specific protein bands were detected using Odyssey® CLx Imaging System (LI-COR, USA).

*2.12. Data analysis*

All data are expressed as the mean ± SEM from independent repeat experiments (N = 3) unless otherwise stated. The number of repeat measurement per experiment (n) is indicated in each figure. All statistical differences were analysed with one-way ANOVA or Kruskal-Wallis test with Dunn's Multiple Comparison Test unless otherwise stated (SPSS Inc., Chicago, IL, USA). A value of $P < 0.05$ was considered statistically significant.

## 3. Results

*3.1. Cobalt (II) ions and nanoparticles inhibit U937 macrophage random migration*

To directly measure the impact of cobalt and chromium on macrophage motility *in vitro*, we first performed time-lapse imaging of U937 macrophages after 12 h of cobalt or chromium treatment using non-cytotoxic concentrations (Supplementary Fig. S2). Fig. 1A–E shows the migration paths for 25 individual cells in each treatment group. The total path length of cells treated with $Co^{2+}$ and CoNPs were significantly shorter than those for untreated control cells ($P < 0.001$, Fig. 1F). Treatment with $Cr^{3+}$ or CrNPs had no significant effect on macrophage migration.

*3.2. Cobalt inhibits U937 macrophages and BMDMs transmigration*

Using transwell migration assay we confirmed the results observed during random cell migration (Fig. 1). The ability of U937 macrophages to migrate through the porous transwell membrane was significantly impaired by pre-treatment with either $Co^{2+}$ or CoNPs (Fig. 2). Exposure to $Co^{2+}$ and CoNPs, reduced the number of transmigrating U937 macrophages by approximately 62% and 55%, respectively, whilst for BMDMs, the corresponding reductions in migration were approximately 45% and 53%, respectively (Fig. 2B). Incubation with $Cr^{3+}$ and CrNPs had no statistically significant effect on the cell migration relative to untreated controls for either U937 macrophages or BMDMs.

*3.3. CoNPs inhibit macrophage migration in vivo*

To determine whether cobalt affects macrophage migration *in vivo*, we quantified the number of macrophages in the mouse peritoneal cavity before and after LPS stimulation in mice with or without cobalt pre-treatment. As neither $Cr^{3+}$ nor CrNPs showed any significant effect on macrophage migration *in vitro*, only cobalt exposure was examined during the *in vivo* study. Mice were injected with cobalt nanoparticles to mimic the generated cobalt *in vivo* dissolution products. Harvested peritoneal macrophages were identified by a flow cytometry gating strategy according to their size and granularity (Fig. 3A), CD11b and F4/80 surface marker expression (Fig. 3B). In mice not stimulated with LPS, the CoNPs pre-treatment had no significant effect on the number of peritoneal macrophages compared with control group (PBS only). After LPS stimulation, a marked efflux of peritoneal macrophages (by approximately 60%, Fig. 3C) from the cavity of control mice (PBS only) was observed, consistent with previously published work [19]. In mice pre-treated with CoNPs, the LPS stimulation had no significant effect in inducing macrophages efflux, with the number of macrophages remained at similar levels to the CoNPs group without LPS treatment, which indicated that the ability of macrophages to migrate out of the peritoneal cavity was significantly inhibited by CoNPs.

*3.4. Cobalt modulates microtubule acetylation in U937 macrophages*

To initiate cell migration, internal forces developed by the actin cytoskeleton are transmitted through cell-substrate adhesion sites while a dynamic turnover of adhesion complexes occurs [20]. Disruption in the cell migration indicates either an alteration in this force transmission or changes in the cell adhesion strength. Uptake of metal particles can impede the force balance between the microtubule (MT) and F-actin by inhibiting MT polymerization in epithelial cells [21]. Therefore, we investigated whether microtubule or cytoskeletal impairment causes the inhibition of macrophage migration. The MT structure of the control and treated cells are shown in Fig. 4A. Both $Co^{2+}$ and CoNPs induced a significant increase in U937 macrophage alpha tubulin acetylation, one of the basic components for MT biopolymer [22], confirmed by immunofluorescence staining (Fig. 4A and B) and Western Blot analysis (Fig. 4C and D). In contrast, chromium ions had no significant effect on the MT organisation or acetylation while CrNPs slightly reduced the MT acetylation, although it was not statistically significant. We also investigated the effect of an inhibitor of a member of the histone deacetylase family, HDAC6, which regulates MT-dependent cell motility via mediating tubulin deacetylation [23]. HDAC6 overexpression induces a global deacetylation of

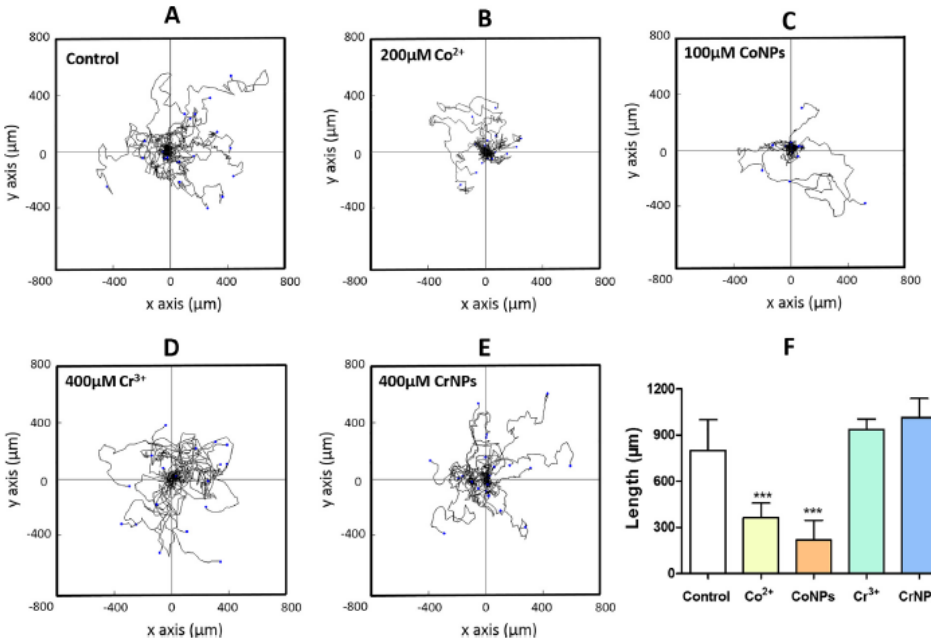


**Fig. 1.** Cobalt ions and nanoparticles reduce U937 macrophage random migration. (A-E): Detailed migration trajectories of cells (n = 25) over a 6-hour period following treatment with cobalt or chromium. Individual tracks were transposed so that each of the cells started at the same origin. (F) Net cell migration length for each treatment with values indicating mean + SEM for N = 3 experiments (n = 25 cells/condition/experiment). Statistical differences from untreated control are based on one-way ANOVA with Bonferroni post-test; ***P < 0.001.

α-tubulin, hence promoting cell chemotactic migration [23]. When U937 cell were treated with a HDAC6 inhibitor, Tubastatin A (5 μM), a hyperacetylation of tubulin was observed (Fig. 4A), showing much higher effect than the cobalt treatment. Tubastatin A also significantly reduced the number of migrating cells in a transwell migration assay, however only partially replicating the effect of cobalt treatment (Fig. 4E). This suggests that cobalt-mediated tubulin acetylation in macrophages does not play the critical role in the downregulation of cell migration.

### 3.5. Cobalt ions and nanoparticles promote macrophage spreading and podosome formation, which are associated with increased cell adhesion

Macrophage migration involves remodelling of the actin cytoskeleton associated with cell spreading, disassembly of existing focal adhesions, and formation of new cell-matrix interactions. SEM imaging revealed that both $Co^{2+}$ and CoNPs significantly increased U937 macrophage spreading with increase in lamellipodia protrusions around the cell periphery (Fig. 5A). In this case, CoNP-treatment had a significantly greater effect than $Co^{2+}$ treatment (Fig. 5B). U937 macrophages expressed characteristic podosome-like punctate adhesion structures, characterised by an actin-rich core surrounded by vinculin adhesion proteins (Fig. 5C). Treatment with either $Co^{2+}$ or CoNPs significantly increased both the podosome number (Fig. 5D) and density within individual cells (Fig. 5E). Cobalt also significantly increased the percentages of cells forming podosomes in BMDMs (Fig. S4). Excessive formation of the adhesion complex can result in a strong anchorage of cells to the underlying substrate, thereby inhibiting cell migration [24]. Hence, we examined whether changes in macrophage morphology and podosome formation during cobalt treatment were associated with alterations in cell adhesion. U937 cells exposed to $Co^{2+}$ showed an increased cell adhesion to the ECM in a concentration-dependent manner (Fig. 5F and G). This effect of $Co^{2+}$ was not evident on BMDMs (data not shown), possibly due to differences in the speed of the cell adhesion to the matrix. Collectively, these results indicate that the cobalt-induced inhibition of macrophage migration is associated with cytoskeletal reorganisation, podosomes formation and increased cell adhesion.

### 3.6. Cobalt-induced podosome formation in U937 macrophages stimulates ECM degradation

Podosomes promote adhesion to the substrate and degrade the components of the ECM. To determine whether cobalt-induced podosomes are able to locally degrade the ECM, we performed an *in vitro* matrix degradation assay based on loss of FITC-conjugated gelatin. Macrophages induced localised degradation as shown by dark areas in the fluorescent-tagged gelatin matrix (indicated by arrows in Fig. 6A). The degradation of gelatin was closely associated with cells expressing podosomes and in some cases, the podosomes were located directly over the degraded matrix (Fig. 6A). Both $Co^{2+}$ and CoNPs promoted matrix degradation (Fig. 6B), with associated statistically significant differences in matrix degradation index (Fig. 6C). Treatment with $Cr^{3+}$ and CrNPs had no significant effect on the ECM degradation (Fig. 6B).

The matrix degradation by podosomes involves the recruitment and activation of matrix metalloproteinases (MMPs) [25]. Using a zymography assay we measured the release and activation of MMPs. We observed release of MMP9 (band at a molecular weight of 82–92 kDa) after cobalt treatment (Fig. 6D). Additionally, a lower band of 82 kDa molecular weight was observed indicating

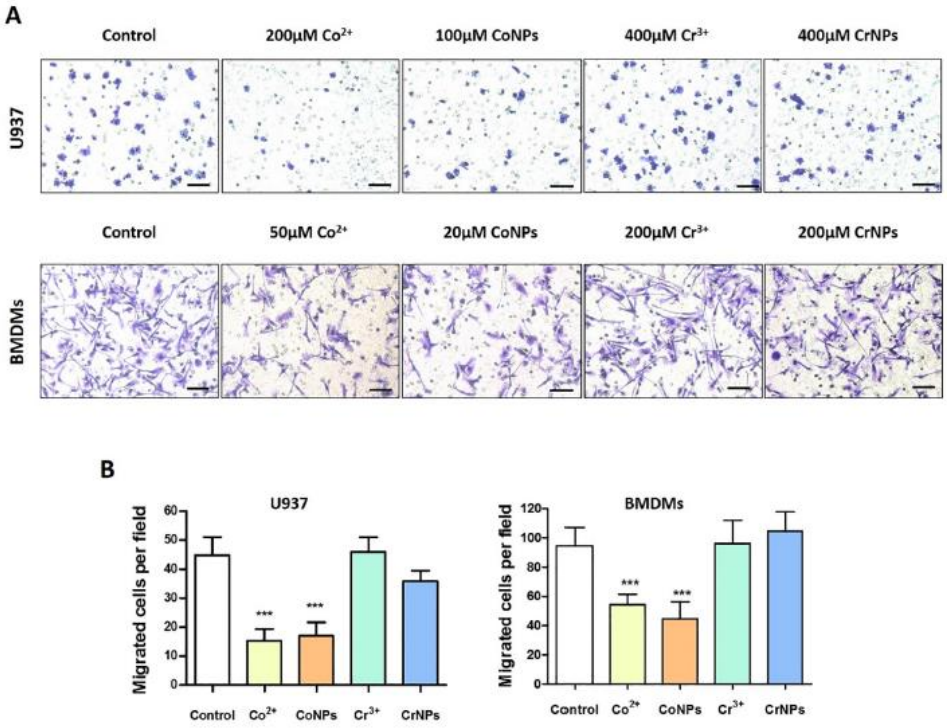


**Fig. 2.** Cobalt ions and nanoparticles reduce transmigration of U937 macrophages and BMDMs. (A) Representative images of migrated U937 macrophages and BMDMs treated by $Co^{2+}$, CoNPs, $Cr^{3+}$ and CrNPs (Scale bar = 100 μm). (B) Quantifications of the migration assay based on three independent experiments. Values represent mean ± SEM. N = 3. For each experiment, 10 random fields were imaged for each treatment (n = 10). Statistically significant differences are indicated relative to untreated control based on one-way ANOVA with Bonferroni post-test; $^{***}P < 0.001$.

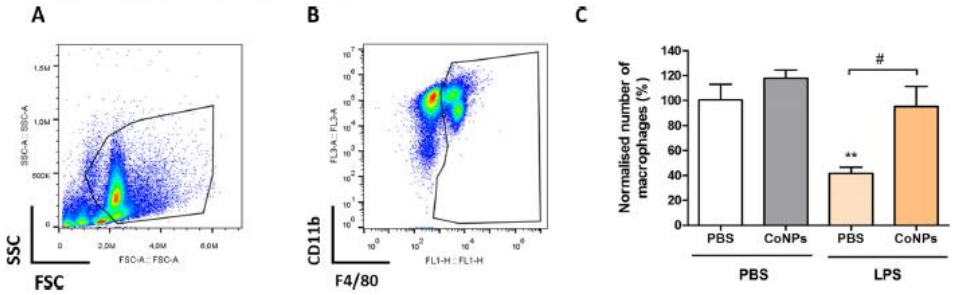


**Fig. 3.** Macrophage migration *in vivo* is inhibited by CoNPs. Representative FACS analysis images showing the gating strategy to identify the peritoneal macrophages based on (A) cell size and granularity, (B) CD11b and F4/80 surface markers expression. (C) Number of harvested macrophages from treated mice from each group, with data normalised to PBS control group (mice injected with PBS twice). Statistically significant differences were determined by one-way ANOVA and Bonferroni's multiple comparison test (n = 5 mice per treatment, **indicates difference from PBS control (PBS only) $P \leq 0.01$; # indicates difference between CoNPs and PBS treatment with LPS, $P < 0.05$).

an active form of MMP9 cleaved from pro-MMP9. $Co^{2+}$ and CoNPs induced pro-MMP9 release was not concentration-dependent, while the formation of active MMP9 was (Fig. 6E). Cobalt exposure had no significant effect on MMP2 release. Immunofluorescent staining revealed that intracellular MMP9 frequently co-localised with cobalt-induced podosomes (Fig. S3). In line with the results shown in Fig. 6B, $Cr^{3+}$ and CrNPs did not cause any significant change in the release of MMP2, pro-MMP9 nor the active form of MMP9 (data not shown).

### *3.7. Inhibition of macrophage migration in the presence of cobalt was associated with ROS production and its down-regulation of RhoA expression.*

Heavy metal ions and nanoparticles can provoke cellular stress, which may lead to alterations in cellular structure and function, and potentially loss of cell viability [26]. Both $Co^{2+}$ and CoNPs induced ROS in a concentration-depended manner in U937 macrophages, and we showed that this also occurs at non-cytotoxic

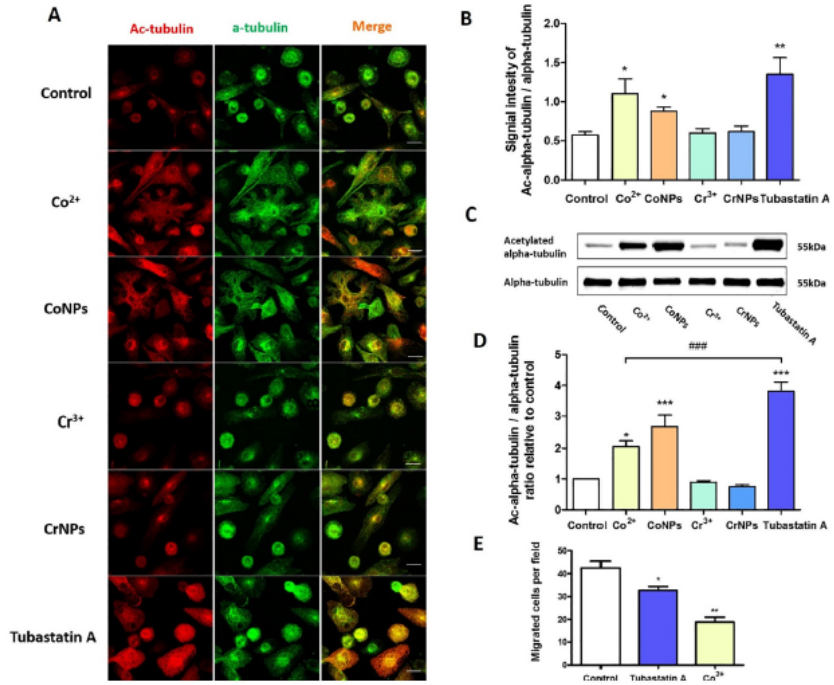


**Fig. 4.** Cobalt-induced hyper-acetylation of tubulin and its effect on macrophage migration. (A) Representative immunofluorescence confocal images of U937 macrophages treated with $Co^{2+}$, CoNPs, $Cr^{3+}$, CrNPs and Tubastatin A for 24 h. Cells were stained for acetylated α-tubulin (red) and α-tubulin (green). Scale bar represents 20 μm. Integrated fluorescent signal intensity for acetylated and non-acetylated tubulin in each cell was quantified and shown in (B) n = 25; values represent mean + SEM; $^{*}P \leq 0.05$; $^{**}P \leq 0.01$; N = 3. (C) Western blots for acetylated α-tubulin and α-tubulin for cells treated with cobalt, chromium, Tubastatin A for 24 h and (D) the corresponding quantification demonstrating increased total α-tubulin acetylation. Values represent mean + SEM; $^{*}/^{***}$ indicate difference from control, $P \leq 0.05/P \leq 0.001$; $^{\#\#\#}$ indicates difference between $Co^{2+}$ and Tubastatin A, $P \leq 0.001$; N = 3. (E) Increased tubulin acetylation with Tubastatin A significantly reduced macrophage transwell migration. Values represent mean + SEM; $^{*}P < 0.05$, $^{**}P \leq 0.01$; N = 3 experiments, n = 10 fields of view per experiment. All statistically significant differences were determined by one-way ANOVA and Bonferroni's multiple comparison test. (For interpretation of the references to colour in this figure legend, the reader is referred to the web version of this article.)

concentrations (Fig. 7A). The maximum increase in ROS production of approximately 90% compared to unstimulated cells, occurred within the first 30 min. This significant increase persisted for 4 h of treatment but decreased after 6 h. Exposure to CoNPs at 100–150 μM induced a transient upregulation in ROS measured at 2 h, with an increase of approximately 75% at 150 μM (Fig. 7B). Co-treatment with ROS scavenger and antioxidant, NAC (N-acetyl-L-cysteine), abolished the cobalt-induced ROS production in cells (Fig. 7A and B). We next tested whether ROS generation was responsible for the cobalt-induced podosome formation and the consequent inhibition of U937 macrophage migration. Co-treatment of $Co^{2+}$-treated cells with NAC resulted in a reduction in the cobalt-induced podosome formation (Fig. 7C and D) and a significant increase in $Co^{2+}$-treated macrophage transmigration (Fig. 7E). As mitochondria and NADPH oxidases are the main sources of cellular ROS, we also tested the effect of a NADPH oxidase inhibitor apocynin (5 μM, 10 μM and 50 μM). However, apocynin was not able to inhibit cobalt-mediated ROS generation nor to restore macrophage migration (data not shown), which suggested that cobalt-mediated ROS increases are mainly mitochondria-derived.

Actin organisation and podosome turnover are tightly regulated by the Rho GTPase, such as RhoA, Rac1 and Cdc42, whose activity is determined by their guanine nucleotide-bound state [27]. To determine if cobalt-induced ROS acts as an upstream regulator to activate Rho GTPases, we investigated the expression of RhoA, Cdc42 and Rac1 after U937 macrophages were treated by $Co^{2+}$ (200 μM) and CoNPs (100 μM) for 24 h. As shown in Fig. 7F and G, cobalt did not affect the Rac1 and Cdc42 levels, but caused decreased RhoA expression indicating that $Co^{2+}$ and CoNPs negatively regulate RhoA signalling. This was further confirmed by down-regulation of the downstream proteins of RhoA signalling, such as pMLC (phospho-myosin Light Chain) and pMYPT (phospho-myosin-binding subunit of myosin phosphatase).

In addition, the treatment of macrophages with the RhoA-specific inhibitor C3 Transferase (2 μg/ml) and RhoA/ROCK1 pathway inhibitor Y-27632 (20 μM) also led to intensive cell spreading and increased podosome formation (Fig. 7H) as observed in cobalt-treated cells. Accordingly, the migration of U937 macrophages were also significantly impaired when RhoA signalling was inhibited by inhibitor C3 Transferase and Y-27632 (Fig. 7H and I). Furthermore, the reduced expression of RhoA level caused by $Co^{2+}$ and CoNPs was significantly reversed by using the NAC (Fig. 7 J and K), which has showed to suppress the cobalt-induced ROS generation and be capable of partially restore the migration ability of U937 macrophages. These data suggest that cobalt-induced ROS production lies upstream of the RhoA signalling and down-regulation of RhoA expression results in remodelling of macrophage cytoskeleton and impaired migration.

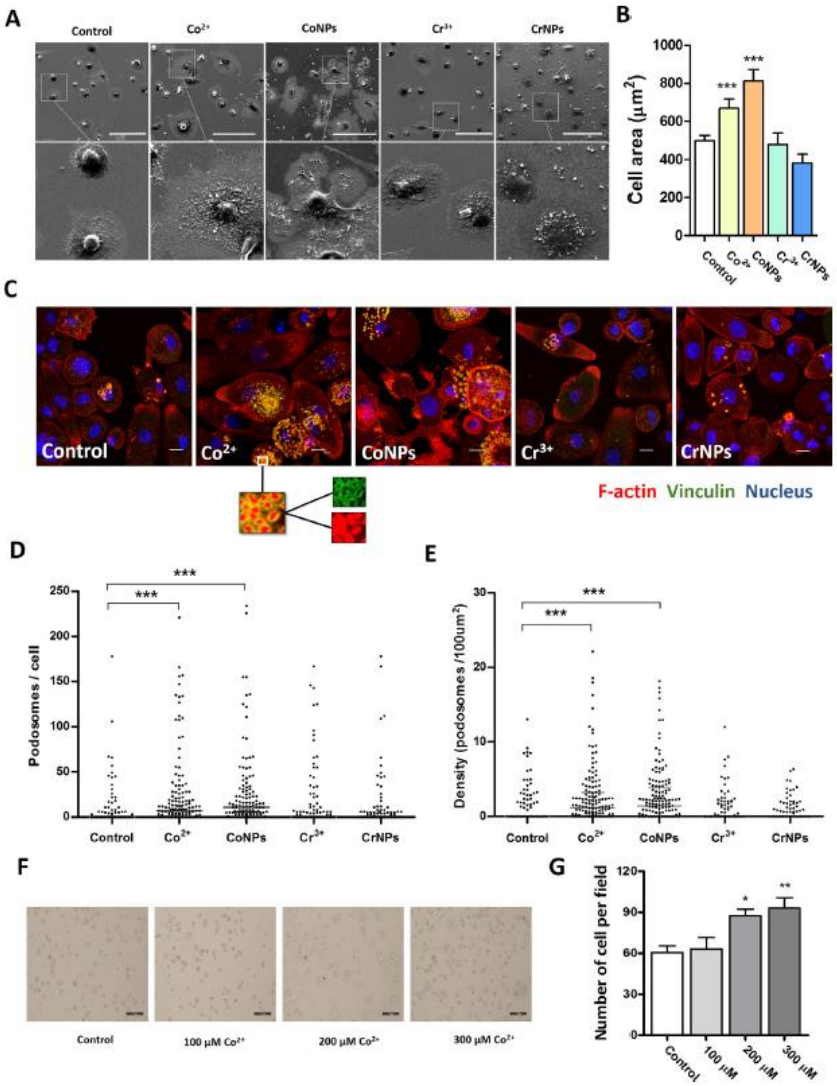


**Fig. 5.** Reduced macrophage migration induced by cobalt is associated with increased cell spreading and podosome formation and cell adhesion to extracellular matrix. (A) Representative SEM images of U937 macrophages incubated for 12 h with $Co^{2+}$ (200 μM), CoNPs (100 μM), $Cr^{3+}$ (400 μM) or CrNPs (400 μM) and untreated control. Scale bar indicates 100 μm. (B) Quantification of projected cell area for each treatment. Values represent mean + SEM for N = 3 separate experiments with n = 150 cells per experiment. Statistically significant differences from untreated control determined by one-way ANOVA and Bonferroni's multiple comparison test. $^{***}P \leq 0.001$. (C) Representative confocal microscopy images showing appearance of punctate podosome adhesion structures consisting of actin core (red) and surrounded by vinculin (green) in U937 macrophages following treatment with cobalt or chromium as described in (A). Scale bar indicates 10 μm. Associated quantification of (D) podosome number/cell and (E) podosome density. n = 150 cells for each group. Data with median shown from one representative experiment out of three; significance was determined by Kruskal-Wallis test and Dunn's Multiple Comparison Test. $^{***}P \leq 0.001$; N = 3. (F) Representative brightfield fields of view images showing that cobalt increased cell adhesion to ECM in a dose-dependent manner, where the scale bar indicates 100 μm, as quantified in (G) showing significantly increased numbers of adherent cells per field of view at 200 μM and 300 μM. Data indicates mean + SEM for N = 3 with n = 10 fields of view per experiment. Statistical significance based on one way ANOVA and Bonferroni's multiple comparison test; $^{*}P \leq 0.05$, $^{**}P \leq 0.01$. (For interpretation of the references to colour in this figure legend, the reader is referred to the web version of this article.)

## 4. Discussion

Macrophages play an essential role in surveillance and coordination of the inflammatory cascade associated with implant stability. The production of CoCr alloy wear debris leads to phagocytosis of the particles by macrophages [28]. This metal debris with associated ions activate the monocyte/macrophage lineage to release a variety of mediators, such as free radicals, nitric oxide, tumour necrosis factor-α (TNF-α), interleukin-1 β (IL-1 β), prostaglandin E2 (PGE2) and IL-6 [29–32], which are influenced by the

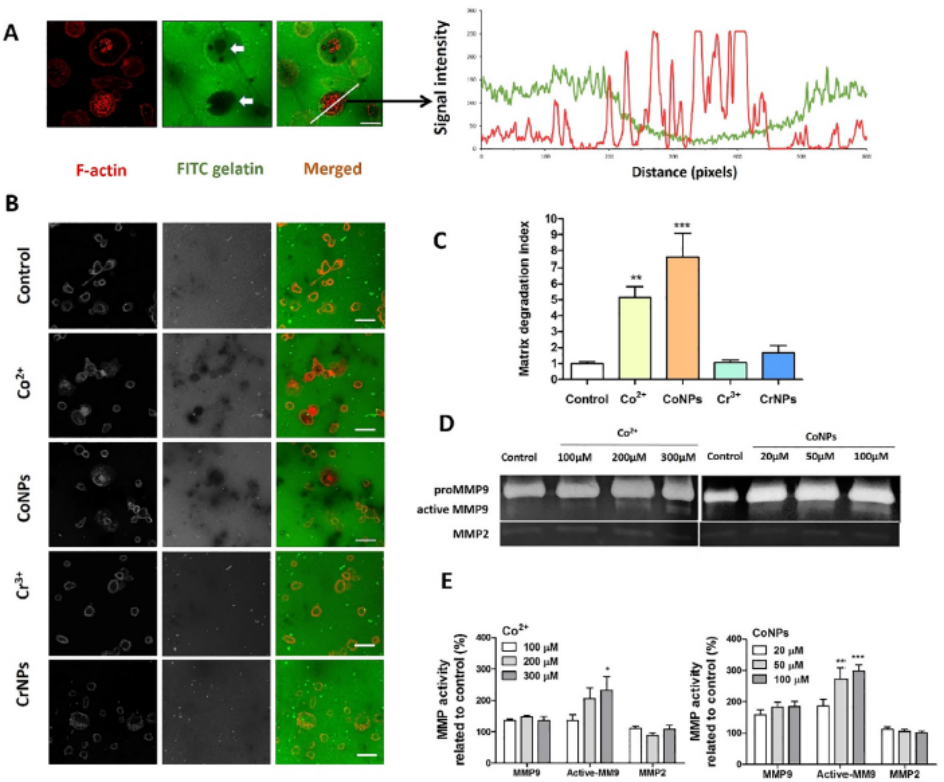


**Fig. 6.** Enhanced ECM degradation induced by cobalt is associated with the release and activation of MMP9, which co-localizes with podosomes. (A) Representative fluorescence microscopy image showing FITC-conjugated gelatin (green) degraded by U937 macrophages counter stained for F-actin (red) podosomes. Associated fluorescence intensity measurements demonstrate the co-localization of areas of gelatin degradation and the F-actin podosomes. Scale bar indicates 10 μm. (B) Representative images showing FITC-conjugated gelatin degradation following 24 h treatment with $Co^{2+}$ (200 μM), CoNPs (100 μM), $Cr^{3+}$ (400 μM) or CrNPs (400 μM) and untreated control. Scale bar indicates 20 μm. (C) Associated measurements of degradation area quantified as degradation index normalized to control group show significantly increased degradation following cobalt treatments. Values represent mean + SEM for N = 3 with n = 10 fields of view per experiment. (D) Zymography gels showing the release and activation of MMP9 by U937 cells due to cobalt treatment. (E) Quantification of the formation of pro-MMP9, active MMP9 and MMP2 based on gelatin zymography results, values represent mean + SEM for N = 5. All statistically significant differences between different groups and control were determined by one way ANOVA and Bonferroni's multiple comparison test; $^{*}P \leq 0.05$, $^{**}P \leq 0.01$, $^{***}P \leq 0.001$. (For interpretation of the references to colour in this figure legend, the reader is referred to the web version of this article.)

concentrations, shape and size of the particles [4]. Metal debris and ions can sensitize the immune system by inducing a delayed type IV hypersensitivity response [33]. Moreover, CoCr nanoparticles have been shown to be able to induce DNA damage and chromosomal aberration across cellular barriers [34]. In our study we elucidated the mechanism of altered macrophage behaviour by metal ions and particles at non-cytotoxic concentrations.

We used a combined *in vitro* and *in vivo* approach to examine the differential response of macrophages to cobalt and chromium ions and nanoparticles. Using a range of techniques, we have demonstrated for the first time that non-toxic levels of cobalt significantly reduce macrophage migration due to impaired egress capacity of macrophages. We have also further elucidated the underpinning molecular mechanism, which involves down-regulation of RhoA expression through induced ROS production. These findings provide new mechanistic explanation of the extensive clinical failures of orthopaedic implants manufactured from CoCr alloys, which are associated with retention of the macrophages and consequent prolonged and unrestrained inflammatory reactions that could lead to implant failure ultimately. In particular, the present *in vitro* results revealed that relatively low levels of both $Co^{2+}$ ions (100 μM) and CoNPs (200 μM) markedly inhibit the random migration and chemotaxis of both U937 macrophages and murine bone marrow derived macrophages (BMDM), while $Cr^{3+}$ and CrNPs demonstrated no significant effect (Figs. 1 and 2). This was confirmed in an *in vivo* peritoneal macrophage efflux experiment, where we found that CoNPs inhibit the macrophage emigration from the cavity triggered by LPS (Fig. 3).

The mechanisms of the particulate-mediated inflammatory response associated with the imbalance in tissue homeostasis remain unclear, although a retention of macrophages within periprosthetic tissues is often reported [35,36]. We report, for the first time, that the retention of macrophages during cobalt exposure is associated with an increase in both podosome formation and cell spreading (Fig. 5). These morphological and structural changes associated with macrophage retention are dependent on ROS formation (Fig. 7). Additionally, during increased podosome formation, an increase in MMP9 production occurs, resulting in a

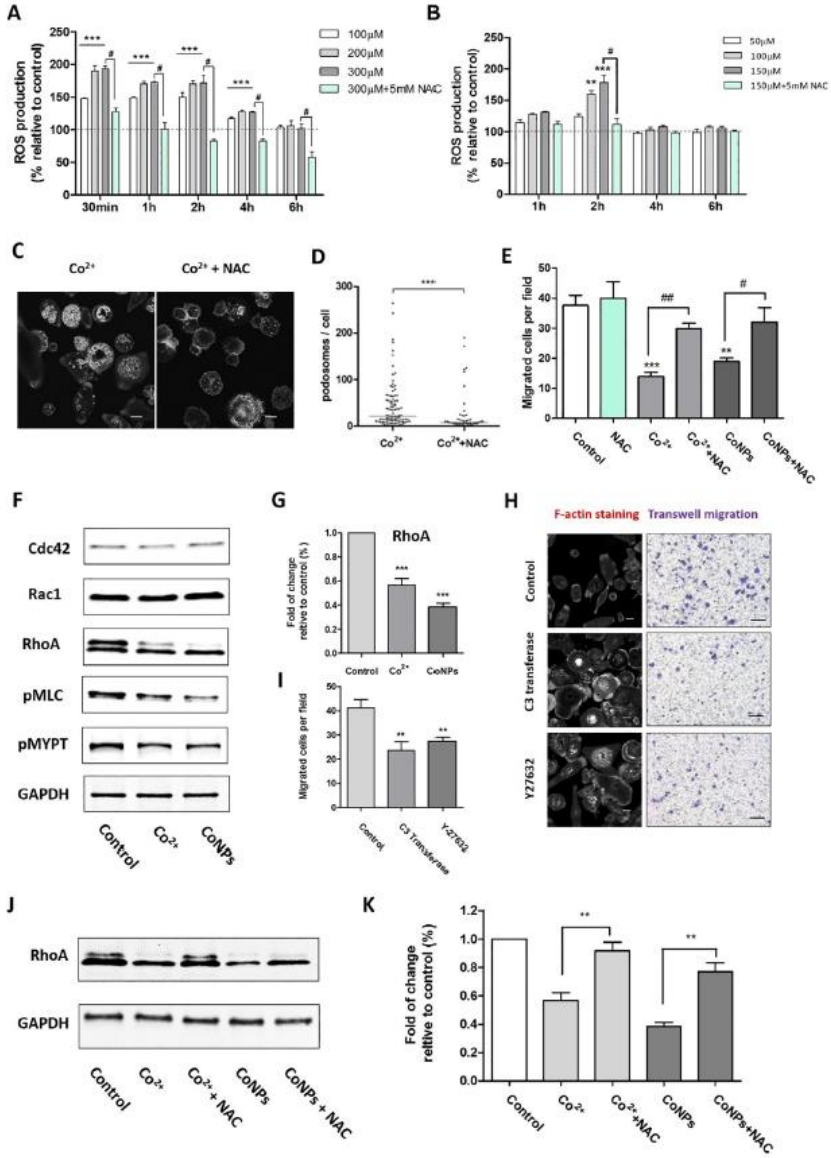


**Fig. 7.** Cobalt stimulates ROS production which stimulates podosome formation and impedes macrophage migration. (A, B) Dose and time dependent ROS production induced by $Co^{2+}$ and CoNPs; values represent mean + SEM from N = 3 separate experiments. Statistically significant differences determined by one-way ANOVA and Bonferroni's multiple comparison test. ($^{*}P \leq 0.01$; $^{***}P \leq 0.001$, ($^{**}$indicates significant upregulation for all of the three concentrations). (C) Fluorescence images showing that the ROS inhibitor, NAC (5 mM, 12 h) prevents $Co^{2+}$ induced upregulation of podosome formation as shown by F-actin labelling with phalloidin and quantified in (D), data with median shown from one representative experiment out of three; significance was determined by Mann-Whitney test. $^{***}P \leq 0.001$; N = 3. (E) Suppression of U937 macrophage transmigration is rescued by treatment with NAC. Data indicates the mean + SEM for number of migrated cells per field of view from 3 separate experiments, N = 3, with n = 10 fields of view per experiment ($^{\#}P \leq 0.05$, $\#\#/^{**}P \leq 0.01$; $\#\#\#/^{***}P \leq 0.001$). Scale bars represents 10 μm. (F) Western blots results for untreated cell and cells treated with $Co^{2+}$ (200 μM) and CoNPs (100 μM) for 24 h. (G) The corresponding quantification demonstrating decreased RhoA expression. Values represent mean + SEM; $^{***}$indicate difference from control, P < 0.001; N = 3. (H) Representative images showing the effects of inhibitor C3 Transferase and Y-27632 on U937 macrophage cytoskeleton organization and migration. (I) Quantification of the effects of C3 Transferase and Y-27632 on U937 macrophage organization. Values represent mean ± SEM. N = 3. For each experiment, 10 random fields were imaged for each treatment (n = 10). $^{**}P < 0.01$. (J) Western blots results showing RhoA level reduced by $Co^{2+}$ and CoNPs could be partially restored by inhibition of ROS with NAC (5 mM). (K) The corresponding quantification of cellular RhoA level with treatment by $Co^{2+}$, CoNPs and NAC. Values represent mean + SEM; $^{**}$indicate difference from control, P < 0.01; N = 3. Scale bars represents 10 μm in (C) and (H).

greater matrix degradation, all driven in a cobalt concentration-dependant manner (Fig. 6). This mechanism reducing macrophage migration in response to $Co^{2+}$ ions and CoNPs provide a new insight into the tissue responses and subsequent implant failure assocaited with CoCr alloys.

The mechanism of cell migration is controlled by a co-ordinated turnover of the actin and microtubule cytoskeletal network [37]. Migration is regulated by actin polymerization with actin/myosin interactions forming contractile forces to retract the cell, while microtubules specify migration directionality [38]. When studying the effect of cobalt and chromium on these critical components of the cell migration machinery, we observed a slightly decrease in the acetylation of α-tubulin in response to CrNPs, without affecting cell motility (Figs. 4 and 2). In contrast, cobalt increased α-tubulin acetylation while inhibiting cell migration. To test whether increased acetylation initiates the inhibition of macrophage migration, we induced tubulin acetylation with Tubastatin A, a potent HDAC6 inhibitor [22]. Tubastatin A treatment resulted in higher levels of α-tubulin acetylation than cobalt, and a reduction in macrophage migration, but to a smaller extend than cobalt (Fig. 4E). These results indicate either a non-specificity of Tubastatin A or that the migration response to cobalt involves additional mechanisms.

Apart from tubulin modifications, we found that cobalt induced alteration in macrophage morphology by enhancing cell spreading and an increase in the number and density of podosomes (Fig. 5A and D). Both cell spreading and podosomes formation involve the deformation of a cell membrane and the strengthening of cell–substrate attachment [39,40]. Podosome-type adhesions are rich in vinculin and other types of adhesion proteins, and regulate cell adhesion to the ECM [40]. Cell spreading and short-lived podosome formations with their adhesion structures are associated with enhanced macrophage migration and invasion [27]. When either process is uncontrolled, cell migration can be hindered [41]. For example, the inflammatory mediator PGE2 promotes macrophage migration in response to chemotactic signals, but at high doses, it reduces macrophage chemotaxis by enhancing cell-substratum adhesion [24]. In our study, we confirmed that the non-toxic concentrations of $Co^{2+}$ led to a concentration-dependent increase in cell adhesion to the ECM substrate (Fig. 5F and G). These results suggest that the reduction in macrophage migration induced by cobalt is due to both the increased cell spreading and the enhanced podosome formation.

We also found that the molecular mechanisms through which cobalt regulated podosome adhesion and reduced migration, involves the formation of ROS (Fig. 7). Both $Co^{2+}$ and CoNPs were shown to promote generation of the oxidative stress and increase ROS levels *in vitro* [42,43]. ROS is generated as a by-product during cellular oxidative metabolism, although its overproduction enhances cellular oxidative stress, transforming cells so they are unable to maintain normal physiological functions [44,45]. ROS are also the key signalling molecules during the progression of inflammatory disorders [46], by modulating the production of inflammatory chemokines and expression of leukocyte adhesion receptors to accumulate circulating monocytes at affected sites [46]. Oxygen radicals produced by local macrophages may further facilitate macrophage accumulation and their activation, resulting in prolonged inflammation. Our findings indicate that the mechanism behind the retention of infiltrated macrophages at the inflamed sites is mediated by ROS through regulating the cytoskeleton reorganization.

The cytoskeleton reorganization in presence of ROS is driven by the ability of ROS to induce reversible oxidation of proteins, which involves direct modification of protein kinases and transcription factors [47]. Major regulators of macrophage motility and cytoskeleton organization are influenced by Rho family GTPase [48–50], F-actin regulation pathways [51] and tyrosine phosphorylation [52,53]. The Rho family of GTPases play critical roles in cell motility by affecting actin organization and microtubule dynamics, myosin activity, and cell–ECM and cell–cell interactions [54]. In this study, we showed for the first time that cobalt-induced ROS formation acts as an upstream regulator to directly inactivate the RhoA, leading to reorganization of macrophage cytoskeleton and impaired cell migration (Fig. 7F–K). Small GTPase Rho is known to stimulate stress fiber formation and hamper the cell migration in many types of cells [55]. It is even reported that inactivation of Rho in transformed fibroblasts by dominant negative RhoA or the C3 exoenzyme would disrupt podosome structure [56], but also that podosome formation in Src-transformed fibroblasts could be promoted by limiting Rho activation [57]. In addition, it was recently revealed that podosome disassembly is associated with the activation of Rho and blockade of RhoA signalling could promote actin core assembly and podosome formation in macrophages [58].

Underlying mechanisms through which biomaterials-induced ROS formation modulates macrophage behaviour are of considerable importance. Despite emerging advances in materials science, biomaterials do not behave like native biological components and frequently incite adverse tissue reactions, which may lead to ultimate failure of the implants. Therefore accurate and facile approaches for screening and evaluating the biocompatibility of biomaterials are of critical interest, especially understanding the cellular behaviour of macrophages because of their decisive role in the long term survival of implanted biomaterials in addition to orchestrating inflammatory processes.

Over recent years, the use of MoM total hip replacement is in a drastic decline due to CoCr-related issues. However, implants containing CoCr alloys are still being widely utilized, such as in dental prosthesis and modular heads in MoP couplings. Significant increase in the amount of metal ion released into the saliva of patients with dental metallic materials has been reported [59]. Modular taper junctions allow for patient-specific fitting of implants. However, numerous retrieval studies have recently documented the adverse tissue reactions and pseudotumor formation adjacent to taper junctions in hip implants [5,7], which are clinically and histologically similar to ALTRs previously seen in failed MoM bearing. The etiology of this soft-tissue damage is also linked to release of metal ions and debris from the modular taper junctions. Therefore, further investigation is required to elucidate these different, yet similar, exposure scenarios. More importantly, a comprehensive biological evaluation of metal exposure is necessary due to the potentially destructive nature of these adverse reactions.

We acknowledge several limitations in this study. Although we have provided an explicit demonstration of the effect of cobalt on macrophage migration behaviour via a range of *in vivo* and *in vitro* techniques, it is still unknown whether macrophage accumulation around MoM hips is caused by a defective migratory ability. A refined animal study with *in vivo* tracking of macrophage recruitment would facilitate further investigation and yield improved understanding. Using commercially available nanoparticles in place of cobalt and chromium wear debris allowed us to decipher the individual role of the two primary elements in the cellular response. Possible synergistic effect of these two metals is of importance and should be addressed in the future studies. Both human U937 cell line and primary murine macrophages were used for data consistency, instead of primary human macrophages. These cellular models excluded the influence of variability in cells from different human donors, as have been used as *in vitro* cell models to study responses to orthopaedic wear products including bone cement, polyethylene, ceramic, metal particles, as well as metal ions [32,60–62]. Findings of our current study, can help us

design further investigations using primary human cells to characterize individual patient's responses to the wear debris.

## 5. Conclusion

Our study identified a new downstream effect of cobalt-induced ROS production and reduced RhoA expression in modulating macrophage migration and cytoskeleton organization. The effects of this signalling cascade lead to an enhancement in macrophage spreading, adhesion and inhibition of migration, which could induce a prolonged immune cell retention thereby propagating the chronic inflammation. The increased podosome formation in macrophages is also associated with enhanced activation of MMP9 and associated increased matrix degradation. The identification of this new mechanism through which cobalt, but not chromium, ions and nanoparticles induce macrophage retention at inflammatory sites provides a novel insight into the metal-associated periprosthetic tissue lesions.

## 6. Acknowledgement

The authors are grateful to the China Scholarship Council (CSC) for the support of Jing Xu.

## Appendix A. Supplementary data

Supplementary data associated with this article can be found, in the online version, at https://doi.org/10.1016/j.actbio.2018.03.054.

## References

[1] W.a.N.I. National Joint Registry for England, 13rd annual report, 2016, (2016).
[2] Y.M. Kwon, A.V. Lombardi, J.J. Jacobs, T.K. Fehring, C.G. Lewis, M.E. Cabanela, Risk stratification algorithm for management of patients with metal-on-metal hip arthroplasty: consensus statement of the American Association of Hip and Knee Surgeons, the American Academy of Orthopaedic Surgeons, and the Hip Society, J. Bone Joint. Surg. Am. 96 (1) (2014) e4.
[3] M.E. Muller, The benefits of metal-on-metal total hip replacements, Clin. Orthop. Relat. Res. 311 (1995) 54–59.
[4] A.K. Madl, M. Kovochich, M. Liong, B.L. Finley, D.J. Paustenbach, G. Oberdorster, Toxicology of wear particles of cobalt-chromium alloy metal-on-metal hip implants Part II: Importance of physicochemical properties and dose in animal and in vitro studies as a basis for risk assessment, Nanomedicine 11 (5) (2015) 1285–1298.
[5] D.R. Plummer, R.A. Berger, W.G. Paprosky, S.M. Sporer, J.J. Jacobs, C.J. Della Valle, Diagnosis and management of adverse local tissue reactions secondary to corrosion at the head-neck junction in patients with metal on polyethylene bearings, J. Arthroplast. 31 (1) (2016) 264–268.
[6] D. Dimitriou, M.H.L. Liow, T.Y. Tsai, W.A. Leone, G.A. Li, Y.M. Kwon, Early outcomes of revision surgery for taper corrosion of dual taper total hip arthroplasty in 187 patients, J. Arthroplast. 31 (7) (2016) 1549–1554.
[7] Y.M. Kwon, S. Khormaee, M.H. Lincoln, T.Y. Tsai, A.A. Freiberg, H.E. Rubash, Asymptomatic pseudotumors in patients with taper corrosion of a dual-taper modular femoral stem MARS-MRI and metal ion study, J. Bone Joint Surg.-Am. 98 (20) (2016).
[8] J.M. Jennings, D.A. Dennis, C.C. Yang, Corrosion of the head-neck junction after total hip arthroplasty, J. Am. Acad. Orthop. Sur. 24 (6) (2016) 349–356.
[9] S.J. Incavo, Goals and challenges of identifying asymptomatic pseudotumors in patients treated with total hip arthroplasty, J. Bone Joint Surg.-Am. 98 (20) (2016).
[10] S.A. Sutphen, L.H. MacLaughlin, A.A. Madsen, J.H. Russell, M.A. McShane, Prevalence of pseudotumor in patients after metal-on-metal hip arthroplasty evaluated with metal ion analysis and MARS-MRI, J. Arthroplast. 31 (1) (2016) 260–263.
[11] Y.M. Kwon, S.J. Ostlere, P. McLardy-Smith, N.A. Athanasou, H.S. Gill, D.W. Murray, "Asymptomatic" pseudotumors after metal-on-metal hip resurfacing arthroplasty: prevalence and metal ion study, J. Arthroplast. 26 (4) (2011) 511–518.
[12] B. Behl, I. Papageorgiou, C. Brown, R. Hall, J.L. Tipper, J. Fisher, E. Ingham, Biological effects of cobalt-chromium nanoparticles and ions on dural fibroblasts and dural epithelial cells, Biomaterials 34 (14) (2013) 3547–3558.
[13] C. Nich, Y. Takakubo, J. Pajarinen, M. Ainola, A. Salem, T. Sillat, A.J. Rao, M. Raska, Y. Tamaki, M. Takagi, Y.T. Konttinen, S.B. Goodman, J. Gallo, Macrophages-Key cells in the response to wear debris from joint replacements, J. Biomed. Mater. Res. A 101 (10) (2013) 3033–3045.
[14] C.N. Serhan, J. Savill, Resolution of inflammation: the beginning programs the end, Nat. Immunol. 6 (12) (2005) 1191–1197.
[15] Z. Xia, B.F. Ricciardi, Z. Liu, C. von Ruhland, M. Ward, A. Lord, L. Hughes, S.R. Goldring, E. Purdue, D. Murray, G. Perino, Nano-analyses of wear particles from metal-on-metal and non-metal-on-metal dual modular neck hip arthroplasty, Nanomedicine 13 (3) (2017) 1205–1217.
[16] S.J. Baskey, E.A. Lehoux, I. Catelas, Effects of cobalt and chromium ions on lymphocyte migration, J. Orthop. Res. 35 (4) (2017) 916–924.
[17] J. Weischenfeldt B. Porse Bone marrow-derived macrophages (BMM): isolation and applications CSH Protoc. 2008 pdb prot5080.
[18] K.H. Martin, K.E. Hayes, E.L. Walk, A.G. Ammer, S.M. Markwell, S.A. Weed, Quantitative measurement of invadopodia-mediated extracellular matrix proteolysis in single and multicellular contexts, J. Vis. Exp. (66) (2012) e4119.
[19] Y.M. Park, M. Febbraio, R.L. Silverstein, CD36 modulates migration of mouse and human macrophages in response to oxidized LDL and may contribute to macrophage trapping in the arterial intima, J. Clin. Invest. 119 (1) (2009) 136–145.
[20] R. Mayor, S. Etienne-Manneville, The front and rear of collective cell migration Nature reviews, Mol. cell Biol. 17 (2) (2016) 97–109.
[21] C.Y. Tay, P.Q. Cai, M.I. Setyawati, W.R. Fang, L.P. Tan, C.H.L. Hong, X.D. Chen, D. T. Leong, Nanoparticles strengthen intracellular tension and retard cellular migration, Nano Lett. 14 (1) (2014) 83–88.
[22] A. Akhmanova, M.O. Steinmetz, Control of microtubule organization and dynamics: two ends in the limelight Nature reviews, Mol. Cell Biol. 16 (12) (2015) 711–726.
[23] C. Hubbert, A. Guardiola, R. Shao, Y. Kawaguchi, A. Ito, A. Nixon, M. Yoshida, X. F. Wang, T.P. Yao, HDAC6 is a microtubule-associated deacetylase, Nature 417 (6887) (2002) 455–458.
[24] I.C. Osma-Garcia, C. Punzon, M. Fresno, M.D. Diaz-Munoz, Dose-dependent effects of prostaglandin E2 in macrophage adhesion and migration, Eur. J. Immunol. 46 (3) (2016) 677–688.
[25] J.G. Evans, P. Matsudaira, Structure and dynamics of macrophage podosomes, Eur. J. Cell Biol. 85 (3–4) (2006) 145–149.
[26] K. Jomova, M. Valko, Advances in metal-induced oxidative stress and human disease, Toxicology 283 (2–3) (2011) 65–87.
[27] S. Linder, M. Aepfelbacher, Podosomes: adhesion hot-spots of invasive cells, Trends Cell Biol. 13 (7) (2003) 376–385.
[28] H.S. Gill, G. Grammatopoulos, S. Adshead, E. Tsialogiannis, E. Tsiridis, Molecular and immune toxicity of CoCr nanoparticles in MoM hip arthroplasty, Trends Mol. Med. 18 (3) (2012) 145–155.
[29] A.M. Kaufman, C.I. Alabre, H.E. Rubash, A.S. Shanbhag, Human macrophage response to UHMWPE TiAlV, CoCr, and alumina particles: analysis of multiple cytokines using protein arrays, J. Biomed. Mater. Res. A 84 (2) (2008) 464–474.
[30] R. VanOs, L.L. Lildhar, E.A. Lehoux, P.E. Beaule, I. Catelas, In vitro macrophage response to nanometer-size chromium oxide particles, J. Biomed. Mater. Res. B Appl. Biomater. 102 (1) (2014) 149–159.
[31] O.M. Posada, R.J. Tate, R.M.D. Meek, M.H. Grant, In Vitro Analyses of the Toxicity Immunological, and Gene Expression Effects of Cobalt-Chromium Alloy Wear Debris and Co Ions Derived from Metal-on-Metal Hip Implants, Lubricants 3 (3) (2015) 539–568.
[32] O.M. Posada, R.J. Tate, M.H. Grant, Effects of CoCr metal wear debris generated from metal-on-metal hip implants and Co ions on human monocyte-like U937 cells, Toxicol. In Vitro 29 (2) (2015) 271–280.
[33] P.A. Potnis, D.K. Dutta, S.C. Wood, Toll-like receptor 4 signaling pathway mediates proinflammatory immune response to cobalt-alloy particles, Cell Immunol. 282 (1) (2013) 53–65.
[34] M.C. Parry, G. Bhabra, A. Sood, F. Machado, L. Cartwright, M. Saunders, E. Ingham, R. Newson, A.W. Blom, C.P. Case, Thresholds for indirect DNA damage across cellular barriers for orthopaedic biomaterials, Biomaterials 31 (16) (2010) 4477–4483.
[35] S.B. Goodman, Wear particles, periprosthetic osteolysis and the immune system, Biomaterials 28 (34) (2007) 5044–5048.
[36] G. Perino, B.F. Ricciardi, S.A. Jerabek, G. Martignoni, G. Wilner, D. Maass, S.R. Goldring, P.E. Purdue, Implant based differences in adverse local tissue reaction in failed total hip arthroplasties: a morphological and immunohistochemical study, BMC Clin. Pathol. 14 (2014) 39.
[37] C. Le Clainche, M.F. Carlier, Regulation of actin assembly associated with protrusion and adhesion in cell migration, Physiol. Rev. 88 (2) (2008) 489–513.
[38] A.J. Ridley, M.A. Schwartz, K. Burridge, R.A. Firtel, M.H. Ginsberg, G. Borisy, J.T. Parsons, A.R. Horwitz, Cell migration: integrating signals from front to back, Science 302 (5651) (2003) 1704–1709.
[39] J.L. McGrath, Cell spreading: the power to simplify, Curr. Biol. 17 (10) (2007) R357–R358.
[40] D.A. Murphy, S.A. Courtneidge, The 'ins' and 'outs' of podosomes and invadopodia: characteristics, formation and function, Nature reviews, Mol. Cell Biol. 12 (7) (2011) 413–426.
[41] D. Ilic, Y. Furuta, S. Kanazawa, N. Takeda, K. Sobue, N. Nakatsuji, S. Nomura, J. Fujimoto, M. Okada, T. Yamamoto, Reduced cell motility and enhanced focal adhesion contact formation in cells from FAK-deficient mice, Nature 377 (6549) (1995) 539–544.
[42] N.S. Chandel, E. Maltepe, E. Goldwasser, C.E. Mathieu, M.C. Simon, P.T. Schumacker, Mitochondrial reactive oxygen species trigger hypoxia-induced transcription, Proc. Natl. Acad. Sci. U.S.A. 95 (20) (1998) 11715–11720.
[43] T. Kamiya, H. Hara, H. Yamada, H. Imai, N. Inagaki, T. Adachi, Cobalt chloride decreases EC-SOD expression through intracellular ROS generation and p38-MAPK pathways in COS7 cells, Free Rad. Res. 42 (11–12) (2008) 949–956.

[44] H. Sauer, M. Wartenberg, J. Hescheler, Reactive oxygen species as intracellular messengers during cell growth and differentiation, Cell Physiol. Biochem. 11 (4) (2001) 173–186.
[45] C.L. Bigarella, R. Liang, S. Ghaffari, Stem cells and the impact of ROS signaling, Development 141 (22) (2014) 4206–4218.
[46] M. Mittal, M.R. Siddiqui, K. Tran, S.P. Reddy, A.B. Malik, Reactive oxygen species in inflammation and tissue injury, Antioxid. Redox Sign 20 (7) (2014) 1126–1167.
[47] T.C. Meng, T. Fukada, N.K. Tonks, Reversible oxidation and inactivation of protein tyrosine phosphatases in vivo, Mol. Cell 9 (2) (2002) 387–399.
[48] G.E. Jones, W.E. Allen, A.J. Ridley, The Rho GTPases in macrophage motility and chemotaxis, Cell Adhes. Commun. 6 (2–3) (1998) 237–245.
[49] V. Konigs, R. Jennings, T. Vogl, M. Horsthemke, A.C. Bachg, Y. Xu, K. Grobe, C. Brakebusch, A. Schwab, M. Bahler, U.G. Knaus, P.J. Hanley, Mouse macrophages completely lacking Rho subfamily GTPases (RhoA, RhoB, and RhoC) have severe lamellipodial retraction defects, but robust chemotactic navigation and altered motility, J. Biol. Chem. 289 (44) (2014) 30772–30784.
[50] A.J. Ridley, Rho GTPase signalling in cell migration, Curr. Opin. Cell Biol. 36 (2015) 103–112.
[51] S. Linder, D. Nelson, M. Weiss, M. Aepfelbacher, Wiskott-Aldrich syndrome protein regulates podosomes in primary human macrophages, Proc. Natl. Acad. Sci. U.S.A. 96 (17) (1999) 9648–9653.
[52] A.R. Dwyer, K.A. Mouchemore, J.H. Steer, A.J. Sunderland, N.G. Sampaio, E.L. Greenland, D.A. Joyce, F.J. Pixley, Src family kinase expression and subcellular localization in macrophages: implications for their role in CSF-1-induced macrophage migration, J. Leukoc. Biol. 100 (1) (2016) 163–175.
[53] G.E. Jones, Cellular signaling in macrophage migration and chemotaxis, J. Leukoc. Biol. 68 (5) (2000) 593–602.
[54] S. Hanna, M. El-Sibai, Signaling networks of Rho GTPases in cell motility, Cell Signal. 25 (10) (2013) 1955–1961.
[55] S. Tojkander, G. Gateva, P. Lappalainen, Actin stress fibers–assembly, dynamics and biological roles, J. Cell. Sci. 125 (Pt 8) (2012) 1855–1864.
[56] R.L. Berdeaux, B. Diaz, L. Kim, G.S. Martin, Active Rho is localized to podosomes induced by oncogenic Src and is required for their assembly and function, J. Cell Biol. 166 (3) (2004) 317–323.
[57] M. Schramp, O. Ying, T.Y. Kim, G.S. Martin, ERK5 promotes Src-induced podosome formation by limiting Rho activation, J. Cell Biol. 181 (7) (2008) 1195–1210.
[58] N.B.M. Rafiq, Z.Z. Lieu, T.T. Jiang, C.H. Yu, P. Matsudaira, G.E. Jones, A.D. Bershadsky, Podosome assembly is controlled by the GTPase ARF1 and its nucleotide exchange factor ARNO, J. Cell Biol. 216 (1) (2017) 181–197.
[59] P. Downarowicz, M. Mikulewicz, Trace metal ions release from fixed orthodontic appliances and DNA damage in oral mucosa cells by in vivo studies: a literature review, Adv. Clin. Exp. Med.: Off. Organ Wroclaw Med. Univ. 26 (7) (2017) 1155–1162.
[60] E. Ingham, T.R. Green, M.H. Stone, R. Kowalski, N. Watkins, J. Fisher, Production of TNF-alpha and bone resorbing activity by macrophages in response to different types of bone cement particles, Biomaterials 21 (10) (2000) 1005–1013.
[61] T. Matsusaki, K. Kawanabe, K. Ise, T. Nakayama, J. Toguchida, T. Nakamura, Gene expression profile of macrophage-like U937 cells in response to polyethylene particles: a novel cell-particle culture system, J. Arthroplast. 22 (7) (2007) 960–965.
[62] E. Yagil-Kelmer, P. Kazmier, M.N. Rahaman, B.S. Bal, R.K. Tessman, D.M. Estes, Comparison of the response of primary human blood monocytes and the U937 human monocytic cell line to two different sizes of alumina ceramic particles, J. Orthop. Res. 22 (4) (2004) 832–838.